

Site U1417¹

J.M. Jaeger, S.P.S. Gulick, L.J. LeVay, H. Asahi, H. Bahlburg, C.L. Belanger, G.B.B. Berbel, L.B. Childress, E.A. Cowan, L. Drab, M. Forwick, A. Fukumura, S. Ge, S.M. Gupta, A. Kioka, S. Konno, C.E. März, K.M. Matsuzaki, E.L. McClymont, A.C. Mix, C.M. Moy, J. Müller, A. Nakamura, T. Ojima, K.D. Ridgway, F. Rodrigues Ribeiro, O.E. Romero, A.L. Slagle, J.S. Stoner, G. St-Onge, I. Suto, M.H. Walczak, and L.L. Worthington²

Chapter contents

Background and objectives	1
Operations	2
Lithostratigraphy	4
Paleontology and biostratigraphy	10
Stratigraphic correlation	13
Geochemistry	15
Physical properties	20
Paleomagnetism	23
Downhole logging	24
Core-log-seismic integration	29
References	32
Figures	36
Tables	109

Background and objectives

Site U1417 is located in the distal Surveyor Fan in the Gulf of Alaska (Fig. F1). The area was originally drilled at Site 178 (~1.5 km from Site U1417) during Leg 18 of the Deep Sea Drilling Project (DSDP) with ~40% recovery, most of which is Late Pleistocene in age (Fig. F2). Site U1417 is ~60 km from the Surveyor Channel, which delivers sediment to this site via overbank processes (Fig. F3).

Drilling targets were three major regional seismic boundaries and associated seismic sequences mapped by Reece et al. (2011) using reprocessed U.S. Geological Survey and 2004 high-resolution and 2008 crustal-scale seismic reflection data to correlate stratigraphic changes and fan morphology through time (Fig. F4). Sequences I and II exhibit layered, laterally semicontinuous reflectors consistent with distal submarine fan (turbiditic) deposition. Sequence III is thinly layered and contains reflectors that are laterally continuous, flatter, and smoother than those in the other sequences. Stratal relationships at the sequence boundaries are highly variable and greatly influenced by basement topography. Sequence II onlaps Sequence I in the areas where Sequence I exhibits topography, but it is conformable in other locations. Sequence III downlaps Sequence II in parts of the distal fan where both sequences pinch out farther from the Surveyor Channel sediment source. At Site U1417, Sequences I–III appear to be conformable (Fig. F3).

Site U1417 lies at the intersection of two crustal-scale seismic profiles acquired during the 2011 R/V *Marcus Langseth* U.S. Extended Continental Shelf project for the U.N. Law of the Sea (Fig. F5; Walton et al., submitted). The shallow primary target for Site U1417 is the Sequence II/III boundary from Reece et al. (2011), which has been mapped onto the 2011 profiles. This sequence boundary, which is mappable throughout the Surveyor Fan (Fig. F6), is proposed to represent an increase in sediment supply to the site as a result of an intensification of glaciation at the mid-Pleistocene transition (MPT) and subsequent delivery to the site via the Surveyor Channel, ice-rafting, and hemipelagic/pelagic deposition. The deeper primary target is the Sequence I/II boundary (Reece et al., 2011), which was also mapped onto the 2011 data and which is proposed to correspond to the onset of tidewater glaciation and to the start of Surveyor Fan deposition in the late Miocene. Additional divisions of these sequences for the purpose of core-log-seismic integration are discussed in “Core-log-seismic integration” and displayed in Figure F7.

¹Jaeger, J.M., Gulick, S.P.S., LeVay, L.J., Asahi, H., Bahlburg, H., Belanger, C.L., Berbel, G.B.B., Childress, L.B., Cowan, E.A., Drab, L., Forwick, M., Fukumura, A., Ge, S., Gupta, S.M., Kioka, A., Konno, S., März, C.E., Matsuzaki, K.M., McClymont, E.L., Mix, A.C., Moy, C.M., Müller, J., Nakamura, A., Ojima, T., Ridgway, K.D., Rodrigues Ribeiro, F., Romero, O.E., Slagle, A.L., Stoner, J.S., St-Onge, G., Suto, I., Walczak, M.H., and Worthington, L.L., 2014. Site U1417. In Jaeger, J.M., Gulick, S.P.S., LeVay, L.J., and the Expedition 341 Scientists, *Proc. IODP*, 341: College Station, TX (Integrated Ocean Drilling Program). doi:10.2204/iodp.proc.341.103.2014

²Expedition 341 Scientists' addresses.

This site was chosen to provide a sedimentary record of Neogene glacial and tectonic processes occurring in the adjacent orogen (Fig. F8). All of Sequences II and III are estimated to correspond with this time period, which would include both the Miocene tectonic uplift of the St. Elias orogeny and the late Miocene to Pleistocene preglacial to glacial conditions, including the initiation of the northwestern Cordilleran ice sheet (NCIS), the intensification of Northern Hemisphere glaciation, and the potential intensification of glacial extent following the MPT. These sequences should also contain a provenance record reflecting the locus of sediment created during the exhumation and uplift of the St. Elias Mountains.

By drilling into Sequence I, Site U1417 allows examination of deposition prior to the onset of the sedimentation associated with establishment of the Surveyor Channel. The channel is proposed to have formed in response to increased sediment supply from the adjacent coastal mountains, the timing of which may correspond with the initiation of the NCIS (Reece et al., 2011). Sequence I includes several seismic facies (Fig. F7) that may yield clues into the changes in depositional setting from the late Oligocene (approximate age of basement) through the Miocene, as this site tectonically migrated northwest from somewhere near modern day British Columbia toward southern Alaska. These sediments should yield insight into the initial uplift of the St. Elias orogen, which provided the enhanced elevation needed for later glaciation.

The Sequence I/II boundary occurs at ~330 m within the drilled interval at Site 178, within a section of fine-grained sand to silty turbidites and interbedded diatomaceous ooze and mud with increasing diamict upsection (Kulm, von Huene, et al., 1973; Reece et al., 2011). The Sequence I/II boundary was dated to be ~5 Ma by Reece et al. (2011), near the beginning of Glacial Interval A of Lagoe et al. (1993), based on $^{40}\text{Ar}/^{39}\text{Ar}$ dating of ash layers (Hogan et al., 1978) (Fig. F2). At ~130 m at Site 178, the Sequence II/III boundary lies within an interval of changing fan lithology. The section from 96 to 141 m contains abundant diamict interbedded with silty clay and diatom-rich intervals, whereas the section from 141 to 280 m contains less diamict, much more silty clay, and fewer diatoms (Kulm, von Huene, et al., 1973; Reece et al., 2011). The Sequence II/III boundary was tentatively dated to ~1 Ma based on correlation with the upper Jaramillo (1r.1n) Subchronozone magnetic polarity reversal identified at Site 178 (Reece et al., 2011) (Fig. F2), making it coincident with the onset of Glacial Interval C of Berger et al. (2008a). Both sequence boundaries are synchronous with doubling of terrigenous sediment flux observed at Ocean Drill-

ing Program (ODP) Site 887 at ~6 and ~1 Ma (Rea and Snoeckx, 1995), but no regional sequence boundary projected into Site 178 appears to correlate with the onset of Glacial Interval B (Reece et al., 2011) based on the $^{40}\text{Ar}/^{39}\text{Ar}$ ages of Hogan et al. (1978) (Fig. F2).

Key lithologies of interest as observed in Site 178 cores include tephtras and other volcanoclastic detritus, variable amounts of ice-rafted debris, biosiliceous-rich intervals, turbidites, and general changes in depositional processes from prefan sedimentation to modern overbank deposition sourced from the Surveyor Channel, ~60 km east of the site. Important contributions to hypothesis testing at this site will come from biostratigraphic and paleomagnetic age models, physical properties changes, and evolution in sedimentary facies in an increasingly glacially influenced setting.

Operations

Transit to Site U1417

After a 1038 nmi transit from Victoria, British Columbia (Canada), averaging 10.8 kt, the vessel arrived at Site U1417. The vessel stabilized over the site at 1101 h (UTC – 8 h) on 4 June 2013. The positioning beacon was deployed at 1121 h on 4 June and remained on the seafloor for the duration of the week. The position reference was a combination of GPS signals and a single acoustic beacon.

Site U1417

Site U1417 consists of five holes (Table T1), ranging in depth from 168.0 to 709.5 m drillers depth below seafloor (DSF) (Fig. F9). A total of 198 cores were recorded for the site. The interval cored with the advanced piston corer (APC) system was 836.5 m, with 811.18 m recovered (97%). The interval cored with the extended core barrel (XCB) system was 381.8 m, with 140.77 m recovered (36.9%). The interval cored with the rotary core barrel (RCB) system was 348.7 m, with 146.92 m recovered (42.1%). The overall recovery for Site U1417 was 70.1%. Total time spent on Site U1417 was 18.6 days.

Hole U1417A

Hole U1417A was spudded at 0315 h on 5 June 2013. The seafloor was calculated to be 4198.6 m drillers depth below rig floor (DRF) (4187.7 meters below sea level). Nonmagnetic core barrels and the APC system were used for Cores 341-U1417A-1H through 20H. Temperature measurements were taken with the advanced piston corer temperature tool (APCT-3) on Cores 4H, 10H, and 13H with good results. APC cor-

ing with the wireline continued through Core 22H with the half APC coring system using steel core barrels. Partial APC strokes were recorded on Cores 6H, 8H, 18H, 19H, 20H, and 21H. The early incomplete strokes were likely due to an obstruction caused by large limestones. Hole U1417A was terminated after Core 22H (168.0 m DSF). At the conclusion of coring, the top drive was set back and the drill string was pulled from the hole. The seafloor was cleared at 0935 h on 6 June, ending Hole U1417A. A total of 22 piston cores were taken over a 168.0 m interval, with 167.74 m recovered (99.8%).

Hole U1417B

After clearing the seafloor, the vessel was offset 20 m east of Hole U1417A. Hole U1417B was spudded at 1225 h on 6 June 2013. Initially, orientation was planned, and the FlexIT tool was deployed. High heave conditions and mechanical shearing forced abandonment of core orientation measurements in Hole U1417B. Nonmagnetic core barrels and the APC system were used for Cores 341-U1417B-1H through 20H. Cores 21H through 33H were cored using the half APC coring system. The XCB system was deployed for Cores 34X through 47X. Hole U1417B was terminated after Core 47X (358.8 m DSF). At the conclusion of coring, the top drive was set back and the drill string was pulled from the hole. The seafloor was cleared at 1645 h on 9 June, ending Hole U1417B. A total of 33 piston cores were taken over a 223.4 m interval, with 211.97 m recovered (94.9%). A total of 14 XCB cores were cut over a 135.4 m interval, with 50.99 m recovered (37.7%). Total core recovery for Hole U1417B was 262.96 m for the 358.8 m cored interval (73.3%).

Hole U1417C

After clearing the seafloor, the vessel was offset 20 m south of Hole U1417B. Hole U1417C was spudded at 1950 h on 9 June 2013, and the hole was washed down 1 m DSF. Orientation with the FlexIT tool was performed for Cores 341-U1417C-3H through 20H with satisfactory results. Nonmagnetic core barrels and the APC system were used for Cores 2H through 25H. Cores 26H through 29H were cored using the half APC coring system. Hole U1417C was terminated after Core 29H. The final depth of Hole U1417C was 226.0 m DSF. At the conclusion of coring, the top drive was set back and the drill string was pulled from the hole. The seafloor was cleared at 0725 h on 11 June, ending Hole U1417C. A total of 28 piston cores were taken over a 225.0 m interval, with 216.83 m recovered (96.4%).

Hole U1417D

After clearing the seafloor, the vessel was offset 20 m west of Hole U1417C. Hole U1417D was spudded at 1155 h on 11 June 2013. Nonmagnetic core barrels and the APC system were used for Cores 341-U1417D-1H through 18H. After Core 18H, the half APC coring system was deployed, and APC coring continued through Core 37H. After Core 20H, a 3.8 m interval was drilled. The XCB system was deployed starting with Core 38X. Coring with the XCB system continued through Core 59X, when the XCB cutting shoe returned to the surface without the cutting structure plus another 1 inch of the length of the shoe. Another XCB core barrel was dropped and was also damaged on recovery. The cutting shoe was then changed to a “softer sediment” type shoe, and coring continued. There was continuing evidence of an obstruction remaining in the hole, and after two more cutting shoe failures, coring was terminated after Core 65X at a final depth of 470.3 m DSF. The drill string was then pulled from the hole, and the bit cleared the rotary table at 1430 h on 16 June, ending Hole U1417D. A total of 36 piston cores were taken over a 220.1 m interval, with 214.64 m recovered (97.5%). One drilled interval during the APC section of the hole was 3.8 m long. A total of 28 XCB cores were cut over a 246.4 m interval, with 89.78 m recovered (36.4%). Total core recovery for Hole U1417D was 304.42 m for the 466.5 m cored interval (65.3%).

Hole U1417E

After clearing the seafloor, the vessel was offset 20 m west of Hole U1417D. Hole U1417E was spudded at 0230 h on 17 June 2013, and the hole was drilled down to 264 m DSF. The wash barrel was then pulled, and Cores 341-U1417E-2R through 5R were cut to 302.2 m DSF. The wash barrel was again deployed, and the hole was advanced with a drilled interval to 399.0 m DSF. The wash barrel was pulled, and RCB coring with nonmagnetic RCB core barrels began with Core 7R and continued through Core 39R to a final depth of 709.5 m DSF. In total, 37 rotary cores were taken over a 348.7 m interval, with 146.92 m recovered (42.1%). There were two drilled intervals in Hole U1417E that added up to 360.8 m of advance without recovery.

A total of 195 bbl of high-viscosity mud was used during the drilling/coring process, and at the conclusion of the drilling/coring phase of Hole U1417E, an additional 50 bbl sweep of high-viscosity mud was pumped to condition the hole for logging. After pumping the final sweep, the rotary shifting tool was

deployed by wireline and the shifting sleeve inside the mechanical bit release was pulled, releasing the bit at the bottom of Hole U1417E. After releasing the bit, the sleeve was shifted back and the top drive was set back. The drill string was then tripped out of the hole, and the end of pipe was set at 81.4 m DSF for logging.

The triple combo tool string was then rigged up and run into the hole, reaching a total depth of 624.0 m wireline log depth below seafloor (WSF) at 0245 h on 21 June. The hole was then logged up, a short repeat pass was recorded, and the tools were pulled to the surface and rigged down. After rigging down the triple combo tool string, the Versatile Seismic Imager (VSI) tool string was rigged up. During the rig up time, the Protective Species Observation watches began, and it became immediately apparent that a small group of northern fur seals were present within the 940 m diameter exclusion zone for this site. The decision was made to terminate the VSI run for the day, pull back the VSI tool string, rig down, and prepare the Formation MicroScanner (FMS)-sonic tool string for deployment. The FMS-sonic tool string was then rigged up and deployed to 571.5 m WSF. Two full passes were made with the tool string, and it was then pulled to the surface and rigged down. The Magnetic Susceptibility Sonde (MSS) tool string was then rigged up and run; this run was the first deployment of the full MSS tool during the Integrated Ocean Drilling Program (IODP). The maximum depth the MSS tool string reached was 204.0 m WSF because of a constriction in the hole. This shallow part of the hole was then logged with two runs, and the tool string was pulled to the surface and rigged down. The VSI tool string was then rigged up and run into the hole. Protective Species Observation watches began at first light. No protected marine species were observed during this period within the exclusion zone, so the seismic source (a parallel cluster of two 250 inch³ Sercel G. Guns) was ramped up starting 1 h after the watches commenced. Watches continued throughout the VSI run, with the guns fired manually as the tool string was run into the hole. The guns were powered down because of the presence of a whale during the manual firing stage. The whale entered the exclusion zone when the guns were powered down and then exited the exclusion zone. As the whale was observed to exit the zone within a short period of time, the guns were then ramped back up using a soft start procedure. Once the VSI tool string was in the hole, firing control was delivered to the Schlumberger engineer. After attempting to position the tool at the deepest possible depth and then moving it up to shallower stations, only one station was successfully completed

at ~211 m WSF, which consisted of two good shots. The tool string was pulled out of the hole to the surface and rigged down. The guns were secured, and the Protective Species Observation watches ceased. All logging equipment was rigged down by 1605 h on 22 June, and the knobbies were removed from the drill string. The drill string was then pulled from the hole.

Lithostratigraphy

Lithologic summaries of the five holes drilled at Site U1417 are shown in Figure F10. The sediment recovered at Site U1417 contains 17 facies. Detailed facies descriptions, information about common marine microfossils, facies occurrence in lithostratigraphic units, and tentative interpretations about depositional environments are summarized in Table T2. The dominant facies (F1a and F1b) are gray (N 4) to dark greenish gray (10Y 4/1) mud and account for >90% of the core recovered. The remaining minor facies, although much less volumetrically significant, are distinctive and allow us to organize the cores into lithostratigraphic units. Photographs of the more common facies are shown in Figure F11. Based on characteristic facies associations, 5 major lithostratigraphic units and 12 subunits are defined (Table T3).

Facies description

Seventeen lithofacies were identified and are outlined in Table T2. The description of the facies for this site is based on the general lithofacies developed for all Expedition 341 sites. Lithofacies described at this site include massive mud with lonestones (F1a); massive mud without lonestones (F1b); silt (F2a); interbedded silt and mud (F2b); very fine to coarse sand (F3a); medium to coarse sand (F3b); interbedded sand and mud (F3c); muddy diamict (F4a); muddy and sandy diamict with lithic and mud clasts and/or terrigenous organic components (F4b); breccia (F4c); interbedded mud and diamict (F4d); diatom ooze (F5a); biosiliceous ooze (F5b); calcareous/carbonate-bearing/rich mud, silt, sand, diamict, and/or diatom ooze (F5c); volcanic ash (F6); volcanoclastic mud and sand (F7); and rock (F8). These facies reflect deposition from suspension fall out, sediment gravity flows, ice rafting, variations in organic productivity, volcanic eruptions, and eolian processes.

The lonestone-bearing, massive and bioturbated mud of Facies F1a is dark gray (N 4) to dark greenish gray (10Y 4/1) (Fig. F11A–F11B; Table T2). Color banding in this facies ranges from gray (N 4) to dark greenish gray (10Y 4/1), and individual bands range

in thickness from 0.1 to 5 cm. Bioturbation ranges from moderate to complete (for bioturbation scale, see “**Lithostratigraphy**” in the “Methods” chapter [Jaeger et al., 2014]). Based on smear slides, the composition of the mud is on average 90% clay size particles and 10% silt particles, with no apparent compositional differences between different color bands. Microfossil content is variable. Biosiliceous components are predominantly diatom microfossils, but minor amounts of sponge spicules and nannofossils are also documented. Lonestone clasts consist mainly of argillite and metasiltstone with secondary amounts of metabasalt and minor amounts of granite and sandstone (Fig. F12A–F12D). Facies F1b (Table T2) consists of greenish gray (10Y 5/1) to dark gray (N 4) mud without lonestones. Microfossil content is variable, as in Facies F1a. *Zoophycos* burrows are common in this facies, and relative to Facies F1a, color banding is not common. Petrographically, the composition of Facies F1b is similar to that of Facies F1a. In a minor number of beds in Facies F1b, diatoms, sponge spicules, and burrows have been pyritized (Fig. F12K).

Facies F2a and F3a (Table T2) consist of very thin to thin silt and sand beds (Fig. F11B) and are discussed together because of their common occurrence in the cores from Site U1417. These two facies range in color from dark gray (N 4) to greenish gray (5GY 5/1) and are mostly interbedded with the mud of Facies F1a and F1b. The silt and sand beds have sharp and sometimes erosional lower contacts with the underlying mud and primarily gradational upper contacts (Fig. F11B). Load casts occur along the bases of some beds in this facies (Fig. F12E). Individual bed thicknesses are 1–5 cm, and normal grading is common. These facies are often well sorted and contain little fine-grained matrix. The grain composition of these two facies is almost entirely quartz and feldspar, with minor amounts of heavy minerals. Quartz in these facies is monocrystalline, and few lithic grains are documented. Less common are silt and sand beds rich in mafic components such as hornblende, biotite, and opaque minerals. The more mafic silt and sand beds are also enriched in heavy minerals relative to the more quartzofeldspathic sand and silt in this facies. In general, quartzofeldspathic sand and silt comprise ~85% of the total sand and silt in these facies. Facies F2b consists of dark gray (N 4) to very dark gray (N 3) interbedded silt and mud. Lower contacts of silt laminae are most often sharp. Upper contacts are sharp or gradational. Bioturbation is none to slight.

Facies F3b (Table T2) consists of dark gray (N 4) to gray (N 5) medium to coarse sand and is distinguished from Facies F3a by its accessory components

(Fig. F11E). This facies often has a sharp lower contact and a gradational upper contact. Bed thickness is up to 40 cm, but average bed thickness is ~10–20 cm. The sand has a very muddy matrix, and intraformational rip-up clasts are common (Fig. F11F). Coal clasts and woody detritus also occur in this facies (Figs. F11E, F12G–F12J). Based on smear slides, the composition of sand in Facies F3b is lithic rich with sedimentary (mainly mudstone and siltstone), volcanic, and metasedimentary (mainly argillite) grains. These sand beds also contain more mica than other sand facies at Site U1417. In smear slides, most mica appears to be biotite, but lighter colored micas are also identified in the visual core descriptions. Quartz in this facies is mainly monocrystalline, but polycrystalline quartz grains are also identified. Heavy minerals are a common minor constituent of Facies F3b. Facies F3b is gradational with the sandy diamict of Facies F4b. Facies F3c consists of interbedded sand and mud (Table T2). This facies is between 7 and 710 cm thick. Graded sand beds have sharp lower boundaries and sharp upper boundaries. Bioturbation is mostly absent in this facies.

Muddy diamict in Facies F4a (Table T2) is characterized by a dark gray (N 4) mud-rich matrix. Distinctive features of this facies are gradational lower contacts and sharp upper contacts defined by the relative clast concentration (Fig. F11C). Common clast sizes are granule and pebble, with clasts being subangular to subrounded. Based on smear slides, the composition of the sand fraction is primarily quartzofeldspathic. Facies F4b consists of muddy and sandy diamict with bed thickness up to 40 cm and containing predominantly mud clasts and/or organic components (Table T2; Fig. F11D). A sand and mud matrix with large outsized intraformational clasts characterizes this facies. Mud clasts can reach 3 cm in diameter. Other common clast types are coal and woody debris. These beds have sharp upper and lower contacts. Petrographically, this facies is characterized by more lithic grains in the sand fraction, similar to those described for Facies 3b, which occurs in close association with Facies F4b. Facies F4c consists of breccia with poorly organized clasts, and most of the clasts appear to be indurated diatom ooze. Internally, individual clasts contain evidence of soft-sediment deformation. Facies F4d consists of dark gray (N 4) interbedded mud and diamict (Table T2). Diamict beds often have gradational lower and sharp upper boundaries. Clasts within the diamict are up to 3 cm in diameter and are predominantly composed of mud clasts.

Facies F5a is characterized by dark gray (N 4) diatom ooze (Table T2; Fig. F11G–F11H). By definition, lithostratigraphic units with this facies contain >50% diatoms (see “**Lithostratigraphy**” in the “Methods”

chapter [Jaeger et al., 2014]). The remaining constituents in this facies are typically mud, and in some cases calcareous mud is documented. Contacts vary between gradational and sharp. Bed thickness for Facies F5 varies from 20 to 150 cm. Bioturbation is common in this facies, including *Zoophycos* burrows (Fig. F11G–F11H).

Facies F6 is defined by gray (5Y 4/1) to brown (5YR 5/3) volcanic ash (Fig. F13). Bed contacts range from sharp to gradational. Compositionally, this facies consists of 80% glass shards (vitric fragments). The remaining framework grains are feldspar, quartz, and opaque minerals. Dark gray (N 4) volcanoclastic mud and sand define Facies 7 (Fig. F13E–F13F). Bed thickness ranges from 1 to 5 cm. These beds consist of a mixture of volcanic glass (typically 10%–20%), quartz, feldspar, and often diatom microfossils. Beds are often bioturbated.

Facies 8 consists of dark gray (N 4) lithified siltstone with abundant calcite cement. These beds occur sporadically and are often associated with poor core recovery.

Lithostratigraphic units

Based on facies associations, five major lithostratigraphic units (I–V) are defined (Table T3; Fig. F10). Units I and V are further divided into subunits. The contacts between lithostratigraphic units at Site U1417 are usually gradational, and the criteria used to define units are discussed below.

Unit I

Subunit IA

Intervals: 341-U1417A-1H-1, 0 cm, to 11H-2, 18 cm; 341-U1417B-1H-1, 0 cm, to 10H-2, 131 cm; 341-U1417C-2H-1, 0 cm, to 10H-2, 48 cm; 341-U1417D-1H-1, 0 cm, to 10H-3, 38 cm

Depths: Hole U1417A = 0–77 m core depth below seafloor (CSF-A); Hole U1417B = 0–79.4 m CSF-A; Hole U1417C = 0–77 m CSF-A; Hole U1417D = 0–78.8 m CSF-A

Age: Middle Pleistocene to Holocene

Subunit IA contains dark gray (N 4) mud (Fig. F11A) with subordinate interbeds of volcanic ash as thick as 4 cm (Table T3; Fig. F13A–F13C). Dispersed granule- to pebble-sized limestones (outsized clasts) are common. Limestone clasts consist mainly of argillite and metasiltstone, with secondary amounts of metabasalt and minor amounts of granite and sandstone (Fig. F12A–F12D). Greenish gray (10Y 5/1) intervals of diatom-bearing mud with approximately five diatom ooze layers between 20 and 40 cm thick alternate with barren gray (N 5) mud. Volcanic ash con-

sists of >80% vitric (glass) framework grains (Fig. F13). Although volcanic ash (>90% primary volcanic grains; see “Lithostratigraphy” in the “Methods” chapter [Jaeger et al., 2014]) comprises <1% of the total described lithology of this subunit, it is considered important. The relative volcanic grain abundance is plotted on the summary diagrams for each hole for reference (Fig. F10).

Subunit IB

Intervals: 341-U1417A-11H-2, 18 cm, to 22H-CC, 38 cm; 341-U1417B-10H-2, 131 cm, to 17H-CC, 17 cm; 341-U1417C-10H-2, 48 cm, to 18H-3, 18 cm; 341-U1417D-10H-3, 38 cm, to 22H-1, 0 cm

Depths: Hole U1417A = 77–168 m CSF-A (bottom of hole); Hole U1417B = 79.4–151.9 m CSF-A; Hole U1417C = 77–154.1 m CSF-A; Hole U1417D = 78.8–166.3 m CSF-A

Age: early to Middle Pleistocene

This subunit shares all lithologic characteristics with Subunit IA; however, it also includes intervals of diatom ooze that occur frequently, with as many as five intervals per core (Table T3; Fig. F11G–F11H). Ooze intervals are generally <10 cm thick. Dispersed granule- to pebble-sized limestones are more common than in Subunit IA. Silt and sand beds are 2–4 cm thick (Fig. F11B). Volcanic ash (>90% primary volcanic grains; see “Lithostratigraphy” in the “Methods” chapter [Jaeger et al., 2014]) represents <1% of the total described lithology of this subunit and consists of >80% vitric (glass) framework grains.

Unit II

Intervals: 341-U1417B-17H-CC, 17 cm, to 37X-CC, 30.5 cm; 341-U1417C-18H-3, 18 cm, to 29H-CC, 7 cm; 341-U1417D-22H-1, 0 cm, to 42X-1, 85 cm

Depths: Hole U1417B = 151.9–256.2 m CSF-A; Hole U1417C = 154.1–226 m CSF-A (bottom of hole); Hole U1417D = 166.3–263.5 m CSF-A

Age: early Pleistocene

This unit is identified by distinct 1–5 cm thick interbeds of fine sand and coarse silt in dark gray (N 4) to greenish gray (10Y 5/1) mud. Mud beds are massive to normally graded and commonly have sharp lower contacts (Table T3). Sand/silt beds occur in the mud at irregularly spaced intervals ranging from 5 to 15 cm. Relative to Unit I, this unit contains fewer limestones; however, they occur throughout the unit and range up to as many as eight clasts per section. Volcanic ash beds are present, with eight beds distributed over Unit II. Diatom-rich intervals, including thin beds of ooze, similar to those in Unit I occur near the top of Unit II.

Unit III

Intervals: 341-U1417B-38X-1, 0 cm, to 41X-1, 40 cm; 341-U1417D-42X-1, 85 cm, to 46X-1, 92 cm; 341-U1417E-2R-1, 7.5 cm, to 5R-CC, 10 cm

Depths: Hole U1417B = 256.2–291.3 m CSF-A; Hole U1417D = 263.5–296.6 m CSF-A; Hole U1417E = 264.1–297.3 m CSF-A

Age: early Pleistocene

This unit is bounded by the first and last occurrences of 4–8 cm thick beds of muddy diamict interbedded with intervals of bioturbated dark gray (N 4) mud up to 40 cm thick (Table T3; Fig. F11C). Core disturbance makes this relationship difficult to observe in many cases. Diamict intervals contain gravel-sized subangular to subrounded clasts in a muddy matrix and have gradational lower contacts and typically sharp upper contacts. Clast abundance increases up-hole in individual beds. Common clast types include argillite and metasiltstone, with secondary amounts of metabasalt.

Unit IV

Intervals: 341-U1417B-41X-1, 40 cm, to 47X-CC, 26 cm; 341-U1417D-46X-1, 92 cm, to 50X-1, 63 cm

Depths: Hole U1417B = 291.3–350.0 m CSF-A (bottom of hole); Hole U1417D = 296.6–335.1 m CSF-A

Age: late Pliocene

Unit IV contains dark gray (N 4) to dark greenish gray (5GY 4/1) clay-rich mud that is commonly highly bioturbated. *Zoophycos* burrows and diatom-bearing intervals as thick as 140 cm are common (Fig. F11G). Lonestones are absent.

Unit V

Intervals:

VA: 341-U1417D-50X-1, 63 cm, to 56X-CC, 19 cm;
 VB: 341-U1417D-56X-CC, 19 cm, to 60X-CC, 10 cm; 341-U1417E-7R-1, 0 cm, to 10R-3, 0 cm;
 VC: 341-U1417D-60X-CC, 10 cm, to 65X-CC, 21 cm; 341-U1417E-10R-3, 0 cm, to 15R-1, 66 cm;
 VD: 341-U1417E-15R-1, 66 cm, to 15R-6, 55 cm;
 VE: 341-U1417E-15R-6, 55 cm, to 29R-3, 11 cm;
 VF: 341-U1417E-29R-3, 11 cm, to 29R-CC, 17 cm;
 VG: 341-U1417E-29R-CC, 17 cm, to 32R-2, 0 cm;
 VH: 341-U1417E-32R-2, 0 cm, to 35R-1, 53 cm;
 VI: 341-U1417E-35R-2, 0 cm, to 39R-6, 13 cm;
 VJ: 341-U1417E-39R-6, 13 cm, to 39R-CC, 23 cm

Depths:

VA: Hole U1417D = 335.1–394.3 m CSF-A;
 VB: Hole U1417D = 394.3–432.0 m CSF-A, Hole U1417E = 399.0–431.0 m CSF-A;
 VC: Hole U1417D = 432.0–461.5 m CSF-A (bottom of hole), Hole U1417E = 431.0–477.7 m CSF-A;
 VD: Hole U1417E = 477.7–484.6 m CSF-A;
 VE: Hole U1417E = 484.6–615.4 m CSF-A;
 VF: Hole U1417E = 615.4–619.0 m CSF-A;
 VG: Hole U1417E = 619.0–642.8 m CSF-A;
 VH: Hole U1417E = 642.8–661.5 m CSF-A;
 VI: Hole U1417E = 661.5–705.9 m CSF-A;
 VJ: Hole U1417E = 705.9–708 m CSF-A (bottom of hole)

Age: Miocene to Pliocene

Unit V contains predominantly dark gray (N 4) mud with subordinate muddy and sandy diamict, interbedded silt/mud and sand/mud, and diatom ooze (Table T3). Because Unit V is highly diverse, it is divided into 10 subunits to differentiate biosiliceous-rich (diatom ooze) intervals from intervals dominated by terrigenous sediment flux (Fig. F10E). Subunits VA, VC, VE, VG, and VI consist mainly of dark gray (N 4) mud, sandy diamict with lithic and mud clasts up to 3 cm diameter, and plant fragments (Fig. F11D); massive and graded sand beds (Fig. F11E–F11F); interbedded silt and mud; and occasional diatom-rich intervals and diatom ooze. The top of Subunit VA is defined by the first occurrence of a 50 cm thick very dark gray (5Y 3/1) sand bed underlain by a sandy diamict bed. Within the subunit, three other sand beds and six other diamict intervals are interbedded with biosiliceous-bearing mud or diatom ooze. The diamict beds contain lithic and mud clasts, as well as plant fragments. Subunit VC has similar characteristics, with mud clasts and coal in the diamict beds. Subunit VE is defined by diamict containing coal clasts interbedded with dark greenish gray (10Y 4/1) interbedded silt and mud. Subunit VG is defined by the occurrence of normally graded sandy mud beds ranging in thickness from 10 to 60 cm interbedded with mud. These sand beds include mud clasts and granules of coal. Subunit VI is interbedded similarly to Subunit VG, except that the intervals of muddy silt are as thick as 180 cm. Fine-grained Subunits VB, VD, VF, VH, and VJ consist mainly of dark gray (N 4) mud with diatom-rich intervals and diatom ooze, the latter occasionally exceeding 150 cm in thickness. Color banding also can be a characteristic feature of these subunits (Fig. F11H). Of these, Subunit VF is most notable because it includes a breccia bed that is 80 cm thick. In Unit V, ash (Fig. F13) and extensional deformation structures (Fig. F12F) are observed occasionally. Plant de-

bris and terrestrial organic detritus (coal) are components of the sandy diamict (Figs. F11E, F12G–F12J).

Petrography

Clast lithologies

The main lithologies of the diamict clasts and lonestones contained in Site U1417 sediment are of low-grade metamorphic origin. In decreasing order of abundance, the lithologies are argillite, metasiltstone, and basalt. Sandstone, siltstone, granite, and quartzite are minor lithologies. These lithologies are unevenly distributed between Holes U1417A–U1417E. The average clast ratio for Site U1417, based on the main lithology types metamorphic (M), sedimentary (S), and igneous (I), is $M_{73}S_{15}I_{12}$.

Bulk mineralogy

X-ray diffraction (XRD) analyses were performed on 131 powdered bulk samples from Holes U1417A–U1417E to delineate the bulk mineralogy and identify compositional trends with age or depth in the cores. Diffraction patterns are shown in Figure F14, and the relative mineral diffraction peak intensities, as defined in “Lithostratigraphy” in the “Methods” chapter (Jaeger et al., 2014), are listed in Table T4. In general, the mineralogy is uniform downhole, although there are some variations in relative peak intensities, which may indicate slight variations in mineral content. Figure F14A shows the scans for 14 representative samples from this site. The primary minerals identified include quartz, plagioclase (feldspar), mica (muscovite/illite and biotite), and the minerals chlorite and/or kaolinite. Quartz and plagioclase are the dominant peaks, with quartz generally the larger. Figure F14B shows the comparative XRD patterns from 4° to $24^\circ 2\theta$, where scans run before and after the samples underwent a glycol treatment (see “Lithostratigraphy” in the “Methods” chapter [Jaeger et al., 2014]). This treatment was used to determine the presence of expandable clay minerals (e.g., smectite). The scans show no indication of expandable clay minerals until ~ 100 m core composite depth below seafloor (CCSF-B) in the cores. From this depth downhole, we observe a shoulder at $\sim 7^\circ 2\theta$ in the samples. After the treatment, a small but distinct peak is observed at $\sim 5^\circ 2\theta$, suggesting the presence of expandable clay minerals. Additional minor mineralogical phases documented in the bulk mineralogy of the cores include calcite associated with well-indurated siltstone intervals and pyrite associated with localized structures such as burrows (Fig. F12K). These phases are most common in lithostratigraphic Unit V. Our preliminary findings are similar to the results of Molnia and Hein (1982) from sam-

ples collected on the continental shelf of the Gulf of Alaska.

Physical properties characteristics of selected lithologies

We integrated physical properties data measured using the onboard core logging systems with our sediment core and smear slide descriptions in an attempt to establish relationships that could be used to map the distribution of selected sedimentary attributes and facies at a higher resolution. Sand, volcanic ash, diatom ooze, lonestones, and diamict beds exhibit somewhat unique variations in magnetic susceptibility, bulk density, natural gamma radiation (NGR), *P*-wave velocity, and color reflectance that can be used to highlight and predict downcore distribution of lithologic features. Because dark gray (N 4) mud is the dominant lithology observed at Site U1417, the physical properties data provided a relatively fast method to identify variations in lithology and identify potential intervals of interest for further study.

Figure F15 provides an example of this comparative technique where downcore variations in magnetic susceptibility, bulk density, NGR, and color reflectance are compared to sediment lithology seen in core imagery and smear slide photomicrographs across the lithostratigraphic Subunit IB–Unit II transition in Hole U1417C. Units of diatom ooze centered at 146.6, 147.25, and 148 m CSF-A are lighter gray in core imagery and correspond with relatively low magnetic susceptibility, gamma ray attenuation (GRA) bulk density, and NGR values and relatively high reflectance index values. We use a color reflectance index calculated from the absolute value of a^*/b^* , which appears to capture the contrast in sediment color across the transitions between mud and ash, ooze, and sand/silt beds. A volcanic ash bed and mafic-rich sand centered between 146.25 and 146.5 m CSF-A result in a complex physical properties data response with respect to magnetic susceptibility. The divergence can be attributed to the difference in mineralogy between the two beds, where the mafic-rich sand has elevated magnetic susceptibility. An interval of interbedded sand and mud centered at 149.8 m CSF-A is well defined by higher magnetic susceptibility and higher color reflectance index values, which mirror the magnetic mineral content of the sand and the change in color across the sand beds, respectively.

Lithostratigraphy and depositional environments

Major characteristics that define the lithostratigraphic units for Site U1417 are summarized in Figure F16.

Unit I

Lithostratigraphic Subunits IA and IB consist mainly of dark gray (N 4) mud with limestones and recurring intervals of diatom ooze in Subunit IB (Tables T2, T3). Limestones are interpreted to be ice-rafted debris deposited from icebergs. The presence of limestones thus seems to be evidence for tidewater glaciation. Our interpretation is that most of the mud in Unit I originated from suspension settling through the water column and from sediment gravity flows reaching the distal portions of the Surveyor Fan (Powell and Molnia, 1989). Sediment reworking and deposition could also be related to temporal variations in bottom current strength and direction. Recurring intervals of diatom ooze in Subunit IB might be related to one or several of the following processes:

- Increased biological productivity in the water column in the vicinity of sea ice margins (Sakshaug, 2004; Smith et al., 1987);
- Increased biological productivity due to optimized oceanographic conditions (e.g., reduced sea ice cover, surface layer overturning, and/or mixing by gyres);
- Enhanced macro (N or P) and/or micro (Fe) nutrient supply from land (volcanic ash, dust, etc.), leading to increased biological productivity (Hamme et al., 2010; Davies et al., 2011; Addison et al., 2012);
- Seawater silica saturation, leading to higher diatom productivity and preservation (e.g., Brzezinski et al., 1998; Dugdale et al., 1995); and/or
- Decreased input of terrigenous sediments (i.e., less dilution).

The source for some of the sediment represented by Unit I is interpreted to be the onshore St. Elias and Chugach Mountains located along the southern coast of Alaska. The dominance of low-grade metamorphic lithologies in the limestones suggests that the Chugach Metamorphic Complex (Gasser et al., 2011) may have been a primary ice-rafted debris source during deposition of both Subunits IA and IB. The fairly even distribution of volcanic ash and volcanoclastic-bearing sand indicates that the location was proximal enough to either the Aleutian or Wrangell volcanic belts to have periodic influxes of pyroclastic detritus.

Unit II

We infer that sedimentary processes in Unit II were generally similar to depositional processes in Unit I (i.e., that sediment supply mainly occurred from suspension fallout, sediment gravity flows, and ice-

bergs). However, the increased number of thin beds of fine sand and coarse silt suggests more frequent and more regular deposition from sediment gravity flows (e.g., low-density turbidity flows) (Lowe, 1982) on the distal Surveyor Fan. In addition, the relative absence of diatom ooze intervals may reflect reduced productivity in the water column. This reduced productivity might be caused by one or several factors, including (1) increased sea ice coverage or a larger distance to the sea ice edge, (2) limited nutrient supply, (3) secondary diagenetic processes (such as the dissolution of silica), and/or (4) increased dilution of biogenic-rich intervals by terrigenous sediment.

Unit III

Unit III is characterized by muddy diamict interbedded with bioturbated dark gray (N 4) mud. As in Units I and II, our interpretation is that the muddy sediment was deposited from suspension, as well as from distal sediment gravity flows and icebergs. The limestones in Unit III are the oldest observed in the sedimentary record at Site U1417 (early Pleistocene or late Pliocene), and they reflect the first appearance at this site of iceberg-derived sediment from calving of tidewater glaciers into the Gulf of Alaska. The accumulation of clasts that form diamict intervals in Unit III in Holes U1417B, U1417D, and U1417E potentially record periods of significantly enhanced ice rafting and/or reduced deposition of mud. Whereas the gradational lower boundaries of the diamict beds most probably mirror a gradual increase in ice rafting, an abrupt termination in ice rafting may have led to the formation of a sharp upper boundary and the onset of “nonglacial” conditions as indicated by the deposition of mud and enhanced bioturbation. The repeated occurrence of couplets of muddy diamict and mud may reflect (1) the recovery of deposits from multiple glacial and interglacial cycles, (2) temporarily increased ice rafting due to enhanced calving from the glacier margin, or (3) dumping from icebergs. Because the pattern of gradual onset and abrupt termination of ice rafting is very similar to “typical” glacial–interglacial cycles, we suggest that the deposits may archive large-scale climatic changes. Further refinement of the shipboard age model may be necessary to confirm this.

Unit IV

The main characteristics of Unit IV are intense bioturbation and diatom-bearing intervals, the absence of limestones, and the presence of isolated fine sand beds. The more intense bioturbation is suggestive of limited terrigenous sediment influx and/or more productive water column conditions.

Unit V

Unit V is divided into subunits to distinguish periods of reduced terrigenous sediment supply and higher biological productivity and/or better preservation (diatom ooze; Subunits VB, VD, VE, VH, and VJ) from periods of higher flux of terrigenous sediment (mud; Subunits VA, VC, VE, VG, and VI). Both periods are interrupted by muddy and sandy diamict deposition. The diamict is interpreted to be deposited from sedimentary gravity flows (e.g., high-density turbidity flow) (Lowe, 1982). A distinctive characteristic of Unit V is the presence of coal clasts and woody plant detritus in the sandy diamict facies (Figs. F11E, F12I–F12J). These components are tentatively interpreted to be derived from the coal-bearing Eocene Kulthieth Formation exposed in the onshore thrust belt in the St. Elias and Chugach Mountains (e.g., Plafker, 1987). Other unique characteristics of Unit V are small normal faults (commonly <2 cm of displacement) in the lower parts of Hole U1417E (Fig. F12F). These faults may be related to deformation along the outer rise of the Pacific plate due to subduction at the Aleutian Trench west of Site U1417. Many active normal faults have been mapped in this portion of the Pacific plate and are related to plate-bending processes (Reece et al., 2013).

The provenance of the sediment documented in Unit V is unclear. A southeastward restoration of the position of the Pacific plate (i.e., accounting for current northwest plate vectors) may show that these submarine fan systems were supplied with sediment from the coastal mountains of the Yukon Territory and northwestern British Columbia (e.g., the Coast Plutonic Complex). However, more detailed provenance studies are required to verify the locations of onshore sources of sediment for Unit V.

Paleontology and biostratigraphy

Samples from Site U1417 reveal rich assemblages of siliceous microfossils, whereas calcareous microfossils are less abundant in most intervals. Diatoms and radiolarians are abundant to rare and well to poorly preserved in several intervals. These diatom and radiolarian assemblages permit the establishment of biostratigraphic schemes, which are complemented by planktonic foraminifers (Fig. F17; Table T5). Changes in the preservational quality and abundance of siliceous microfossils and in the diagenetic alteration of calcareous microfossils appear to correlate with changes in pore water chemistry (silica concentrations and magnesium, calcium, and alkalinity concentrations, respectively; see “Geochemistry”). According to our biostratigraphic datums,

summarized in Table T5, the deepest recovered sediments from Site U1417 are ~10 Ma. Beyond the biostratigraphic schemes, the micropaleontologic assemblages provide insight into paleoclimatologic and paleoceanographic conditions of the subarctic northeast Pacific Ocean. In particular, the relative abundances of certain diatoms, radiolarians, and planktonic foraminifers suggest climatic variations between warm and cool intervals (Figs. F18, F19). Elements of the benthic foraminiferal fauna and diatom flora also suggest the transport of biogenic material from shallower water environments (Fig. F19).

Diatoms

We investigated core catcher samples and sediment from selected split core sections from Holes U1417A–U1417E to define the sediment age and paleoenvironmental conditions (Tables T5, T6). For a detailed description of diatom zonal scheme and taxonomy, see “Paleontology and biostratigraphy” in the “Methods” chapter (Jaeger et al., 2014).

Diatom biostratigraphy

A total of 464 slides, which include samples from the core catcher and split core sections, were prepared for diatom analyses from Holes U1417A–U1417E (Table T6). Eight diatom datums were observed at Site U1417 (Table T5). Diatoms associated with North Pacific Diatom Zones 6B–12 were present (late Miocene–Pleistocene).

Diatom paleoenvironmental considerations

Valve abundance and preservation varies strongly throughout the sediment column (Figs. F17). High to moderate abundances are mostly recorded in the upper ~200 m CCSF-B and between ~300 and ~420 m CCSF-B (Fig. F19). Except for a few samples, the intervals from 245 to 300 and 440 to 800 m CCSF-B are barren of diatoms. In general, valve preservation closely matches the total diatom abundance and tends to be good when abundance is high. Variations in preservation and abundance and shifts in the assemblage possibly reflect past paleoceanographic changes in the pelagic and the coastal regions of the Gulf of Alaska.

The Site U1417 diatom community mostly consists of Pliocene and Pleistocene species, typical of cold waters of the high-latitude northeastern and subarctic Pacific Ocean. The well-preserved, cold-to-temperate water species *Neodenticula seminae* (Simonsen et Kanaya) Akiba et Yanagisawa is common in the uppermost ~200–225 m CCSF-B (Table T6; Fig. F18). In present-day observations, periods of high relative abundances of *N. seminae* correspond to periods of

high opal and organic carbon fluxes in the northeast Pacific (Takahashi et al., 1990). Based on her survey of the diatom community preserved in surface (Holocene) sediments of the Bering and Okhotsk Seas, Sancetta (1982) concluded that *N. seminae* is a good tracer of the main path of the Alaska Current and a good indicator of the variability of paleohydrographic and paleoclimatic conditions in the Gulf of Alaska. However, because not all diatom valves are equally affected by dissolution, its downcore record should be cautiously interpreted.

The composition of the cold-water species diatom assemblage differs between the uppermost ~200 m and the interval from ~300 to 435 m CCSF-B. A major downhole shift toward a relative increase of *Coscinodiscus marginatus*, a decrease of *Actinocyclus curvatulus*, and the disappearance of *N. seminae* occurs in the cold-water assemblage around ~225 m CCSF-B (Table T6; Fig. F18). This shift may be associated with the intensification of Northern Hemisphere glaciation after 2.6–3 Ma and the development of the modern halocline system in the subarctic Pacific (Swann et al., 2006). Because *C. marginatus* is apparently well adapted to present-day high nutrient supply during short periods of low-incident radiation (Takahashi et al., 1990), its higher relative contribution between ~300 and 470 m CCSF-B at Site U1417 can be interpreted as reflecting enhanced productivity during periods of reduced solar radiation. According to the diatom flux study of Takahashi et al. (1990), the well-silicified centric diatom *A. curvatulus* peaks during modern spring flux maxima in the northeast Pacific. During the late Quaternary, it had its highest relative contribution during glacials in the Bering Sea (Katsuki and Takahashi, 2005).

Other cold-water species present at Site U1417 are *Actinocyclus ochotensis* Jousé, *Asteromphalus robustus* Castracane, *Bacteriosira fragilis* (Gran) Gran, *Rhizosolenia hebetata* f. *hiemalis* J.W. Bailey, *Shionodiscus trifultus*, *Thalassiosira gravida* Cleve, and *Thalassiosira hyalina* (Grunow in Cleve et Grunow) Gran (Sancetta, 1982; Medlin and Priddle, 1990; Koizumi 2008). Their occurrences are sporadic, and they have low abundances at Site U1417 (Table T6). Warm-water species *Rhizosolenia hebetata* f. *semispina* (Hensen) Gran, *Shionodiscus oestrupii* (G. Fryxell) A.J. Alverson et al., and *Thalassiosira leptopus* (Grunow in Van Heurck) Hasle et G. Fryxell (Koizumi, 2008) are rare components of the Site U1417 assemblage. Temperate-water species *Thalassiothrix* spp. and *Stephanopyxis* spp. (Hasle and Syvertsen, 1996) are sporadically recorded.

Rare occurrences of *Achnanthes* spp., *Cocconeis* spp., *Grammatophora* spp., *Rhabdonema* spp., and *Paralia*

sulcata (Ehrenberg) Cleve at Site U1417 also point to a certain degree of downslope transport from the Alaskan coast into the deeper pelagic waters overlying Site U1417. In addition, the sporadic occurrences of several freshwater/neritic marine species (e.g., *Achnanthes lanceolata* [Brébisson ex Kützing] Grunow and *Cyclotella* spp.) (Table T6) may reflect periods of enhanced terrigenous input into the pelagic realm of the Gulf of Alaska. Similarly, the recurrent presence of resting spores of *Chaetoceros* in the uppermost ~250 m CCSF-B (Fig. F19) is indicative of downslope transport into deeper waters of the Gulf of Alaska.

A striking feature of the sediments from Site U1417 is the occurrence of interbedded diatom-rich sediments suggestive of diatom ooze (See “**Lithostratigraphy**”). These diatom-rich sediments between ~20 and 180 m CCSF-B and between ~360 and 430 m CCSF-B are primarily composed of *N. seminae*, *Thalassiothrix* spp., and *Coscinodiscus* spp. and alternate with mixed sediments (Fig. F16).

Radiolarians

A total of 196 samples in Holes U1417A–U1417E were prepared for radiolarian analyses. Radiolarians are abundant in the upper part of Site U1417 (Fig. F17). However, for depths below ~210 m CCSF-B, the occurrence of radiolarians is sporadic and abundances are low. The preservation of radiolarians is good to poor in the upper ~200 m CSF-A and decreases to poor at greater depths. Fluctuations in species abundance are presented in Table T7.

Radiolarian biostratigraphy

Nine radiolarian datums are present at Site U1417; they indicate sediment ages from late Miocene to present (Table T5; see Fig. F10 in the “Methods” chapter [Jaeger et al., 2014]).

Radiolarian paleoenvironmental considerations

The paleoenvironmental conditions at Site U1417 are inferred by using key radiolarian species grouped according to their common ecological responses to environmental control factors (sea-surface temperature and salinity). These groups are based on multivariate cluster and factor analyses of radiolarians preserved in surface sediment from the North Pacific (Kamikuri et al., 2008) and the Central Indian Ocean (Gupta, 1996), in the sediment traps of the Indian Ocean (Gupta et al., 2002), in the modern radiolarian mapping of the world oceans (Boltovskoy et al., 2010), and from late Miocene sediments (Gupta and Srinivasan, 1992). *Cycladophora davisiana* and *Spongopyle osculosa* are grouped as cold deepwater species (>200 m), whereas *Ceratospyrus borealis*, *Actinomma*

boreale, *Stylodictya validispina*, and *Larcopyle buestchlii* are cold-water species living in the upper ~200 m of the water column. The subarctic-temperate group is composed of *Lithelius minor* and *Larcopyle weddellium*. Cold-water radiolarians (both deepwater and surface species) have higher relative abundances in the upper ~225 m CCSF-B of the sediment record, whereas between ~300 and 400 m CCSF-B, temperate species increase in relative abundance (Fig. F18).

Foraminifers

Core catcher samples from Holes U1417A–U1417D were examined for planktonic foraminifers from the >125 µm size fraction in 85 samples (Table T8) and for benthic foraminifers from the >63 µm size fraction in 105 samples (Table T9). Samples from Hole U1417E would not disaggregate and were not investigated. Most core catcher samples were dominated by siliciclastic material in the >63 µm size fraction, although a few samples were dominated by diatoms or had very little sand-sized material.

Planktonic foraminifers

Sixteen planktonic foraminifer species were encountered in Holes U1417A–U1417D (Table T8). Assemblages are composed of subarctic to temperate water species, dominated by *Neogloboquadrina pachyderma*. Preservation varies from poor to good, generally decreasing in quality with depth (Fig. F17). Furthermore, the high number of barren samples (40 of 89 samples) suggests diagenetic dissolution of foraminifer shells in the sediments.

The lack of a continuous planktonic foraminiferal record because of poor preservation at Site U1417 makes it difficult to determine precise biozones. At Site U1417, the last occurrence (LO) of *Neogloboquadrina inglei* (0.7 ± 0.1 Ma) (Kucera and Kennett, 2000) is recognized (Table T5). *Neogloboquadrina kagaensis* (LO 1.9 ± 0.1 Ma) (Kennett et al., 2000) was also found but appears in only two samples (Table T8).

The most striking change in the planktonic foraminiferal assemblage is a change in the coiling direction of neogloboquadrinids (Figs. F18, F19). An abrupt decrease in dextral coiling neogloboquadrinids occurs between 255.29 and 275.74 m CCSF-B (298.55 and 318.99 m core composite depth below seafloor [CCSF-A]). The timing of this shift roughly corresponds to the interval from the latest part of the *Cycladophora sakaii* Zone (1.9–3.3 Ma) to the earliest part of the *Eucyrtidium matuyamai* Zone (1.3–1.9 Ma) and roughly corresponds to the datum event defined by a change in the coiling direction of *N. pachyderma* on the California margin (~2.0 Ma) (Lagoe and Thompson, 1988). However, numerous barren inter-

vals make it difficult to constrain the timing of this event in the Gulf of Alaska margin. The relative abundance of dextral coiling specimens of neogloboquadrinids has long been used as an indicator of sea-surface temperature during the Quaternary because of their preference for warm-water environments (Kucera, 2007). Taking this environmental preference, as well as the timing of evolutionary changes in the *Neogloboquadrina* plexus (Kucera and Kennett, 2000), into account, the change in coiling direction is probably due to a major cooling of surface waters beginning around 2.0–2.2 Ma in the northeastern Pacific.

Brown-colored foraminifer shells were occasionally observed in the core catcher samples. Brown-colored shells are dominant in Samples 341-U1417C-14H-CC through 16H-7W, 49–59 cm (121.90–140.58 m CCSF-B), and 341-U1417D-28H-CC (222.42 m CCSF-B). Brown-colored foraminifers were also reported in the Bering Sea (Cook et al., 2011) and in the northwestern Pacific (Ohkushi et al., 2005). Further studies suggested that this color change in foraminifer shells is attributed to the postdepositional diagenesis during authigenic carbonate precipitation associated with anaerobic methane oxidation (Cook et al., 2011; Uchida et al., 2004). At Site U1417, the pore water profile shows an abrupt drop in alkalinity and a magnesium minimum in the pore waters between ~200 and 300 m CCSF-B. These pore water features are coincident with the occurrence of brownish foraminifer shells, suggesting the precipitation of authigenic carbonates within that interval (see “Geochemistry”).

Benthic foraminifers

Of the 105 core catcher samples that were examined from Holes U1417A–U1417D, 52 contained benthic foraminifers, but abundances were generally low (Figs. F17). Low abundances and numerous barren intervals may reflect dissolution and/or dilution by siliciclastic particles and diatoms. Sixty-nine species or species groups are identified (Table T9), although identifications should be taken as tentative. Benthic foraminiferal assemblages at this site are dominated by individuals in the 63–150 µm size fraction in most samples. However, assemblages from Samples 341-U1417D-62X-CC (435.36 m CCSF-B) and 64X-CC (444.49 m CCSF-B) are dominated by individuals >150 µm. Assemblages are diverse, with ~3–25 species or species groups per sample for those samples that contain at least 10 individuals (median = 10 species/sample). Preservation of foraminifers ranges from very good to poor, with poor preservation observed in ~40% of the core catchers (Table T9; Fig. F17).

The taxonomic composition among samples is highly variable with respect to the rare taxa (Table T9). However, the samples can be grouped into three main assemblage types united by their most abundant taxa. The majority of samples contain assemblages with dominant to abundant *Gyroidina* spp. and major contributions from *Melonis pompilioides*, *Pullenia salisburyi*, and *Eilohedra vitrea*. This composition is consistent with middle to lower bathyal environments from the modern Gulf of Alaska (Bergen and O’Neil, 1979) and with the present water depth of Site U1417.

Cassidulina teretis dominates some samples, including Samples 341-U1417D-62X-CC and 64X-CC, where coal and plant material is also preserved (see “Lithostratigraphy”). In the Gulf of Alaska, *C. teretis* and other *Cassidulina* species are most abundant in middle to outer neritic environments (Bergen and O’Neil, 1979), suggesting transport from shallower waters. Species considered indicative of shelf environments from Oregon to Alaska, including *Triferina angulosa*, *Quinqueloculina* sp., *Lagena laevis*, *Eggerella advena*, and *Karrierella baccata* (see Culver and Buzas, 1985), are also occasionally encountered at Site U1417, further suggesting transport of foraminifers from the shelf to the deep ocean.

Nonionella labradorica and *Buccella inusitata* characterize a third assemblage that occurs in Samples 341-U1417D-3H-CC to 6H-CC (23.06–47.80 m CCSF-B). *N. labradorica* is reported to reach abundances >10% at ~200 m water depth in the Gulf of Alaska, with a second increase below ~1500–2000 m water depth (Bergen and O’Neil, 1979). These species are also characteristic of Pliocene to Pleistocene assemblages from the Japan Trench area interpreted to be from 1500–2000 m water depth (Keller, 1980). Thus, this assemblage also suggests transport from environments shallower than the present water depth at Site U1417.

Other microfossils

Ostracods

Ostracods were present in 10 samples examined for benthic foraminifers but were not taxonomically described (comments in Table T9).

Calcareous nannofossils

Calcareous nannofossils were found in isolated intervals in Holes U1417B–U1417D. Overall, the number of species observed was very low (~2–5 species/sample), which is likely the result of either dissolution or environmental influence. The most common species found are *Coccolithus pelagicus*, *Dictyococcites productus*, and small reticulofenestrids (<3 μm). The small

reticulofenestrids may be a combination of specimens of *Reticulofenestra* and *Gephyrocapsa*, but no central area structures were observed that allowed identification of *Gephyrocapsa*. The best-preserved nannofossils are found within diatom-rich intervals in the upper ~130 m CCSF-B.

Summary

Age models derived from diatoms, radiolarians, and planktonic foraminifers generally agree (Table T5; Fig. F20). In some intervals, ages were inverted stratigraphically, suggesting reworking or transport of older material to the site. Reworking and transport is also indicated by shallower water benthic foraminifers, diatom resting spores, and coastal diatom specimens (Fig. F19).

The preserved microfossils at Site U1417 provide an excellent opportunity to document the biotic response to climatic change in both the surface and deeper ocean. Marked variations the relative abundances of taxa potentially reflect major changes in global climate variations linked to fluctuations in ice volume and reorganization of North Pacific circulation during the Pliocene and the Pleistocene (Figs. F18, F19). Numerous barren intervals make it difficult to interpret the environmental conditions during the Miocene. However, in intervals where radiolarians are present, the species composition indicates temperate surface water conditions during the Miocene. Both planktonic foraminifers and radiolarians from this site record cooler conditions in the upper ~225 m CCSF-B than in older parts of the record. Coincidentally, the diatom flora shifts to a more diverse assemblage above ~215 m CCSF-B, with only a few monospecific *C. marginatus* intervals. Low preservation of siliceous microfossils prevents the observation of this transition around this specific depth. Observed barren intervals at the site may be due to either lower diatom and radiolarian productivity or to increased dissolution suggested by the retention of dissolution resistant taxa in nearly barren intervals.

Stratigraphic correlation

The composite depth scale at Site U1417 was constructed from 0.0 to 750.82 m CCSF-A (as defined in “Stratigraphic correlation” in the “Methods” chapter [Jaeger et al., 2014]). The splice consists of one complete and continuous interval from the mudline to 224.2 m core composite depth below seafloor (CCSF-D). At greater depths, intervals of correlation were found between holes but were not considered sufficiently continuous to warrant development of a deeper “floating” shipboard splice.

The splice ranges from the top of Core 341-U1417D-1H (the mudline) through Core 341-U1417C-22H (Tables T10, T11). To the extent possible, the splice was constructed from Holes U1417C and U1417D because Hole U1417A was sampled at sea and the shallowest 10 cores from Hole U1417B were recovered during heavy weather, when ship heave compromised the quality of many of the cores. In Hole U1417C, many of the APC cores taken deeper than ~150 m CCSF-A had significant flow-in, likely due to incomplete penetration. To the extent possible, these intervals were identified and excluded from the splice.

Correlations between holes were accomplished using IODP Correlator software (version 1.695). All splice tie points were checked by examining digital line-scan images with Corelyzer (version 2.0.2), linked to Correlator. During coring, real-time development of composite depths and guidance for coring operations relied initially on Special Task Multisensor Logger (STMSL) GRA density and magnetic susceptibility data. The final composite depth scale (CCSF-A) and the splice (CCSF-D scale) are based primarily on the stratigraphic correlation of magnetic susceptibility and GRA density from the Whole-Round Multisensor Logger (WRMSL) (Figs. F21, F22) with verification from NGR and reflectance spectroscopy color data from the Section Half Multisensor Logger (SHMSL).

The CCSF-A and CCSF-D scales were constructed by assuming that the uppermost sediment (the mudline) in Core 341-U1417D-1H represents the sediment/water interface. An approximate mudline was also recovered in Cores 341-U1417A-1H and 341-U1417B-1H and 2H, confirming the fidelity of the top of the recovered interval. Core 341-U1417D-1H serves as the “anchor” in the composite depth scale and is the only core with depths that are the same on the CCSF-A and CCSF-D scales. From this anchor, we worked downhole, correlating variations in core logging data between holes on a core-by-core basis using Correlator.

A few splice tie points are uncertain. In particular, the splice points between 341-U1417C-7H-7, 16.86 cm, and 341-U1417D-7H-1, 34.84 cm (62.18 m CCSF-A), between 341-U1417C-8H-7, 57.10 cm, and 341-U1417A-10H-1, 32.74 cm (76.12 m CCSF-A), and between 341-U1417A-21H-3, 135.07 cm, and 341-U1417B-18H-1, 12.14 cm (186.76 m CCSF-A), all have little overlap to constrain the splice points and should be used cautiously. The tie point between 341-U1417B-22H-4, 47.19 cm, and 341-U1417C-22H-1, 16.37 cm (211.29 m CCSF-A), is equivocal.

Within the splice, the CCSF-A depth scale is defined as equivalent to the CCSF-D depth scale. Note that

the CCSF-D scale rigorously applies only to the spliced interval. Intervals outside the splice, although available with CCSF-A depth assignments, should not be expected to correlate precisely with fine-scale details within the splice or with other holes because of variation in the relative spacing of features in different holes. Such apparent depth differences of specific features may reflect coring artifacts or fine-scale spatial variations in sediment accumulation and preservation at and below the seafloor.

The cumulative offset between CCSF-A and the CCSF-A or CCSF-D depth scales is nonlinear (Fig. F23). The affine growth factor (a measure of the fractional stretching of the composite section relative to the drilled interval; see “Stratigraphic correlation” in the “Methods” chapter [Jaeger et al., 2014]) averages 1.1348 at Site U1417 in the APC-cored interval from 0 to 208.8 m CCSF-A or CCSF-D. Anomalies around this relatively uniform affine growth relationship may be explained by significant ship heave (especially during coring of Hole U1417B), imprecision of tide corrections on coring depths, and potential distortion of cores by piston effects.

The affine growth factor is 1.2608 in the interval from 208.8 to 266.75 m CCSF-A. This high rate of affine growth is an artifact introduced by construction of the CCSF-A depth scale; because few features correlated well among the holes in this interval, we sometimes appended cores either within or between holes rather than making firm correlations of specific features within cores. This method artificially expands the apparent length of recovered material. At depths greater than the splice, we observed significant correlation among holes between 220.4 and 232.4 m CCSF-A (Cores 341-U1417B-25H and 341-U1417D-28H and 30H) and from 259.0 to 263 m CCSF-A (Cores 341-U1417B-31H, 341-U1418C-26H and 27H, and 341-U1417D-35X and 36X). We considered these correlations not sufficiently reliable to warrant construction of a floating splice or precise tie points between holes.

Deeper than 266.75 m CCSF-A, cores were recovered with either the XCB or RCB tools. In this interval, affine values were nominally constant at 43.26 m, which is the highest affine value within the APC-cored interval (Core 341-U1417C-29H). Exceptions are Cores 341-U1417B-40X and 44X and 341-U1417D-45X, 46X, 58X, and 59X. These six cores all include minor adjustments to their affine values to align significant sedimentary features or shipboard observations of paleomagnetic reversals relative to those found in Hole U1417E (which was given a constant affine value of 43.26 m). Correlations between holes based on XCB or RCB cores should be considered uncertain.

Calculation of mass accumulation rates based on the CCSF-A or CCSF-D scales must correct for the affine growth factor. To facilitate this process, the CCSF-B depth scale compressed the CCSF-A and CCSF-D scales into a scale that has the same total depth of sediment column as the interval actually drilled (see “**Stratigraphic correlation**” in the “Methods” chapter [Jaeger et al., 2014]). The following three equations define transformation of the CCSF-A or CCSF-D depth scale into CCSF-B depths (Fig. F23):

From 0 to 208.80 m CCSF-A/CCSF-D:

$$\text{CCSF-B} = 0.865 \times \text{CCSF-A/CCSF-D}.$$

From 208.80 to 266.75 m CCSF-A/CCSF-D:

$$\text{CCSF-B} = 0.7392 \times \text{CCSF-A/CCSF-D} + 26.307.$$

For 266.75 m CCSF-A/CCSF-D:

$$\text{CCSF-B} = \text{CCSF-A/CCSF-D} - 43.26.$$

Initial age model

All the available paleomagnetic and biostratigraphic age datums (Tables T5, T12) (see “**Paleontology and Biostratigraphy**” and “**Paleomagnetism**”) were considered while constructing minimum and maximum shipboard age models (Fig. F24; Table T13); together, these preliminary age models span most of the uncertainty in the shipboard datums. The age models were constructed in the CCSF-B depth scale and are also provided in the CCSF-A depth scale.

When geomagnetic polarity boundaries and/or reversals were observed in several holes, the average depth and its uncertainty were calculated in the CCSF-B scale. All identified paleomagnetic reversals were included in the shipboard minimum and maximum age models.

Uncertainty in the biostratigraphic datums mostly reflects the shipboard sampling interval and the presence of barren zones. Two biostratigraphic datums were considered outliers relative to well-constrained paleomagnetic datums. The LO of the diatom *Actinocyclus oculatus* (Sample 341-U1417D-9H-3W, 80 cm) and the LO of the diatom *Neodenticula koizumii* (Sample 341-U1417D-15H-3, 130 cm) were not included in the maximum and minimum age models. All other biostratigraphic datums were accommodated within the uncertainties of their published ages and relatively coarse shipboard sampling. Relatively few biostratigraphic datums were detected in the interval from 460 m CCSF-A (416.74 CCSF-B) to the base of the site. For purposes of constraining the oldest ages at Site U1417, we assumed that basaltic basement was at 838 ± 8 m CCSF-A (794.74 m

CCSF-B based on site survey geophysical data). The oceanic basement is Pacific plate basaltic crust that can be associated with Chron C17–C18 based on the EMAG2 magnetic anomalies (Maus et al., 2009), which span from 37 to 41.2 Ma (Ogg, 2012).

Based on these initial shipboard minimum and maximum age models, the interval older than ~10 Ma (averaged over 10–39 Ma) has sediment accumulation rates of <10 m/m.y. Sediment accumulation rates (averaged within equally spaced increments of 0.5 m.y.) increase through time, peaking at values >110 m/m.y. in the intervals 0–1 and 2–2.5 Ma (Fig. F25). Such a rise in sedimentation rates is consistent with the gradual northward tectonic drift of the site, as well as acceleration of sediment inputs from regional tectonics and glacial forcing (based on the presence of lonestones and diamicts of probable ice-rafted origin within the last ~2.5 m.y.) and further acceleration of glacial erosion in the last ~1.0 m.y., following the MPT (Clark et al., 2006); Fig. F16).

Geochemistry

Interstitial water chemistry

Interstitial water (IW) samples were taken in Holes U1417A and U1417C–U1417E at variable sampling resolution with depth in hole; sampling was designed to include overlaps in the sampled intervals between each successive hole. The following results are expressed on the CCSF-B scale for Site U1417 (see “**Stratigraphic correlation**”).

In Hole U1417A, 26 IW samples were taken with a resolution of three samples per core in Cores 341-U1417A-1H and 2H, two samples per core in Cores 3H through 6H, and one sample per core deeper than Core 6H. Whole rounds for IW analyses were 5 cm long in Cores 341-U1417A-1H through 16H and 10 cm long in Cores 17H through 22H. All samples from Hole U1417A were collected from APC cores (0–165.14 m CCSF-B). In Hole U1417C, 11 IW samples were taken from Cores 341-U1417C-17H through 28H (149.09–221.65 m CCSF-B), with a more irregular depth resolution (1–2 samples per core) than in Hole U1417A depending upon core recovery. In Hole U1417D, 13 IW samples were taken from Cores 341-U1417D-32H through 59X (207.15–421.22 m CCSF-B), with irregular spacing due to variable core recovery.

In Hole U1417E, 22 IW samples were taken from Cores 341-U1417E-7R through 39R (401.26–643.84 m CCSF-B). Hole U1417E was drilled using the RCB system, which has the potential for contamination of IW samples by surface seawater and drilling muds (e.g., Chambers and Cranston, 1991). However, suc-

successful recovery of uncontaminated RCB sequences for IW analysis has been reported (e.g., Shipboard Scientific Party, 2000; Fulthorpe et al., 2011). The intervals of higher (>40%) recovery in Hole U1417E allowed IW sampling on complete 10 or 15 cm long whole rounds, and we did not identify evidence for contamination with seawater in the chemical analyses (see below). The compositions of IW samples taken from overlapping depths between the different holes were in good agreement, allowing construction of composite IW records. All chemical parameters analyzed in the IW samples at Site U1417 are similar to respective low-resolution data from original Site 178 drilled in 1971 at the same location (Kulm et al., 1973; Waterman et al., 1973).

The applied squeezing pressures ranged from 8,000 to 28,000 psi, and the amounts of extracted IW ranged between 25 and 40 mL. Splits of the IW samples were taken and processed following methods outlined in “Geochemistry” in the “Methods” chapter (Jaeger et al., 2014). IW splits also were preserved for shore-based analysis of dissolved trace metals, oxygen/sulfur/calcium/strontium isotopes, dissolved inorganic carbon, and silica.

Alkalinity, pH, chloride, and salinity

An alkalinity peak occurs at 28.9 m CCSF-B (16.1 mM), followed by a decrease to 3.6 mM by 218.0 m CCSF-B (Fig. F26A). A second peak occurs at 375.6 m CCSF-B (12.6 mM) before an overall downcore decrease, with some small oscillations, to 2.23 mM (702.8 m CCSF-B). The pH values fluctuate between 7.36 and 8.28. We observed an overall increase in both the range and absolute pH values downcore at Site U1417 (Fig. F26B).

Chloride (titrated) concentrations range between 546 and 565 mM (Fig. F26I), largely without a clear downcore trend apart from a chloride maximum at 37.6 m CCSF-B.

Salinity gradually and steadily decreases from 34 to 30 from 0 to 288.0 m CCSF-B (Fig. F26H). Salinity remains at 30 deeper than this depth, except for two slight increases to 31 at 375–430 m CCSF-B and deeper than 662.3 m CCSF-B.

Dissolved ammonium, phosphate, and silica

Dissolved ammonium at Site U1417 increases rapidly with depth in the uppermost 20 m, from 0.161 mM (1.3 m CCSF-B) to 1.104 mM (20.3 m CCSF-B) (Fig. F26D). Deeper than 20.3 m CCSF-B, ammonium concentrations remain between 1.0 and 1.2 mM and then decrease downcore deeper than 400 m CCSF-B to values <0.5 mM.

Phosphate concentrations are highest in the upper 30 m, with maxima at 14.6 m CCSF-B (38.2 μM) and 28.9 m CCSF-B (35.5 μM) (Fig. F27J). Deeper than 29 m CCSF-B, phosphate rapidly decreases to 12.9 μM at 37.6 m CCSF-B, followed by a more gradual decrease to 3.7 μM at 165.1 m CCSF-B. Phosphate concentrations remain low downcore (<4 μM), apart from a slight increase to ~6 μM between 300 and 375 m CCSF-B.

Silica concentrations display a number of significant and abrupt transitions (Fig. F26G). A steep increase from 600 to 800 μM within the uppermost 15 m CCSF-B is followed by a more gradual increase to a value of 1054 μM at 177.2 m CCSF-B. Silica concentrations of ~1000 μM are sustained downcore, apart from three intervals of low concentrations: 215–290 m CCSF-B (as low as 300 μM), 518–596 m CCSF-B (as low as 192 μM), and deeper than 643.8 m CCSF-B (as low as 160 μM).

Dissolved sulfate, calcium, magnesium, potassium, sodium, and bromide

Sulfate concentrations decrease continuously with depth in the upper 200 m CCSF-B, from 21.47 mM (1.3 m CCSF-B) to 0.93 mM (207.2 m CCSF-B) (Fig. F26C). Over this depth interval, the sulfate gradient is variable, with the steepest decrease occurring between 1.3 and 20.3 m CCSF-B (to 16.85 mM). Total sulfate depletion (to values below the detection limit) is not reached, but deeper than 200 m CCSF-B, sulfate concentrations remain below 2 mM. An increase in sulfate occurs deeper than 643 m CCSF-B, reaching ~7 mM at 681.8 and 702.8 m CCSF-B.

Calcium concentrations increase overall with depth at Site U1417, from 10.5 mM (1.3 m CCSF-B) to 30.3 mM (681.8 m CCSF-B) (Fig. F27A). Two intermediate maxima occur in the upper 90 m (12.6 mM at 14.6 m CCSF-B and 12.4 mM at 52.1 m CCSF-B). A steep increase in calcium concentrations deeper than 100.2 m CCSF-B leads to a third, broad maximum between 207.2 and 254.6 m CCSF-B (~16–17 mM). Calcium concentrations decrease slightly between 288.0 and 316.3 m CCSF-B and then increase again to reach values of ~30 mM at the bottom of the hole.

Magnesium concentrations decrease overall with depth, from 50.7 mM (1.3 m CCSF-B) to 15.3 mM (702.8 m CCSF-B) (Fig. F27C). This trend is interrupted by a magnesium increase from 24.0 to 30.5 mM between 254.6 and 375.6 m CCSF-B. Calcium and magnesium concentrations are negatively correlated (Pearson’s correlation coefficient of –0.93) at Site U1417 deeper than 90 m CCSF-B, indicating a common control over these downcore profiles (discussed further below).

The potassium profile at Site U1417 shows an overall downcore decrease in two main steps: from 11.2 mM at 1.3 m CCSF-B to 8.6 mM at 100.2 m CCSF-B and from 6.7 mM at 421.2 m CCSF-B to 3.8 mM at 574.9 m CCSF-B (Fig. F27B). Deeper than 600 m CCSF-B, potassium concentrations increase to reach 5.6 mM at the bottom of the hole (702.8 m CCSF-B).

Sodium concentrations at Site U1417 mostly range between 463 and 480 mM, with the highest values between 9.5 and 20.3 m CCSF-B (Fig. F26J). An increased range of sodium concentrations is recorded deeper than 100 m CCSF-B, with an overall downcore increase from 100 to 260 m CCSF-B. A sharp drop in sodium concentration occurs at 400 m CCSF-B, followed by an overall downcore increase to the bottom of the hole.

Bromide concentrations at Site U1417 increase steeply between 1.3 and 12.1 m CCSF-B and remain ~0.9 mM down to 700 m CCSF-B (Fig. F26E).

Dissolved manganese, iron, barium, strontium, boron, and lithium

Both iron and manganese concentrations at Site U1417 are highest in the uppermost 100 m CCSF-B, decreasing downcore from maximum concentrations of 18 and 112 μM , respectively (Fig. F27H–F27I). Deeper than 100 m CCSF-B, iron concentrations are below the quantification limit. In contrast, manganese concentrations are more variable and show a number of maxima and minima (ranging between 5 and 43 μM).

Barium concentrations are <10 μM in the uppermost 100 m CCSF-B at Site U1417 (Fig. F27F). Between 100 and 215 m CCSF-B, barium concentrations double; they further increase to 440 μM in the interval between 200 and 620 m CCSF-B. Farther downcore, barium decreases to low values (~30 μM) by 643 m CCSF-B. Detectable barium concentrations are limited to the sediment interval with lowest sulfate concentrations.

Strontium concentrations at Site U1417 first increase slowly and then more rapidly from ~100 μM at the top of the record to as high as 180 μM by 215 m CCSF-B (Fig. F27G). Between ~215 and 600 m CCSF-B, strontium remains around 180 μM . Deeper than this interval, strontium concentrations slightly decrease to ~130 μM again to the bottom of the hole.

Boron concentrations display a pronounced maximum in the uppermost 45 m CCSF-B of Site U1417, reaching values of 650 μM (Fig. F27E). Deeper than this depth, boron decreases to values around 300 μM by 240 m CCSF-B and mostly ranges between 200 and 300 μM to the bottom of the hole.

Lithium concentrations at Site U1417 decrease within the uppermost 10 m CCSF-B from 32 to 12 μM and then slowly increase downcore and reach 24 μM at ~240 m CCSF-B (Fig. F27D). Deeper than 260 m CCSF-B, lithium concentrations increase more steeply, reaching values of 55 μM by ~410 m CCSF-B. Following a local minimum and another maximum, lithium concentrations decrease to 34 μM around 565 m CCSF-B, followed by a steep increase to maximum values of 103 μM at the bottom of the hole.

Volatile hydrocarbons

Headspace gas samples were collected at a resolution of one per core in Holes U1417A (Cores 1H through 22H), U1417B (Cores 21H through 47X), U1417D (Cores 32H through 65X), and U1417E (Cores 7R through 39R). Methane is by far the dominant hydrocarbon gas detected in Holes U1417A and U1417B and most of Hole U1417D and remains at low concentrations (generally <7 ppmv) to 424.7 m CCSF-B (Fig. F26F). Slightly elevated methane concentrations are found in the uppermost 130 m (5–13 ppmv). Deeper than 431.1 m CCSF-B, methane concentrations increase with depth by two to three orders of magnitude in Holes U1417D and U1417E, reaching a maximum of 5117 ppmv at 498.9 m CCSF-B. In Hole U1417E, methane concentrations decrease abruptly at 643.8 m CCSF-B. Ethane is present deeper than 439.2 m CCSF-B in low concentrations (<2 ppmv). C_1/C_2 ratios thus remain high, between 500 and 5000.

Bulk sediment geochemistry

IW squeeze cakes and discrete core samples were analyzed from Site U1417 for total carbon, total nitrogen (TN), and total inorganic carbon. From these analyses, total organic carbon (TOC) and calcium carbonate (CaCO_3) were calculated as described in “Geochemistry” in the “Methods” chapter (Jaeger et al., 2014). In total, 55 samples were analyzed from Hole U1417A (Cores 1H through 22H), 1 from Hole U1417B (Core 16H-CC), 11 from Hole U1417C (Cores 17H through 28H), 44 from Hole U1417D (Cores 7H through 64X), and 35 from Hole U1417E (Cores 4R through 39R). Discrete samples were selected in collaboration with the Lithostratigraphy group to ensure that the main lithologies were analyzed. All of these geochemical results are consistent with the low-resolution analyses of Site 178 (Kulm et al., 1973).

TOC contents mostly range between 0.1 and 0.6 wt% at Site U1417 (Fig. F28A–F28B). No consistent trend is discernible in the uppermost 200 m other than a very slight overall downcore decrease. Deeper

than 300 m CCSF-B, TOC increases slightly downcore to 564.7 m CCSF-B (0.85 wt%) within lithostratigraphic Unit V, which contains visible plant debris and suspected fragments of coal or shale within a diamict facies (see **“Lithostratigraphy”**). Variable but slightly reduced TOC contents occur deeper than 600 m CCSF-B. Several discrete samples from specific lithologies show elevated TOC contents: two diatom oozes (0.85 wt%, 357.6 m CCSF-B; 1.39 wt%, 365.0 m CCSF-B), diamicts suspected to contain coal or shale clasts (9.08 wt%, 364.1 m CCSF-B; 2.38 wt%, 442.2 m CCSF-B; 1.14 wt%, 466.9 m CCSF-B; 1.49 wt%, 681.8 m CCSF-B), woody debris within a sandy bed (6.49 wt%; 535.2 m CCSF-B), and a dark gray mud (1.79 wt%; 565.0 m CCSF-B). A TOC content of 59.80 wt% was recorded for an angular clast suspected to be coal or shale within a diamict unit (441.4 m CCSF-B) (see **“Lithostratigraphy”**).

TN contents range between 0 and 0.2 wt% at Site U1417 (Fig. **F28C**). Nitrogen contents are higher overall in Hole U1417A (~0.1 wt%) than in the other holes at Site U1417, indicating a systematic bias related to a saturated nitrogen column in the gas chromatograph. There are small fluctuations in TN deeper than 200 m CCSF-B (0–0.1 wt%). Several discrete samples from specific lithologies record higher TN contents: in a diatom ooze (0.2 wt%; 364.1 m CCSF-B), in a suspected coal or shale clast (1.0 wt%; 441.4 m CCSF-B), and in sediment around a pyritized limestone (1.1 wt%; 143.9 m CCSF-B).

Organic carbon to TN (C/N) ratios range between 0 and 30, increasing progressively downcore from 0–5 in the uppermost 100 m CCSF-B to values of 0–30 at the bottom of the hole. Considerably higher C/N ratios (50–60) are recorded in a suspected coal or shale sample (441.4 m CCSF-B) and in woody debris (535.2 m CCSF-B). C/N ratios in the uppermost 100 m CCSF-B (Hole U1417A) fall within the range of fresh organic matter and are consistent with contributions of terrigenous organics (both refractory eroded material and relatively fresh plant material) matter to modern sediments off Alaska (Walinsky et al. 2009), but these ratios may be underestimated from C/N ratios as a result of contributions from the inorganic N pool (e.g., clay mineral-bound ammonium) (Fig. **F28F**). This phenomenon has been observed in other low-TOC marine sediments such as in the Arctic Ocean (e.g., Schubert and Calvert, 2001; Jakobsson, 2004). The increasing C/N ratios deeper than 100 m CCSF-B are consistent with a mixed marine-terrestrial origin for the sediments at Site U1417 (see **“Lithostratigraphy”**). However, determination of the relative contributions of organic and inorganic N is required to assess this interpretation fully.

CaCO₃ contents range mostly between 0 and 1.5 wt% at Site U1417 (Fig. **F28D–F28E**). Between 200 and 265 m CCSF-B and deeper than 345 m CCSF-B, CaCO₃ contents are still low but range from 0 to 3 wt%. Contents exceeding 2 wt% include one data point associated with a diatom-rich interval (4 wt%, 61.1 m CCSF-B; interval 341-U1417A-9H-4W, 74–76 cm). XRD analysis identified the presence of dolomite (see XRD data in the Laboratory Information Management System [LIMS] database) in this sample, which likely accounts for the high inorganic C percentage and which is not corrected for in the calculations of CaCO₃ (see **“Geochemistry”** in the **“Methods”** chapter [Jaeger et al., 2014]). A suspected authigenic carbonate layer at 336.9 m CCSF-B (interval 341-U1417D-50X-2, 102–106 cm) has 21 wt% CaCO₃. The maximum CaCO₃ value (38 wt%) is recorded at 450.9 m CCSF-B (interval 341-U1417D-64X-1W, 0–3 cm) in a highly cemented sandstone (low-Mg calcite according to XRD analysis; see XRD data in LIMS).

Interpretation

Site U1417 geochemistry indicates relatively low rates of organic matter remineralization, reflecting limited input of organic matter to the sediments. The low TOC and TN contents at Site U1417 are typical for an oligotrophic deepwater setting, and sediments are not strongly influenced by diagenetic reactions. A contribution of inorganic N to the bulk sediment composition, most likely related to clay-bound ammonium (Schubert and Calvert, 2001), is supported by the continuous downcore depletion of ammonium deeper than ~30 m CCSF-B. The low CaCO₃ contents are equally typical for a subarctic deepwater setting with high terrigenous dilution, as well as with corrosive bottom waters and overall low biogenic carbonate preservation. The sparse occurrence and low preservation of calcareous micro- and nanofossils support this interpretation (see **“Paleontology and biostratigraphy”**).

A number of IW parameters point to a zone of increased organic matter remineralization between ~10 and 40 m CCSF-B at Site U1417 (Figs. **F27**, **F29**). Dissimilatory manganese and iron reduction release dissolved manganese, iron, and adsorbed phosphate (potentially also boron) into the pore waters (Froelich et al., 1979). Following upward diffusion, these metals reprecipitate as authigenic manganese and iron (oxyhydr)oxides (Froelich et al., 1979), as seen in the brown sediment layer directly beneath the mudline at Site U1417. Downward diffusion probably leads to precipitation of authigenic manganese and iron carbonates, iron sulfides, iron phosphates, and/or iron-rich clay minerals. Beneath the zone of

dissimilatory manganese and iron reduction, the steep linear sulfate gradient from the sediment/water interface to ~20–30 m CCSF-B implies enhanced organoclastic sulfate reduction rates that lead to (1) degradation of organic matter, increasing alkalinity, ammonium, bromide, and phosphate concentrations and (2) production of hydrogen sulfide, reacting with iron oxides to form iron sulfides and releasing iron-bound phosphate (Gieskes, 1973, 1975). The variable pattern and overall low concentrations of methane in this part of the sediment succession (≤ 13 ppmv in all samples) do not support the establishment of a distinct sulfate–methane transition zone (SMTZ) but might indicate very low rates of methanogenesis occurring within the uppermost ~100 m of the sediment column. Deeper than ~30 m CCSF-B, the sulfate gradient becomes less steep, but sulfate is nevertheless decreasing, indicating continuous sulfate reduction at lower rates in the deeper sediments that leads to almost full sulfate depletion at ~200 m CCSF-B.

From the major diagenetic reaction zone between ~10 and 40 m CCSF-B, alkalinity, ammonium, bromide, and phosphate diffuse to respective sinks in the sediment or water column. Ammonium might be incorporated into clay minerals, whereas alkalinity and phosphate likely precipitate as authigenic carbonate and apatite, respectively (Hein et al., 1979a; Rutenberg and Berner, 1993). A distinct sink for alkalinity is located between 215 and 290 m CCSF-B, and slightly higher inorganic carbon values in this zone (1–2 wt% CaCO_3) and lower IW magnesium concentrations suggest the precipitation of authigenic carbonate (Hein et al., 1979a; Raiswell and Fisher, 2004). This interpretation is supported by the presence of brownish, probably dolomite-coated foraminifers in this depth interval (see [“Paleontology and biostratigraphy”](#)), beneath which foraminifer abundance falls from few to barren as alkalinity increases. In addition, the very steep downward phosphate gradient might indicate the formation of Fe(II) phosphates (e.g., vivianite), as indicated by the possible detection of its oxidation products (e.g., koninckite) by XRD analysis (see XRD data in LIMS). Deeper in the sediment, a local alkalinity maximum around 375 m CCSF-B suggests another zone of enhanced organic matter remineralization, supported by slightly elevated ammonium and phosphate concentrations.

The finding of substantially increased methane concentrations only deeper than ~420 m CCSF-B but almost total sulfate depletion around 200 m CCSF-B suggests that sulfate is not currently consumed by anaerobic methane oxidation in an SMTZ. Nevertheless, a discrete sink for alkalinity and magnesium

deeper than 375 m CCSF-B supports precipitation of authigenic carbonate. This process also could explain the occurrence of an indurated/cemented sandstone layer at the bottom of Hole U1417D (450.9 m CCSF-B) that was only partially recovered during coring. Because of problems with the disaggregation of core catcher samples from Hole U1417E (see [“Paleontology and biostratigraphy”](#)), foraminifer abundance (and preservation state) and any potential association with the alkalinity sink could not be investigated.

As sulfate concentrations reach lowest values at ~200 m CCSF-B, pore water barium concentrations begin to increase with depth, possibly because of the dissolution of biogenic barite (barium sulfate) at greater depths. This dissolution occurs because IW become undersaturated with respect to sulfate (Waterman et al., 1973). The top of the barite dissolution zone is clearly confined by the sulfate penetration depth (the depth of total IW sulfate depletion), and precipitation of authigenic barite is most likely occurring at this geochemical transition (von Breymann et al., 1992). Strontium concentrations seem to follow the barium pattern, which might be related to the relatively high strontium content in barite. The lower boundary of the zone of barium- and strontium-enriched IW is related to a slight but consistent increase in sulfate concentrations deeper than 500 m CCSF-B. Methane production is roughly confined to the sulfate-depleted zone as well, but a direct overlap of the methane and the sulfate profiles was not observed shallower than the methanogenic zone (possibly because of incomplete methane recovery in low-methane samples and/or a decrease of methane production over time). However, there is a second SMTZ located around 650 m CCSF-B. Sulfate may be diffusing upward, possibly from a source that exists at, or deeper than, the sediment/basalt contact (D’Hondt, Jørgensen, Miller, et al., 2003), ~80–100 m beneath the deepest pore water sample, based on a tentative shipboard correlation to DSDP Leg 18 results (Fig. F30; Kulm, Von Huene, et al., 1973). This hypothesis is supported by lithium concentrations higher than the seawater value of 26 μM toward the base of the IW record (>100 μM), which are due to leaching of the basalt by seawater (e.g., Mayer, Pisias, Janecek, et al., 1992; Zhang et al., 1998).

The patterns of dissolved calcium, magnesium, and potassium also indicate geochemical transformation processes occurring in the sediments. Calcium might precipitate as authigenic carbonate and/or apatite, possibly explaining its variable pattern in the uppermost ~100 m CCSF-B of sediment. However, sources of dissolved calcium located deeper than this may be related to the alteration of volcanic ash or the basalt

underlying the sediments (Gieskes, 1975; Gieskes and Lawrence, 1981). Alteration of ash/basalt may be responsible for the downcore decrease of magnesium deeper than ~400 m CCSF-B, suggesting the neo-formation of magnesium-rich clay minerals (e.g., smectites), whereas the magnesium removal around 250 m CCSF-B is most likely caused by authigenic carbonate formation (see above). Potassium, magnesium, and iron might be incorporated into either clay minerals or zeolites formed by alteration of diatom frustules (Michalopoulos and Aller, 1995). Iron-rich clays may be forming (see XRD data in LIMS), but the terrestrial source area also contains iron-rich clay minerals (Hein et al., 1979b).

Dissolved silica concentrations exceed those of modern North Pacific Deep Water (~160 μM), indicating dissolution of silica below the seafloor, likely from volcanic ash and/or biogenic opal. High IW silica concentrations correspond to the presence of biosiliceous oozes, whereas IW silica concentrations are low when these oozes are absent between 200 and 300 m CCSF-B and between 500 and 600 m CCSF-B (see “[Lithostratigraphy](#)”). The potential precipitation of authigenic clay minerals and removal of dissolved silica from the IW might also account, in part, for the low silica concentrations observed between 200 and 300 m CCSF-B (lithostratigraphic Unit II). At these depths, volcanic ash is present as a silica source (see “[Lithostratigraphy](#)”). Diffusion upward from the underlying basalt may explain the trend in dissolved silica deeper than 600 m CCSF-B, but this depth interval is also marked by the presence of biosiliceous ooze, which may induce higher silica input.

The patterns in chloride, sodium, and (less indicative) salinity in the uppermost 60 m CCSF-B are most likely related to the burial of higher salinity Last Glacial Maximum seawater that is diffusing away from this subsurface maximum (Figs. [F26](#), [F29](#)) (McDuff, 1985; Gieskes et al., 1998).

Physical properties

Physical properties measurements were taken on samples from each of the five holes drilled at Site U1417 to provide basic information for characterizing the drilled section using whole-round cores, split cores, and discrete samples. After cores were divided into sections, all whole-round sections longer than ~30 cm were measured through the GRA bulk densitometer and magnetic susceptibility loop on the STMSL at 2.5–5.0 cm intervals with 2 s measurements. After reaching thermal equilibrium with ambient temperature (~4 h), GRA bulk density, magnetic susceptibility, and compressional wave (*P*-wave) velocity were measured with the WRMSL at

2.5 cm intervals with 5 s measurements. Some damaged sections with split and/or patched core liners were too wide to fit through the WRMSL and/or the STMSL loop magnetic susceptibility meters and therefore could not be logged with any of the core logger instrumentation. After WRMSL scanning, whole-round sections were logged for NGR at 10 cm intervals with eight detectors. Color spectrometry, color reflectance, and magnetic susceptibility were measured on the split cores using the SHMSL at 2.5 cm resolution. Discrete *P*-wave measurements and shear strength measurements were made on split sediment cores from working-half sections on the Section Half Measurement Gantry. Moisture and density (MAD) were measured on 10 cm³ plugs collected from the working halves. Summaries of all the physical properties measured with the multisensor loggers on each hole, as well as discrete bulk density and *P*-wave velocity, are provided in Figures [F31](#), [F32](#), [F33](#), [F34](#), and [F35](#).

Gamma ray attenuation bulk density

Variations in GRA bulk density can reflect changes in mineralogy/lithology, consolidation, porosity, and coring disturbance. Whole-round GRA bulk density averages ~1.8 g/cm³ in the APC cores and displays downhole cyclic variability on the order of ~0.5 g/cm³ (Figs. [F31](#), [F32](#), [F33](#), [F34](#), [F35](#)). A trend toward higher values with depth in the APC cores is consistent with increasing sediment compaction/consolidation. However, whole-round GRA values abruptly decrease corresponding to the depth at which we transitioned from APC core collection to XCB core collection in Holes U1417B and U1417D (Figs. [F32](#), [F34](#)). This transition to decreasing values partially reflects incomplete core recovery associated with XCB and RCB coring methods, as the width of the recovered sediments fails to completely fill the core liner and the GRA measurements are therefore calibrated for a larger sediment volume than is actually contained in XCB- and RCB-acquired cores.

The negative bias in core logger physical properties measurements associated with a partially filled core liner is confirmed by plotting discrete MAD bulk density values against the equivalent WRMSL GRA bulk density values from corresponding depths in the same core (Fig. [F36](#)). When all discrete MAD values from the combined APC, XCB, and RCB cores are considered, there is considerable scatter in the relationship with WRMSL GRA bulk density and trend toward lower WRMSL GRA bulk densities relative to discrete samples, with a slope of 0.92. However, when only APC cores (which were almost uniformly recovered with full liners) are considered, the relationship between discrete MAD and WRMSL GRA

bulk densities collapses onto a linear trend with a slope of ~ 1 .

Magnetic susceptibility

Because the WRMSL loop magnetic susceptibility meter has a response function with a ~ 4.5 cm width at half height (see “**Physical properties**” in the “Methods” chapter [Jaeger et al., 2014]), whereas the point-source magnetic susceptibility data is sensitive over ~ 1 cm, both the point source and loop magnetic susceptibility data sets were smoothed with a Gaussian filter of 10 cm ($\pm 3\sigma$) and then interpolated to constant resolution (note that data in the LIMS database are recorded at their raw measurement resolution). Although the relationship between point-source magnetic susceptibility and loop magnetic susceptibility appears to be linear, there is an offset in the overall magnitude of the measurements, with loop magnetic susceptibility being on average $1.68\times$ greater than the point-source measurements (Fig. F37). We evaluate all volumetric magnetic susceptibility measurements in instrument units (IU) because of the lack of available absolute calibration standards (see “**Physical properties**” in the “Methods” chapter [Jaeger et al., 2014]).

Volumetric WRMSL loop magnetic susceptibility (κ) averages around ~ 120 IU downhole at the site (Figs. F31, F32, F33, F34, F35). A few anomalously high values >1000 IU in Hole U1417D are associated with fragments of tungsten carbide drill bit teeth that broke off of XCB cutting shoes. Cyclic variability between 50 and 100 IU is present throughout the core, and a trend toward higher values with depth in the APC cores may reflect sediment compaction. A decrease in WRMSL loop magnetic susceptibility and an increase in the difference between loop and magnetic susceptibility deeper than ~ 190 m CCSF-B (~ 225 m CSF-A) in Holes U1417B and U1417D (Figs. F32, F34) are associated with the transition to XCB core collection and likely reflect reduced sediment diameter in the core liner (as discussed in “**Gamma ray attenuation bulk density**”). The negative bias observed in loop magnetic susceptibility associated with incompletely filled core liners is consistent with decreases in measured GRA bulk density also driven by the deviation from calibration volume (Fig. F38). After smoothing with a Gaussian filter of 10 cm ($\pm 3\sigma$) to correct for the differing response functions of the instruments, we can use this relationship to generate a volume-corrected mass magnetic susceptibility (χ) with units of cm^3/g (Fig. F38). This mass (GRA normalized) magnetic susceptibility can be used to evaluate changes in lithology independent of variable porosity, different coring tech-

niques, and recovery efficiencies. Correcting for sediment volume reduces variance in χ by $\sim 10\%$ relative to the equivalently smoothed raw WRMSL magnetic susceptibility data normalized by the mean core GRA bulk density.

Compressional wave velocity

P-wave velocity was measured on the WRMSL *P*-wave logger (PWL) (see “**Physical properties**” in the “Methods” chapter [Jaeger et al., 2014]) in Holes U1417A–U1417D to ~ 220 m CSF-A at a resolution of 2.5 cm (Fig. F39). Reasonable measurements could only be obtained for core depths shallower than ~ 220 m CSF-A because of the development of void spaces within the core liners after switching to XCB coring in Holes U1417B and U1417D. WRMSL *P*-wave velocity values gradually increase downhole, closely following GRA bulk densities (Figs. F31, F32, F33, F34), ranging from ~ 1470 m/s at the seafloor to ~ 1650 m/s at ~ 220 m CSF-A (Fig. F36).

Discrete *P*-wave measurements using the *P*-wave caliper tool (PWC) were taken in Holes U1417A, U1417D, and U1417E with ~ 20 m overlap of measurements between holes. In Holes U1417A and U1417D, PWL and PWC measurements overlapped at all depths shallower than ~ 220 m CCSF-B (Fig. F40). PWC values were automatically picked where possible and manually picked when the automatic picker encountered errors when the calipers did not have sufficient contact with the sample because of very soft sediment or bad coupling with the liner. In cases where both automatic and manual picks were recorded, the manual picks are systematically faster than the automatic picks (Figs. F40, F41). The PWL and automated PWC velocities track well deeper than ~ 15 m CCSF-B, and a scatter plot shows that the two measurements are significantly correlated (Fig. F40). However, care must be taken when making interpretations based on the discrete velocity data because the sampling is biased by both core recovery and sampling rate in different lithology types.

Deeper than ~ 200 m CCSF-B, the rate of velocity change with depth increases to ~ 420 m CCSF-B (Fig. F41). The inflection point at ~ 200 m CCSF-B may be associated with the transition from lithostratigraphic Unit I to Unit II, where the abundances of limestones and biosiliceous oozes decrease (see “**Lithostratigraphy**”). Deeper than ~ 420 m CCSF-B, elevated velocities (~ 2420 – 5700 m/s) are correlated to cemented intervals, whereas lower values (<1650 m/s) are associated with diatom ooze (Fig. F41) (see “**Lithostratigraphy**”).

Natural gamma radiation

We analyzed NGR at 10 cm intervals on all whole-round core sections that exceeded 50 cm in length, with minimum section length limited by the response function of the sodium iodide detectors (see “[Physical properties](#)” in the “Methods” chapter [Jaeger et al., 2014]). Each measurement reflects the integration of 5 min of counts (i.e., 10 min of counting per section, consisting of 5 min at each of two positions separated by 10 cm). NGR values show downhole cyclic variability between 7 and 50 counts per second (Figs. [F31](#), [F32](#), [F33](#), [F34](#), [F35](#)) with a mean and standard deviation of 31 and 6, respectively. As NGR counts reflect minerals that fix K, U, and Th, high-frequency variations are likely associated with changes in lithology. NGR variability parallels trends in GRA bulk density and *P*-wave velocity, which also suggests the dominant influence of terrigenous input. Low NGR values frequently correspond with low magnetic susceptibility and increased lightness (L^*).

The high-frequency variability in NGR is superimposed on a long-term increase downhole between 0 and 220 m CCSF-B in Holes U1417A–U1417D, interrupted by a decrease in counts between 220 and 360 m CCSF-B, and partially recovering to higher values below 360 m CCSF-B (Fig. [F42](#)). Low NGR counts deeper than 220 m CCSF-B may partly be attributed to the smaller diameter of recovered sediment in the core liner and/or section voids during XCB coring at Holes U1417B and U1417D. For WRMSL magnetic susceptibility, after smoothing the data with a Gaussian filter of 50 cm ($\pm 3\sigma$) to accommodate for the varying response functions of the instruments, we can normalize the volumetric NGR to the WRMSL GRA bulk density to correct for variability in sediment volume. Although this treatment reduces the overall variance in the NGR record by ~50% relative to the Gaussian-smoothed uncorrected NGR data normalized by the mean core GRA bulk density, the decrease in NGR observed between 225 and 360 m CCSF-B persists in a reduced form deeper than 300 m CCSF-B (Fig. [F42](#)). We therefore propose that the lower volume-normalized NGR values between 300 and 360 m CCSF-B correspond to a lithology change in the late Pliocene (see “[Lithostratigraphy](#)”).

Moisture and density

MAD bulk density values in Holes U1417A, U1417D, and U1417E were calculated from mass and volume measurements on discrete samples from the working halves of split cores (see “[Physical properties](#)” in the “Methods” chapter [Jaeger et al., 2014]). Depending on core recovery, quality, and lithology, one to

three samples were taken per core. The lithologies associated with samples were recorded in the log sheet if distinct from the dominant sediment (i.e., a sandy event deposit or a biosiliceous layer). Where lithology is undefined in these records, the sample was taken from the dominant lithology within that core. A total of 220 samples were analyzed for MAD: 58 samples from Hole U1417A, 97 samples from Hole U1417D, and 65 samples from Hole U1417E.

MAD values correspond well with GRA bulk densities measured on the WRMSL in Hole U1417A (Fig. [F43](#)). Starting at ~225 m CCSF-B, GRA bulk density values are less than the MAD densities because of reduced sediment diameter recovery in the XCB and RCB cores (see “[Gamma ray attenuation bulk density](#)”). MAD densities increase downhole to ~300 m CCSF-B, ranging from ~1.5–1.8 g/cm³ at the seafloor to ~1.8–2.1 g/cm³ at ~300 m CCSF-B. From ~300 to 430 m CCSF-B a population of low-density samples ranges from ~1.4 to ~1.8 g/cm³. At ~430 m CSF-A, densities increase to ~1.7–2.0 g/cm³. Between ~430 and ~700 m CCSF-B, density remains relatively constant, with increased scatter below ~620 m CCSF-B associated with biosiliceous layers, sand-rich intervals, and cemented sections (see “[Lithostratigraphy](#)”).

Bulk grain density values are fairly constant between the seafloor and ~300 m CCSF-B, ranging between ~2.8 and 3.0 g/cm³ (Fig. [F44](#)). Variability increases slightly between ~300 and 430 m CCSF-B, with a population of low bulk grain densities corresponding to low bulk densities. Between ~430 and 620 m CCSF-B, variability again decreases, averaging between ~2.8 and 2.9 g/cm³. A secondary population of elevated scatter occurs deeper than 620 m CCSF-B, with grain densities up to ~3 g/cm³.

Porosity (percent pore space of wet sediment volume) measured on discrete samples decreases with depth to ~310 m CCSF-B, showing a normal consolidation curve. At ~310 m CSSF-B, discrete values increase to ~52%–62% and then decrease to ~45% at ~470 m CCSF-B (Fig. [F44](#)). Deeper than ~620 m CCSF-B, more scatter was observed because of measurements associated with biosiliceous material and cemented sections. Deeper than ~450 m CCSF-B, sand-rich sediment and clay and silt sediment show normal consolidation. Diatom-rich sediment shows high porosity, which reflects the presence of the porous diatom frustules (Fig. [F44](#)).

Shear strength

Shear strength measurements were performed on working section halves from Holes U1417A and U1417D using the automated vane shear (AVS) test-

ing system (see “**Physical properties**” in the “Methods” chapter [Jaeger et al., 2014]). Efforts were made to avoid the locations of obvious drilling disturbance or cracks in the half-core sample. Measurements were taken as close as possible to the positions of the MAD samples.

Shear strength indicates that sediments range from very soft (0–20 kPa) to very stiff (120–180 kPa). The rate of change of shear strength with depth decreases at ~40 m CCSF-B (Fig. F45). Values are more scattered deeper than 100 m CCSF-B. All samples were taken in the dominant lithology of dark gray-greenish mud, so it is unlikely that the increasing variability of shear strength measurements is due to lithology alone. Rather, as the mud gets stiffer with depth, other factors such as cracking may affect the measurement. Shear strength measurements were halted at Core 341-U1417D-43X when samples were sufficiently hardened to break destructively upon penetration of the vane.

Geothermal gradient

Temperature measurements were conducted using the APCT-3 during APC coring in Hole U1417A. Three temperature measurements were taken in total (Fig. F46A), and a geothermal gradient was successfully obtained (Cores 341-U1417A-4H, 10H, and 13H) between 33.9 and 104.4 m CSF-A. The best fit line to temperature versus depth data was derived from the results (Fig. F46B):

$$T(z) = 0.0605 \times z + 1.9156 (R^2 = 0.9991),$$

where $T(z)$ is in situ temperature at depth z (m CSF-A). The estimated geothermal gradient is therefore 61°C/km. Note that this geothermal gradient was established for depths shallower than 120 m CSF-A.

Paleomagnetism

The natural remanent magnetization (NRM) of Site U1417 archive-half cores was measured before and after alternating field (AF) demagnetization. Peak AFs were restricted to a maximum of 20 mT for sections recovered using the APC system with standard (full and half length) and nonmagnetic core barrels (see “**Operations**”). Higher AFs of up to 40 mT were used for a few sections recovered using the XCB and RCB systems (Table T14). The number of demagnetization steps and the peak field used reflected the demagnetization characteristics of the sediments, the severity of the drill string magnetic overprint, the desire to use low peak fields to preserve the magnetization for future shore-based studies, and the need to

maintain core flow through the laboratory. Sections completely disturbed by drilling, as noted by the lithostratigraphy and/or paleomagnetism groups, were not measured. Data associated with intervals affected by obvious drilling deformation or measurement error (flux jumps; e.g., Richter et al., 2007) were culled prior to interpretation.

For sections recovered through APC drilling, the NRM intensities at Site U1417 are strong both before (10^{-1} A/m, with occasional decimeter-scale intervals of >25) and after (10^{-2} A/m) demagnetization (Fig. F47). Intensities show variability at both the meter and decameter scales through this part of the sequence, reflecting lithology (see “**Lithostratigraphy**”) and, for the demagnetized intensity, geomagnetic field variability. High intensities of up to >0.25 A/m before demagnetization are more commonly observed in Holes U1417C and U1417D and could reflect a stress-induced progressive increase in the magnetization of the drill string or bottom-hole assembly (e.g., Richter et al., 2007). No clear correlation was observed between core barrel type (full, half, or nonmagnetic) employed and magnetization.

In the XCB- and RCB-cored materials, magnetic intensity shows greater variability, reflecting lithologic changes and variable core quality (Fig. F48; see “**Lithostratigraphy**”). NRM intensities after demagnetization continue to be in the 10^{-2} A/m range, transitioning to lower values through the ~300–350 m CSF-A interval, corresponding to lithostratigraphic Unit IV. Intensities are variable between ~350 and 475 m CSF-A, corresponding to lithostratigraphic Subunits VA and VC, ranging from 10^{-4} to 10^{-2} A/m. Deeper than ~475 m CSF-A, intensities are consistently lower, in the 10^{-3} to 10^{-4} A/m range, and vary on an ~50 m scale.

In the APC-recovered interval, transformation of depths to CCSF-B (see “**Stratigraphic correlation**”) allows comparison between holes that facilitates polarity interpretation. After demagnetization at peak fields of 10 or 20 mT, intensities are reduced to the 10^{-2} A/m range and are consistent between all holes (Fig. F47). Steep positive inclinations observed in the APC section prior to demagnetization consistent with a low-coercivity drill string magnetic overprint are removed by peak AF demagnetization of 10 mT in the upper ~160 m CCSF-B (Fig. F49). Within this interval, polarity can be unambiguously determined. Inclinations associated with normal and reversed polarities vary around the values expected (approximately $\pm 72^\circ$) for a geocentric axial dipole at the site latitude. Declinations show serial correlation within-core. Inclination from Holes U1417A–U1417D documents a continuous sequence (see “**Stratigraphic**”

correlation”), allowing correlation to the geomagnetic polarity timescale (GPTS; Cande and Kent 1995) on the geologic timescale (Hilgen et al., 2012). When polarity transitions occur within a core, declination changes are consistent with inclination-based polarity interpretations (Fig. F49). The Matuyama/Brunhes boundary and the upper Matuyama Chronozone (C1r) containing the Jaramillo Subchronozone (C1r.1n) are clearly identified. A short interval of normal polarity deeper than the Jaramillo polarity zone is observed in multiple holes and is correlated with the Cobb Mountain Subchronozone (C1r.2n). Deeper than ~160 m CCSF-B, unambiguous recognition of polarity transitions is more difficult, even in the APC-recovered sections (Fig. F49). We do partially observe the Olduvai (C2n) and Reunion (C2r.1n) Subchronozones and correlate their apparent polarity boundaries to the GPTS. Figure F49 and Tables T12 and T15 document these polarity zonations and corresponding age interpretations.

In the XCB- and RCB-recovered intervals, the Gauss (2An) to Matuyama (2r) polarity transition is clearly observed in correlative sections of Holes U1417B, U1417D, and U1417E (Fig. F50; Table T15). At greater depths, correlations are more ambiguous. Although both negative and positive inclinations were recovered deeper than ~300 m CCSF-B, with apparent transitions often captured in a single XCB/RCB core section, interpretation of directional data is complicated by low core recovery and in particular by biscuiting. The quality of the paleomagnetic record within these few recovered meters suggests either that the extremely condensed section around the observed polarity reversals is recovered from the top, middle, or bottom of the drilled interval or that the recovered interval characterized by hard biscuits and softer slurry represents coherently recovered pieces spread through each drilled interval. The options that limit the stratigraphic emplacement of the coherent biscuits within the softer slurry in the XCB/RCB cores include either a narrow episode of recovery near the top or bottom of the drilled interval or evenly distributed recovery through the entire core length. To improve recognition of polarity zonations and to assess the nature of material within the XCB and RCB cores, we assume the latter option of distributed emplacement and linearly expand each measurement made at 2.5 cm intervals on the recovered core evenly through the drilled interval depth. This simplistic approach assumes that recovered material is derived equally from within the cored interval. An alternative approach using the biscuit boundaries to guide expansion is beyond the time constraints of shipboard research. The results of this exercise, constrained by biostratigraphy, are shown

in Figure F50, revealing a recognizable pattern of polarity reversals in the XCB/RCB portions of Holes U1417B, U1417D, and U1417E. Much of the Gauss (C2An) and Gilbert (C2Ar) Chronozones can be recognized and correlated to the GPTS in Holes U1417B, U1417D, and U1417E (Tables T12, T15). However, whether the lowest normal polarity interval observed at ~425 m CCSF-B reflects the Thvera (C3n.4n) or Sidufjall (C3n.3n) is unclear. At deeper intervals, guided by biostratigraphic datums (see “Paleontology and biostratigraphy”), correlations are made to the top of Chron C3An at ~475 m CCSF-B and to Chron C3Bn at ~585 m CCSF-B. Deeper than ~600 m CCSF-B, the placement of polarity boundaries is equivocal.

Shore-based analyses will allow significant refinement of these interpretations. Much of the ambiguity could result from the inability of the low level of AF demagnetization to fully remove the drill string overprint, especially in intervals where XCB and RCB drilling was applied. Additionally, targeting better preserved and more specific lithologies by discrete sampling will likely lead to more reliable results.

Downhole logging

Logging operations

Logging operations for Site U1417 began after completion of RCB operations in Hole U1417E at 1315 h (local) on 20 June 2013 to a total depth of 709.5 m DSF. In preparation for logging, the hole was flushed with a 50 bbl sweep of high-viscosity mud and the RCB bit was released. The pipe was pulled to a depth of 81.4 m DSF. Four tool strings were deployed in Hole U1417E during logging operations: the triple combo, the FMS-sonic, the MSS, and the VSI (Fig. F51; see “Downhole logging” in the “Methods” chapter [Jaeger et al., 2014]).

The first deployment was the triple combo tool string, which was made up of gamma ray, porosity, density, resistivity, and magnetic susceptibility tools. The tool string was lowered into the hole at 2120 h on 20 June, completing a downlog to a total depth of 624 m WSF, where it was blocked from downhole progress by a bridge in the hole. The main uplog pass was then conducted at a speed of 900 ft/h and ran up through the pipe and past the seafloor. The tool string was run back down the hole for a short repeat pass from 225 m WSF at a speed of 1800 ft/h.

The second deployment was the FMS-sonic tool string, after an attempt to run the VSI tool string was postponed because of the presence of marine mammals (see “Operations”). The string was run into the

hole at 1132 h on 21 June and reached a total depth of 571 m WSF, unable to pass a bridged section of the hole. Two full passes of the hole were made from 571 m WSF: the first at a speed of 1200 ft/h while recording all Dipole Shear Sonic Imager (DSI) modes (monopole compressional, upper dipole, lower dipole, crossed dipoles, and Stoneley) and the second at 1800 ft/h while recording only standard DSI modes (monopole compressional, upper dipole, and lower dipole). The tool string was rigged down by 2230 h.

The MSS tool string was run next in Hole U1417E. This run was the first at-sea attempt to deploy the full MSS-B tool (comprising the deep-reading and high-resolution magnetic susceptibility sensors). The tool string was rigged up at 2240 h and run into the hole, reaching a final depth of 204 m WSF. The high-resolution MSS sensor has a stiff bowspring to keep it eccentralized, which may have prevented the tool string from passing the bridges in shallow sections of the hole. Two full uplog passes were recorded from 204 m WSF, and the tool was rigged down by 0530 h on 22 June.

The last tool run was the VSI tool string. Protected Species Observation began at first light on 22 June, and the air gun ramp-up began 1 h later, as no protected species were observed in the 940 m diameter exclusion zone for this site (see [“Operations”](#)). The air guns were positioned ~7 m below the sea surface for the vertical seismic profile (VSP) in Hole U1417E. The rig-up of the VSI tool string started at 0545 h, and the air guns were fired every 5–15 min as the tool string was run into the hole. At 0830 h, the tool string reached a final depth of 218 m WSF; considerable efforts to reach deeper depths were unsuccessful. It was difficult to get a good clamp with the VSI caliper arm because of the irregular borehole diameter, and many of the recorded seismic waveforms were noisy. Two of the station locations, both closer to 211 m WSF, yielded reasonable first arrival times. At 1305 h, the tool string was run back up the hole. The tool string was rigged down by 1551 h, and logging operations were complete by 1605 h on 22 June.

Seas were relatively calm for the duration of logging operations. The average heave was 0.5 m (peak-to-peak).

Data processing and quality assessment

All logging curves were depth-matched using the total gamma ray log from the main pass of the triple combo as a reference, allowing a unified depth scale to be produced. Features in gamma ray logs from the other tool string passes were aligned to the reference log to produce a complete depth-matched data set.

Logging data were then depth-shifted to the seafloor as identified by a stepwise increase in the gamma ray value, leading to wireline log matched depth below seafloor (WMSF). The triple combo main pass identified seafloor at 4200 m water depth.

The quality of the downhole logs was affected by the range in borehole diameter, estimated by the hydraulic caliper on the Hostile Environment Litho-Density Sonde (HLDS) and by the FMS calipers (Figs. [F52](#), [F53](#)). The caliper logs show an irregular shape through much of the open borehole (ranging from <5 to ≥18 inches [the maximum extent of the HLDS caliper arm]), with up to 13 inches of horizontal range over just a few meters vertical depth. All four tool strings deployed in Hole U1417E were blocked at various depths in the borehole by narrow sections or bridges. Significant problems occurred at 242, 246, and 624 m WSF for the triple combo and 300 and 366 m WSF for the FMS-sonic.

As a result of varying borehole conditions associated with rugosity and borehole diameter, logging data vary in quality. Most logs exhibit anomalous high-frequency variability in the upper 305 m WMSF section of the hole, where caliper logs indicate that the hole is dominated by thin washouts and bridges, but data quality improves deeper than 305 m WMSF. In general, gamma ray, resistivity, magnetic susceptibility, and *P*-wave velocity were the least affected by variable hole diameter. Features in gamma ray data associated with very wide or very narrow borehole diameters should be treated with caution; fewer gamma rays reach the tool detector in a wider borehole, and more reach the detector where the borehole is narrower. Density and porosity were highly affected in the upper 305 m WMSF, with average density values close to water density and anomalously high porosity (close to 100%) through most of the interval (Fig. [F52](#)). Magnetic susceptibility logs show reasonable responses throughout the borehole (see [“Magnetic susceptibility logs”](#)), although these logs exhibit a clear downhole drift presumably related to tool temperature.

The quality of the logs can also be assessed by comparison with measurements made on cores from the same site (Fig. [F52](#)). Total natural gamma ray from the triple combo show good agreement with scaled NGR core logging data from the base of the pipe to ~220 m WMSF. Deeper than 220 m WMSF, the two data sets show similar trends but the core NGR data are offset, likely due to the change in coring technique at ~220 m WMSF (from the APC system to the XCB system) that can result in a lower volume of sediment being counted (see [“Physical properties”](#)). Density logs appear to underestimate formation density in the shallowest 305 m WMSF interval where

borehole diameter is highly variable, as shown by comparison with the core-based MAD data shown in Figure F52. However, these data show good correspondence deeper than 305 m WMSF, where the borehole condition and log quality are improved. Porosity logs are anomalously high throughout the hole, as compared to MAD porosity data. The Accelerator Porosity Sonde was not designed for high-porosity formations (>50–60 pu) and often overestimates porosity in wide and rugose boreholes; therefore, these data should not be considered in interpretation. Resistivity logs show reasonable responses throughout the hole, despite poor borehole conditions, and postcruise density and porosity estimates may be attempted with caution from resistivity using Archie's relationship (Archie, 1942).

FMS data quality relies on a number of factors, including an in-gauge hole, regular borehole walls, and good contact between the tool's pads and the borehole wall. Processing of the FMS image data allows a speed correction to be applied that takes account of variations in the speed of the tool, including stick and slip, measured by the General Purpose Inclinometry Tool incorporated into the tool string. Two processing methods were applied to the speed-corrected images. Static processing normalizes the entire measured resistivity range for the full depth of the borehole to allow for assessment of large-scale resistivity variations. Dynamic processing rescales the color intensity over a sliding 2 m depth window to highlight local features. Despite borehole conditions, FMS images seem to be of good quality, with the pads making contact with the borehole walls through much of the logged interval. Large depth shifts (>0.5 m) were needed through much of the borehole, so the absolute depth reference for these images (wireline log speed-corrected depth below seafloor; WSSF) should be considered with caution.

The DSI recorded P&S monopole, upper dipole, and lower dipole modes in Hole U1417E. To optimize sonic velocity measurements in this sediment, the monopole and upper dipole utilized standard (high) frequency and the lower dipole transmitted/received at a lower frequency. The resulting slowness data were subsequently converted to acoustic velocities (V_p [monopole] and V_s [upper and lower dipole]). In Figure F53, distinctive orange-red areas in the V_p and V_s tracks indicate greater coherence in recorded sonic waveforms, and blue colors indicate little or no coherence. These data show that although the DSI was able to capture both compressional and flexural arrivals in the deeper intervals of the hole (deeper than 305 m WMSF), there was no coherence for flexural arrivals in the shallower section, and thus no V_s data were recorded.

In addition, at some depths between the base of the pipe and ~260 m WMSF, the automatic picking of the wave arrivals (black curve in Fig. F53) failed to recognize the compressional wave because of its proximity to the fluid wave in this very slow formation, and thus no V_p data were recorded. Postcruise processing could refine the V_p profile in the shallowest 305 m WMSF to provide a better estimate of compressional velocity in the poorly picked interval.

Logging stratigraphy

Downhole logging data for Hole U1417E are summarized in Figures F52, F53, F54, and F55. The logged interval is divided into two logging units primarily on the basis of borehole condition. Logging Unit 2 is further divided into two subunits on the basis of trends and distinctive features in the gamma ray, resistivity, magnetic susceptibility, and sonic logs.

Logging Unit 1 (base of drill pipe to 305 m WMSF)

Logging Unit 1 is characterized by highly variable borehole diameter, ranging from <5 inches to the 18 inch limit of the HLDS caliper arm. This irregular borehole shape has an influence on the responses of all logging tools, so the logs in this interval may be compromised by the poor borehole condition. Within this unit, the gamma ray, magnetic susceptibility, and P -wave velocity logs appear to display coherent character despite centimeter-scale noise (Figs. F52, F53, F54). The gamma radiation signal is coherent between the triple combo and FMS-sonic tool strings and ranges from 10 to 66 gAPI. The signal shows a relatively consistent trend from the base of the pipe to 255 m WMSF, with a mean value of 38 gAPI. Between 255 and 280 m WMSF, borehole diameter changes dramatically, and all logs are dominated by the effects of hole size. Deeper than 280 m WMSF, the gamma radiation signal varies around higher values (typically ~50 gAPI) relative to the shallower section of the hole. Gamma radiation is dominated by the radioactivity of potassium and thorium, with uranium contributing a relatively minor component (Fig. F54). The potassium and thorium curves follow similar patterns throughout this unit and may be tracking clay content, as both potassium and thorium are found in clay minerals. Isolated peaks in thorium at 165 and 235 m WMSF may be indicative of volcanic ash beds or interbedded sand/silt layers.

Both resistivity (Fig. F52) and P -wave velocity (Fig. F53) logs show slightly increasing trends with depth in logging Unit 1. Local peaks in P -wave velocity between ~200 and 305 m WMSF may be correlated with sand/silt layers.

Magnetic susceptibility data from Hole U1417E generally exhibit lower frequency variations from the base of the drill pipe to 280 m WMSF, with the exception of local peaks (Fig. F55). High-resolution data show many centimeter-scale features with elevated susceptibility in logging Unit 1; most have sharp boundaries, but several features have gradational boundaries. Deeper than 280 m WMSF, the amplitude of the background variability in susceptibility increases slightly.

FMS images (example intervals in Fig. F56) show that logging Unit 1 is generally more conductive than Unit 2. Within Unit 1 there are sharply bounded submeter to multiple meter-scale alternations between highly resistive and highly conductive layers. A distinct interval of higher resistivity observed in the FMS images between ~260 and 305 m WMSF coincides generally with the increase in gamma ray signal in this unit (Fig. F52).

Logging Unit 2 (305–624 m WMSF)

Logging Unit 2 is distinguished from Unit 1 primarily by improved condition of the borehole wall. Consequently, the logging data are of better quality throughout Unit 2. Although there are still thin washed-out intervals and bridged sections, there are also intervals between 305 and 624 m WMSF in which the borehole is nearly in gauge (~10 inches). Logging Unit 2 is divided into two subunits.

Logging Subunit 2A (305–476 m WMSF)

Logging Subunit 2A is characterized by total gamma ray values ranging from 25 to 66 gAPI (mean = 45 gAPI) (Fig. F54). The gamma ray signal is dominated by Th and K content, similar to the signal in logging Unit 1. A slightly higher contribution from U in Unit 2 may indicate a greater content of organic matter. The density log gradually increases with depth in this subunit (Fig. F52).

Resistivity (Fig. F52) and *P*-wave velocity logs (Fig. F53) show similar trends, generally increasing in value with depth in Subunit 2A. *P*-wave velocity increases from ~1500 m/s at the top of the subunit to >2000 m/s at the base. Local resistivity peaks correspond in most cases to *P*-wave velocity peaks, suggesting that both are responses to lithologic variations.

Magnetic susceptibility logs (Figs. F52, F55) display strong variability, with higher amplitude changes than in the overlying unit. Local peaks may indicate the presence of increased detrital sediments and/or centimeter-scale silt beds within a lower susceptibility background. FMS images show that Subunit 2B is a transition zone between a more conductive shal-

lower formation and more resistive deeper formation (Fig. F56). These images highlight an alternation between sharp and gradational contacts at the meter scale.

Within Subunit 2A, there is a distinctive interval between ~409 and 425 m WMSF in which many of the logs show unusual behavior. Gamma radiation, density, and resistivity values decrease sharply within this interval (Fig. F52) and then increase at the base, whereas *P*-wave increases throughout the interval (Fig. F53). The magnetic susceptibility signal drops significantly until the base, which coincides with a susceptibility peak (Fig. F52). The FMS images show a moderately resistive interval, with a highly resistive layer at the base. Together, these data suggest that there is a discrete layer of unusual character at this depth, with corresponding characteristics in core physical properties data (Fig. F52). However, there is no clear evidence of such a distinct feature observed in cores.

Logging Subunit 2B (476–624 m WMSF)

Logging Subunit 2B is mainly characterized by higher values in gamma radiation and density (Fig. F52). The upper boundary of this subunit is distinguished by an abrupt change in the character of magnetic susceptibility (Fig. F52) to lower amplitude variability and a step decrease in *P*-wave velocity (Fig. F53). The mean gamma ray value is 52 gAPI, and the downhole patterns in U, Th, and K measurements correspond within this subunit (Fig. F54). A change in the ratio of Th and K to the total gamma ray counts relative to Subunit 2A may indicate a change in the source of radioisotopic inputs this interval.

Density values are slightly higher than in Subunit 2A, increasing to >2.0 g/cm³ at the base of the logged interval (Fig. F52). The *P*-wave log shows a sharp decrease to ~1600 m/s at 480 m WMSF, followed by a general increase to the base of the logged interval (Fig. F53). Within Subunit 2B, magnetic susceptibility (Fig. F52) displays low to moderate amplitude variation but generally higher values from 540 to 580 m WMSF, which coincides with a general increase in gamma ray and density logs. FMS images display very resistive material with few sharp contacts and few conductive zones.

Magnetic susceptibility logs

Site U1417 marks the first at-sea deployment of the full MSS (officially MSS-B), built by Lamont-Doherty Earth Observatory between 2010 and 2012 to replace an earlier version of the tool. Comprising both a deep-reading sensor (MSS-DR), which was also incor-

porated into the triple combo, and a high-resolution sensor (MSS-HR), the full MSS tool has the capability to make magnetic susceptibility measurements at 10 and 40 cm vertical resolution.

In Hole U1417E, deep-reading magnetic susceptibility measurements were repeatable between multiple passes of the triple combo tool string (the first logging run), as well as with the MSS tool string (the third logging run) (Figs. F51, F55). High-resolution magnetic susceptibility is also repeatable between multiple passes of the MSS tool string.

The trend superimposed upon all magnetic susceptibility logs is most likely related to internal tool temperature. When the temperature of the MSS increases linearly with depth, for example as observed in the MSS data from all passes with the triple combo tool string, a simple linear temperature correction was applied. This correction was also applied to MSS data from the downlog with the MSS tool string but not to MSS data from the uplog passes because of evidence of nonlinear tool temperature effects. Figure F55 shows the uncorrected and corrected MSS-DR data for the main pass of the triple combo, as well as the similarly corrected high-resolution downlog measurement of the MSS run.

The high-resolution magnetic susceptibility signal appears to track natural gamma ray variation (Fig. F55). The small (<1 m) vertical offset observed could come from the discrepancy between the vertical resolution of the Hostile Environment Natural Gamma Ray Sonde (~20–30 cm) and the MSS-HR sensor (~10 cm). As expected, the high-resolution magnetic susceptibility data seem to record more fine-scale features than either gamma radiation or deep-reading susceptibility measurements. For example, at 116 m WMSF, the high-resolution data show multiple higher amplitude peaks, whereas the deep-reading data show only one broad peak in accordance with different vertical resolutions of the two sensors (see “Downhole logging” in the “Methods” chapter [Jaeger et al., 2014]).

In general, the trends and high values of magnetic susceptibility from the deep-reading and high-resolution measurements in Hole U1417E are the same. Postcruise investigations using core-based magnetic susceptibility data from Site U1417, for which a composite splice exists to ~220 m CCSF-D, should help to understand temperature response and improve the calibration of the MSS, as well as better resolve high-resolution susceptibility variations at this site.

Formation MicroScanner images

Despite the rugosity of the borehole wall associated with high-frequency changes in borehole diameter,

FMS resistivity images reveal differences in textures and lithologies throughout the logged interval of Hole U1417E (Fig. F56). In the statically processed images from FMS-sonic Pass 1, the submeter-scale alternating intervals of conductive and resistive lithologies characterizing logging Unit 1 are shown in contrast to the moderately resistive to highly resistive units in logging Subunit 2A and the highly resistive lithologies in logging Subunit 2B (example sections in Fig. F56). Based on the images, most if not all of the bedding in the logged interval has horizontal to subhorizontal orientation. The boundaries between different layers are generally distinct, though there are more sharp boundaries observed in Unit 1 than in Unit 2.

Vertical seismic profile and sonic velocity

One objective of the expedition was to establish the age and lithologic origin of the seismic reflections identified in the seismic survey data in the Gulf of Alaska. The VSP provides a good intermediate step in integrating the core and wireline logging data (recorded in depth) with seismic data (recorded in two-way traveltime).

Data acquired during the VSP are summarized in Table T16 and Figures F51 and F57. Although >45 shots were fired, most of the sonic waveforms recorded downhole during the VSP were noisy because of the limited extent of accessible open hole and the rugose borehole wall through this interval. The VSI caliper arm had a difficult time achieving good clamping force because of the soft formation and poor contact with the rough borehole wall. Despite these limitations, two stations close to 211 m WMSF provided check shot arrival times. Figure F57 shows the waveforms measured by the vertical direction geophone of the VSI and the direct arrivals. Table T16 lists the values of the measured and corrected arrival times. The measured traveltimes are the differences between the arrival of the acoustic pulse at a hydrophone located directly below the air gun array and the arrival at the borehole receiver. The corrected traveltimes are the traveltimes from the sea surface to the borehole receiver, which account for the depth of the air guns (7 m below sea level for Hole U1417E) and for the depth of the hydrophone below the air guns (2 m).

Approximating a linear trend, sonic velocities (between 150 and 557 m WMSF, the interval with the best *P*-wave data quality) increase downhole at ~0.15 km/s per 100 m. The similarity of the resistivity log to the sonic velocity log (Fig. F53) indicates that a pseudosonic log, constructed from the resistivity data to extend to ~615 m WMSF and calibrated with discrete *P*-wave measurements from cores to extend

to the base of the hole, could potentially be used as input for a synthetic seismogram.

Core-log-seismic integration

For the purposes of shipboard data correlation for Site U1417, we compared data displayed in the following two depth scales: WMSF (see “[Downhole logging](#)”) and CCSF-B (a compressed composite depth scale; see “[Stratigraphic correlation](#)”) for logging and core data, respectively. Logging data were depth-matched between different tool strings using the gamma ray logs recorded on each logging run and then shifted to the WMSF depth scale based on the step increase in gamma ray across the seafloor (see “[Downhole logging](#)” in the “Methods” chapter). For Site U1417, the maximum observed depth shift was ~4 m. Adding this potential error in depth to uncertainties in the depth of a given feature in CCSF-B results in an ~10 m potential depth error when comparing core-based measurements or lithologic boundaries to downhole logs. Core physical properties were measured in Holes U1417A–U1417E (see “[Physical properties](#)”), whereas logging data were recorded only in Hole U1417E (see “[Downhole logging](#)”).

To begin correlating lithostratigraphic and logging units with features observed in the seismic data, we converted lithostratigraphic and logging unit boundaries from depth in meters (CCSF-B/WMSF) to two-way traveltime (TWT) using the average velocity of each unit. Average *P*-wave velocity was derived from physical properties measurements using data from the WRMSL PWL at depths shallower than ~220 m CCSF-B and from the downhole sonic logs deeper in the hole (see “[Physical properties](#)” and “[Downhole logging](#)”).

Lithostratigraphy–downhole logging data integration

We combined sediment core observations and physical properties data with downhole logging data from Site U1417 to (1) evaluate how representative the recovered cores are relative to the portion of the sedimentary section that was logged, (2) determine the nature and extent of sediment not recovered in the XCB/RCB drilling process, and (3) examine whether observed sedimentary units and features can be correlated to borehole data and ultimately be described at higher vertical resolution at Site U1417. We first compare magnetic susceptibility measurements made on whole-round and split cores from the shipboard core logging systems (WRMSL and SHMSL; see

“[Physical properties](#)”) with temperature-corrected downhole data from the deep-reading magnetic susceptibility sensor on the triple combo tool string. We then evaluate whether similar lithostratigraphic units can be characterized by downhole resistivity and natural gamma ray measurements also recorded with the triple combo tool string (see “[Downhole logging](#)”).

In Figure F58, we compare lithostratigraphic unit boundaries, core recovery, the distribution of diamict intervals, sand-rich units, and magnetic susceptibility measurements recorded in the borehole and on cores. In general, logged and whole-core magnetic susceptibility exhibit similar trends and variability when compared over the same measured interval. We observe that transitions between intervals of high and low magnetic susceptibility in the log data correspond to lithostratigraphic boundaries in the core. These changes are particularly evident at the transitions from lithostratigraphic Units II to III, Units III to IV, and Subunits VC to VD. In areas of lower core recovery, the exact lithostratigraphic unit boundaries may have an error range of a few meters due to recovered intervals being assumed to reside at the top of each cored interval. We also observe an association between relatively high downhole log magnetic susceptibility values and occurrences of sand. Another primary observation is that the highest magnetic susceptibility measured in the downhole logs between 350 and 440 m CCSF-B corresponds to the occurrence of diamict intervals in lithostratigraphic Subunit VA and at the lithostratigraphic Subunit VB–VC transition (Fig. F58). A photograph of a representative core section (341-U1417D-53X-1, 0–75 cm) shows two intervals of diamict with high magnetic susceptibility values separated by an interval of mud with low magnetic susceptibility values (Fig. F58). The image also shows that the diamict intervals consist of fractured and “biscuited” blocks. We speculate that these diamict intervals are responsible for the high magnetic susceptibility values observed in the log data and that poor core recovery (21% in Core 53X) prevented full representation in the cored record. Lithostratigraphic Unit III is interpreted to be an ice-rafted diamict (see “[Lithostratigraphy](#)”), and poor borehole conditions across this interval (270–300 m CCSF-B) may have reduced the amplitude of the logged magnetic susceptibility signal. The base of the ice-rafted diamict interval of lithostratigraphic Unit III correlates with an improvement in borehole conditions for logging (logging Unit 1/2 boundary; see “[Downhole logging](#)”) to within meters. Overall, the logging data provide evidence for the occurrence of diamict intervals at

Site U1417. Based on these initial observations, we speculate that the deeper diamicts, possibly representing sediment gravity flow deposits, are a primary part of the sedimentary section between 350 and 400 m CCSF-B and between 450 and 500 m CCSF-B and the thickness of these lithologies are underestimated in the cored intervals.

In Figure F59, we compare downhole resistivity; total gamma ray; and K, Th, and U in standard deviation units to the lithostratigraphy, as well as the distribution of sand, ash, and volcanoclastic lithologies. Resistivity and natural gamma ray profiles are generally low in the shallowest 150 m of the logged interval (~80–230 m WMSF) and exhibit a step increase at ~250 m WMSF. Resistivity increases from 250 m WMSF to the base of the logged interval but continues to exhibit a high degree of variability. Low resistivity values in the shallowest 250 m of the sedimentary section may be related to the occurrence of mud-dominated lithologies. However, borehole dimensions are highly variable within this interval and it is difficult to attribute these variations solely to lithology. In general, we observe multiple examples where volcanoclastic sand/silt corresponds with increases in standardized downhole profiles of total gamma radiation and K. Sand layers generally have high magnetic susceptibility and low gamma ray counts—a good example of this relationship occurs at 450 m CCSF-B/WMSF. The highly resolved NGR profiles provide an opportunity to map the distribution of facies throughout the logged interval, particularly where there is poor recovery in the drilling process.

Physical properties–downhole logging data correlation

In general, there seems to be a good correspondence between the physical properties and logging data, with a vertical offset on the order of a few meters. The focus of shipboard correlation was the depth interval from ~305 to 615 m CCSF-B/WMSF within logging Subunit 2B, where reasonable borehole conditions resulted in logging data of higher quality (see “Downhole logging;” Fig. F60).

The natural gamma ray log shows good agreement with core NGR to within a few meters depth (Fig. F60); core NGR has been corrected for volume using GRA density (see “Physical properties”). The high degree of correspondence indicates both that the downhole gamma ray log is not compromised by the variability in borehole diameter within this part of the hole and that the volume correction significantly improves the fit between the downhole log and core-based NGR data. The increasing trend with depth in both data sets supports the interpretation of higher

natural radioactivity inputs likely associated with relatively muddier lithologies deeper at Site U1417.

The bulk density data also show variable agreement between downhole log, core logger, and discrete core samples. There is more scatter in the GRA density from the core logger; however, the downhole density log values generally correspond to the higher end in the range of GRA density values (Fig. F60). Discrete MAD measurements overlap with the downhole density log, showing a similar range in values. Because core measurements are necessarily limited to recovered intervals and lithologies, comparison of the log and core data suggests that recovery in this part of the hole is biased toward high-density lithologies and that lower density lithologies may not be fully recovered in cores. Although the MAD data are interpreted as showing a change in trend to increasing density below ~470 m CCSF-B (see “Physical properties”), the density log suggests that the change in trend may occur at a shallower depth (~420 m WMSF). There are corresponding changes to increased values in the resistivity and *P*-wave velocity logs at the same depth, suggesting that this depth may represent a significant transition.

Discrete *P*-wave velocity measurements on core show good correspondence with the *P*-wave velocity log to ~430 m CCSF-B/WMSF (Fig. F60). Deeper in the borehole, the *P*-wave velocity log shows generally higher velocities than the discrete core data. The lower velocity for the discrete measurements at these deeper intervals could be due to biased core recovery, choice of lithology selected for sampling, or fracturing of the split-core samples during measurements given the increasing induration downcore. However, below ~420 m CCSF-B, isolated elevated velocities (>4000 m/s) are measured on specific discrete samples (not displayed at the scale of Fig. F60) and correlated to cemented intervals in the recovered core, whereas lower velocities are correlated to diatom ooze (see “Lithostratigraphy” and “Physical properties”). The *P*-wave velocity log, with a sampling interval of ~15 cm and a vertical resolution of ~100 cm, may show intermediate velocities as it averages across centimeter-scale variations between faster and slower lithologies.

Magnetic susceptibility data show reasonable agreement between log and core measurements (Fig. F60). The magnetic susceptibility log, from the deep-reading sensor of the MSS, has been corrected for temperature (see “Downhole logging”). Core magnetic susceptibility data from the loop have been corrected for volume using GRA density (see “Physical properties” 2014). Although there is considerable scatter in the core magnetic susceptibility, there is a clear distinction in the range and am-

plitude of values across the logging Subunit 2A/2B boundary at ~470–480 m WMSF. Both log and core data show higher susceptibility values above ~470 m CCSF-B/WMSF.

Higher resolution comparison of core and downhole logging data will require detailed correlation of these two data sets. Although core recovery is lower in the XCB and RCB cored intervals (deeper than ~220 m CCSF-B), which could limit the success of core-log integration, Figure F60 shows distinctive features in both data sets that can likely be matched more precisely. These efforts can be undertaken postcruise, utilizing the total gamma radiation and magnetic susceptibility data and more detailed comparison to both visual core description and seismic images.

Seismic sequences and correlation with lithostratigraphy and downhole logs

Seismic Lines MGL1109MSC01 (Fig. F61) and MGL1109MSC14 (Fig. F62), acquired in 2011 aboard the R/V *Marcus Langseth*, cross Site U1417 (Walton et al., submitted). The primary seismic sequences on each profile, Sequences I–III, are interpreted after Reece et al. (2011). In preparation for core-log-seismic integration, Sequence I was divided into three subsections, IA–IC. Subsection IC was further subdivided into Intervals IC1 and IC2. Each of these sequence boundaries defines either a change in dominant seismic facies or a truncation surface.

Seismic Sequence III is characterized by smooth, continuous reflectors and limited seismic transparency. At Site U1417, the Seismic Sequence II/III boundary (~5805 ms TWT) is defined by high-amplitude variation. Below the two prominent reflectors at the top of Sequence II, the section loses amplitude and shows similar seismic characteristics to Sequence III. Based on our estimated depth to TWT conversion, Seismic Sequence III corresponds to lithostratigraphic Unit I: dark gray mud with thin beds of volcanic ash (Subunit IA) and gray mud with thin beds of volcanic ash and diatom ooze (Subunit IB). An increase in lonestones (outsized clasts) in Subunit IB may correspond to a package of higher amplitude reflectors at ~5.71 s TWT (using a velocity of 1518 m/s) bounded above and below by semitransparent facies (Fig. F30).

Seismic Sequence II is characterized by smooth, continuous reflectors that are semitransparent in the seismic profile. Based on our depth to TWT conversion, this sequence corresponds to lithostratigraphic Units II–IV: gray mud with 1–5 cm thick interbeds of fine sand and coarse silt (Unit II), thick beds of diamict interbedded with gray mud (Unit III), and a highly bioturbated gray mud with diatom-bearing

intervals (Unit IV). Two check shots close to 211 m WMSF correlate to the seismic data at 5.87 s TWT within Seismic Sequence II. The Unit III/IV boundary appears to map to the lower part of Seismic Sequence II, where a pair of medium-amplitude reflectors lies just above the high-amplitude package that defines the boundary between Seismic Sequences II and I. The boundary between logging Units 1 and 2 may correlate to increased reflectivity in the lower part of Sequence II (Fig. F30). However, establishing the precise position of lithostratigraphic Units III and IV relative to the Sequence II/I boundary will require more core-log-seismic analysis.

The Seismic Sequence II/I boundary (~6000 ms TWT) is located at the top of a prominent grouping of high-amplitude reflectors that are slightly more chaotic and discontinuous than those observed in Sequence II. Sequence I can be divided into three distinct seismic facies packages: Sequence IC, characterized by high-amplitude, semicontinuous reflectors; Sequence IB, a seismically transparent section with faint, semicontinuous reflectors; and Sequence IA, a high-amplitude chaotic layer overlying acoustic basement. Sequence IC is composed of two distinct packages (Sequences IC1 and Sequence IC2) divided by a truncation surface. The base of Sequence I was not penetrated at Site U1417; based on correlation with Site 178, Sequence I is ~400 m thick at Site 178 (Fig. F30). With our estimated velocities, the lithostratigraphic Unit IV/V boundary at ~350 m CCSF-B maps to ~6.05 s TWT, which is at or just below the top of Seismic Sequence I (Fig. F30). A series of thick high-amplitude reflectors comprise this boundary and may be related to the presence of cemented intervals that inhibited core recovery. Lithologically, the boundary between Units IV and V represents a change from to highly bioturbated gray mud with diatom-bearing intervals (Unit IV) to gray mud with diamict, interbedded silt and sand, and diatom ooze (Unit V).

Because of the lack of check shots deeper in the borehole, precise correlation between Seismic Sequence I, lithologic Units IV and V, and logging Unit 2 will need to be undertaken postcruise; however, some comparisons between lithofacies, seismic facies, and log character can be discussed. In general, the increased velocity and density contrasts within logging Subunit 2A and the upper part of Subunit 2B likely correspond to the series of brighter reflectors that define Seismic Sequence IC, and in turn these may correlate with the various lithofacies of lithostratigraphic Unit IV and Subunits VC or VD. The boundary between logging Units 2A and 2B may be associated with a large negative-amplitude reflector that separates seismic Subunits 1B and 1C at ~6.19 s

TWT (Fig. F30). If that correlation is validated, then the remaining lithostratigraphic Subunits VE–VJ and the lower part of logging Unit 2B all lie within Seismic Sequences IB and IA. Correlations deeper in the borehole can be checked against results from Site 178 (Shipboard Scientific Party, 1973), located ~1.5 km away, by using the basement depth of 780 m DSF and creating a pinned traveltime/depth boundary at the top of the basement during the creation of a synthetic seismogram.

References

- Addison, J.A., Finney, B.P., Dean, W.E., Davies, M.H., Mix, A.C., Stoner, J.S., and Jaeger, J.M., 2012. Productivity and sedimentary $\delta^{15}\text{N}$ variability for the last 17,000 years along the northern Gulf of Alaska continental slope. *Paleoceanography*, 27(1):PA1206. doi:10.1029/2011PA002161
- Archie, G.E., 1942. The electrical resistivity log as an aid in determining some reservoir characteristics. *J. Pet. Technol.*, 5:1–8.
- Bergen, F.W., and O’Neil, P., 1979. Distribution of Holocene foraminifera in the Gulf of Alaska. *J. Paleontol.*, 53(6):1267–1292. <http://www.jstor.org/stable/1304134>
- Berger, A.L., Gulick, S.P.S., Spotila, J.A., Upton, P., Jaeger, J.M., Chapman, J.B., Worthington, L.A., Pavlis, T.L., Ridgway, K.D., Willems, B.A., and McAleer, R.J., 2008a. Quaternary tectonic response to intensified glacial erosion in an orogenic wedge. *Nat. Geosci.*, 1:793–799. doi:10.1038/ngeo334
- Berger, A.L., Spotila, J.A., Chapman, J.B., Pavlis, T.L., Enkelmann, E., Ruppert, N.A., and Buscher, J.T., 2008b. Architecture, kinematics, and exhumation of a convergent orogenic wedge: a thermochronological investigation of tectonic–climatic interactions within the central St. Elias orogen, Alaska. *Earth Planet. Sci. Lett.*, 270(1–2):13–24. doi:10.1016/j.epsl.2008.02.034
- Boltovskoy, D., Kling, S.A., Takahashi, K., and Bjørklund, K., 2010. World atlas of distribution of Recent polycystina (Radiolaria). *Palaeontol. Electron.*, 13:1–229. http://palaeo-electronica.org/2010_3/215/index.html
- Brzezinski, M.A., Villareal, T.A., and Lipschultz, F., 1998. Silica production and the contribution of diatoms to new and primary production in the central North Pacific. *Mar. Ecol.: Prog. Ser.*, 167:89–104. doi:10.3354/meps167089
- Cande, S.C., and Kent, D.V., 1995. Revised calibration of the geomagnetic polarity timescale for the Late Cretaceous and Cenozoic. *J. Geophys. Res.: Solid Earth*, 100(B4):6093–6095. doi:10.1029/94JB03098
- Chambers, S.R., and Cranston, R.E., 1991. Interstitial-water geochemistry of Kerguelen Plateau sediments. In Barron, J., Larsen, B., et al., *Proc. ODP, Sci. Results*, 119: College Station, TX (Ocean Drilling Program), 347–374. doi:10.2973/odp.proc.sr.119.169.1991
- Clark, P.U., Archer, D., Pollard, D., Blum, J.D., Rial, J.A., Brovkin, V., Mix, A.C., Pisias, N.G., and Roy, M., 2006. The middle Pleistocene transition: characteristics, mechanisms, and implications for long-term changes in atmospheric pCO_2 . *Quat. Sci. Rev.*, 25(23–24):3150–3184. doi:10.1016/j.quascirev.2006.07.008
- Cook, M.S., Keigwin, L.D., Birgel, D., and Hinrichs, K.-U., 2011. Repeated pulses of vertical methane flux recorded in glacial sediments from the southeast Bering Sea. *Paleoceanography*, 26(2):PA2210. doi:10.1029/2010PA001993
- Culver, S.J., and Buzas, M.A., 1985. Distribution of Recent benthic foraminifera off the North American Pacific coast from Oregon to Alaska. *Smithsonian Contrib. Mar. Sci.*, 26.
- Davies, M.H., Mix, A.C., Stoner, J.S., Addison, J.A., Jaeger, J., Finney, B., and Wiest, J., 2011. The deglacial transition on the southeastern Alaskan margin: meltwater input, sea level rise, marine productivity, and sedimentary anoxia. *Paleoceanography*, 26(2):PA2223. doi:10.1029/2010PA002051
- D’Hondt, S.L., Jørgensen, B.B., Miller, D.J., et al., 2003. *Proc. ODP, Init. Repts.*, 201: College Station, TX (Ocean Drilling Program). doi:10.2973/odp.proc.ir.201.2003
- Dugdale, R.C., Wilkerson, F.P., and Minas, H.J., 1995. The role of a silicate pump in driving new production. *Deep-Sea Res., Part 1*, 42(5):697–719. doi:10.1016/0967-0637(95)00015-X
- Elliott, J.L., Larsen, C.F., Freymueller, J.T., and Motyka, R.J., 2010. Tectonic block motion and glacial isostatic adjustment in southeast Alaska and adjacent Canada constrained by GPS measurements. *J. Geophys. Res.: Solid Earth*, 115(B9):B09407. doi:10.1029/2009JB007139
- Enkelmann, E., Zeitler, P.K., Garver, J.I., Pavlis, T.L., and Hooks, B.P., 2010. The thermochronological record of tectonic and surface process interaction at the Yakutat–North American collision zone in southeast Alaska. *Am. J. Sci.*, 310:231–260. doi:10.2475/04.2010.01
- Finzel, E.S., Trop, J.M., Ridgway, K.D., and Enkelmann, E., 2011. Upper plate proxies for flat-slab subduction processes in southern Alaska. *Earth Planet. Sci. Lett.*, 303(3–4):348–360. doi:10.1016/j.epsl.2011.01.014
- Froelich, P.N., Klinkhammer, G.P., Bender, M.L., Luedtke, N.A., Heath, G.R., Cullen, D., Dauphin, P., Hammond, D., Hartman, B., and Maynard, V., 1979. Early oxidation of organic matter in pelagic sediments of the eastern equatorial Atlantic: suboxic diagenesis. *Geochim. Cosmochim. Acta*, 43(7):1075–1090. doi:10.1016/0016-7037(79)90095-4
- Fulthorpe, C.S., Hoyanagi, K., Blum, P., and the Expedition 317 Scientists, 2011. *Proc. IODP*, 317: Tokyo (Integrated Ocean Drilling Program Management International, Inc.). doi:10.2204/iodp.proc.317.2011
- Gasser, D., Bruand, E., Stüwe, K., Foster, D.A., Schuster, R., Fügenschuh, B., and Pavlis, T., 2011. Formation of a metamorphic complex along an obliquely convergent margin: structural and thermochronological evolution of the Chugach Metamorphic Complex, southern Alaska. *Tectonics*, 30(2):TC2012. doi:10.1029/2010TC002776
- Gieskes, J.M., 1973. Interstitial water studies, Leg 15: alkalinity, pH, Mg, Ca, Si, PO_4 , and NH_4 . In Heezen, B.C.,

- MacGregor, I.D., et al., *Init. Repts. DSDP*, 20: Washington, DC (U.S. Govt. Printing Office), 813–829. doi:10.2973/dsdp.proc.20.210.1973
- Gieskes, J.M., 1975. Chemistry of interstitial waters of marine sediments. *Annu. Rev. Earth Planet. Sci.*, 3:433–453. doi:10.1146/annurev.ea.03.050175.002245
- Gieskes, J.M., and Lawrence, J.R., 1981. Alteration of volcanic matter in deep-sea sediments: evidence from the chemical composition of interstitial waters from deep sea drilling cores. *Geochim. Cosmochim. Acta*, 45(10):1687–1703. doi:10.1016/0016-7037(81)90004-1
- Gieskes, J.M., Schrag, D., Chan, L.-H., Zhang, L., and Murray, R.W., 1998. Geochemistry of interstitial waters. In Saunders, A.D., Larsen, H.C., and Wise, S.W., Jr. (Eds.), *Proc. ODP, Sci. Results*, 152: College Station, TX (Ocean Drilling Program), 293–305. doi:10.2973/odp.proc.sr.152.228.1998
- Gulick, S.P.S., Jaeger, J.M., Mix, A.C., Asahi, H., Bahlburg, H., Belanger, C., Berbel, G.B.B., Childress, L., Cowan, E., Drab, L., Forwick, M., Fukumura, A., Ge, S., Gupta, S., Kioka, A., Konn, S., LeVay, L.J., März, C., Matsuzaki, K., McClymont, E., Moy, C., Müller, J., Nakamura, A., Ojima, T., Ribiero, F.R., Ridgway, K., Romero, O., Slagle, A., Stoner, J., St-Onge, G., Suto, I., Walczak, M.D., Worthington, L., Bailey, I., Enkelmann, E., Reece, R., and Swartz, J., submitted. Mid-Pleistocene climate transition drives net mass loss from rapidly uplifting St. Elias Mountains, Alaska. *Proc. Natl. Acad. Sci. U. S. A.*
- Gulick, S.P.S., Lowe, L.A., Pavlis, T.L., Gardner, J.V., and Mayer, L.A., 2007. Geophysical insights into the Transition fault debate: propagating strike slip in response to stalling Yakutat block subduction in the Gulf of Alaska. *Geology*, 35(8):763–766. doi:10.1130/G23585A.1
- Gupta, S.M., 1996. Quantitative radiolarian assemblages in surface sediments from the central Indian Basin and their paleomonsoon significance. *J. Geol. Soc. India*, 47:339–354. <http://drs.nio.org/drs/handle/2264/2240>
- Gupta, S.M., Mohan, R., and Guptha, M.V.S., 2002. Radiolarian fluxes from the southern Bay of Bengal: sediment trap results. *Deep-Sea Res., Part I*, 49(9):1669–1688. doi:10.1016/S0967-0637(02)00085-7
- Gupta, S.M., and Srinivasan, M.S., 1992. Late Miocene radiolarian biostratigraphy and paleoceanography of Sawai Bay Formation, Neill Island, Andamans, India. *Micropaleontology*, 38(3):209–235. doi:10.2307/1485789
- Hamme, R.C., Webley, P.W., Crawford, W.R., Whitney, F.A., DeGrandpre, M.D., Emerson, S.R., Eriksen, C.C., Giesbrecht, K.E., Gower, J.F.R., Kavanaugh, M.T., Peña, M.A., Sabine, C.L., Batten, S.D., Coogan, L.A., Grundle, D.S., and Lockwood, D., 2010. Volcanic ash fuels anomalous plankton bloom in subarctic northeast Pacific. *Geophys. Res. Lett.*, 37(19):L19604. doi:10.1029/2010GL044629
- Hasle, G.R., and Syvertsen, E.E., 1996. Marine diatoms. In Tomas, C.R. (Ed.), *Identifying Marine Diatoms and Dinoflagellates*: San Diego (Academic Press), 5–385. doi:10.1016/B978-012693015-3/50005-X
- Hein, J.R., O’Neil, J.R., and Jones, M.G., 1979a. Origin of authigenic carbonates in sediment from the deep Bering Sea. *Sedimentology*, 26(5):681–705. doi:10.1111/j.1365-3091.1979.tb00937.x
- Hein, J.R., Yeh, H.-W., and Alexander, E., 1979b. Origin of iron-rich montmorillonite from the manganese nodule belt of the north equatorial Pacific. *Clays Clay Miner.*, 27(3):185–194. doi:10.1346/CCMN.1979.0270303
- Hilgen, F.J., Lourens, L.J., and Van Dam, J.A., 2012. The Neogene period. In Gradstein, F.M., Ogg, J.G., Schmitz, M.D., and Ogg, G.M. (Eds.), *The Geologic Time Scale*: Oxford (Elsevier), 923–978. doi:10.1016/B978-0-444-59425-9.00029-9
- Hogan, L.G., Scheidegger, K.F., Kulm, L.D., Dymond, J., and Mikkelsen, N., 1978. Biostratigraphic and tectonic implications of ⁴⁰Ar–³⁹Ar dates of ash layers from the northeast Gulf of Alaska. *Geol. Soc. Am. Bull.*, 89(8):1259–1264. doi:10.1130/0016-7606(1978)89<1259:BATIOA>2.0.CO;2
- Jakobsson, M., Grantz, A., Kristoffersen, Y., Macnab, R., MacDonald, R.W., Sakshaug, E., Stein, R., and Jokat, W., 2004. The Arctic Ocean: boundary conditions and background information. In Stein, R., and MacDonald, R.W., (Eds.), *The Organic Carbon Cycle in the Arctic Ocean*: Heidelberg (Springer-Verlag), 1–32. doi:10.1007/978-3-642-18912-8_1
- Jaeger, J.M., Gulick, S.P.S., LeVay, L.J., Asahi, H., Bahlburg, H., Belanger, C.L., Berbel, G.B.B., Childress, L.B., Cowan, E.A., Drab, L., Forwick, M., Fukumura, A., Ge, S., Gupta, S.M., Kioka, A., Konno, S., März, C.E., Matsuzaki, K.M., McClymont, E.L., Mix, A.C., Moy, C.M., Müller, J., Nakamura, A., Ojima, T., Ridgway, K.D., Rodrigues Ribeiro, F., Romero, O.E., Slagle, A.L., Stoner, J.S., St-Onge, G., Suto, I., Walczak, M.H., and Worthington, L.L., 2014. Methods. In Jaeger, J.M., Gulick, S.P.S., LeVay, L.J., and the Expedition 341 Scientists, *Proc. IODP*, 341: College Station, TX (Integrated Ocean Drilling Program). doi:10.2204/iodp.proc.341.102.2014
- Kamikuri, S., Motoyama, I., and Nishimura, A., 2008. Radiolarian assemblages in surface sediments along longitude 175°E in the Pacific Ocean. *Mar. Micropaleontol.*, 69(2):151–172. doi:10.1016/j.marmicro.2008.07.005
- Katsuki, K., and Takahashi, K., 2005. Diatoms as paleoenvironmental proxies for seasonal productivity, sea-ice and surface circulation in the Bering Sea during the late Quaternary. *Deep-Sea Res., Part II*, 52(16–18):2110–2130. doi:10.1016/j.dsr2.2005.07.001
- Keller, G., 1980. Benthic foraminifers and paleobathymetry of the Japan Trench area, Leg 57, Deep Sea Drilling Project. In Scientific Party, *Init. Repts. DSDP*, 56, 57: Washington, DC (U.S. Govt. Printing Office), 835–865. doi:10.2973/dsdp.proc.5657.124.1980
- Kennett, J.P., Rozo-Vera, G.A., and Machain Castillo, M.L., 2000. Latest Neogene planktonic foraminiferal biostratigraphy of the California margin. In Lyle, M., Koizumi, I., Richter, C., and Moore, T.C. (Eds.), *Proc. ODP, Sci. Results*, 167: College Station, TX (Ocean Drilling Program), 41–62. doi:10.2973/odp.proc.sr.167.212.2000
- Koizumi, I., 2008. Diatom-derived SSTs (*Td'* ratio) indicate warm seas off Japan during the middle Holocene (8.2–3.3 kyr BP). *Mar. Micropaleontol.*, 69(3–4):263–281. doi:10.1016/j.marmicro.2008.08.004

- Kreemer, C., Holt, W.E., and Haines, A.J., 2003. An integrated global model of present-day plate motions and plate boundary deformation. *Geophys. J. Int.*, 154(1):8–34. doi:10.1046/j.1365-246X.2003.01917.x
- Kucera, M., 2007. Planktonic foraminifera as tracers of past oceanic environments. In Hillaire, M., and de Vernal, A. (Eds.), *Proxies in Late Cenozoic Paleoceanography*. Dev. Mar. Geol., 1:213–262. doi:10.1016/S1572-5480(07)01011-1
- Kucera, M., and Kennett, J.P., 2000. Biochronology and evolutionary implications of late Neogene California margin planktonic foraminiferal events. *Mar. Micropaleontol.*, 40(1–2):67–81. doi:10.1016/S0377-8398(00)00029-3
- Kulm, L.D., von Huene, R., et al., 1973. *Init. Repts. DSDP*, 18: Washington, DC (U.S. Govt. Printing Office). doi:10.2973/dsdp.proc.18.1973
- Lagoe, M.B., Eyles, C.H., Eyles, N., and Hale, C., 1993. Timing of late Cenozoic tidewater glaciation in the far North Pacific. *Geol. Soc. Am. Bull.*, 105(12):1542–1560. doi:10.1130/0016-7606(1993)105<1542:TOLCTG>2.3.CO;2
- Lagoe, M.B., and Thompson, P.R., 1988. Chronostratigraphic significance of late Cenozoic planktonic foraminifera from the Ventura Basin, California: potential for improving tectonic and depositional interpretation. *J. Foraminiferal Res.*, 18(3):250–266. doi:10.2113/gsjfr.18.3.250
- Lagoe, M.B., and Zellers, S.D., 1996. Depositional and microfaunal response to Pliocene climate change and tectonics in the eastern Gulf of Alaska. *Mar. Micropaleontol.*, 27(1–4):121–140. doi:10.1016/0377-8398(95)00055-0
- Lisiecki, L.E., and Raymo, M.E., 2005. A Pliocene–Pleistocene stack of 57 globally distributed benthic $\delta^{18}\text{O}$ records. *Paleoceanography*, 20(1):PA1003. doi:10.1029/2004PA001071
- Lowe, D.R., 1982. Sediment gravity flows, II. Depositional models with special reference to the deposits of high-density turbidity currents. *J. Sediment. Petrol.*, 52(1):279–297. <http://jsedres.sepmonline.org/cgi/content/abstract/52/1/279>
- Maus, S., Barckhausen, U., Berkenbosch, H., Bournas, N., Brozena, J., Childers, V., Dostaler, F., Fairhead, J.D., Finn, C., von Frese, R.R.B., Gaina, C., Golynsky, S., Kucks, R., Lühr, H., Milligan, P., Mogren, S., Müller, R.D., Olesen, O., Pilkington, M., Saltus, R., Schreckenberger, B., Thébaud, E., and Caratori Tontini, F., 2009. EMAG2: a 2-arc min resolution Earth Magnetic Anomaly Grid compiled from satellite, airborne, and marine magnetic measurements. *Geochem., Geophys., Geosyst.*, 10(8):Q08005. doi:10.1029/2009GC002471
- Mayer, L., Piasias, N., Janecek, T., et al., 1992. *Proc. ODP, Init. Repts.*, 138: College Station, TX (Ocean Drilling Program). doi:10.2973/odp.proc.sr.138.1995
- McDuff, R.E., 1985. The chemistry of interstitial waters, Deep Sea Drilling Project Leg 86. In Heath, G.R., Burckle, L.H., et al., *Init. Repts. DSDP*, 86: Washington, DC (U.S. Govt. Printing Office), 675–687. doi:10.2973/dsdp.proc.86.131.1985
- Medlin, L.K., and Priddle, J. (Eds.), 1990. *Polar Marine Diatoms*: Cambridge (British Antarct. Surv.).
- Michalopoulos, P., and Aller, R.C., 1995. Rapid clay mineral formation in Amazon delta sediments: reverse weathering and oceanic elemental cycles. *Science*, 270(5236):614–617. doi:10.1126/science.270.5236.614
- Molnia, B.F., and Hein, J.R., 1982. Clay mineralogy of a glacially dominated, subarctic continental shelf: north-eastern Gulf of Alaska. *J. Sediment. Petrol.*, 52(2):515–527. doi:10.1306/212F7F90-2B24-11D7-8648000102C1865D
- Ogg, J.G., 2012. Geomagnetic polarity time scale. In Gradstein, F.M., Ogg, J.G., Schmitz, M.D., and Ogg, G.M. (Eds.), *The Geologic Time Scale 2012*: Amsterdam (Elsevier), 85–113. doi:10.1016/B978-0-444-59425-9.00005-6
- Ohkushi, K., Ahagon, N., Uchida, M., and Shibata, Y., 2005. Foraminiferal isotope anomalies from northwestern Pacific marginal sediments. *Geochem., Geophys., Geosyst.*, 6(4):Q04005. doi:10.1029/2004GC000787
- Plafker, G., 1987. Regional geology and petroleum potential of the northern Gulf of Alaska continental margin. In Scholl, D.W., Grantz, A., and Vedder, J.G. (Eds.), *Petroleum Geology Potential of the Continental Margin of Western North America and Adjacent Ocean Basins*. Earth Sci. Ser. (N. Y.), 6:229–268.
- Powell, R.D., and Molnia, B.F., 1989. Glacimarine sedimentary processes, facies and morphology of the south-southeast Alaska shelf and fjords. *Mar. Geol.*, 85(2–4):359–390. doi:10.1016/0025-3227(89)90160-6
- Raiswell, R., and Fisher, Q.J., 2004. Rates of carbonate cementation associated with sulphate reduction in DSDP/ODP sediments: implications for the formation of concretions. *Chem. Geol.*, 211(1–2):71–85. doi:10.1016/j.chemgeo.2004.06.020
- Rea, D.K., and Snoeckx, H., 1995. Sediment fluxes in the Gulf of Alaska: paleoceanographic record from Site 887 on the Patton-Murray Seamount platform. In Rea, D.K., Basov, I.A., Scholl, D.W., and Allan, J.F. (Eds.), *Proc. ODP, Sci. Results*, 145: College Station, TX (Ocean Drilling Program), 247–256. doi:10.2973/odp.proc.sr.145.122.1995
- Reece, R.S., Gulick, S.P.S., Christeson, G.L., Horton, B.K., van Avendonk, H., and Barth, G., 2013. The role of far-field tectonic stress in oceanic intraplate deformation, Gulf of Alaska. *J. Geophys. Res.: Solid Earth*, 118(5):1862–1872. doi:10.1002/jgrb.50177
- Reece, R.S., Gulick, S.P.S., Horton, B.K., Christeson, G.L., and Worthington, L.L., 2011. Tectonic and climatic influence on the evolution of the Surveyor Fan and channel system, Gulf of Alaska. *Geosphere*, 7(4):830–844. doi:10.1130/GES00654.1
- Richter, C., Acton, G., Endris, C., and Radsted, M., 2007. Handbook for shipboard paleomagnetists. *ODP Tech. Note*, 34. doi:10.2973/odp.tn.34.2007
- Ruttenberg, K.C., and Berner, R.A., 1993. Authigenic apatite formation and burial in sediments from non-upwelling, continental margin environments. *Geochim.*

- Cosmochim. Acta*, 57(5):991–1007. doi:10.1016/0016-7037(93)90035-U
- Sakshaug, E., 2004. Primary and secondary production in the Arctic Seas. In Stein, R., and Macdonald, R.W. (Eds.), *The Organic Carbon Cycle in the Arctic Ocean*: Berlin (Springer-Verlag), 57–81. doi:10.1007/978-3-642-18912-8_3
- Sancetta, C., 1982. Distribution of diatom species in surface sediments of the Bering and Okhotsk Seas. *Microplanktonology*, 28(3):221–257. doi:10.2307/1485181
- Schubert, C.J., and Calvert, S.E., 2001. Nitrogen and carbon isotopic composition of marine and terrestrial organic matter in Arctic Ocean sediments: implications for nutrient utilization and organic matter composition. *Deep-Sea Res., Part I*, 48(3):789–810. doi:10.1016/S0967-0637(00)00069-8
- Shipboard Scientific Party, 1973. Site 178. In Kulm, L.D., von Huene, R., et al., *Init. Repts. DSDP*, 18: Washington, DC (U.S. Govt. Printing Office), 287–376. doi:10.2973/dsdp.proc.18.109.1973
- Shipboard Scientific Party, 2000. Site 1149. In Plank, T., Ludden, J.N., Escutia, C., et al., *Proc. ODP, Init. Repts.*, 185: College Station, TX (Ocean Drilling Program), 1–190. doi:10.2973/odp.proc.ir.185.104.2000
- Smith, W.H.F., and Sandwell, D.T., 1997. Global seafloor topography from satellite altimetry and ship depth soundings. *Science*, 277(5334):1956–1962. doi:10.1126/science.277.5334.1956
- Smith, W.O., Jr., Baumann, M.E.M., Wilson, D.L., and Aletsee, L., 1987. Phytoplankton biomass and productivity in the marginal ice zone of the Fram Strait during summer 1984. *J. Geophys. Res.: Oceans*, 92(C7):6777–6786. doi:10.1029/JC092iC07p06777
- Stevenson, A.J., and Embley, R., 1987. Deep-sea fan bodies, terrigenous turbidite sedimentation, and petroleum geology, Gulf of Alaska. In Scholl, D.W., Grantz, A., and Vedder, J.G. (Eds.), *Geology and Resource Potential of the Western North America and Adjacent Ocean Basins—Beaufort Sea to Baja California*. Circum-Pac. Council. Energy Min. Resour., Earth Sci. Ser., 6:503–522.
- Swann, G.E.A., Maslin, M.A., Leng, M.J., Sloane, H.J., and Jaug, G.H., 2006. Diatom $\delta^{18}\text{O}$ evidence for the development of the modern halocline system in the subarctic northwest Pacific at the onset of major Northern Hemisphere glaciation. *Paleoceanography*, 21(1):PA1009. doi:10.1029/2005PA001147
- Takahashi, K., Billings, J.D., and Morgan, J.K., 1990. Oceanic province: assessment from the time-series diatom fluxes in the northeastern Pacific. *Limnol. Oceanogr.*, 35(1):154–165. doi:10.4319/lo.1990.35.1.0154
- Uchida, M., Shibata, Y., Ohkushi, K., Ahagon, N., and Hoshiya, M., 2004. Episodic methane release events from Last Glacial marginal sediments in the western North Pacific. *Geochem., Geophys., Geosyst.*, 5(8):Q08005. doi:10.1029/2004GC000699
- von Breyman, M.T., Brumsack, H., and Emeis, K.C., 1992. Depositional and diagenetic behavior of barium in the Japan Sea. In Pisciotto, K.A., Ingle, J.C., Jr., von Breyman, M.T., Barron, J., et al., *Proc. ODP, Sci. Results*, 127/128 (Pt. 1): College Station, TX (Ocean Drilling Program), 651–665. doi:10.2973/odp.proc.sr.127128-1.168.1992
- von Huene, R., Larson, E., and Crouch, J., 1973. Preliminary study of ice-rafted erratics as indicators of glacial advances in the Gulf of Alaska. In Kulm, L.D., von Huene, R., et al., *Init. Repts. DSDP*, 18: Washington (U.S. Govt. Printing Office), 835–842. doi:10.2973/dsdp.proc.18.121.1973
- Walinsky, S.E., Prah, F.G., Mix, A.C., Finney, B.P., Jaeger, J.M., and Rosen, G.P., 2009. Distribution and composition of organic matter in surface sediments of coastal southeast Alaska. *Cont. Shelf Res.*, 29(13):1565–1579. doi:10.1016/j.csr.2009.04.006
- Walton, M.L., Gulick, S.P.S., Reece, R.S., Barth, G.A., Christeson, G.L., and van Avendonk, H., submitted. Tectonic control on deposition and evolution of the Baranof Fan, Gulf of Alaska. *Geosphere*.
- Waterman, L.S., Sayles, F.L., and Manheim, F.T., 1973. Appendix II: interstitial water studies on small core samples, Legs 16, 17, and 18. In Kulm, L.D., von Huene, R., et al., *Init. Repts. DSDP*, 18: Washington (U.S. Govt. Printing Office), 1001–1012. doi:10.2973/dsdp.proc.18.app2.1973
- Yanagisawa, Y., and Akiba, F., 1998. Refined Neogene diatom biostratigraphy for the northwest Pacific around Japan, with an introduction of code numbers for selected diatom biohorizons. *Chishitsugaku Zasshi*, 104(6):395–414. doi:10.5575/geosoc.104.395
- Zachos, J., Pagani, M., Sloan, L., Thomas, E., and Billups, K., 2001. Trends, rhythms, and aberrations in global climate 65 Ma to present. *Science*, 292(5517):686–693. doi:10.1126/science.1059412
- Zhang, L., Chan, L.-H., and Gieskes, J.M., 1998. Lithium isotope geochemistry of pore waters from Ocean Drilling Program Sites 918 and 919, Irminger Basin. *Geochim. Cosmochim. Acta*, 62(14):2437–2450. doi:10.1016/S0016-7037(98)00178-1

Publication: 22 November 2014
MS 341-103



Figure F1. 3-D perspective view of the bathymetry/topography of the southern Alaska continental margin, showing tectonic boundaries and the Surveyor Fan in high-resolution bathymetry. HSV = Hinchinbrook Sea Valley, ASV = Alek Sea Valley, BT = Bering Trough, GS = Giacomini Seamount, KT = Kayak Trough, PS = Pamplona Spur, YSV = Yakutat Sea Valley. Plate boundaries adapted from Gulick et al. (2007). High-resolution bathymetry from Gardner et al. (2006). Remaining bathymetry from Smith and Sandwell (1997). Yakutat Terrane motion relative to North America from Elliott et al. (2010). Pacific plate motion from Kreemer et al. (2003). Inset: Location of Alaska Coastal Current (ACC), Alaska Current (AC), and NOAA wave buoy 46001. Modified from Reece et al. (2013).

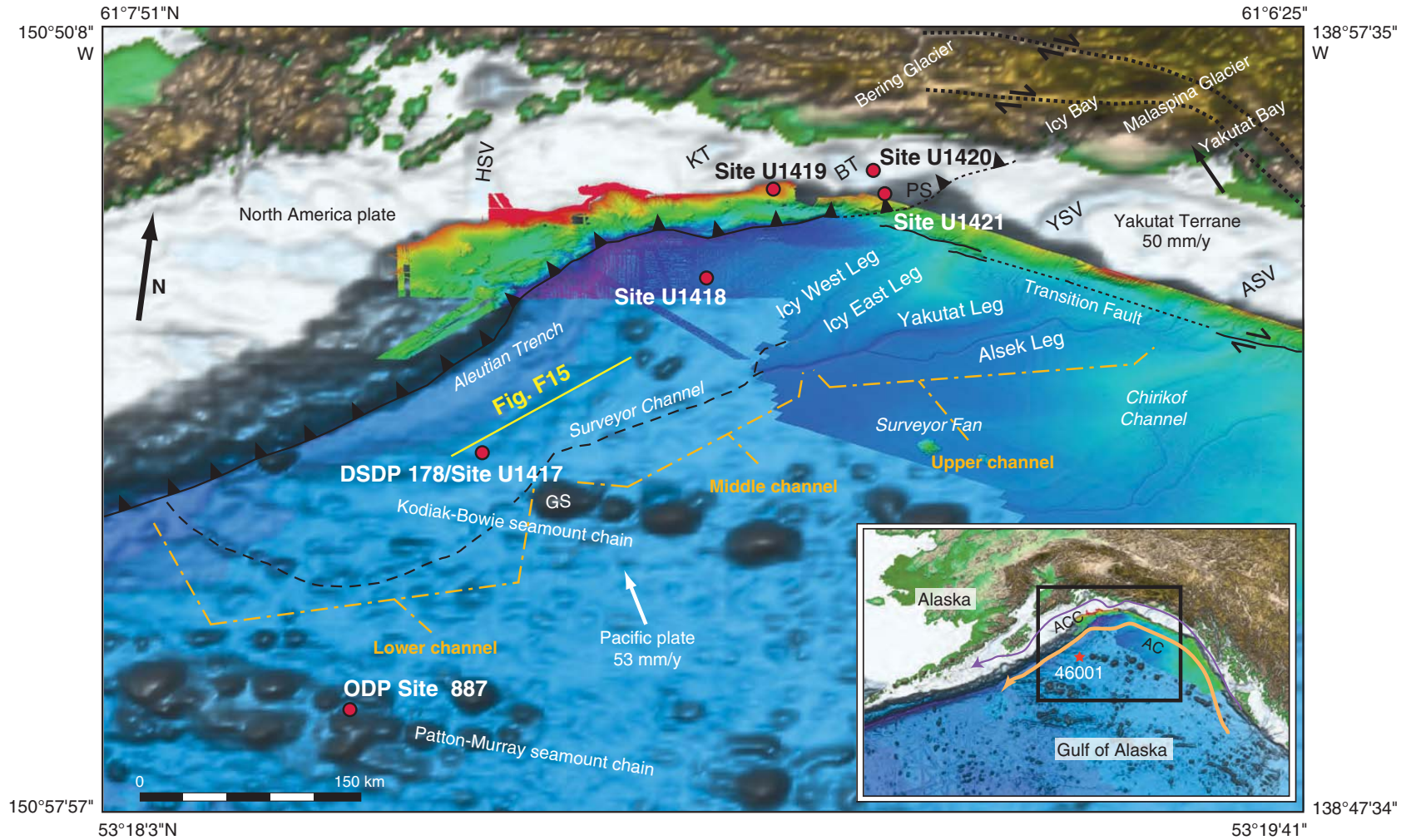


Figure F2. Lithology and age control, DSDP Site 178. Modified from Lagoe et al. (1993). Partial seismic section from Line 13 of 1989 USGS Survey F689 (Fig. F1). IRD = ice-rafted debris, Ja = Jaramillo, OI = Olduvai. GI A, GI B, GI C = Glacial Intervals A, B, and C. MPW = mid-Pliocene warm period. $^{40}\text{Ar}/^{39}\text{Ar}$ ages from Hogan et al. (1978). Magnetic polarity stratigraphy from von Huene et al. (1973). Modified from Reece et al. (2011).

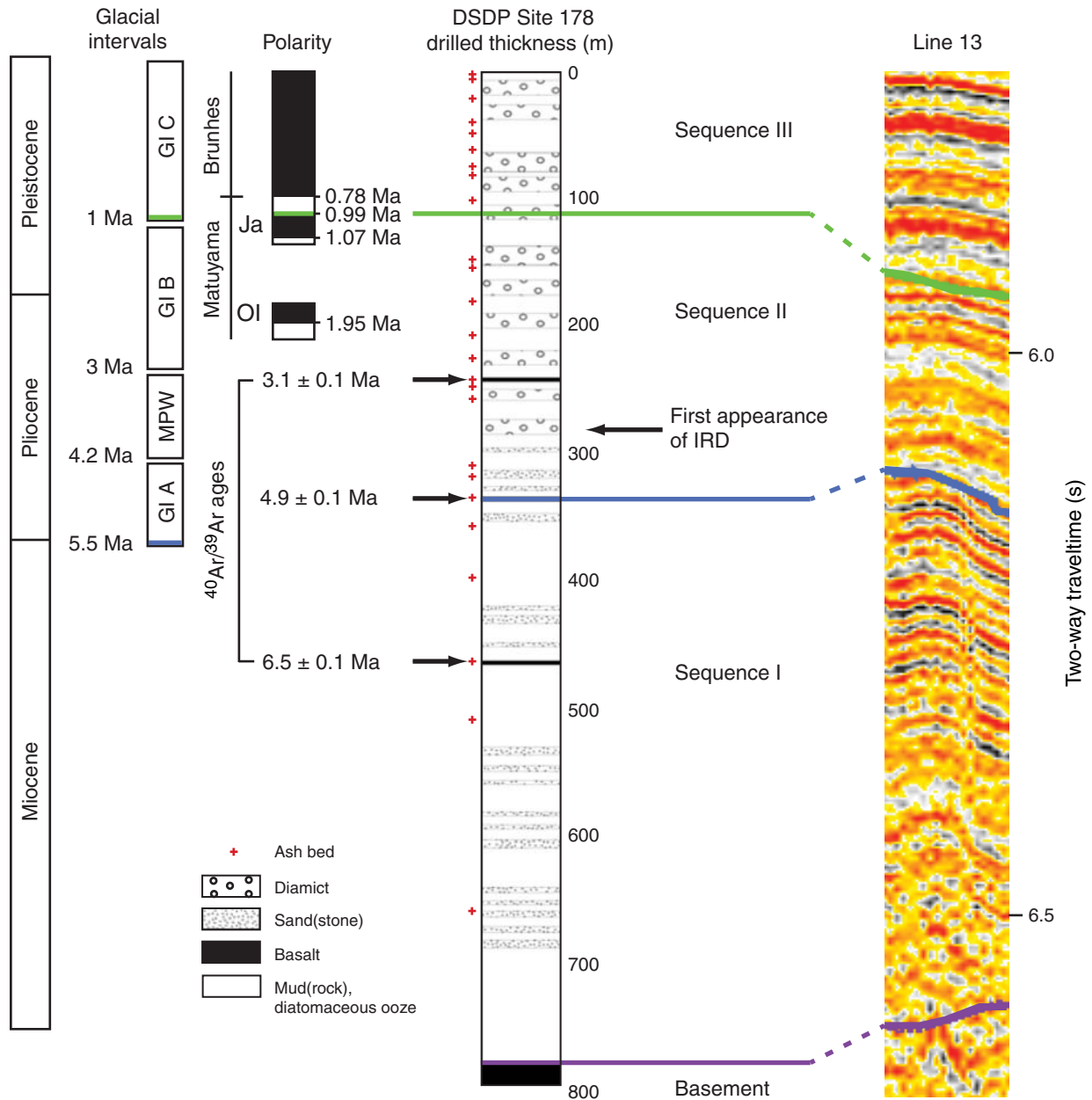


Figure F3. A. From left to right, a seismic transect from MGL1109 Line 1 toward the east, to MGL1109 Line 14 heading northeast, to MGL1109 Line 13 heading east. Seismic sequences can be mapped from Site U1417 to the Surveyor Channel. VE = vertical exaggeration. B. Multibeam bathymetry map showing location of Site U1417, DSDP Site 178, and seismic profiles relative to the Surveyor Channel, Kodiak-Bowie Seamounts, Aleutian Trench, and Kodiak Island, Alaska (Gulick et al., submitted).

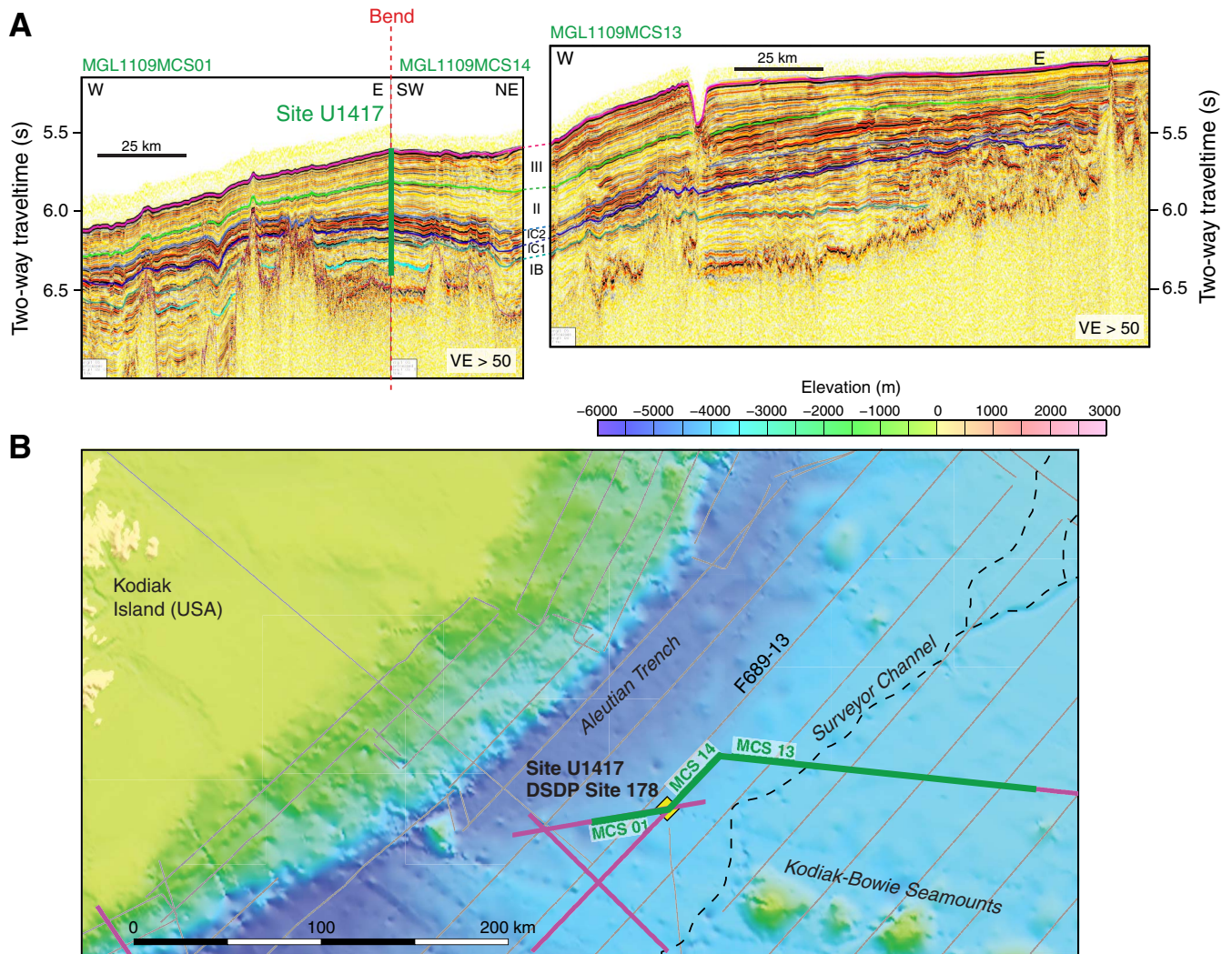




Figure F4. Seismic reflection Line 13 from 1989 USGS Survey F689 showing sequences newly defined by Reece et al. (2013) and approximate correlation to DSDP Site 178. See Figure F1 for line location. Vertical exaggeration (VE) assumes 2000 m/s sediment acoustic velocity. Modified from Reece et al. (2011).

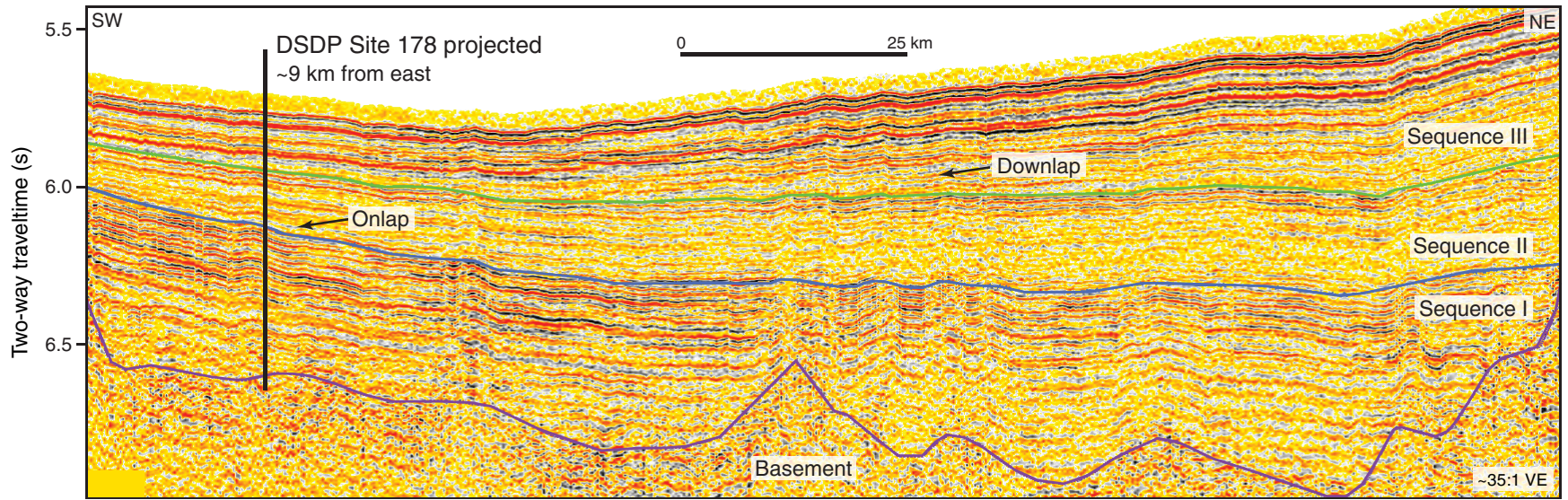


Figure F5. Bathymetry close to Site U1417, showing minimal local topography. Depth is in meters. Site U1417 lies at the intersection of seismic Lines MGL1109MCS01 and MGL1109MCS14 and is ~1.5 km from DSDP Site 178. Red dots are USGS Line L-6-81 with shot point times noted. For MGL1109 lines, numbers refer to shot points.

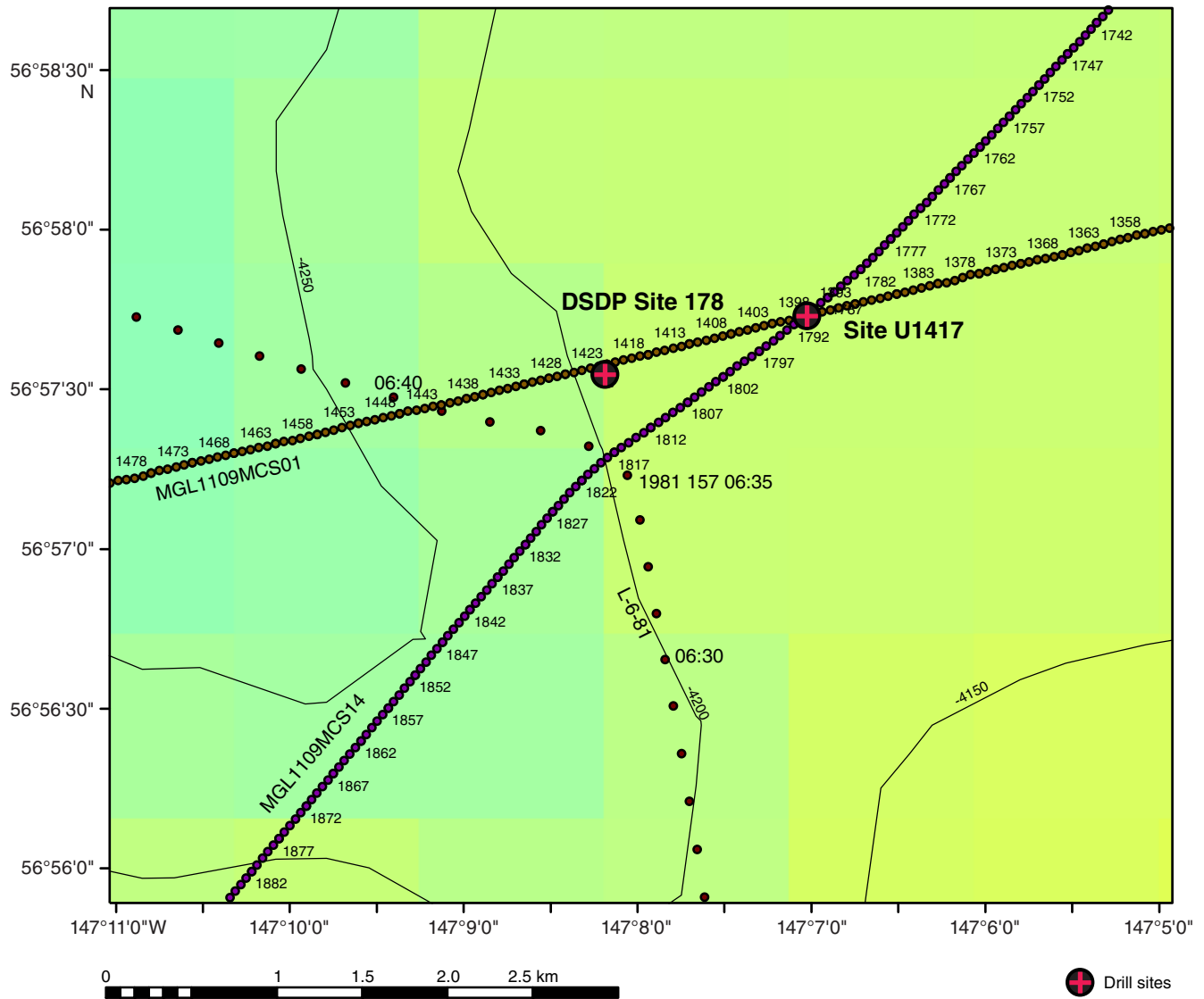




Figure F6. Two-way traveltimes thickness maps. **A.** Sequence I, Pacific plate formation prior to ~5.5 Ma. **B.** Sequence II, ~5.5–1 Ma. **C.** Sequence III, ~1 Ma to present. **D.** Seismic reflection data track lines used in calculation. ASV = Alek Sea Valley, BT = Bering Trough, KT = Kayak Trough, YSV = Yakutat Sea Valley. From Reece et al. (2011).

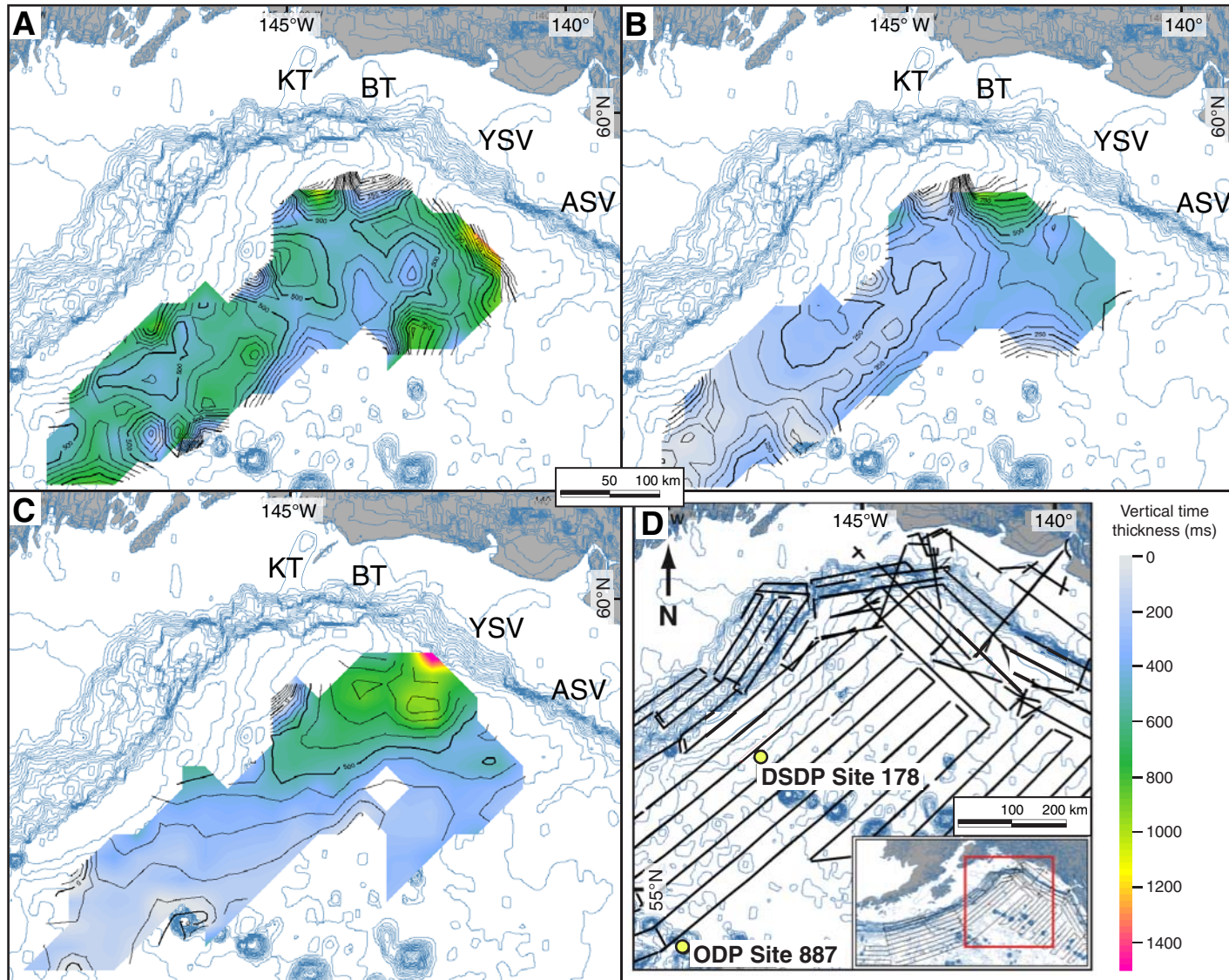




Figure F7. Uninterpreted and interpreted versions of MGL1109MCS14 showing location of Site U1417. Seismic sequences I–III are from Reece et al. (2011), and subsequences are broken out as seismic units for the purpose of core-log-seismic integration.

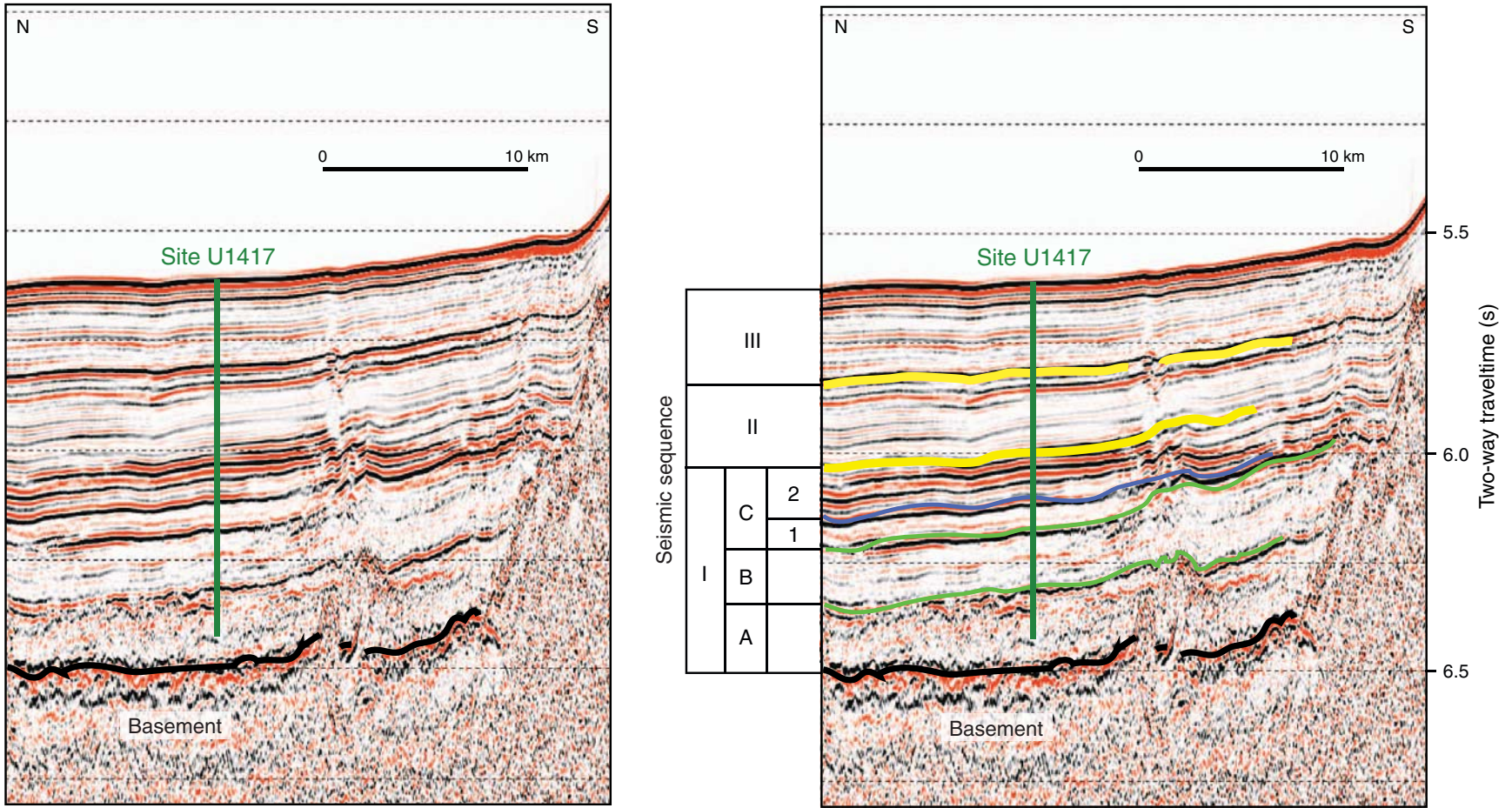




Figure F8. Stratigraphic, depositional, tectonic, and climatic history of the Gulf of Alaska (GoA) and adjacent regions, modified from Lagoe et al. (1993) and Berger et al. (2008a). Lithologic data from Lagoe et al. (1993), Rea and Snoeckx (1995), and Lagoe and Zellers (1996). Bedrock temperature paths vs. time from Berger et al. (2008a). Tectonic events from Lagoe et al. (1993), Stevenson and Embley (1987), Berger et al. (2008a, 2008b), Enkelmann et al. (2010), and Finzel et al. (2011). Oxygen isotope data from global stacks of Lisiecki and Raymo (2005) (black) and Zachos et al. (2001) (gray). IRD = ice-rafted debris. AHe = apatite (U-Th)/He, AFT = apatite fission track, ZHe = zircon (U-Th)/He. MPW = mid-Pliocene warm period.

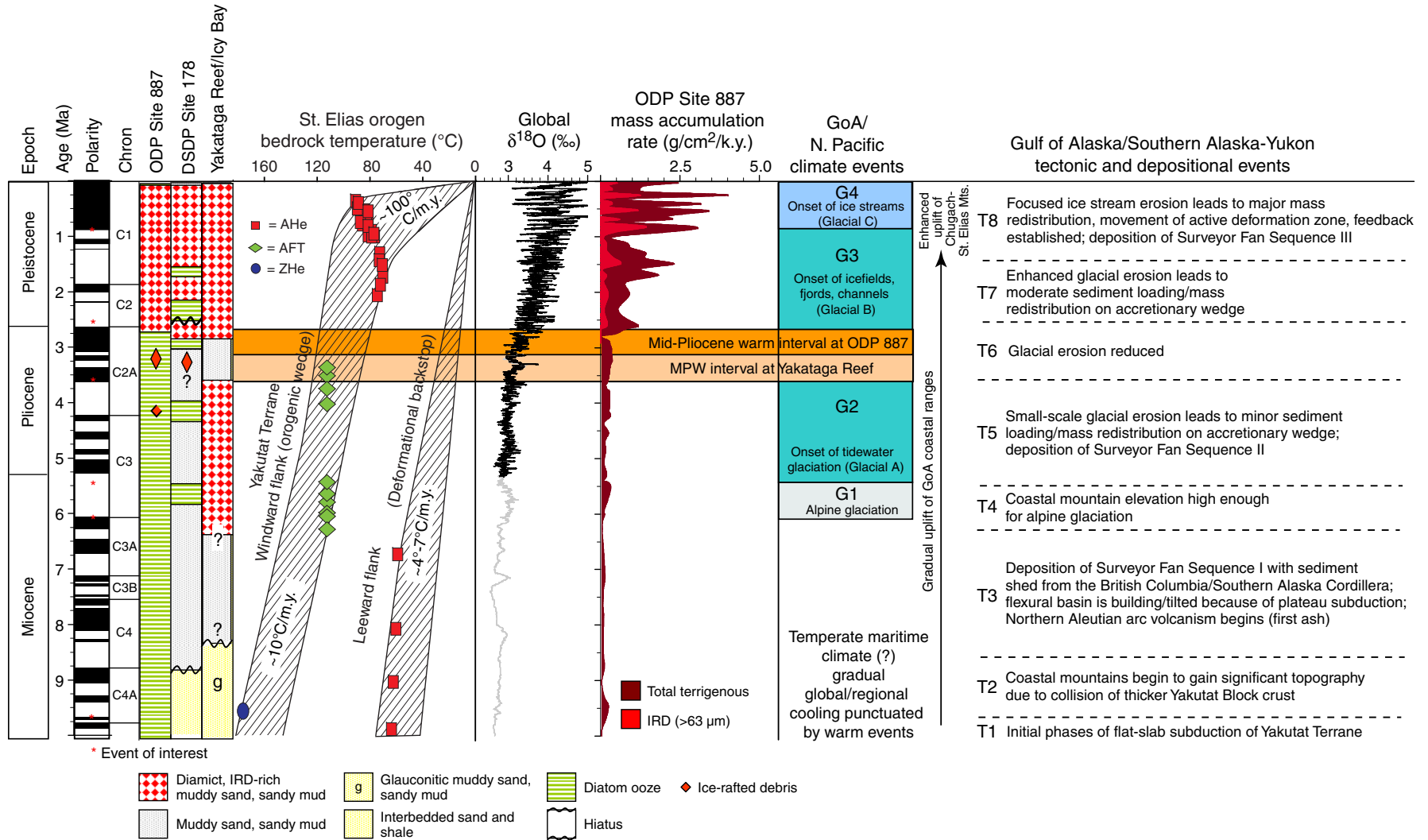


Figure F9. Core recovery, Site U1417.

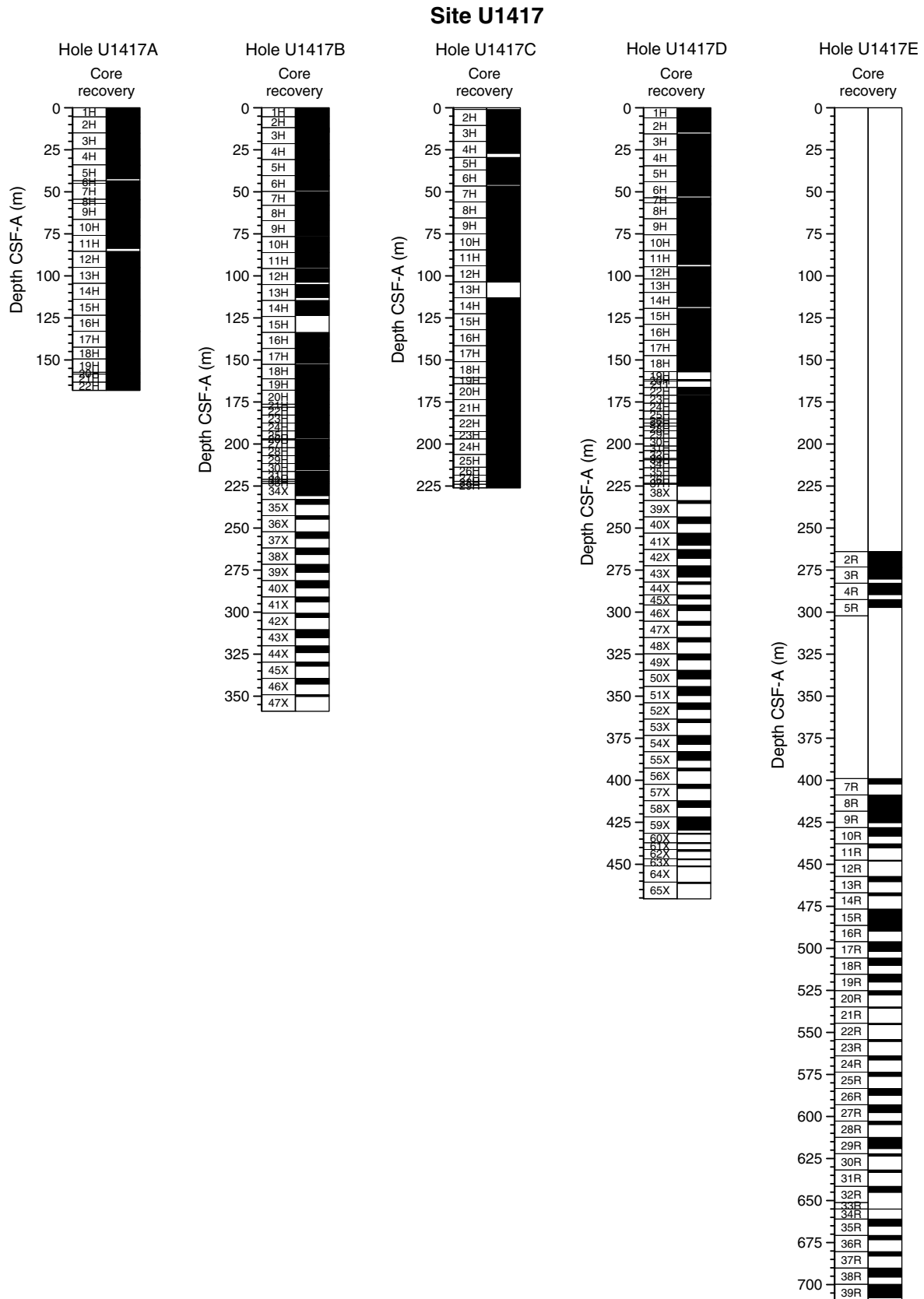


Figure F10. Hole summaries, Site U1417. Volcanic grain abundance: 1 = trace, 2 = volcanoclastic bearing, 3 = volcanoclastic rich, 4 = ash. GRA = gamma ray attenuation. A. Hole U1417A. (Continued on next four pages.)

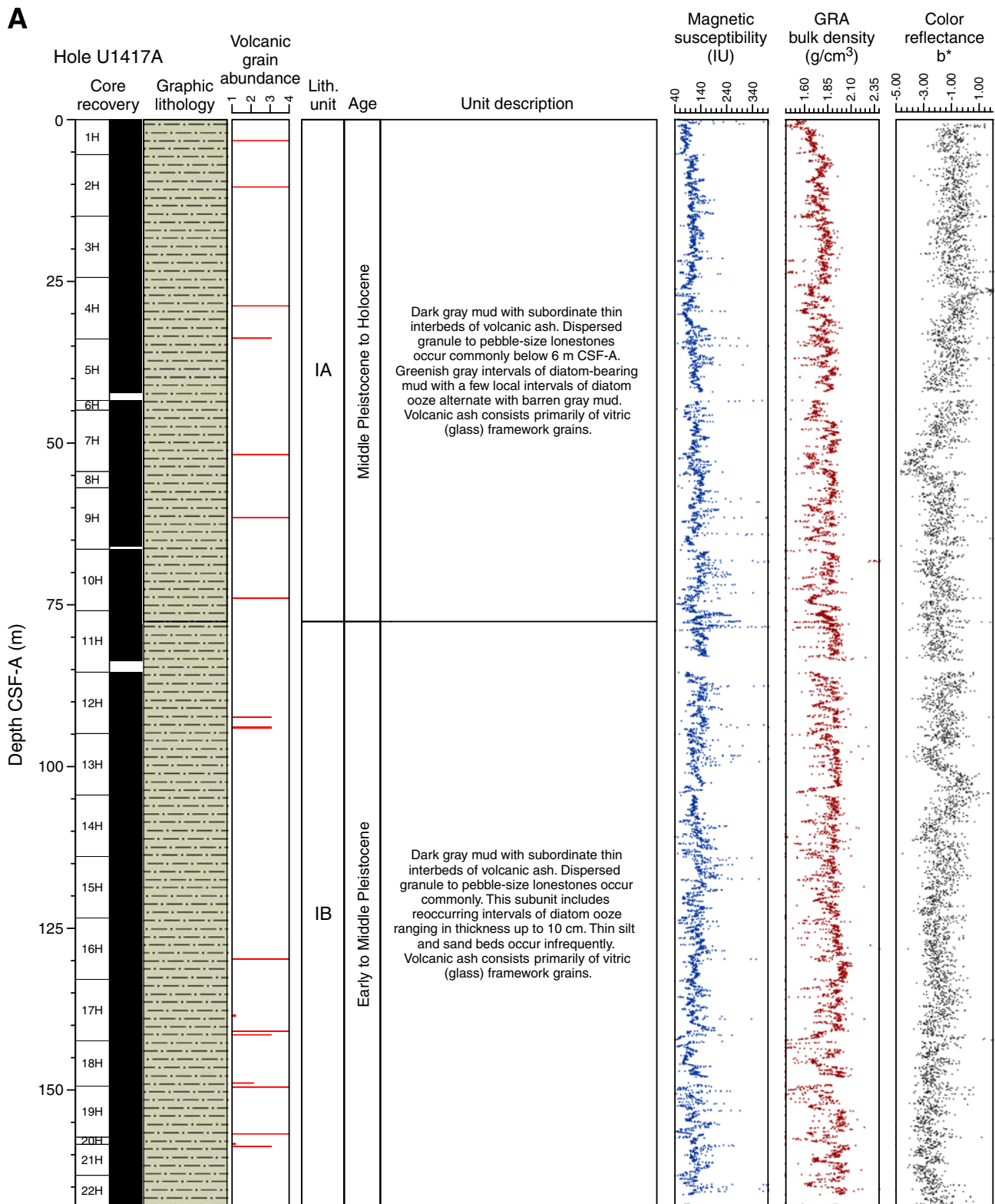


Figure F10 (continued). B. Hole U1417B. (Continued on next page.)

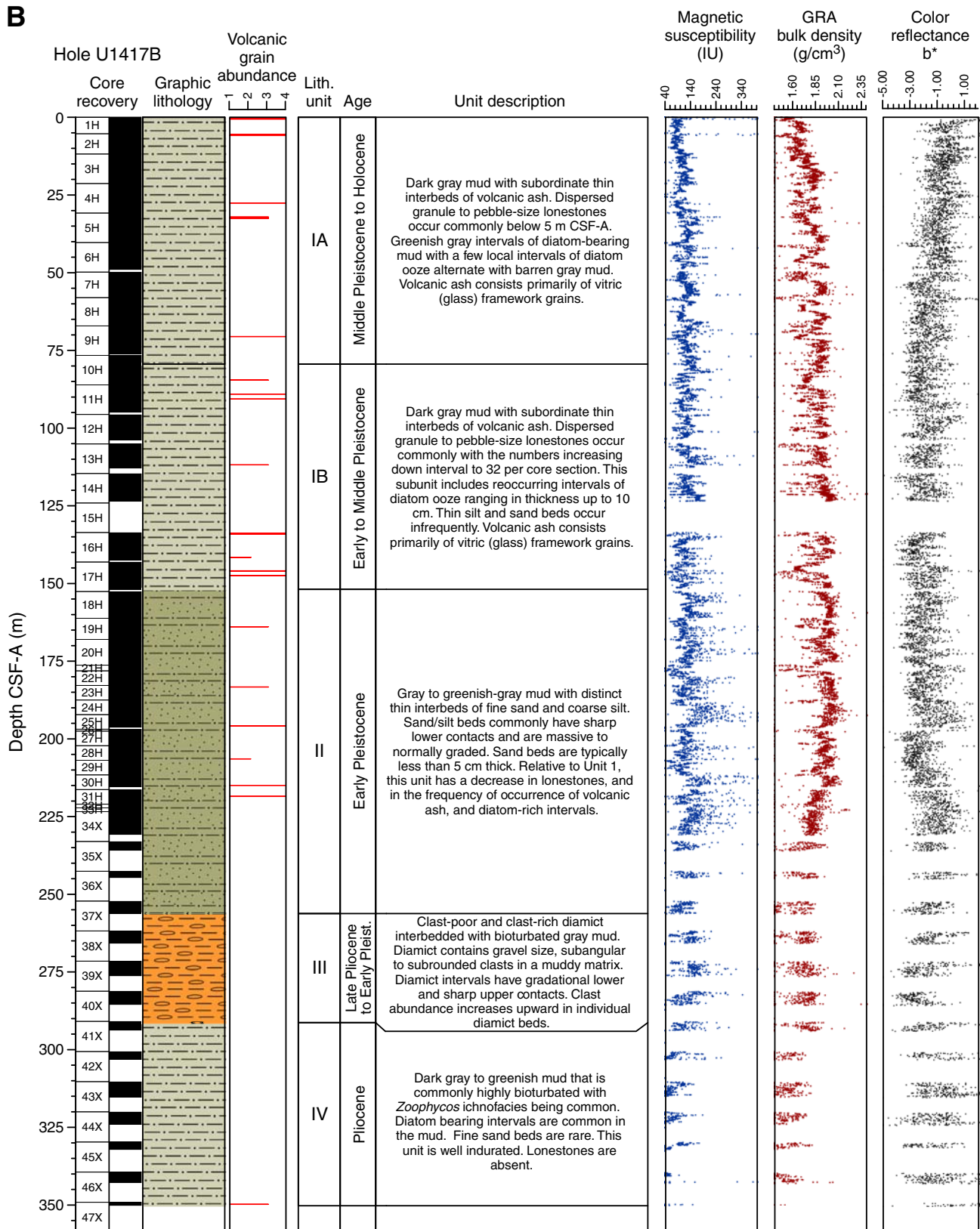


Figure F10 (continued). C. Hole U1417C. (Continued on next page.)

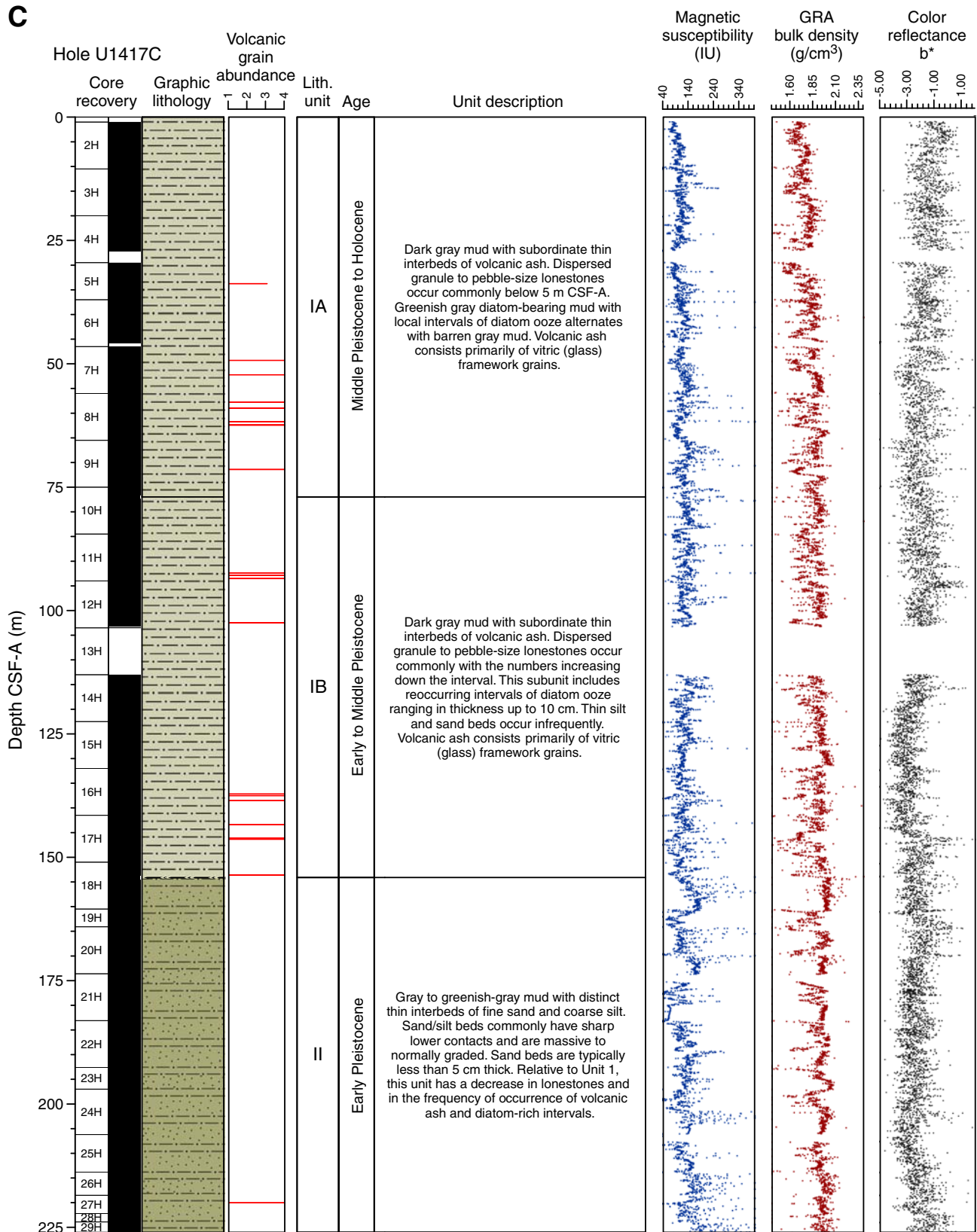


Figure F10 (continued). D. Hole U1417D. (Continued on next page.)

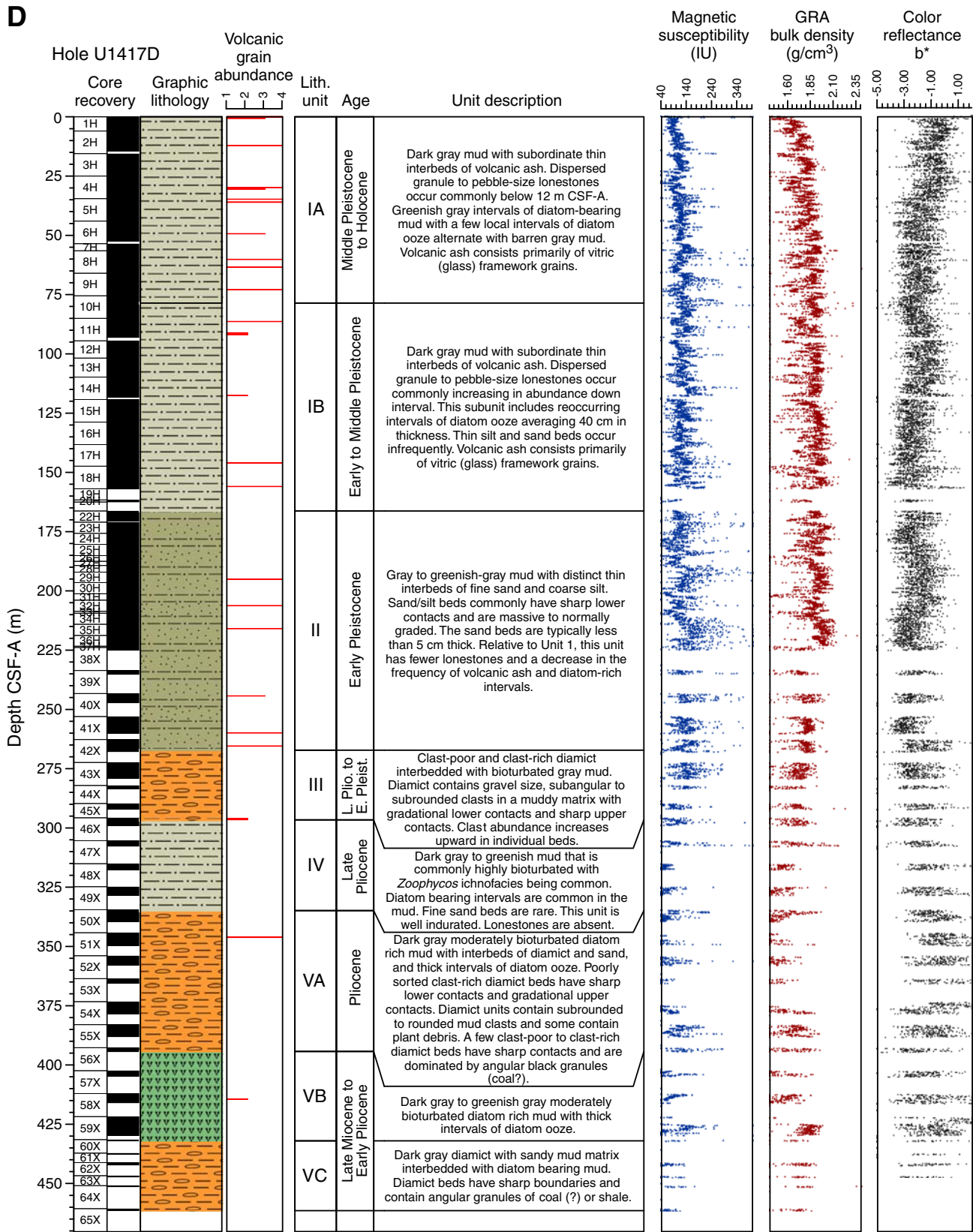


Figure F10 (continued). E. Hole U1417E.

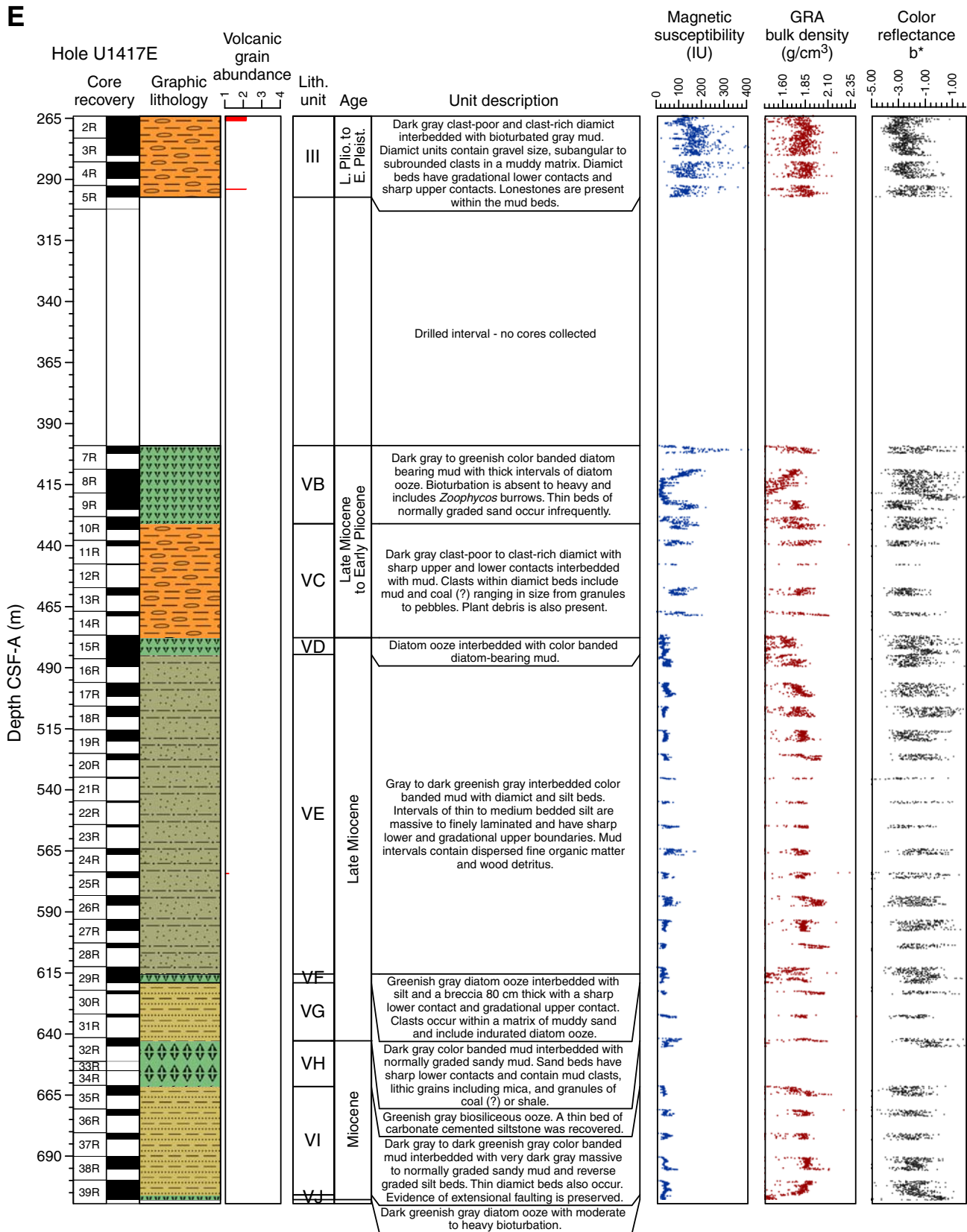


Figure F11. Primary lithologies of Site U1417. **A.** Dark gray (N 4) mud (Facies F1b; interval 341-U1417D-3H-3A, 93–100 cm). **B.** Interbedded sand and mud; sand is normally graded (Facies F3c; interval 341-U1417C-17H-6A, 80–96 cm). **C.** Muddy diamict with upward increasing abundance of subangular to subrounded clasts (Facies F4a; interval 341-U1417B-38X-1A, 56–66 cm). Note the gradational lower and sharp upper contacts. **D.** Muddy and sandy diamict with abundant mud rip-up clasts (Facies F4b; interval 341-U1417D-52X-3A, 4–11 cm). **E.** Muddy and sandy diamict with abundant dark coal clasts (Facies F4b; interval 341-U1417D-64X-1A, 40–47 cm). Note that the diamict grades upward into coarse sand of Facies F3b. **F.** Muddy and sandy diamict with dark organic components and lighter-colored mud clasts (Facies F4b; interval 341-U1417E-39R-1A, 43–52 cm). **G.** Bioturbated diatom ooze with *Zoophycos* burrows (Facies F5a; interval 341-U1417D-57X-1A, 69–77 cm). The ooze is the lighter colored greenish lithology in the center of the photo. **H.** Color-banded and bioturbated diatom ooze (Facies F5a; interval 341-U1417E-29R-2A, 12–38 cm).

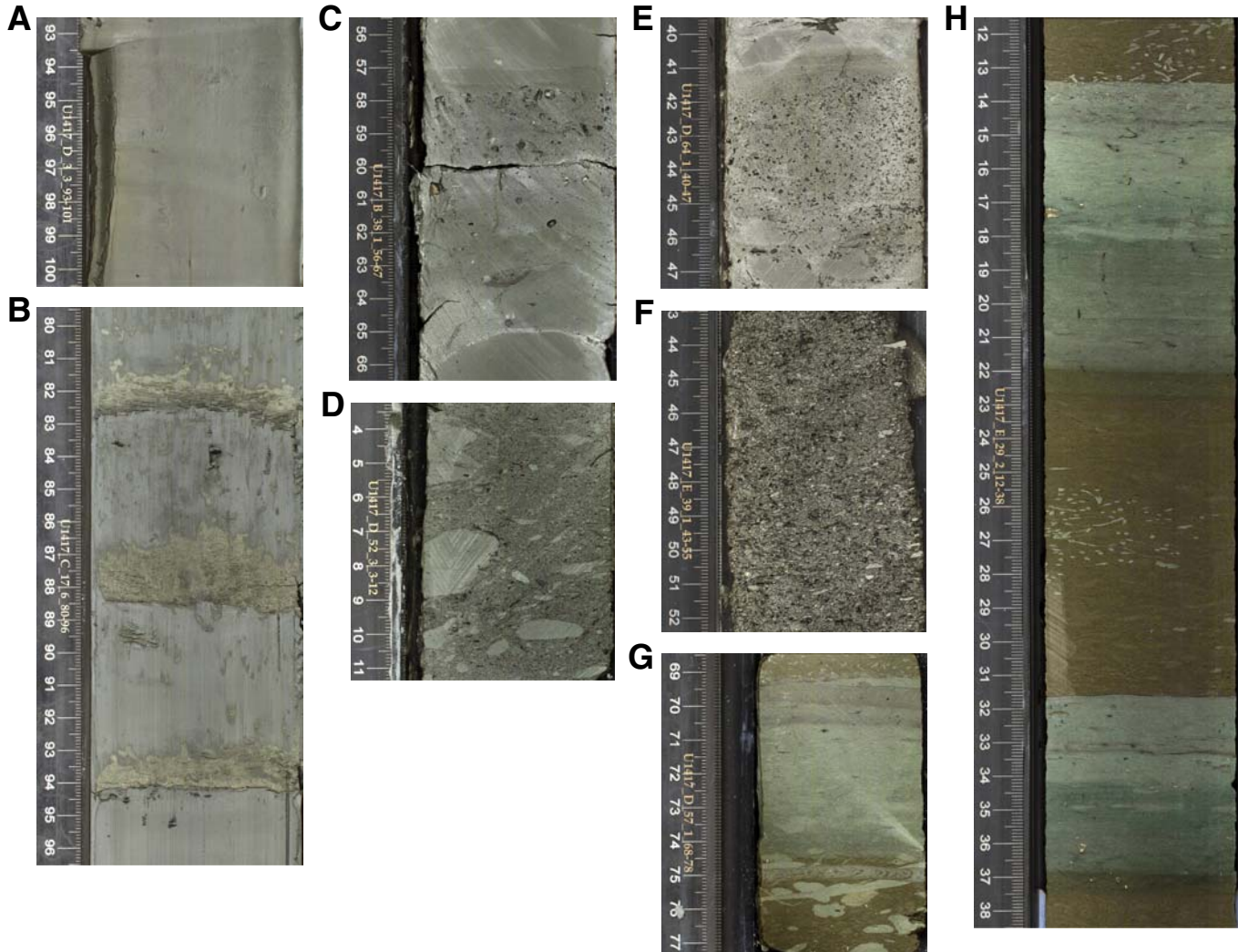


Figure F12. Lonestones and sedimentary and deformational structures, Site U1417. **A.** Argillite lonestone (interval 341-U1417B-27H-1A, 1–4 cm). **B.** Sandstone lonestone (interval 341-U1417C-24H-6A, 12–18 cm). **C.** Metabasalt lonestone (interval 341-U1417C-6H-3A, 58–64 cm). **D.** Granite lonestone (interval 341-U1417C-7H-5A, 41–43 cm). **E.** Load casts at base of normally graded sand (Facies F3a; interval 341-U1417C-20H-2A, 133–136 cm). **F.** Normal faults in diatom ooze (interval 341-U1417E-36R-2A, 18–23 cm). **G.** Woody fragment at base of a muddy and sandy diamict (Facies F4b; interval 341-U1417E-31R-1A, 40–41 cm). **H.** Microscope image of woody fragment encountered in a smear slide (interval 341-U1417D-60X-CC). **I.** Scanning electron microscope image of woody fragment (interval 341-U1417D-51X-3A, 74 cm). **J.** Detail of woody fragment shown in I. **K.** Pyritized worm tube (interval 341-U1417C-15H-1A, 46 cm).

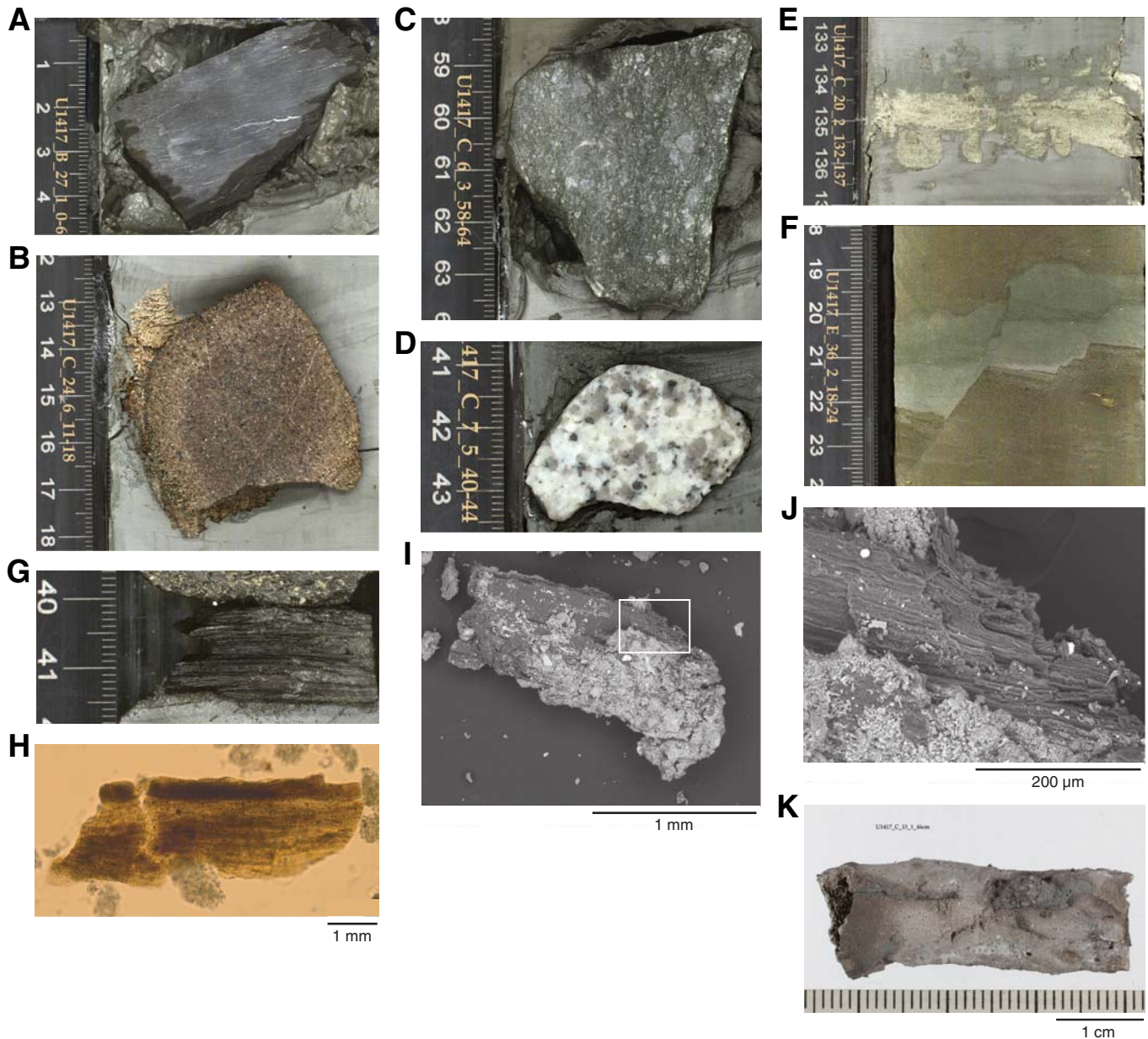


Figure F13. Ash images, Site U1417. A–C. Glassy ash containing 5% lithic grains (interval 341-U1417D-8H-5, 94–97 cm; (A) core, (B) smear slide, (C) detail of scanning electron microscope image. D. Well-sorted silt-bearing glassy ash (interval 341-U1417A-17H-6, 48–55 cm). E, F. Highly bioturbated mud with glassy ash lenses (interval 341-U1417D-51X-2, 35–38 cm); (E) core, (F) smear slide. Ash is the lighter colored lithology. Note diatom fossil in lower center of F.

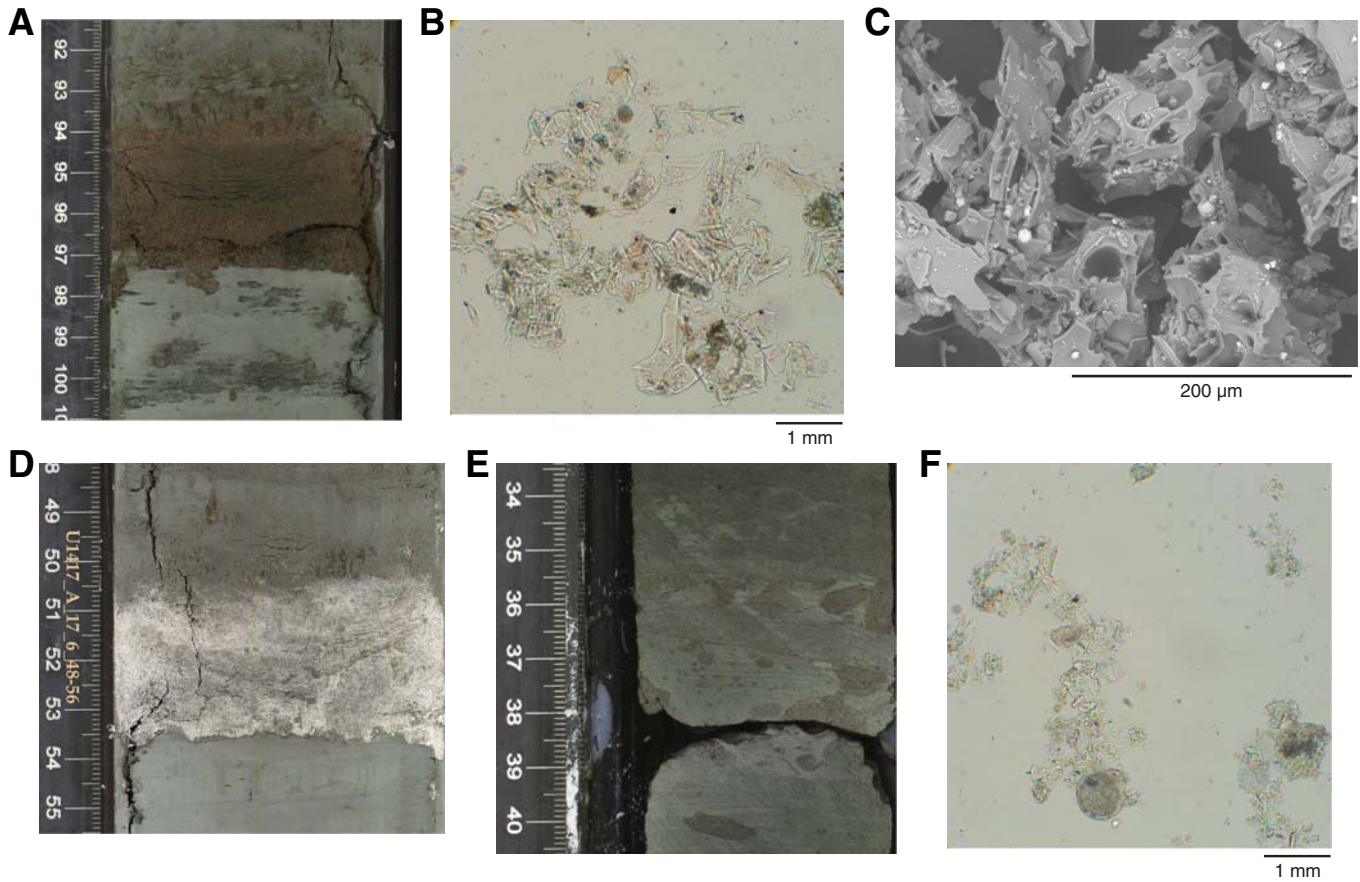


Figure F14. A. X-ray powder diffraction patterns, Holes U1417A–U1417E. Bulk mineralogy is nearly constant downhole, although minor changes in relative peak intensities occur. (Continued on next page.)

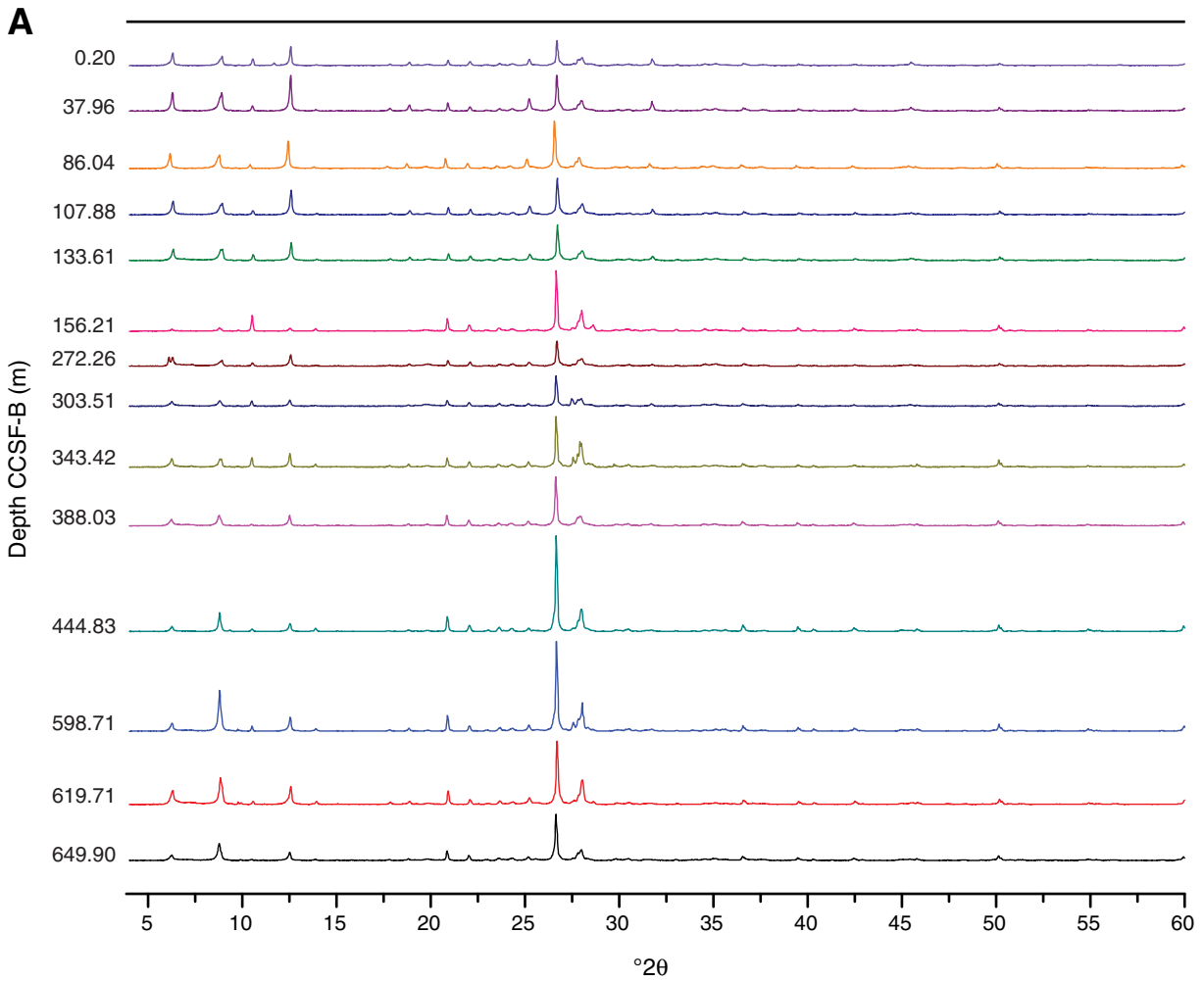


Figure F14 (continued). B. Comparative X-ray diffraction patterns from 4° to 24°2θ, Site U1417. Scans show downhole samples before (left) and after (right) treatment with glycolate to assess the presence of expandable clay minerals.

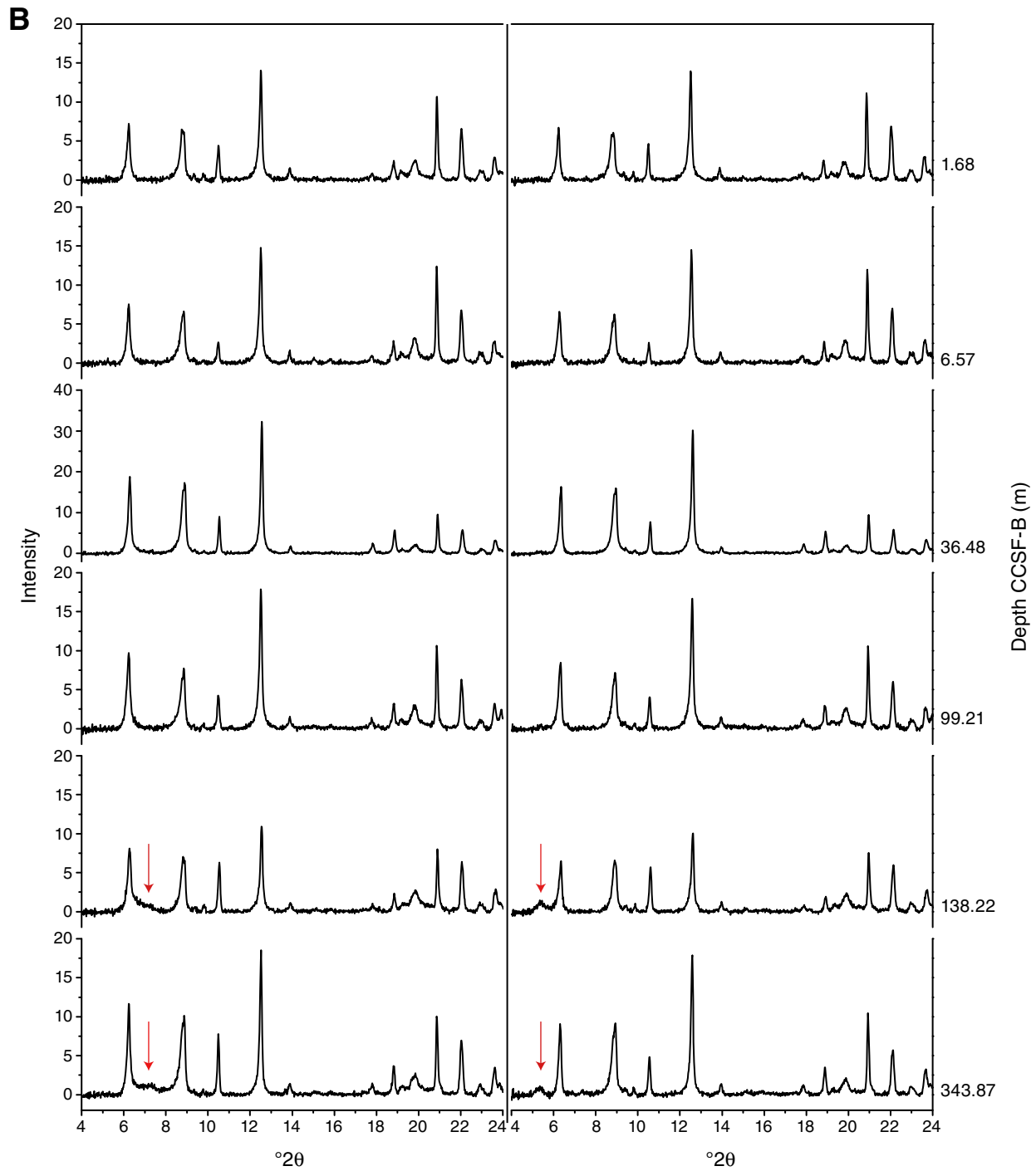


Figure F15. Diagram illustrating common relationships between lithology, clast count, and physical properties at the lithostratigraphic Subunit IB–Unit II transition (Sections 341-U1417C-17H-3A through 18H-1A). Decreases in magnetic susceptibility, gamma ray attenuation (GRA) bulk density, and natural gamma radiation, combined with increases in color reflectance index, highlight the location of diatom ooze. Mafic-rich sand corresponds to an increase in magnetic susceptibility, whereas volcanic ash dominated by glass shards shows no change in magnetic susceptibility. Photomicrographs of smear slides to right of the figure illustrate major lithologies present over specific intervals.

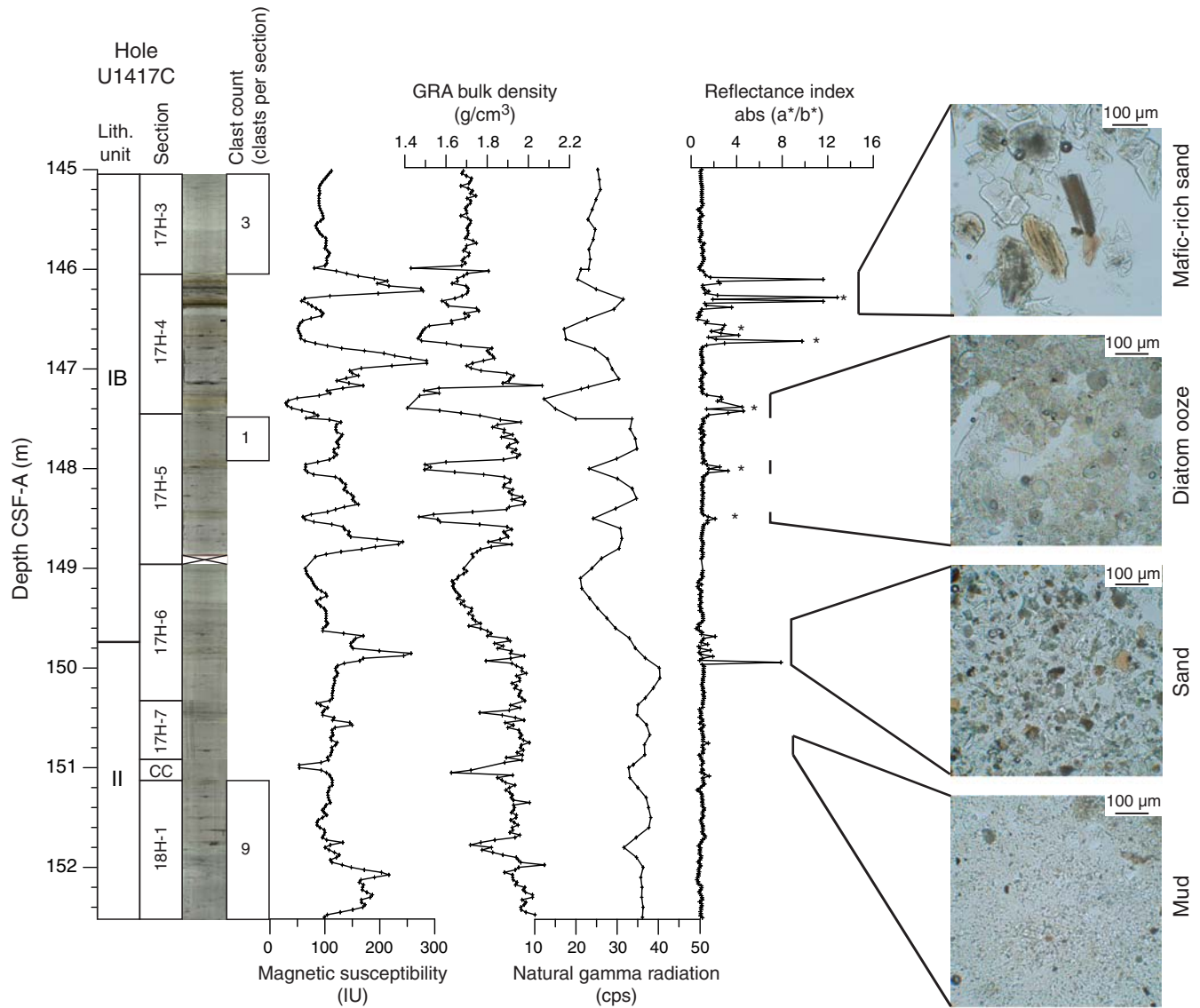




Figure F16. Schematic diagram of lithostratigraphic units and major lithologies using combined data from Holes U1417A–U1417E. Lonestone counts are the number of clasts >2 mm diameter per meter of described section. Diamict includes both ice-rafted and gravity flow interpretations. With the exception of lonestone counts, downcore profiles show the middepth location of each feature/intervals in the overall sedimentary sequence. Solid lines = Neogene epoch boundaries that coincide with or are within 10 m of a measured paleomagnetic reversal. Dashed lines = uncertain locations of epoch boundaries estimated from the shipboard age model.

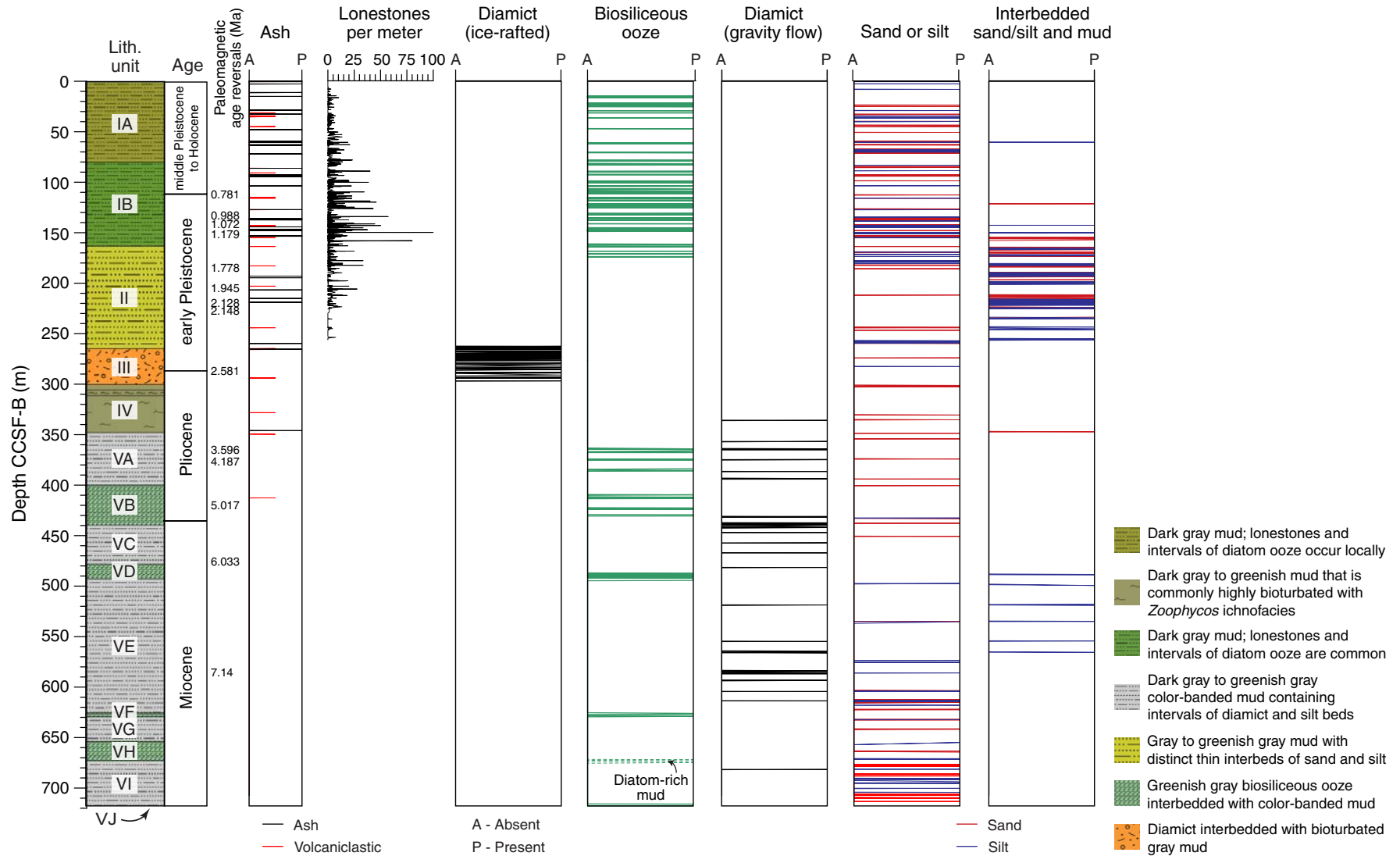




Figure F18. Micropaleontological age datums and rank abundances of taxa indicative of paleoclimatic conditions, shown as a composite from Holes U1417A–U1417E. Relative abundance of foraminifers is shown. NPD = Neogene North Pacific Diatom zone of Yanagisawa and Akiba (1998), CM = California margin. Abundance: A = abundant, C = common, F = few, R = rare, P = present, X = present.

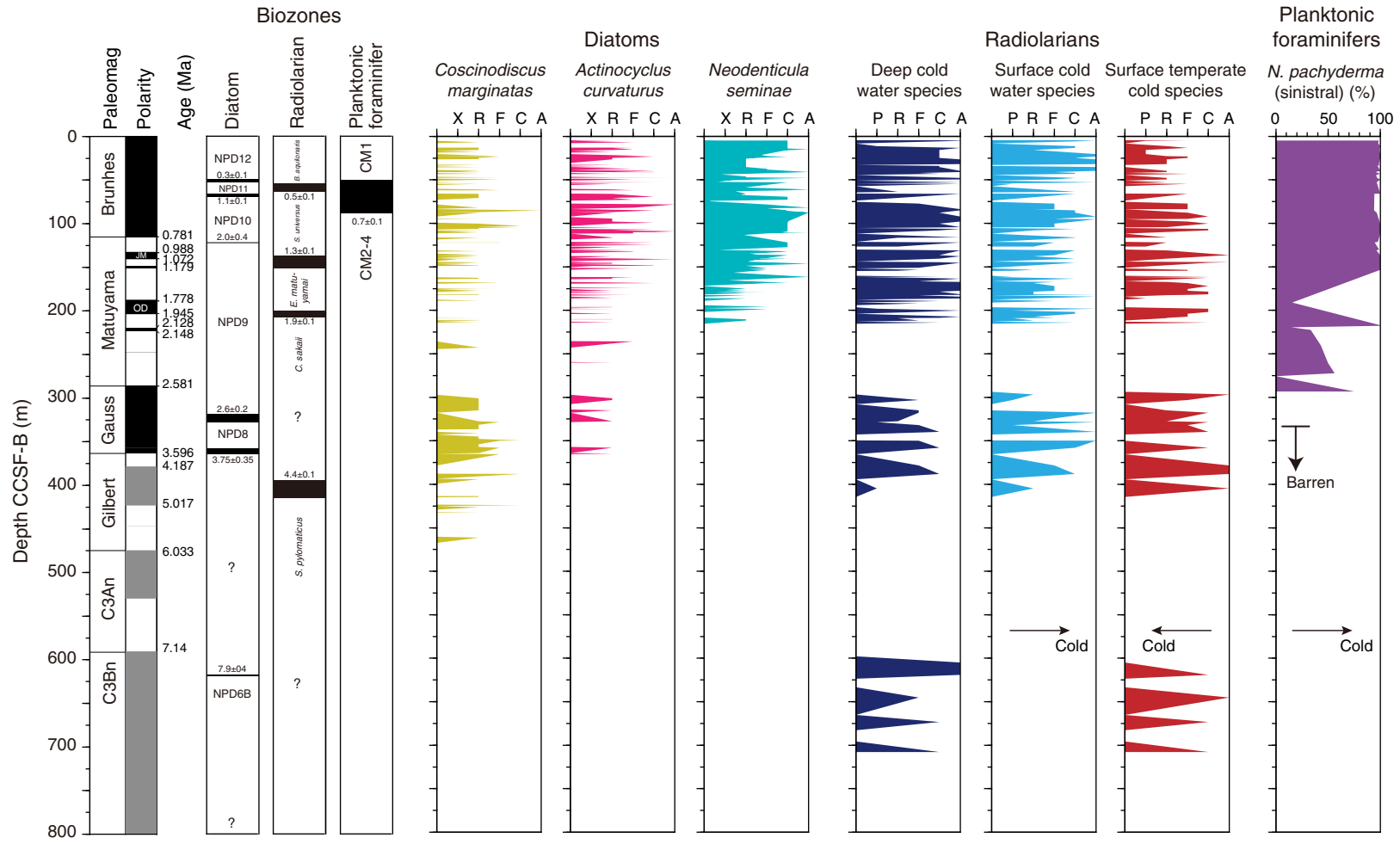




Figure F19. Micropaleontological age datums, group abundances (black plots), and rank abundances (color plots) of important paleoenvironmental indicators, shown as a composite of Holes U1417A–U1417E. Diatoms are plotted using the highest of individual species abundances within each species suite, estimated from the number of valves per field of view. Rank abundance of cold-water radiolarians is estimated from the proportional abundances of cold-water species in the total radiolarian assemblage. Rank abundance of *Neogloboquadrina pachyderma* (dextral), a warm-water indicator, is estimated from its proportional abundance in the total foraminiferal assemblage. NPD = Neogene North Pacific Diatom zone of Yanagisawa and Akiba (1998), CM = California margin. Abundance: D = dominant, A = abundant, C = common, F = few, R = rare, P = present, X = present, B = barren.

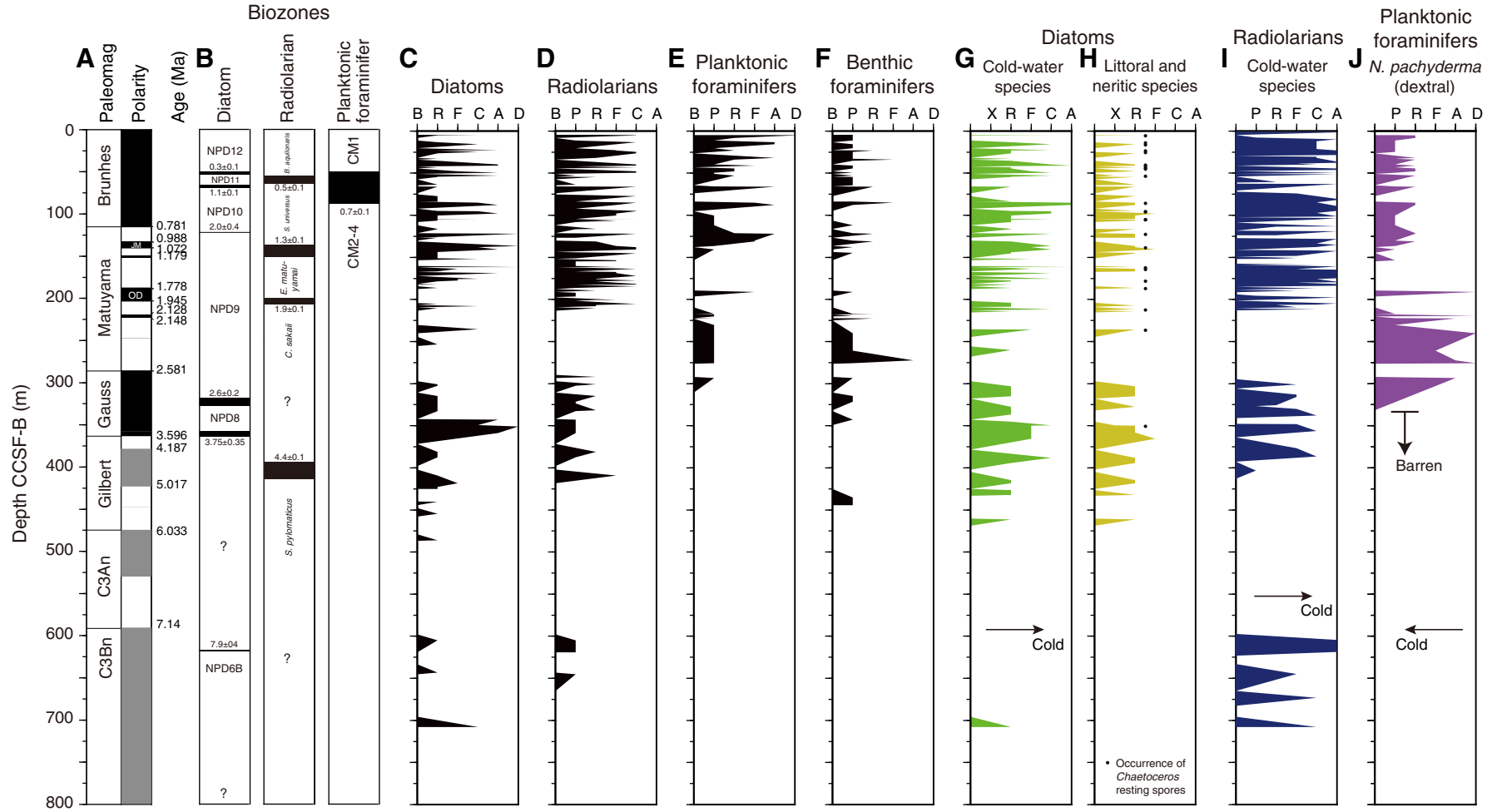


Figure F20. Micropaleontological age datums and rank abundance of important biostratigraphic diatom and radiolarian indicators, shown as a composite from Holes U1417A–U1417E. Composite diatom biostratigraphy shows relative abundance (%) of eight diatom species (*Neodenticula seminae*, *Proboscia curvirostris*, *Proboscia barboi*, *Actynocyclus oculatus*, *Neodenticula koizumii*, *Neodenticula kamtschatica*, *Shionodiscus oestrupii*, and *Stephanopyxis horridus*). Composite radiolarian biostratigraphy shows relative abundance (%) of ten radiolarian species (*Lynchnocanoma sakaii*, *Axoprunum acqulionium*, *Stylocosporium universus*, *Eucyrtidium matuyamaei*, *Sphaeropyle robusta*, *Cycladophora sakaii*, *Cycladophora davisiana*, *Thecosphaera akitaensis*, *Phormocyrtis fistula*, and *Thecosphaera pseudojaponica*). NPD = Neogene North Pacific Diatom zone of Yanagisawa and Akiba (1998). FO = first occurrence, LO = last occurrence.

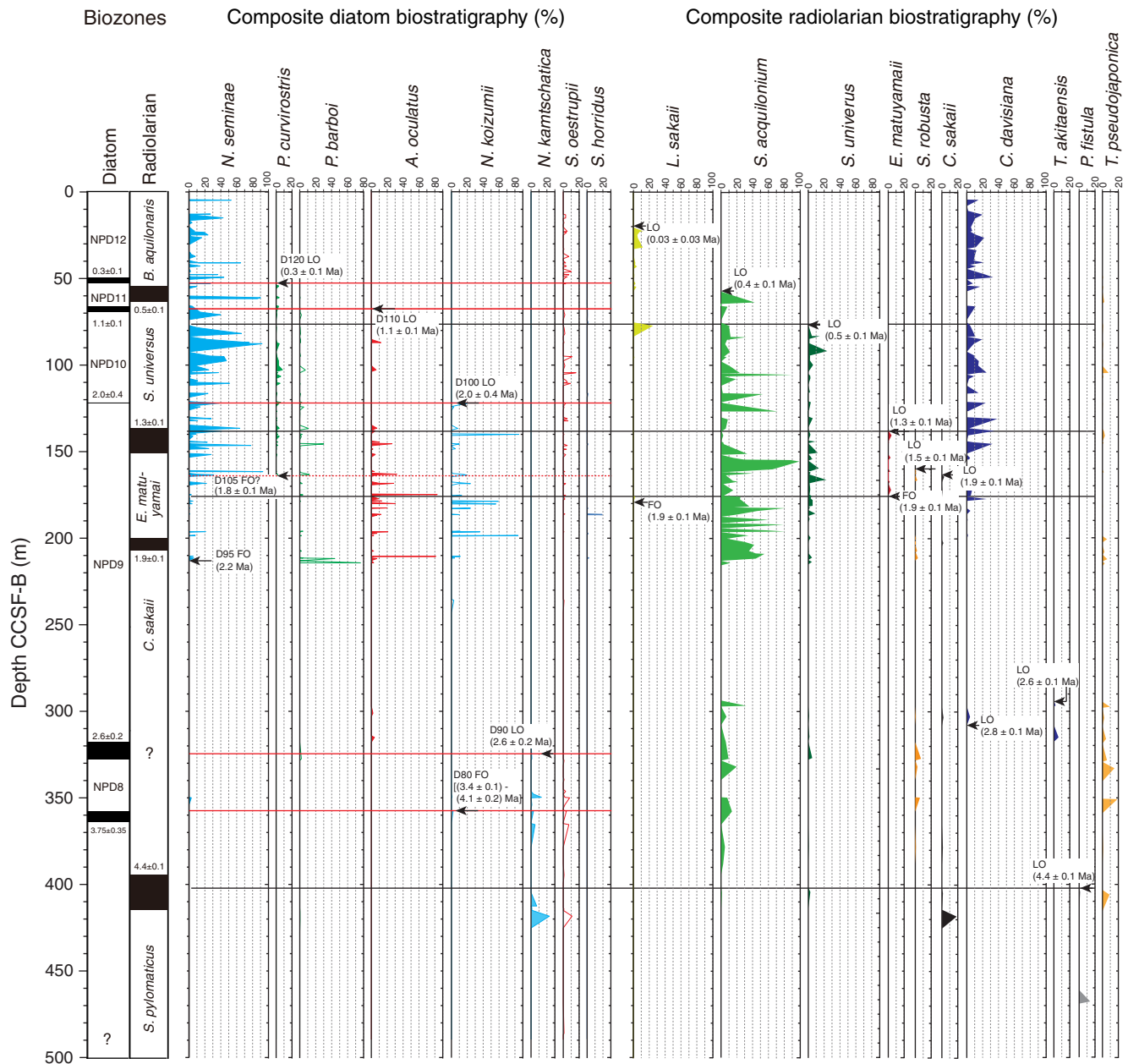


Figure F21. Magnetic susceptibility data for the interval of the continuous splice in Holes U1417A–U1417D and the splice record. Gray boxes = intervals used to construct the splice with core numbers noted, dashed vertical lines = intervals where tie points should be treated with caution (see text for details). **A.** 0–50 m CCSF-A. (Continued on next three pages.)

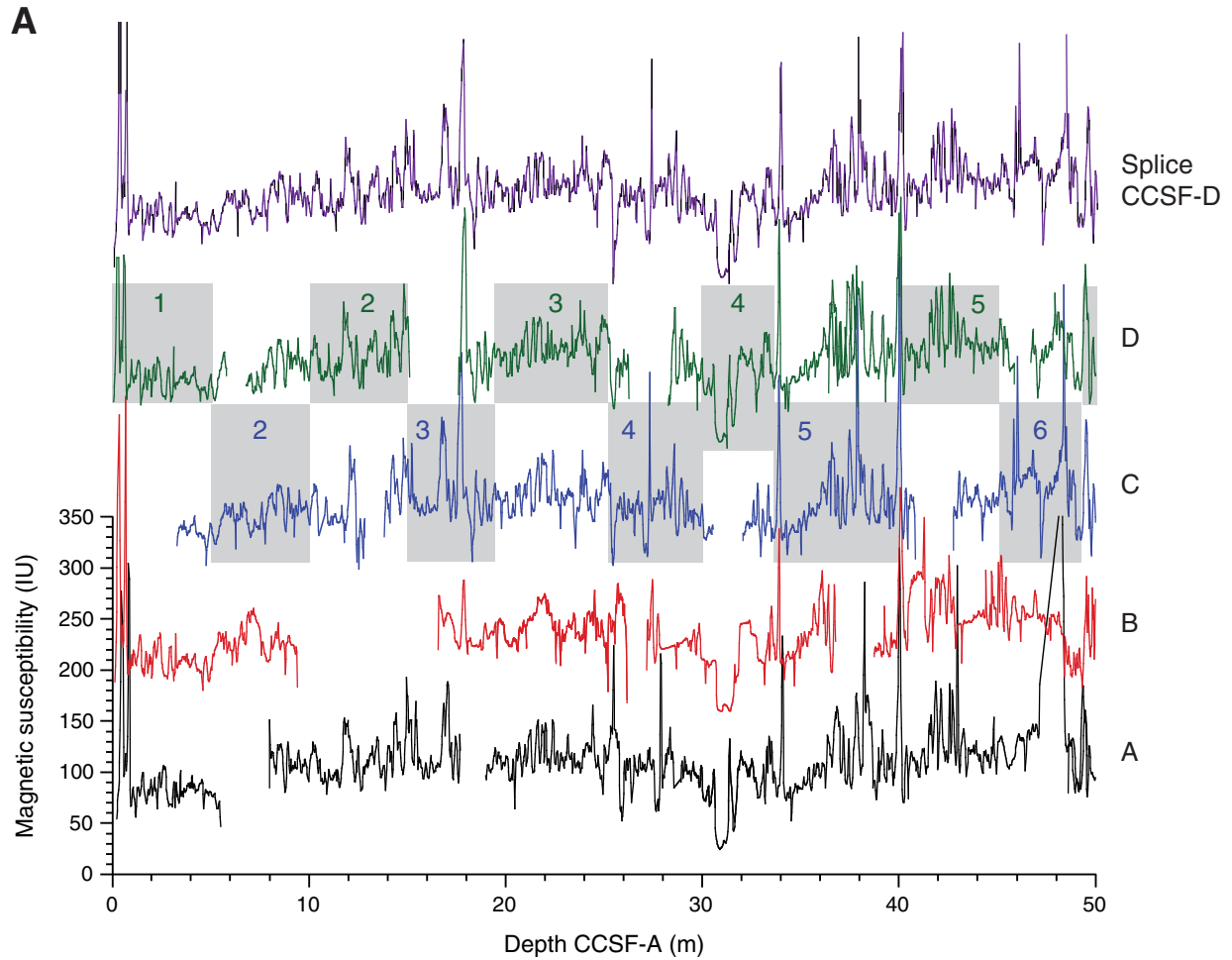


Figure F21 (continued). B. 50–100 m CCSF-A. (Continued on next page.)

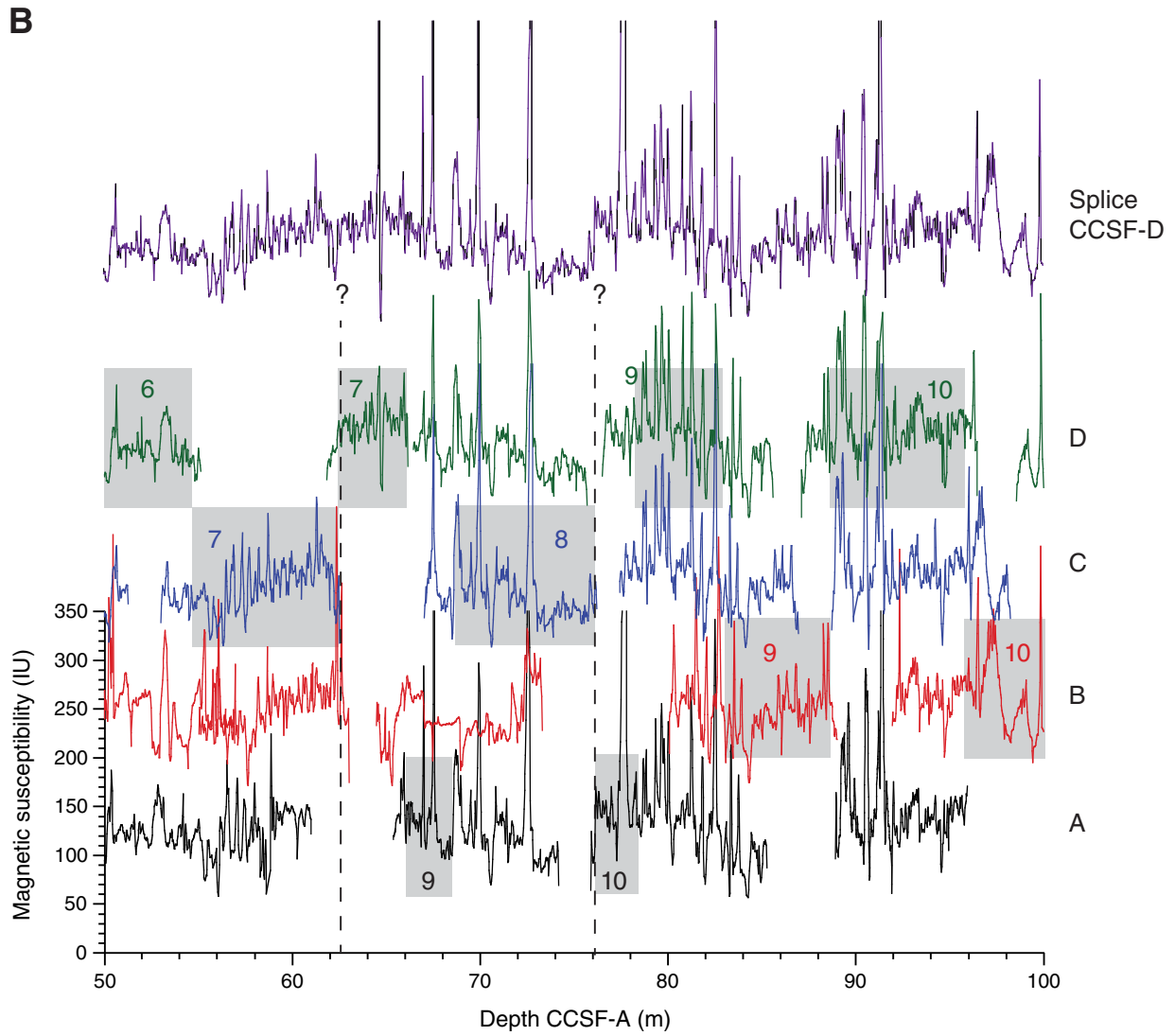


Figure F21 (continued). C. 100–150 m CCSF-A. (Continued on next page.)

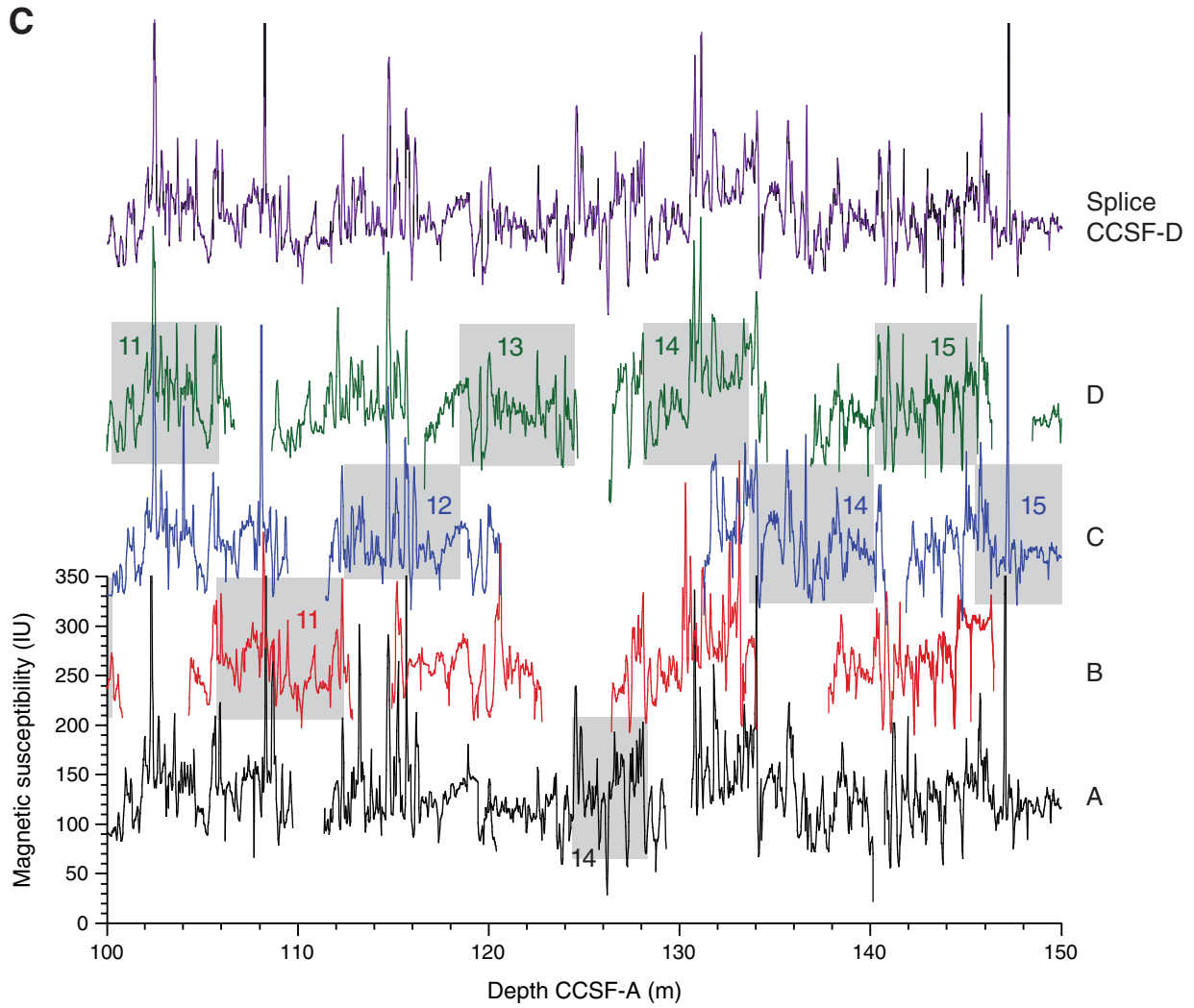


Figure F21 (continued). D. 150–225 m CCSF-A.

D

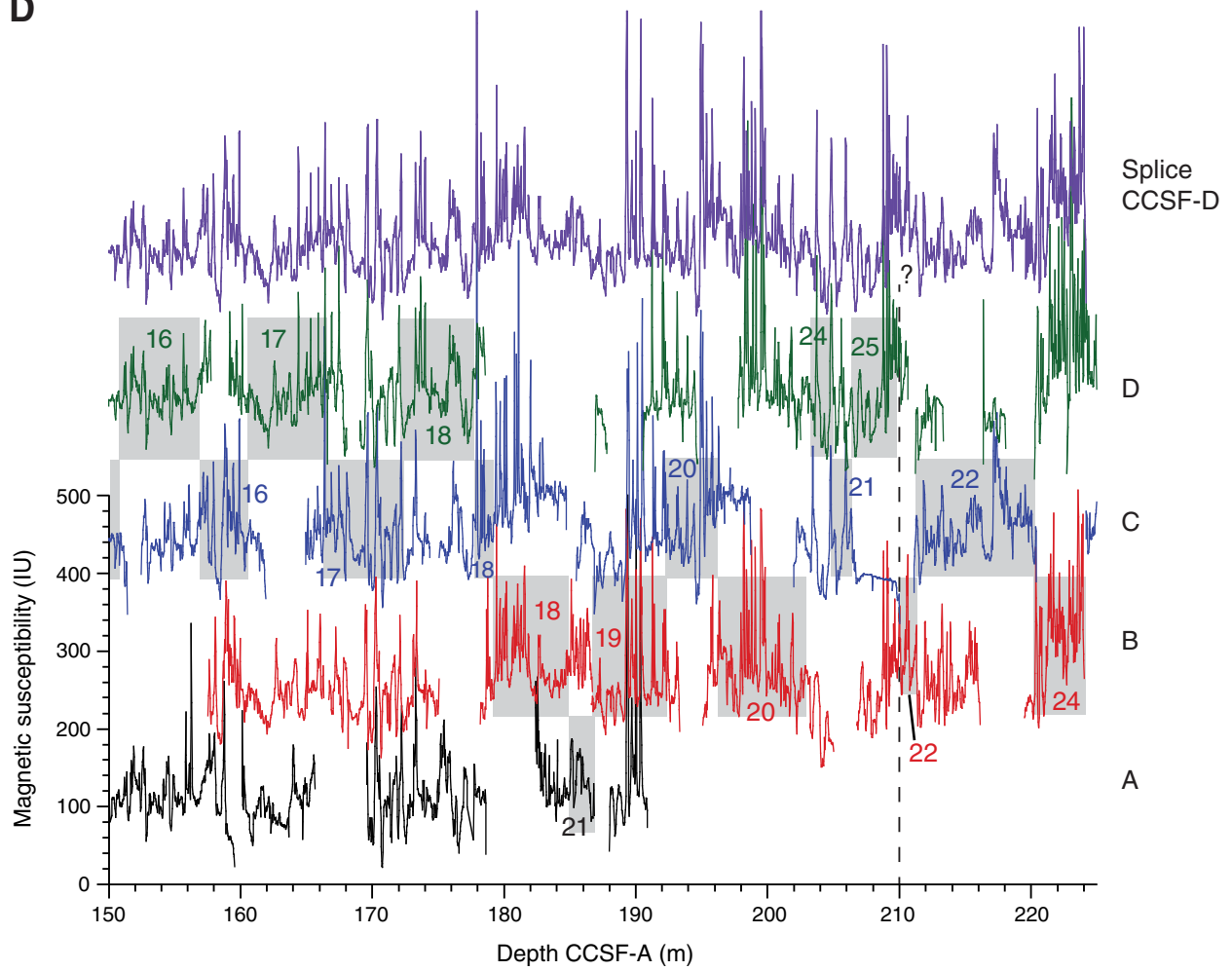


Figure F22. GRA bulk density data for the interval of the continuous splice in Holes U1417A–U1417D and the splice record. Gray boxes = intervals used to construct the splice with core numbers noted, dashed vertical lines = intervals where tie points should be treated with caution (see text for details). A. 0–50 m CCSF-A. (Continued on next three pages.)

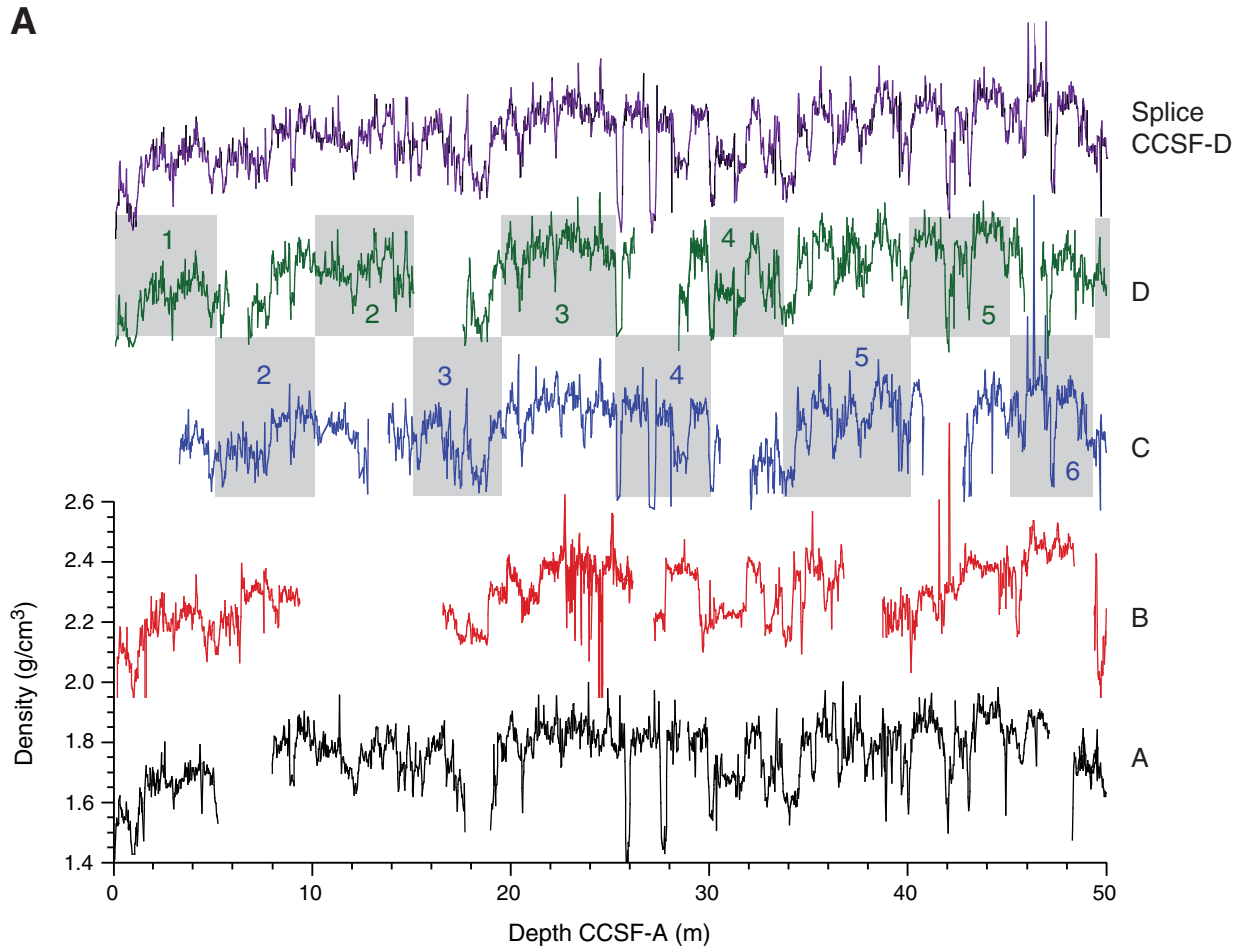


Figure F22 (continued). B. 50–100 m CCSF-A. (Continued on next page.)

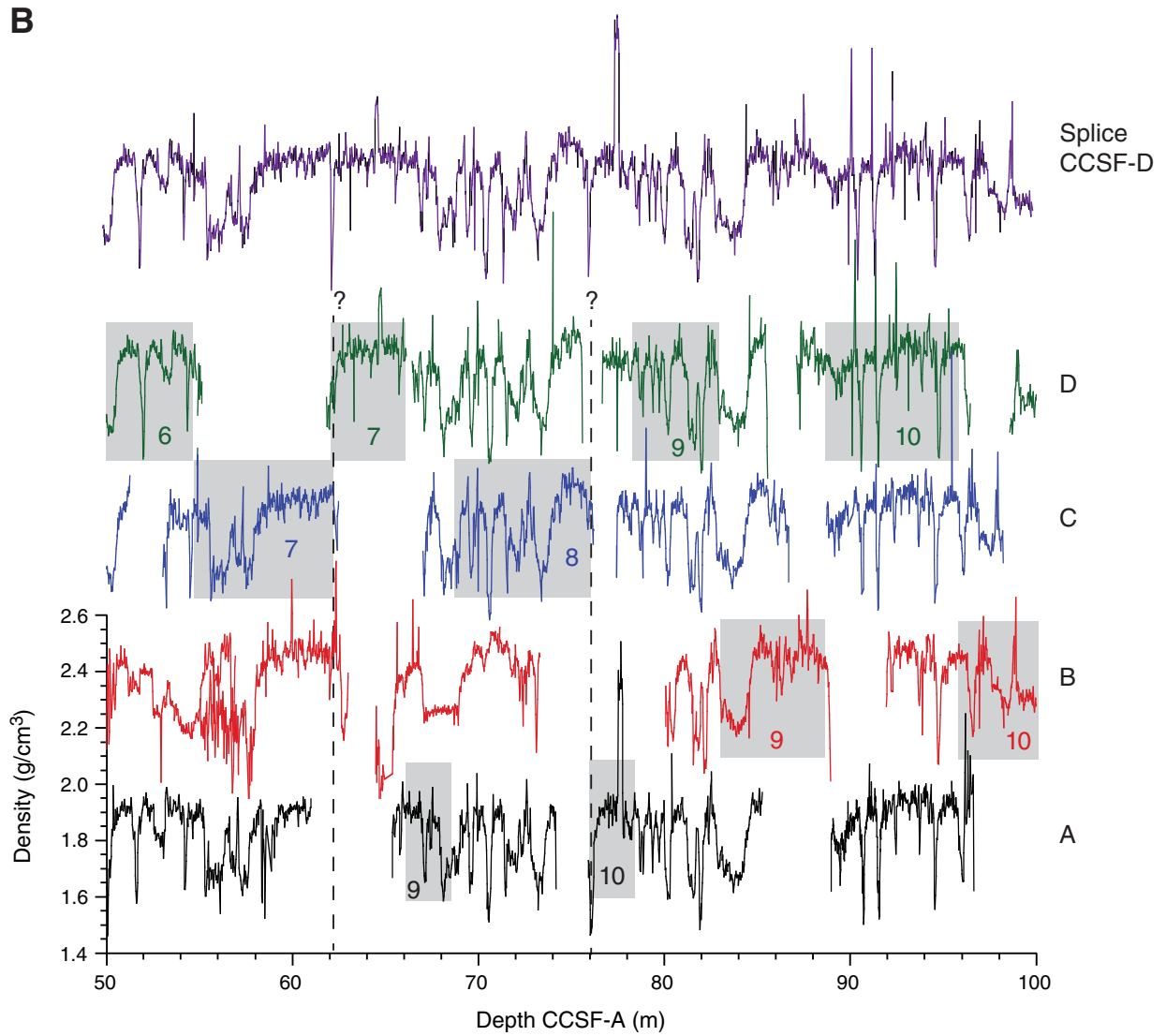


Figure F22 (continued). C. 100–150 m CCSF-A. (Continued on next page.)

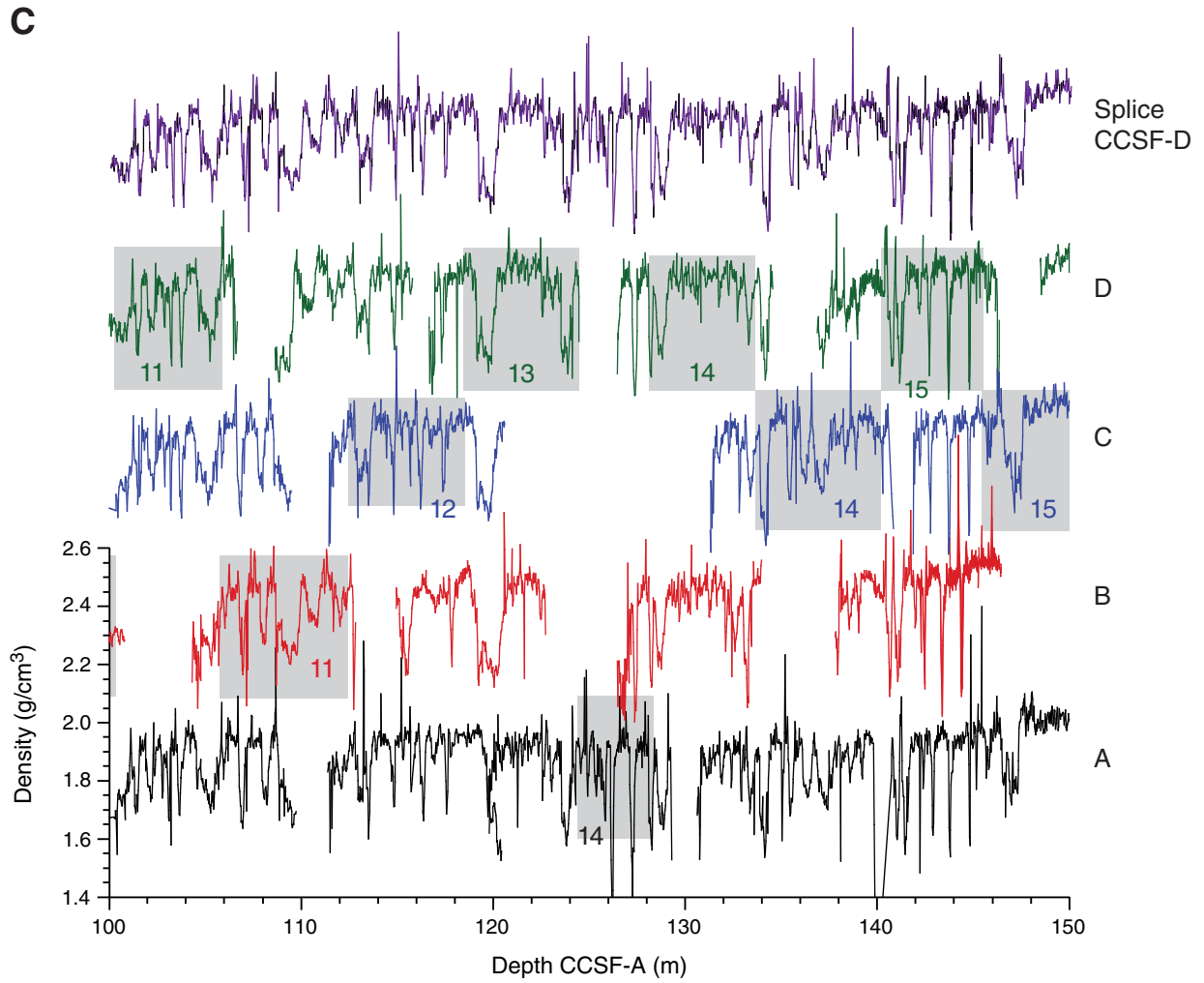


Figure F22 (continued). D. 150–225 m CCSF-A.

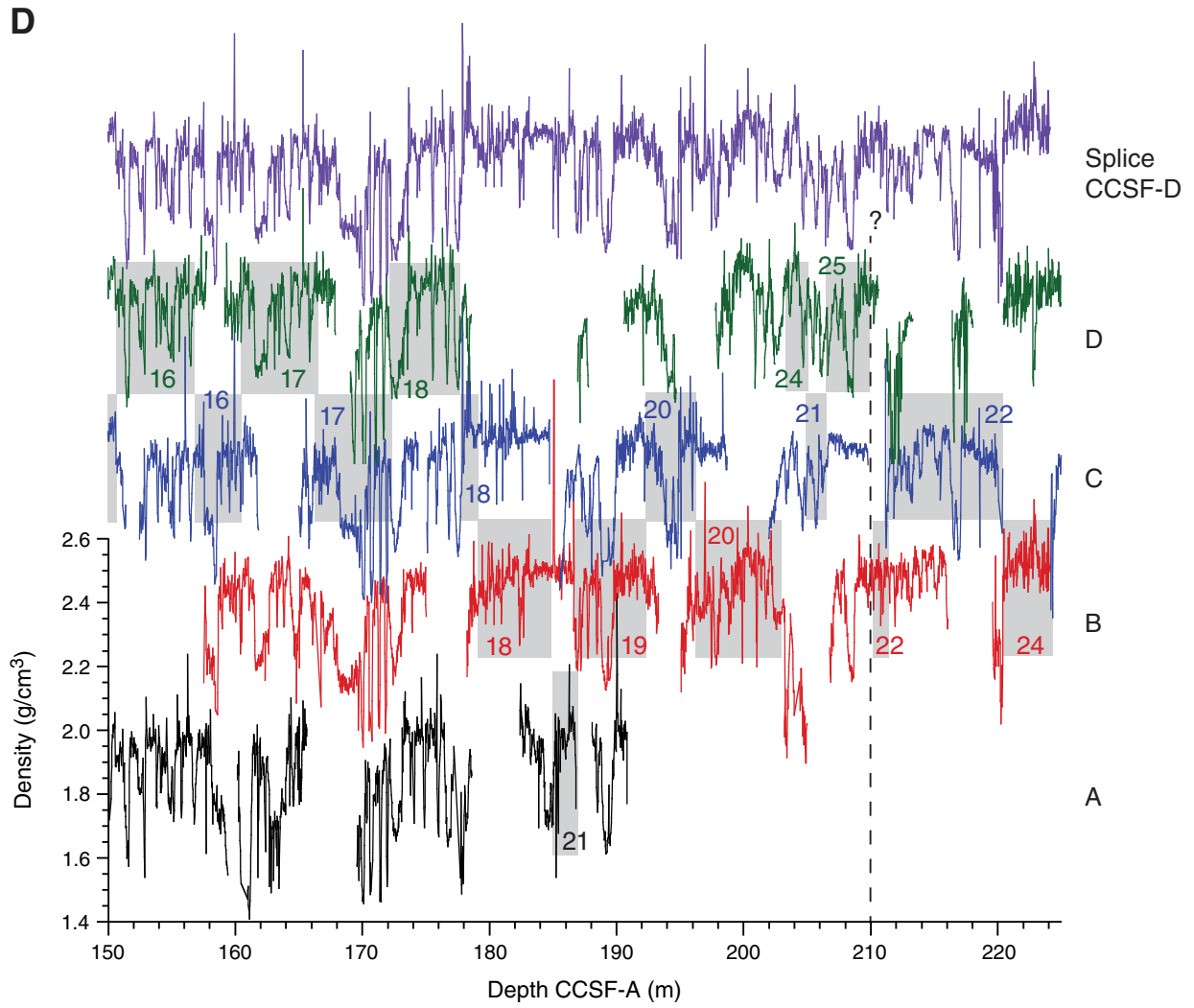


Figure F23. Affine values, Holes U1417A–U1417E. Equations denote the relationship between the affine values and core top depth for each of the two segments of the line of best fit (black line).

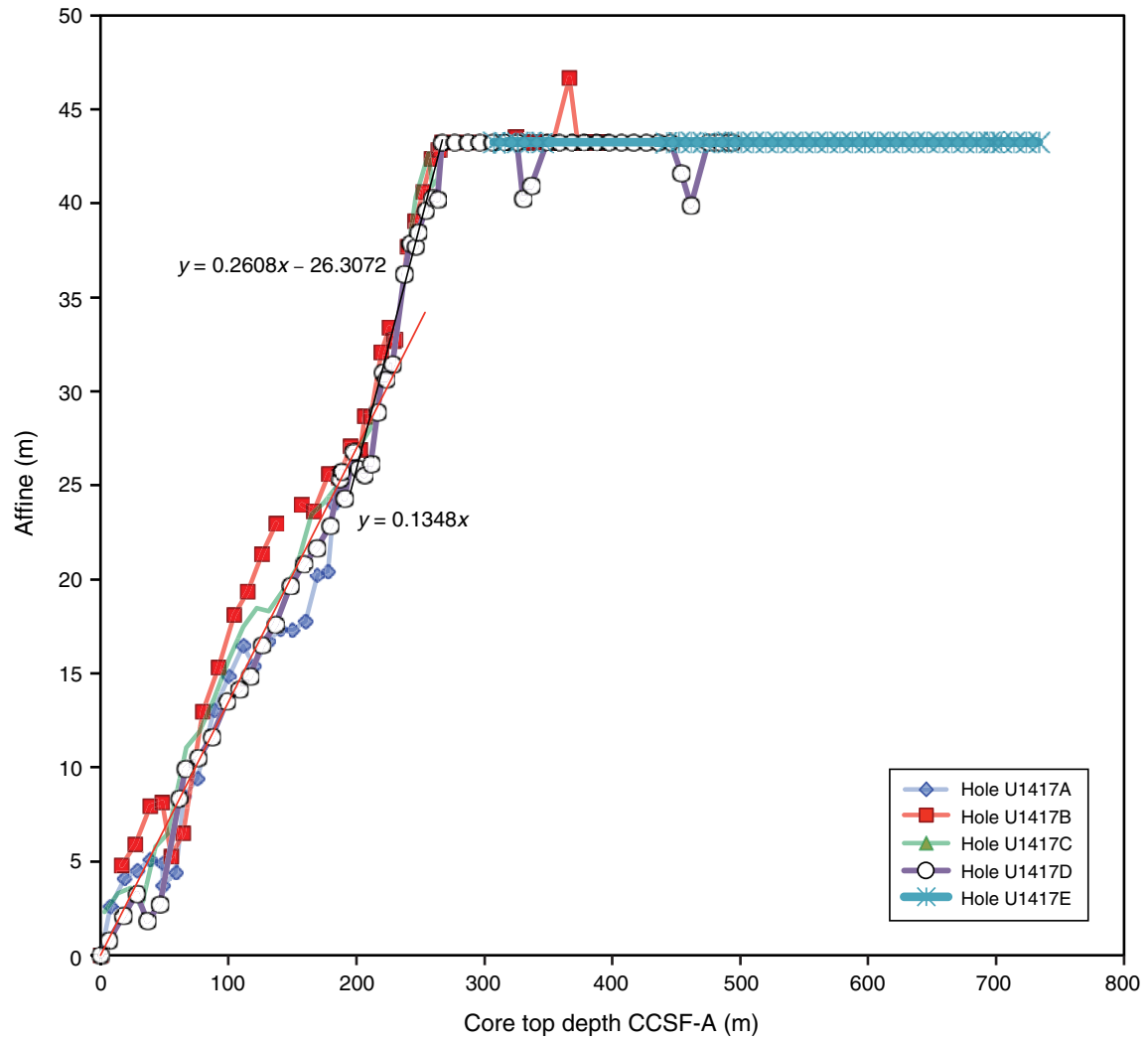




Figure F24. Shipboard age model, Site U1417. Diamonds = biostratigraphic ages, squares = paleomagnetic ages, triangles = extrapolation from the base of the borehole to underlying oceanic crust. Bars on the datums are depth and age uncertainties, here assumed to represent $\pm 2\sigma$ uncertainties. Red and blue lines are visually estimated minimum and maximum initial age models. A. 0–40 Ma. B. 0–12 Ma. C. 0–5 Ma.

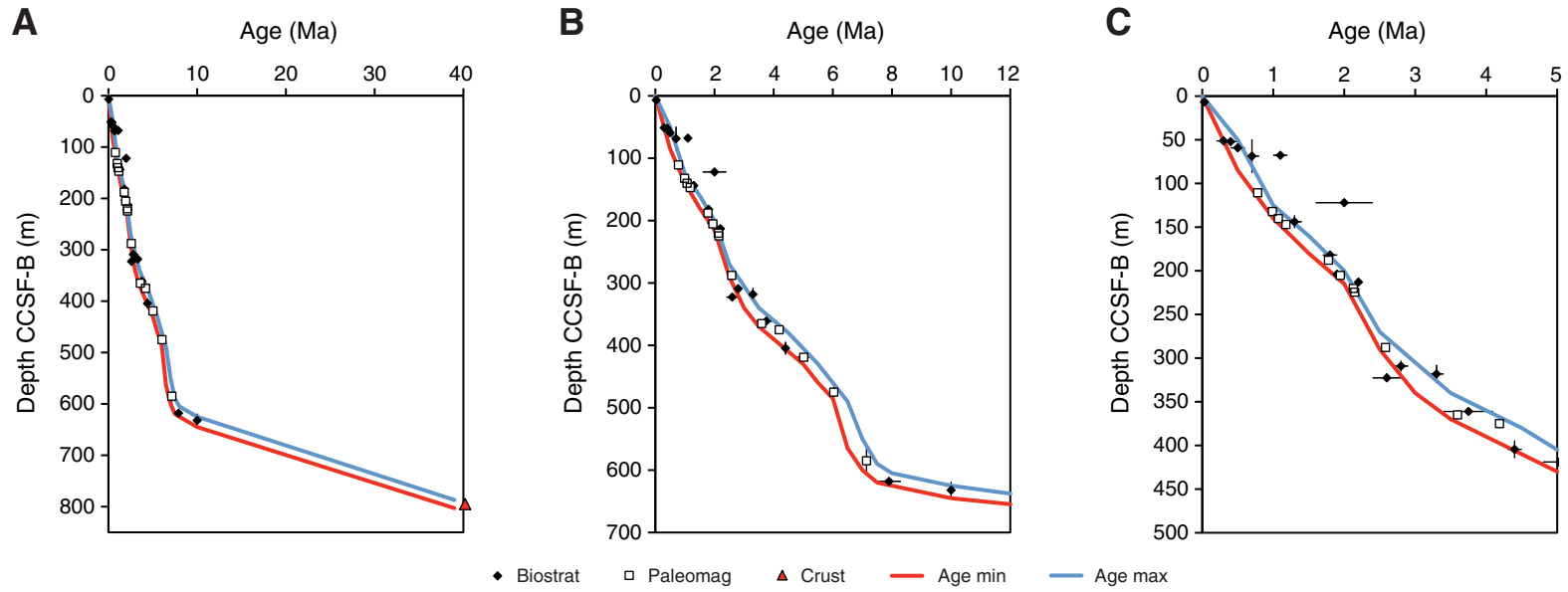


Figure F25. Sedimentation rates estimated based on CCSF-B depth model and shipboard age models, Site U1417. Average sedimentation rates (solid line) are calculated over 0.5 m.y. intervals from 0 to 10 Ma and over a single interval of 10–39 Ma. Uncertainties ($\pm 1\sigma$) in sedimentation rate, estimated from 500 iterations of a Monte-Carlo sedimentation model, are bracketed by dashed lines. **A.** 0–40 Ma. **B.** Sedimentation rates as a function of m CCSF-B depth. **C.** 0–12 Ma. **D.** 0–5 Ma, with sedimentation rates (solid black lines) and uncertainties (dashed black lines) superimposed on the global $\delta^{18}\text{O}$ stack in pink (data from Lisiecki and Raymo, 2005) with long-term $\delta^{18}\text{O}$ variations (red line, $\delta^{18}\text{O}$ data smoothed with a Gaussian filter of 500 ka $\pm 3\sigma$ width).

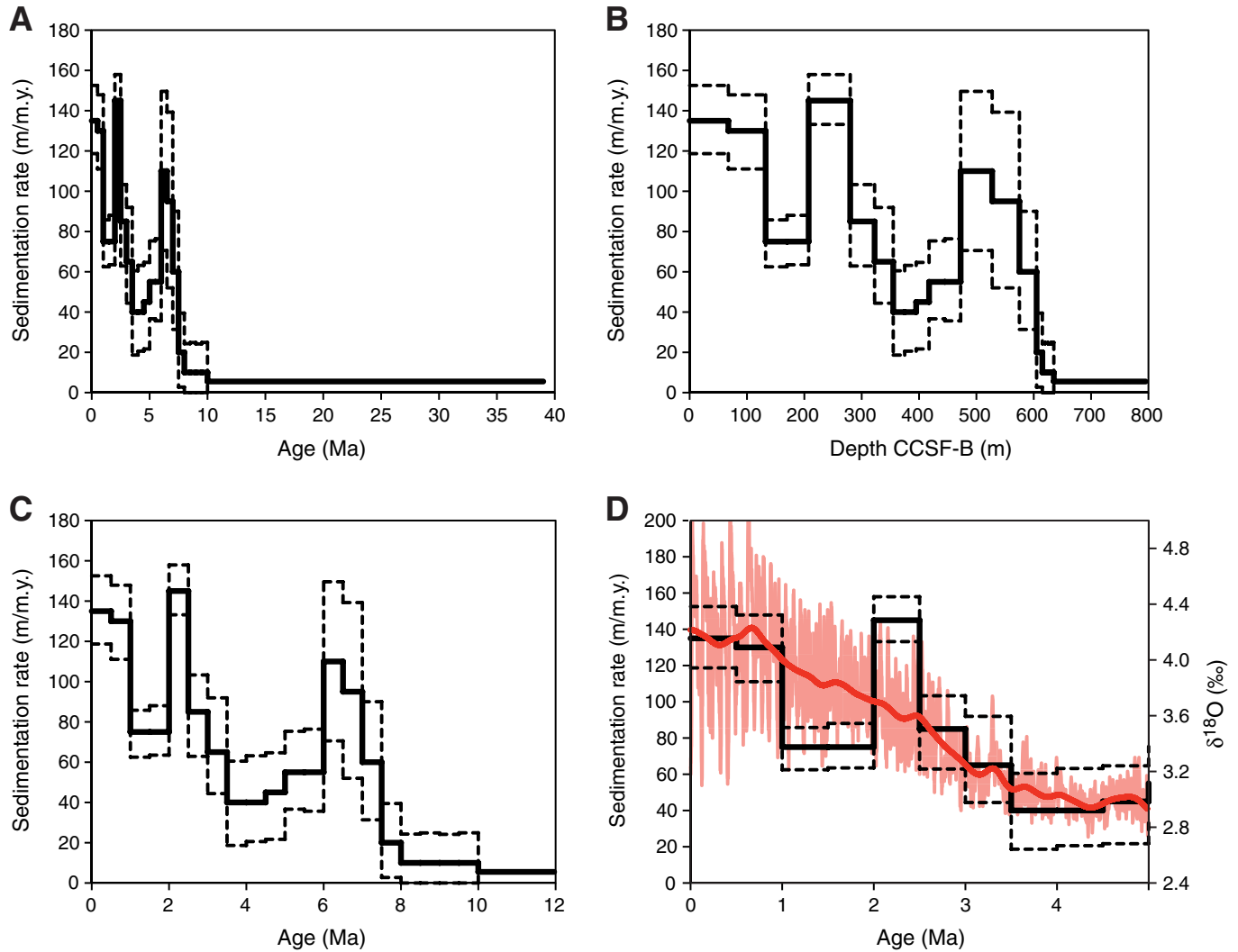




Figure F26. Dissolved chemical concentrations and headspace gas, Site U1417. **A.** Alkalinity. **B.** pH. **C.** Sulfate. **D.** Ammonium. **E.** Bromide. **F.** Methane. **G.** Silica. **H.** Salinity. **I.** Chloride. **J.** Sodium. Full details of Lithology column are shown in Figure F16 (see “Lithostratigraphy”).

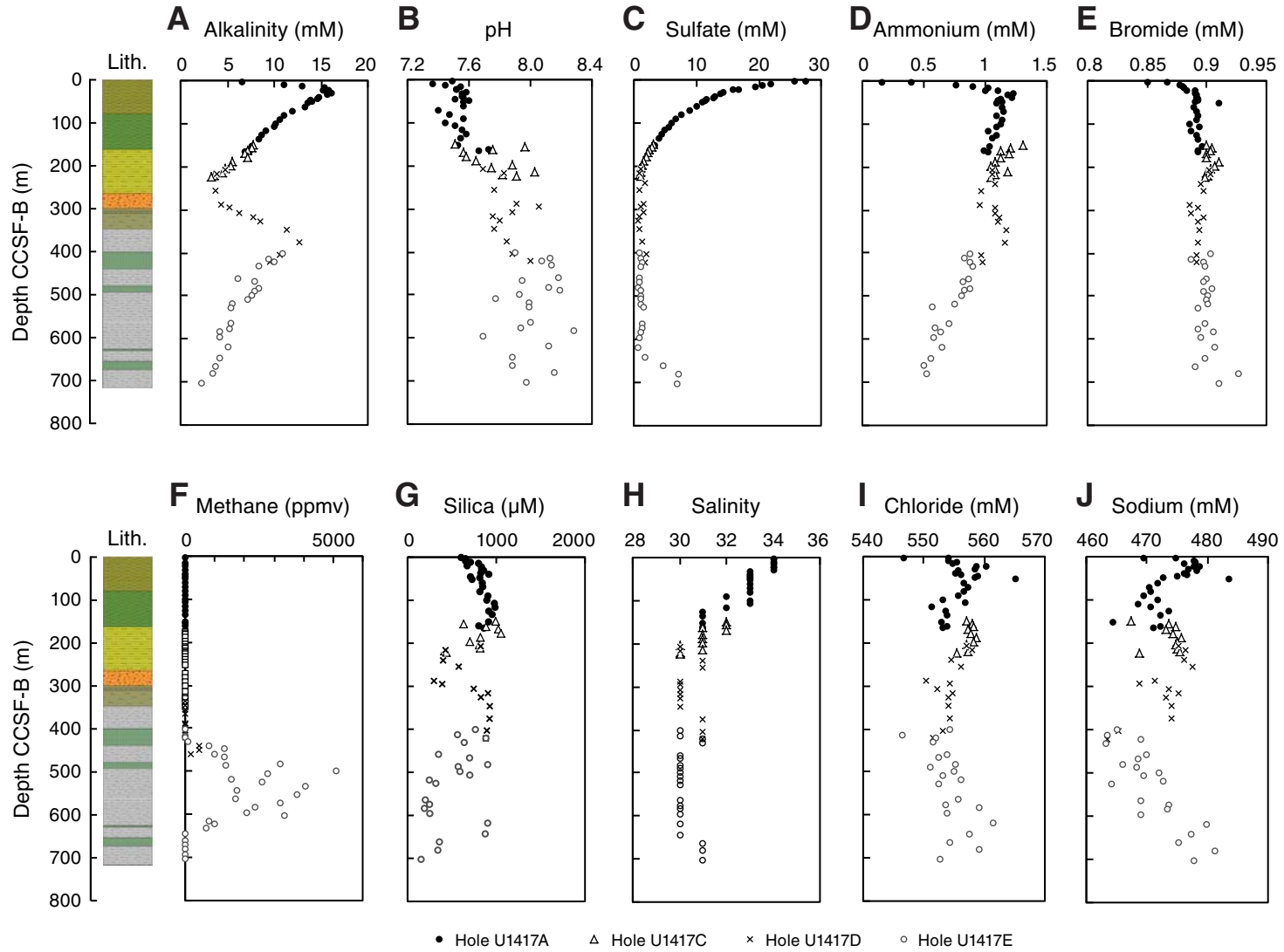




Figure F27. Dissolved chemical concentrations, Site U1417. **A.** Calcium. **B.** Potassium. **C.** Magnesium. **D.** Lithium. **E.** Boron. **F.** Barium. **G.** Strontium. **H.** Iron. **I.** Manganese. **J.** Phosphate. Full details of Lithology column are shown in Figure F16 (see “**Lithostratigraphy**”).

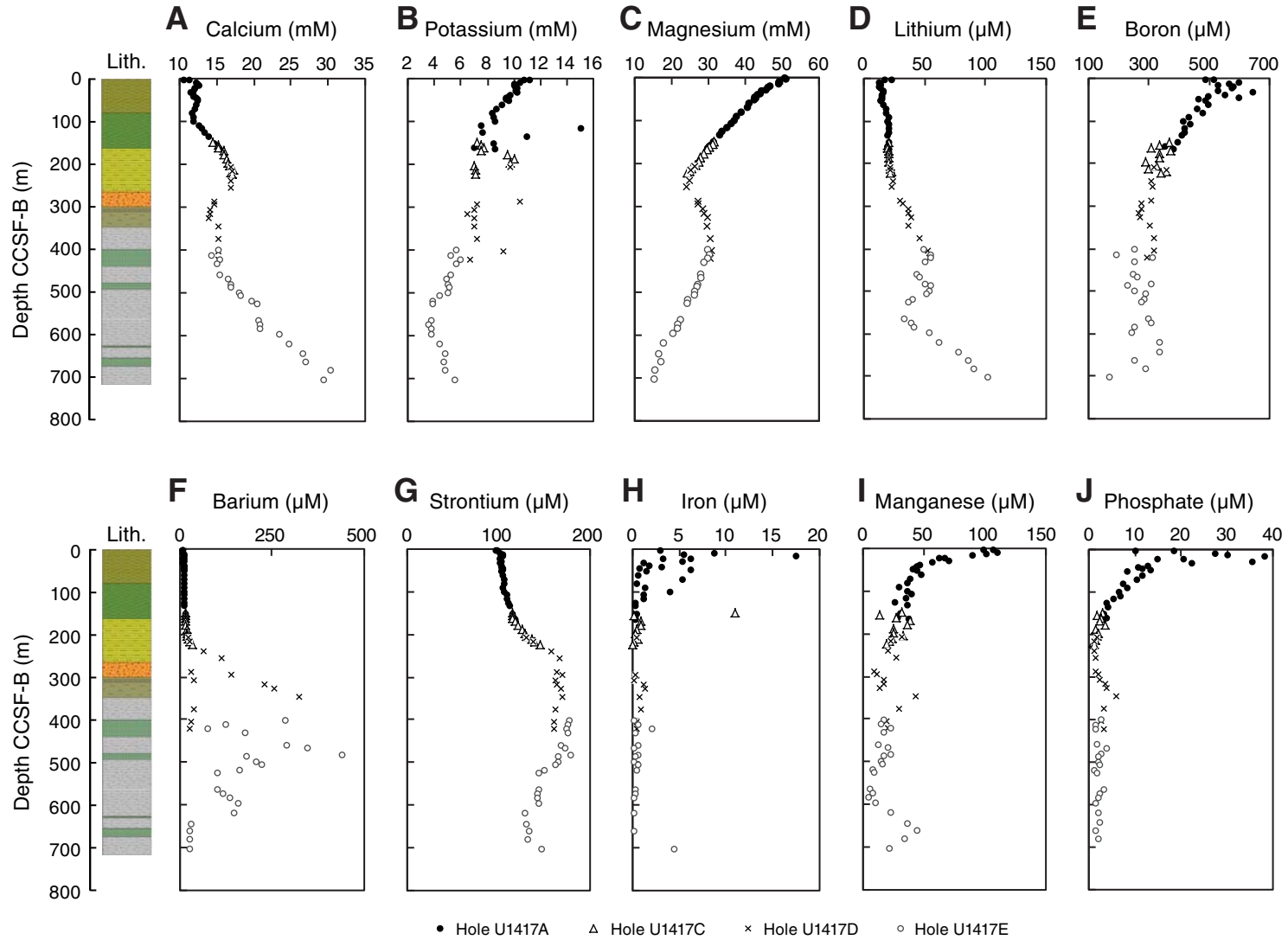




Figure F28. Solid-phase chemical parameters, Site U1417. **A.** Full range of total organic carbon (TOC) content. **B.** Subset of TOC content (<2.5 wt%). **C.** Total nitrogen (TN). **D.** Full range of CaCO₃ content. **E.** Subset of CaCO₃ content (<5 wt%). **F.** Scatter plot of TOC vs. TN. The potential contribution of inorganic N to the TN signal is estimated where the linear regression line intercepts the γ -axis (e.g., Schubert and Calvert, 2001). Full details of Lithology column are shown in Figure F16 (see “Lithostratigraphy”).

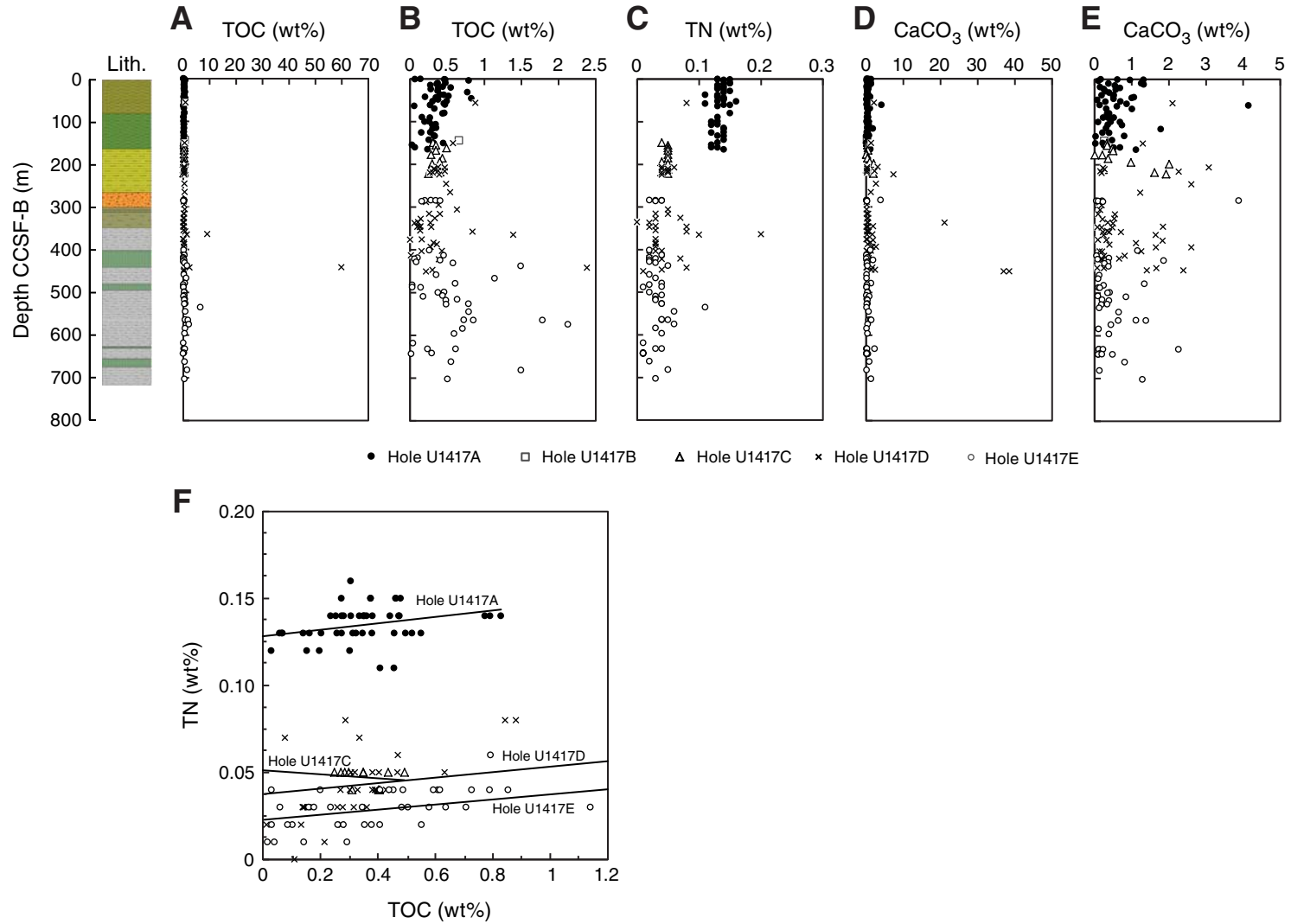




Figure F29. Dissolved chemical concentrations, solid-phase chemical parameters, and headspace gas concentrations for the upper 150 m CCSF-B at Site U1417. **A.** Alkalinity. **B.** Sulfate. **C.** Ammonium. **D.** Chloride. **E.** Sodium. **F.** Phosphate. **G.** Calcium. **H.** Total organic carbon (TOC). **I.** CaCO₃. **J.** Methane.

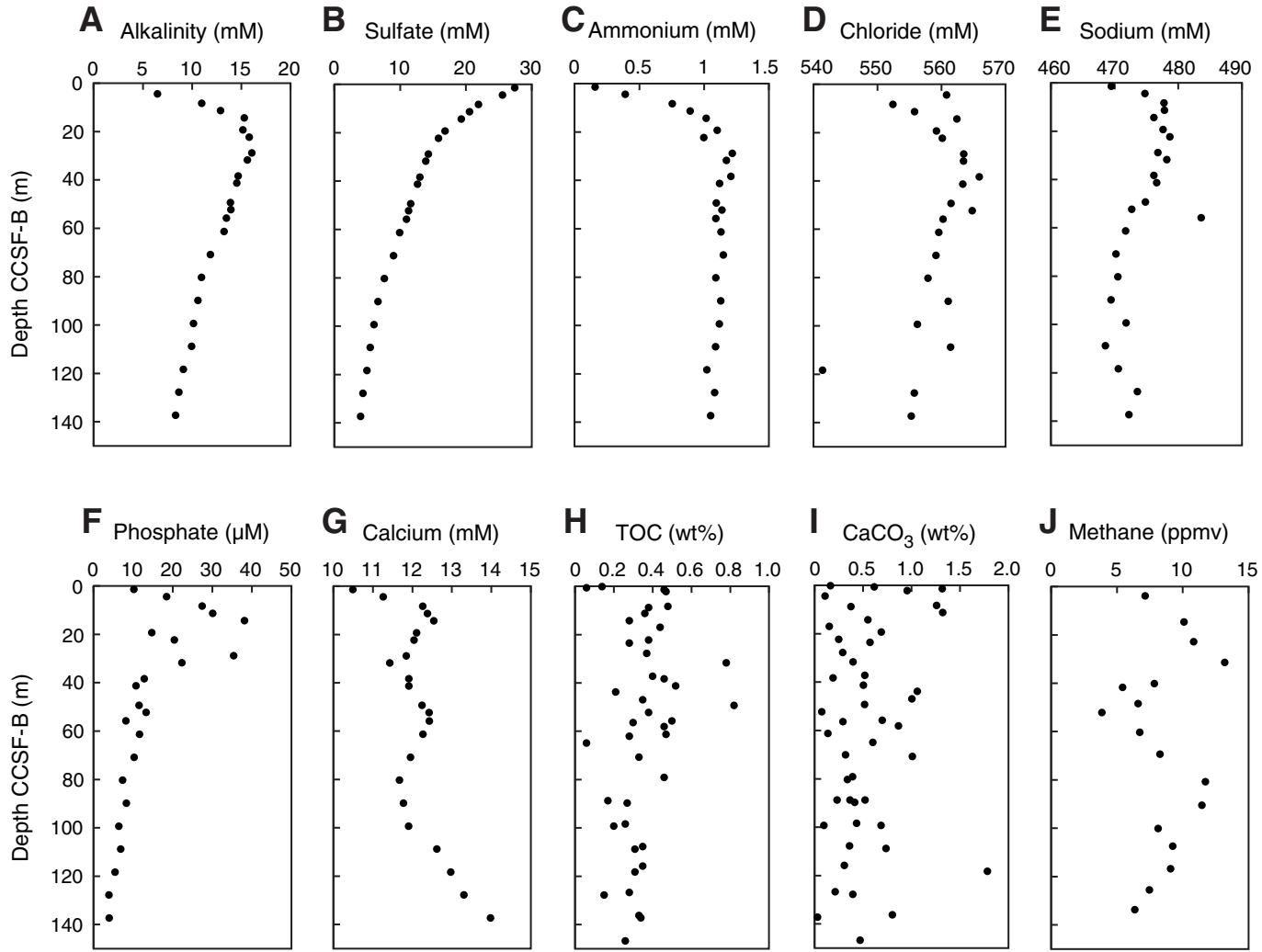




Figure F30. Downhole density and sonic logs, discrete physical properties measurements, and seismic reflection Profile MGL1109MCS01. Seismic Sequences I–III are interpreted after Reece et al. (2011) and demarcated by yellow horizons. Subsections of Sequence I (A–C) are demarcated by green horizons. Subsections of Sequence IC (IC1 and IC2) are demarcated by a blue horizon. Subsections are interpreted based on dominant seismic character. Note lack of check shot calibration below 211 m WMSF and up to ~10 m depth offset when comparing CCSF-B and WMSF. MAD = moisture and density, GRA = gamma ray attenuation, WRMSL = Whole-Round Multisensor Logger. *P*-wave data: closed symbols = automatic velocity picks, open symbols = manual velocity picks. TWT = two-way traveltime, VSP = vertical seismic profile, VE = vertical exaggeration.

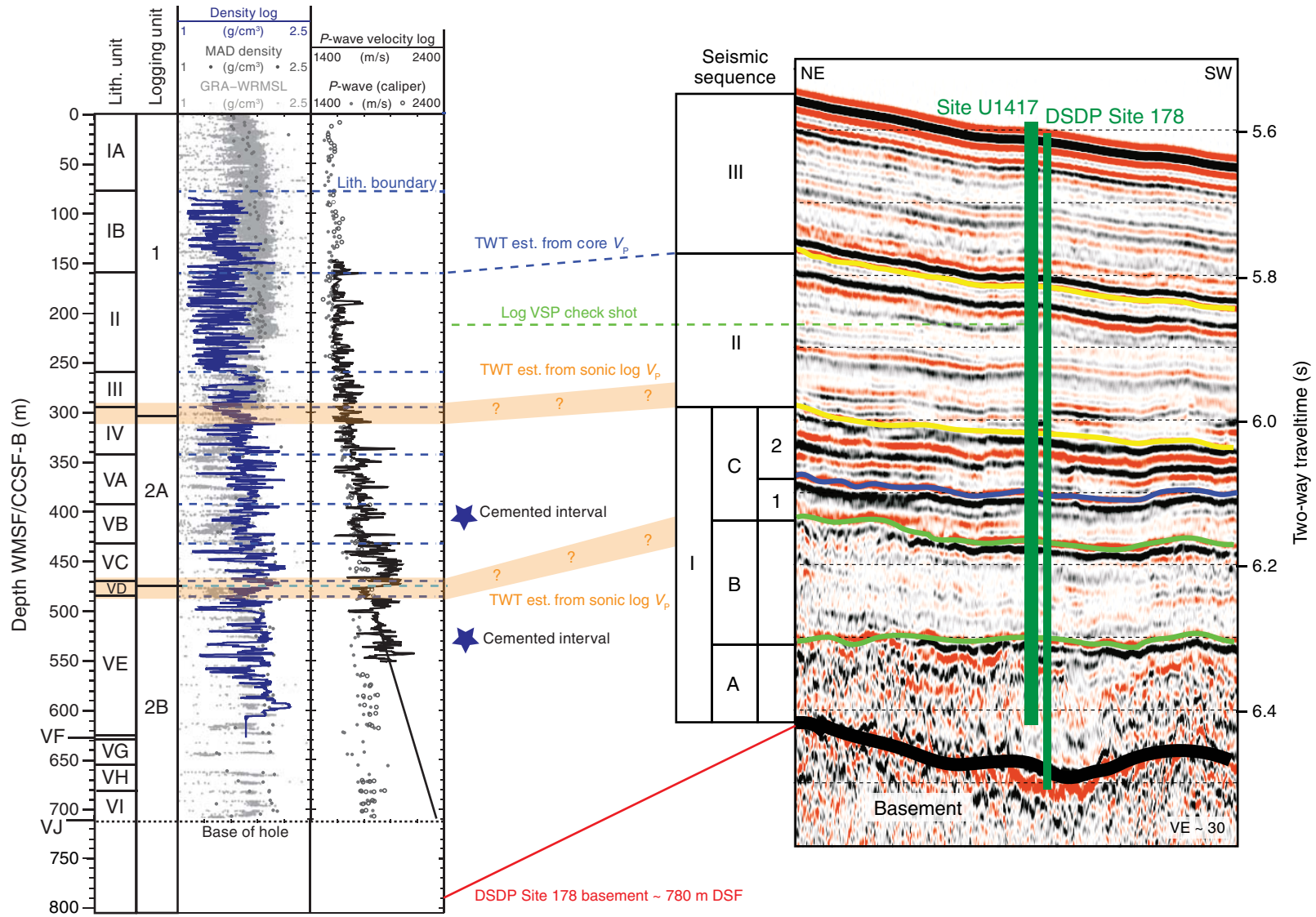


Figure F31. Physical properties measurements, Hole U1417A. WRMSL = Whole-Round Multisensor Logger, MS = magnetic susceptibility. MAD = moisture and density, GRA = gamma ray attenuation. NGR = natural gamma radiation.

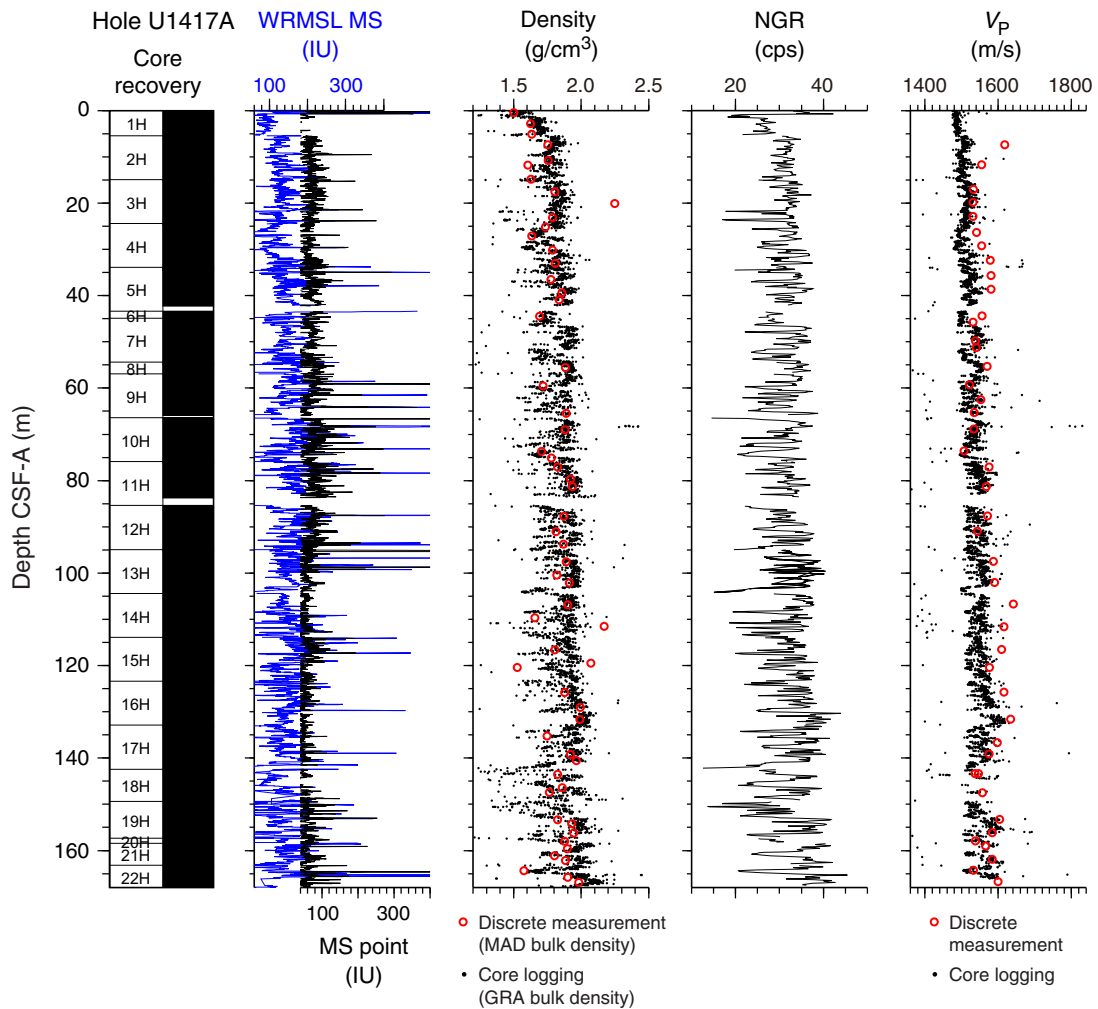


Figure F32. Physical properties measurements, Hole U1417B. WRMSL = Whole-Round Multisensor Logger, MS = magnetic susceptibility. GRA = gamma ray attenuation. NGR = natural gamma radiation.

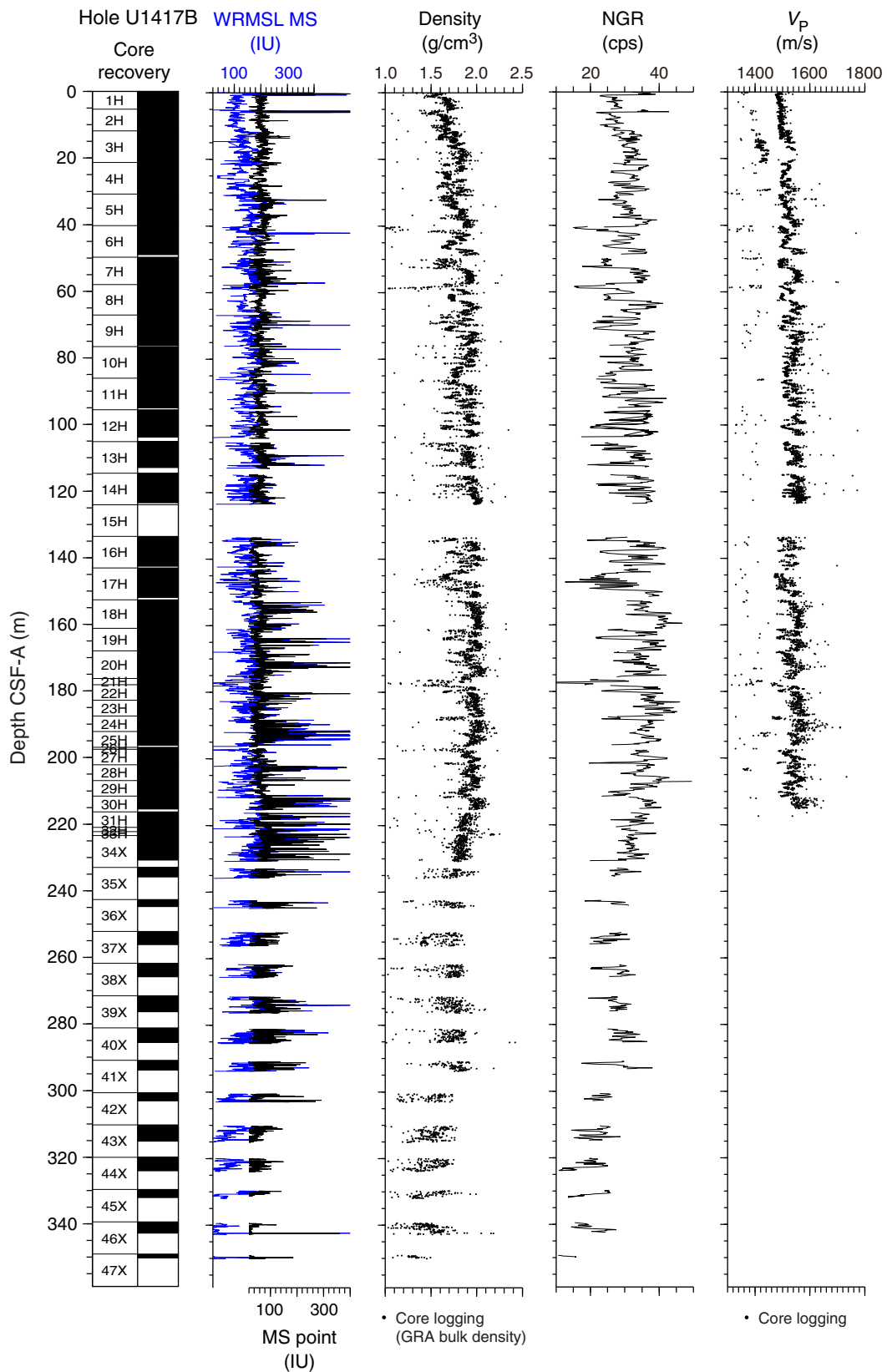


Figure F33. Physical properties measurements, Hole U1417C. WRMSL = Whole-Round Multisensor Logger, MS = magnetic susceptibility. GRA = gamma ray attenuation. NGR = natural gamma radiation.

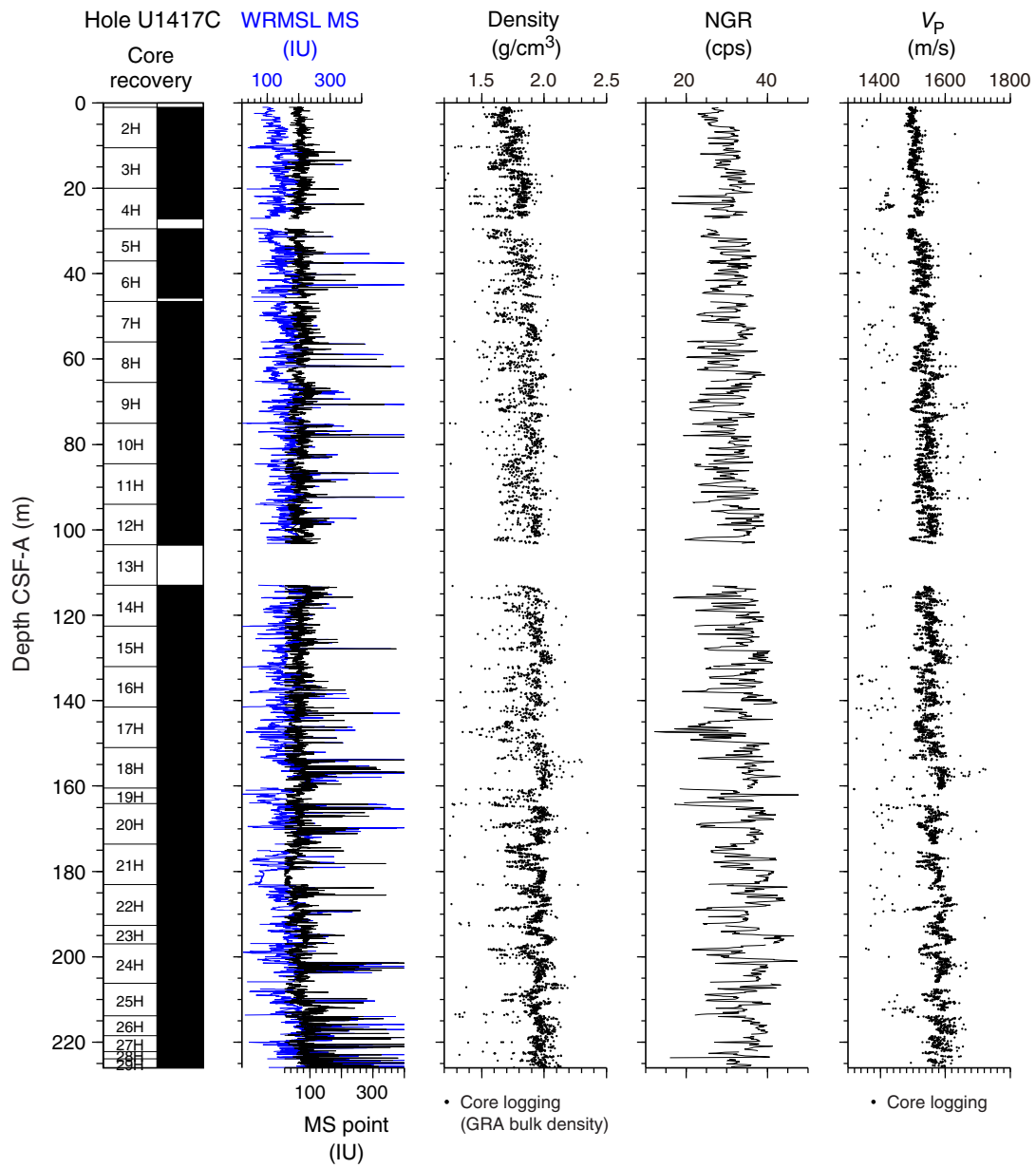


Figure F34. Physical properties measurements, Hole U1417D. WRMSL = Whole-Round Multisensor Logger, MS = magnetic susceptibility. MAD = moisture and density, GRA = gamma ray attenuation. NGR = natural gamma radiation.

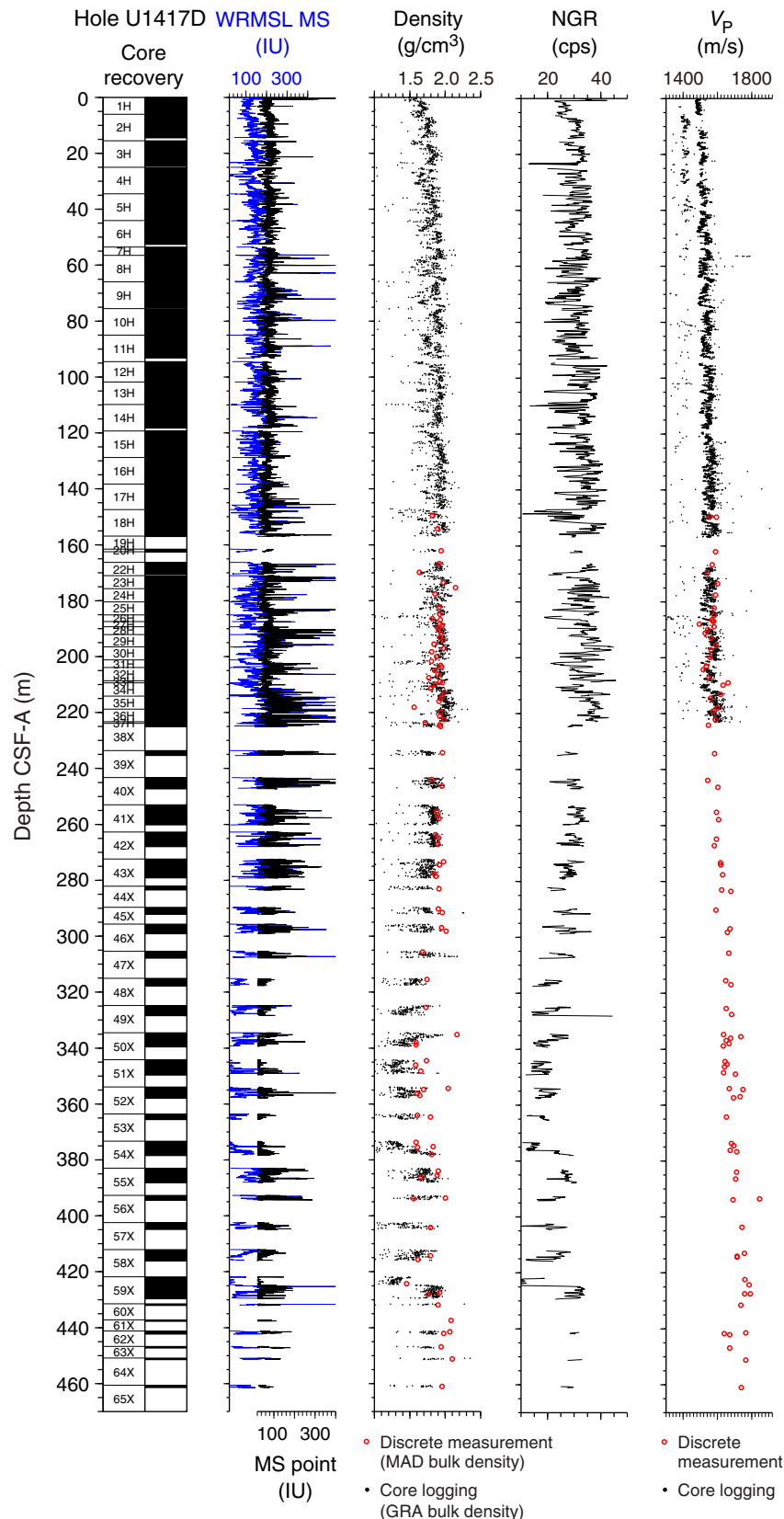


Figure F35. Physical properties measurements, Hole U1417E. WRMSL = Whole-Round Multisensor Logger, MS = magnetic susceptibility. MAD = moisture and density, GRA = gamma ray attenuation. NGR = natural gamma radiation.

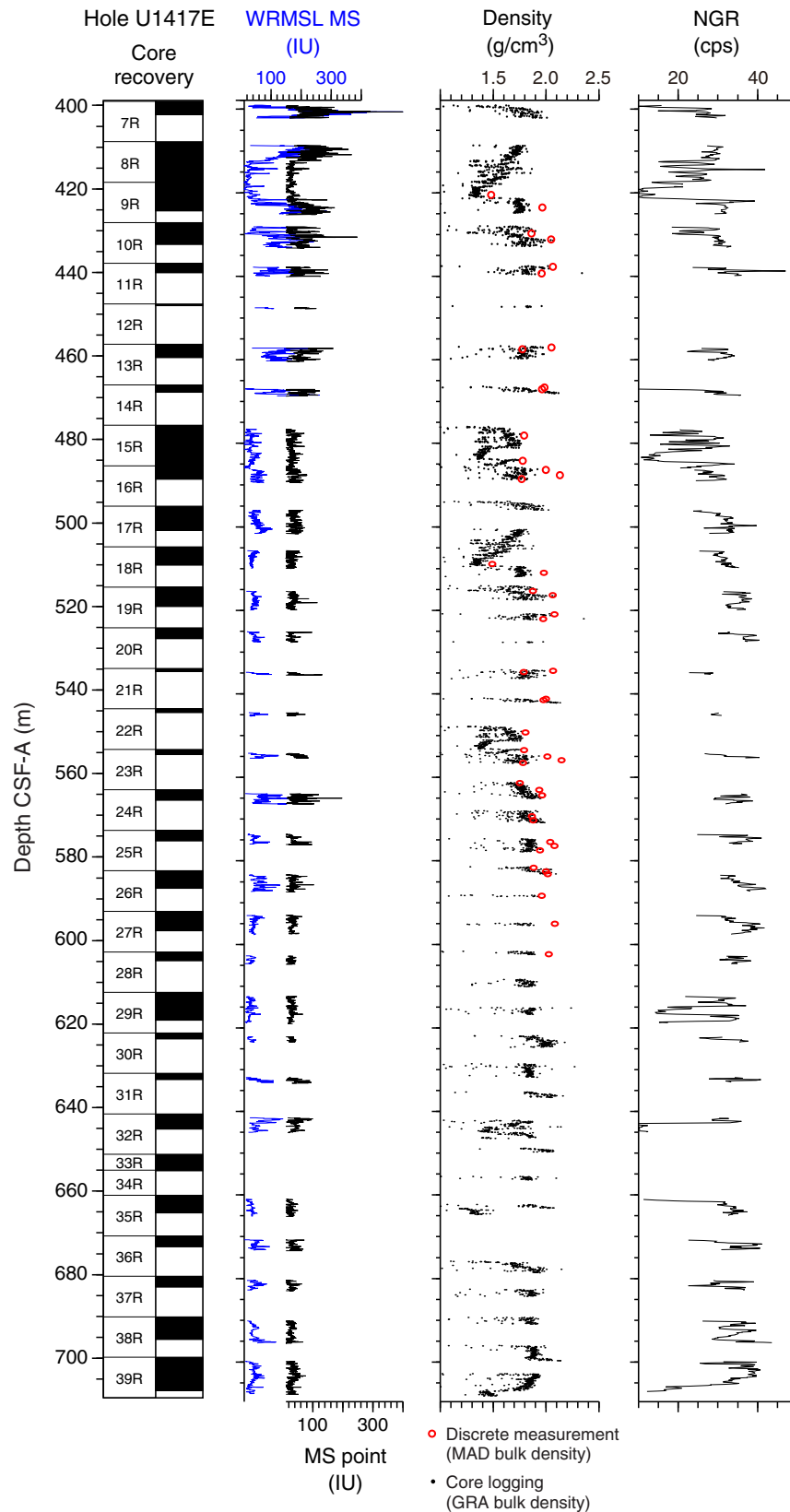


Figure F36. Discrete moisture and density (MAD) bulk sediment density measurements (dots) from Holes U1417A–U1417E compared to Whole-Round Multisensor Logger (WRMSL) gamma ray attenuation (GRA) bulk density measurements from equivalent depths in core. Diamonds denote measurements from APC-derived cores only.

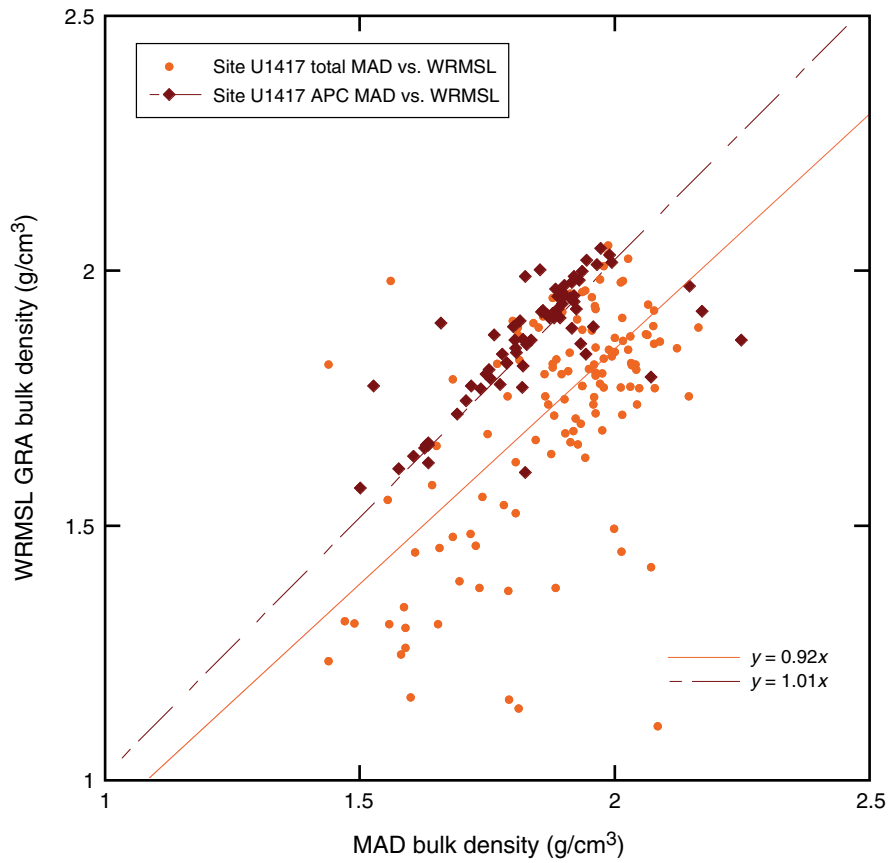


Figure F37. Point-source magnetic susceptibility (MS) data from the advanced piston corer portions of Holes U1417A–U1417D compared to Whole-Round Multisensor Logger (WRMSL) loop MS data from equivalent depths in those cores.

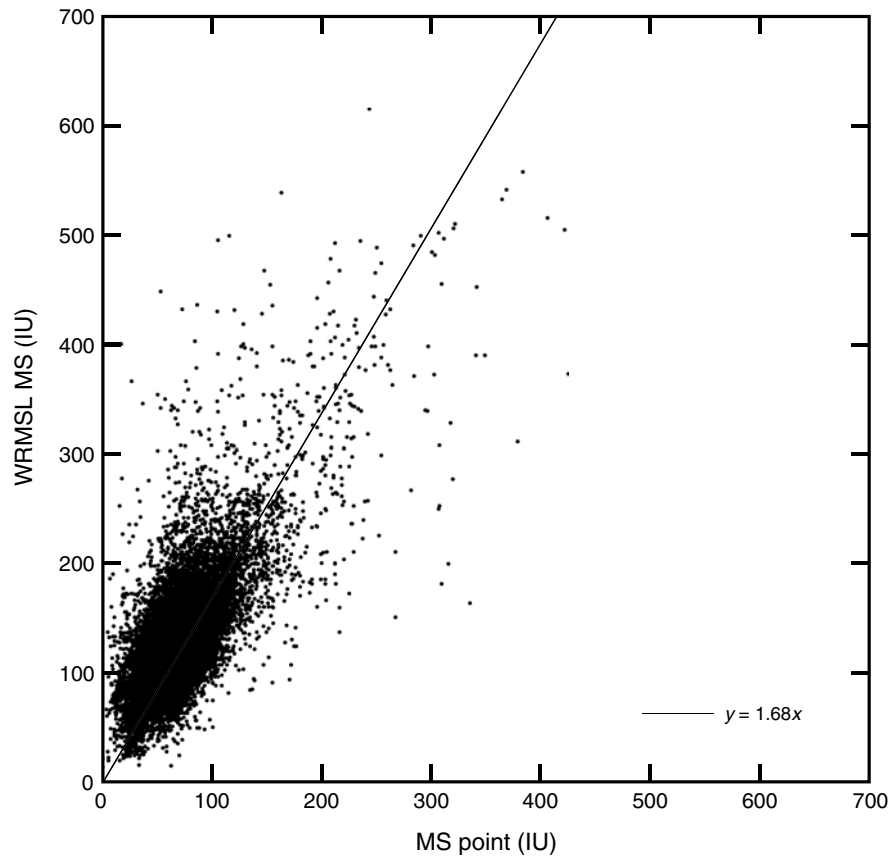


Figure F38. Whole-Round Multisensor Logger (WRMSL) gamma ray attenuation (GRA) bulk density compared to WRMSL magnetic susceptibility (MS) data, Site U1417. Both data sets are shown after Gaussian smoothing with a 10 cm window ($\pm 3\sigma$) and interpolation to constant resolution at 2.5 cm. WRMSL MS (κ , black) is also shown corrected for variability in recovered sediment volume by normalizing to WRMSL GRA bulk density (χ , blue). Data in the upper 220 m CCSF-B reflect the stratigraphic composite splice (see “[Stratigraphic correlation](#)”); deeper than this point, data from XCB and RCB cores in Holes U1417B, U1417D, and U1417E are combined to form a single composite section. In this lower portion, we use an average of all available data at depths for which there are overlaps in recovery.

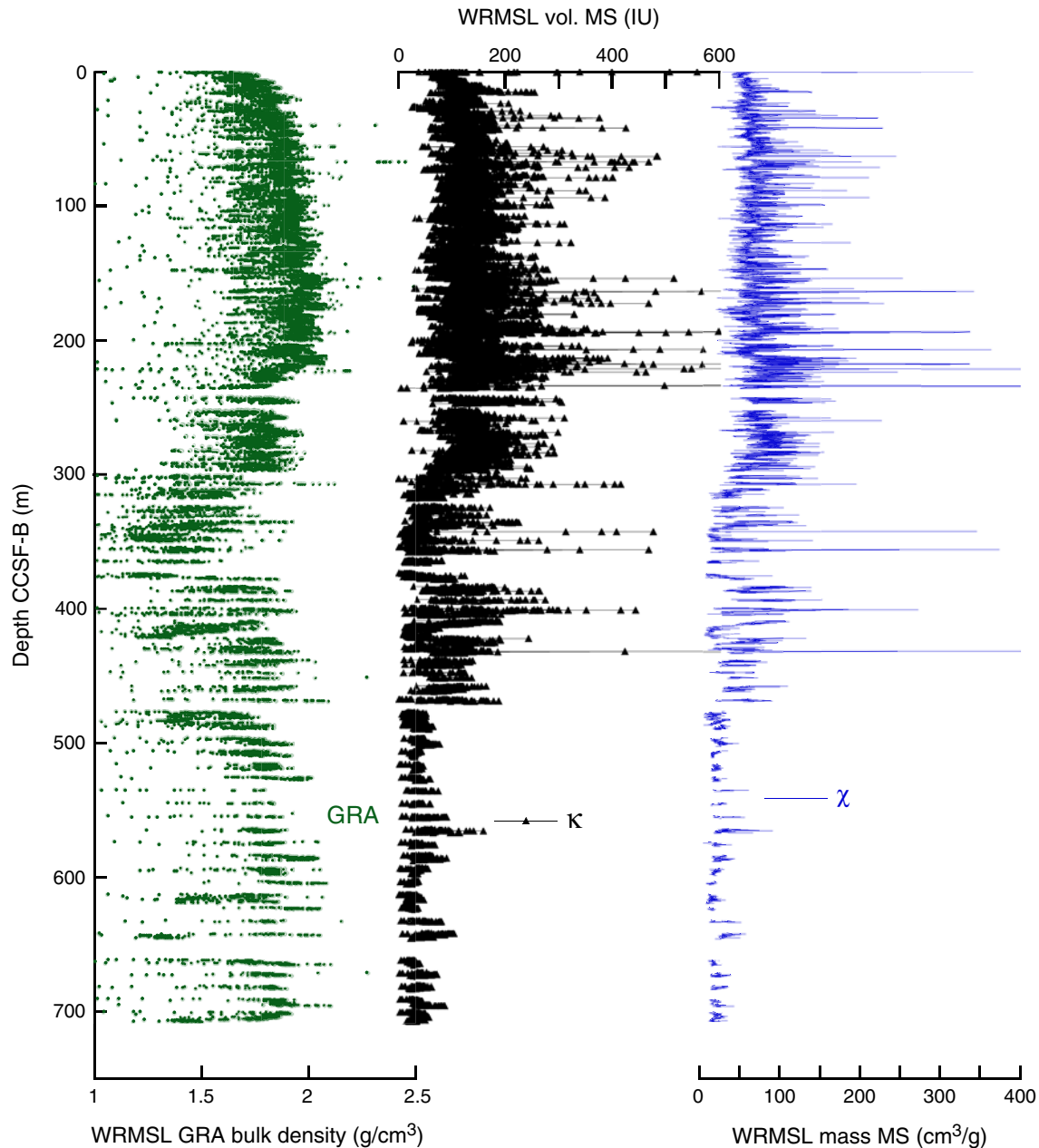


Figure F39. *P*-wave velocity measured by the WRMSL at 2.5 cm resolution, Holes U1417A–U1417D.

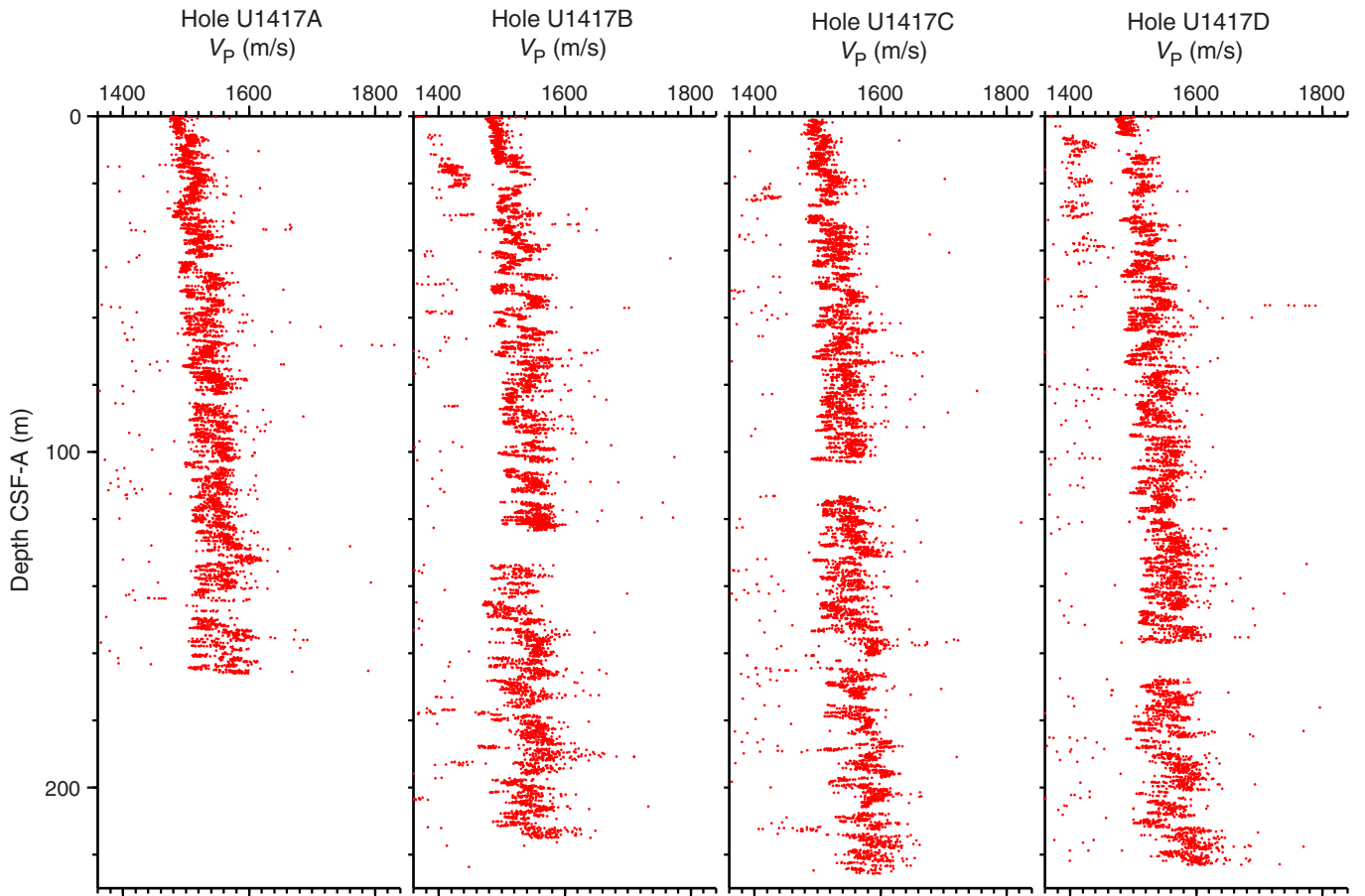


Figure F40. *P*-wave velocity measured by the Whole-Round Multisensor Logger (WRMSL) on whole-round sections and the *P*-wave caliper (PWC) on working half sections. **A.** Combined plot. **B.** Scatter plot, showing correlation between core logger and discrete measurements. The black trend line reflects all values from Holes U1417A and U1417D.

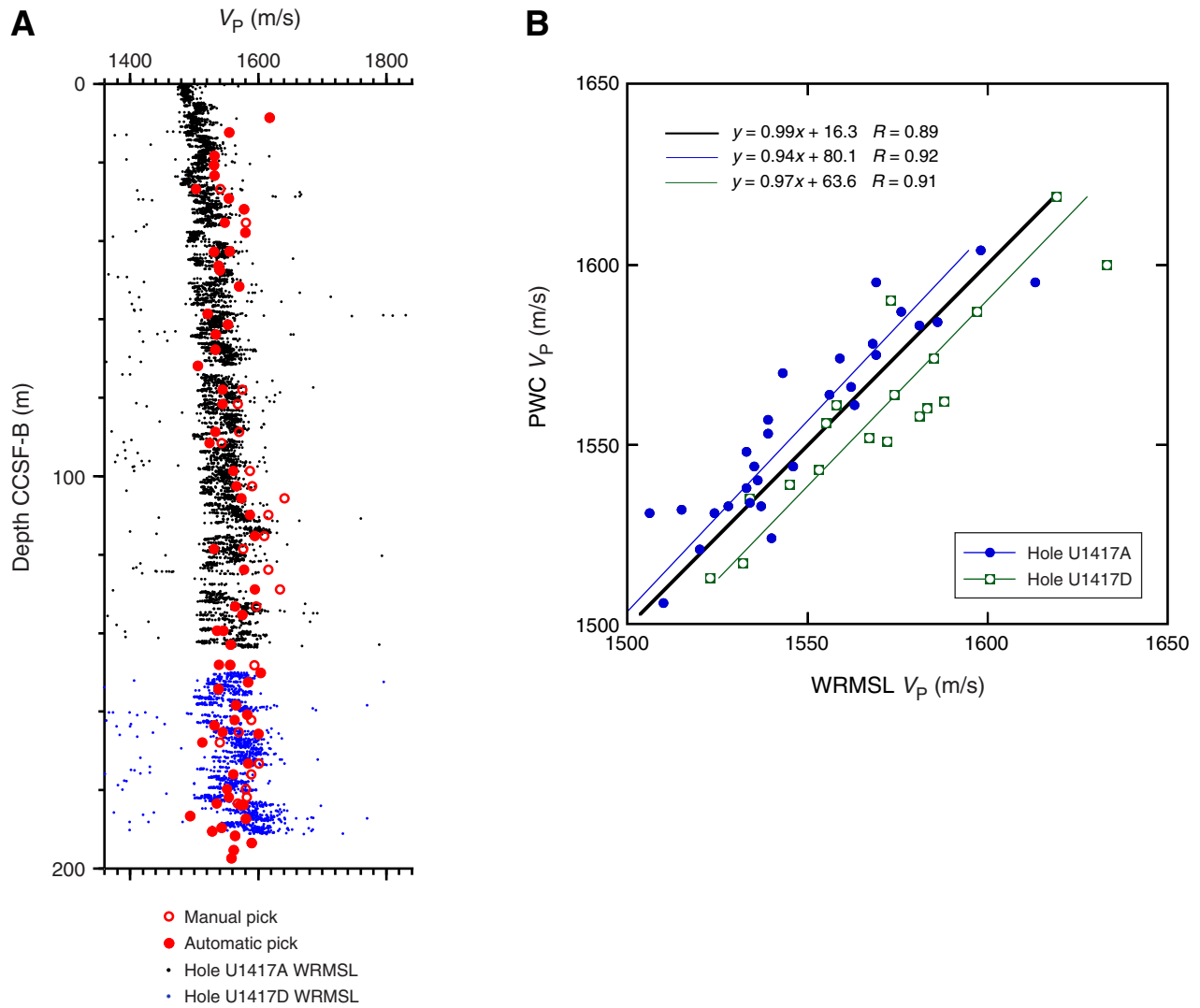


Figure F41. *P*-wave velocity measured by the *P*-wave caliper, Holes U1417A, U1417D, and U1417E. Left: velocities between 1450 and 1980 m/s. Right: velocities between 1480 and 6000 m/s.

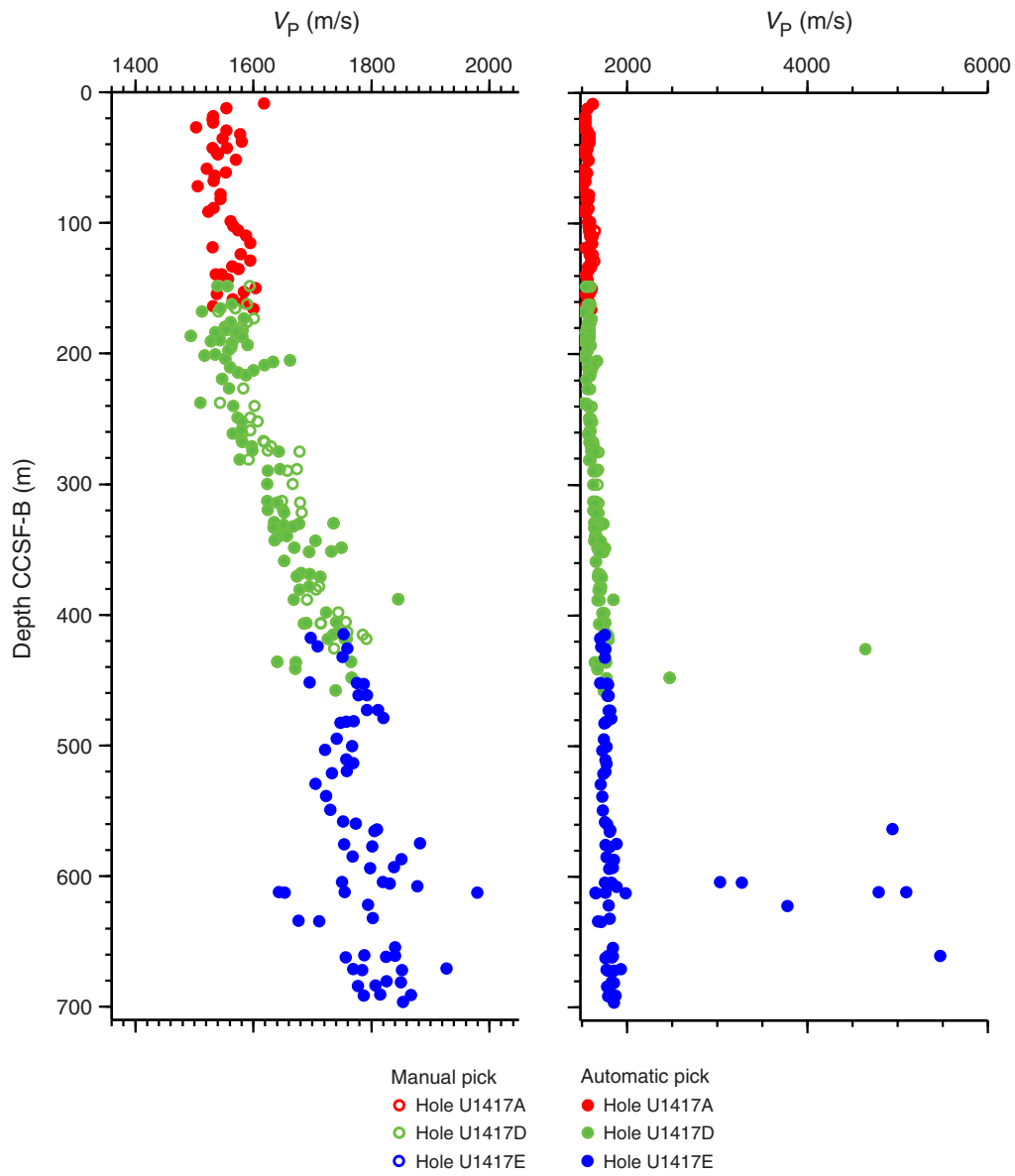


Figure F42. Whole-Round Multisensor Logger (WRMSL) gamma ray attenuation (GRA) bulk density compared to natural gamma radiation (NGR) data, Site U1417. Both data sets are shown after Gaussian smoothing with a 50 cm window ($\pm 3\sigma$) and interpolation to constant resolution at 10 cm. NGR is also shown corrected for variability in recovered sediment volume by normalizing to WRMSL GRA bulk density. Data in the upper 220 m CCSF-B reflect the stratigraphic composite splice (see “**Stratigraphic correlation**”); data from deeper than 220 m CCSF-B obtained from XCB and RCB cores in Holes U1417B, U1417D, and U1417E are combined to form a single composite section. In this lower portion, we use an average of all available data at depths for which there are overlaps in recovery.

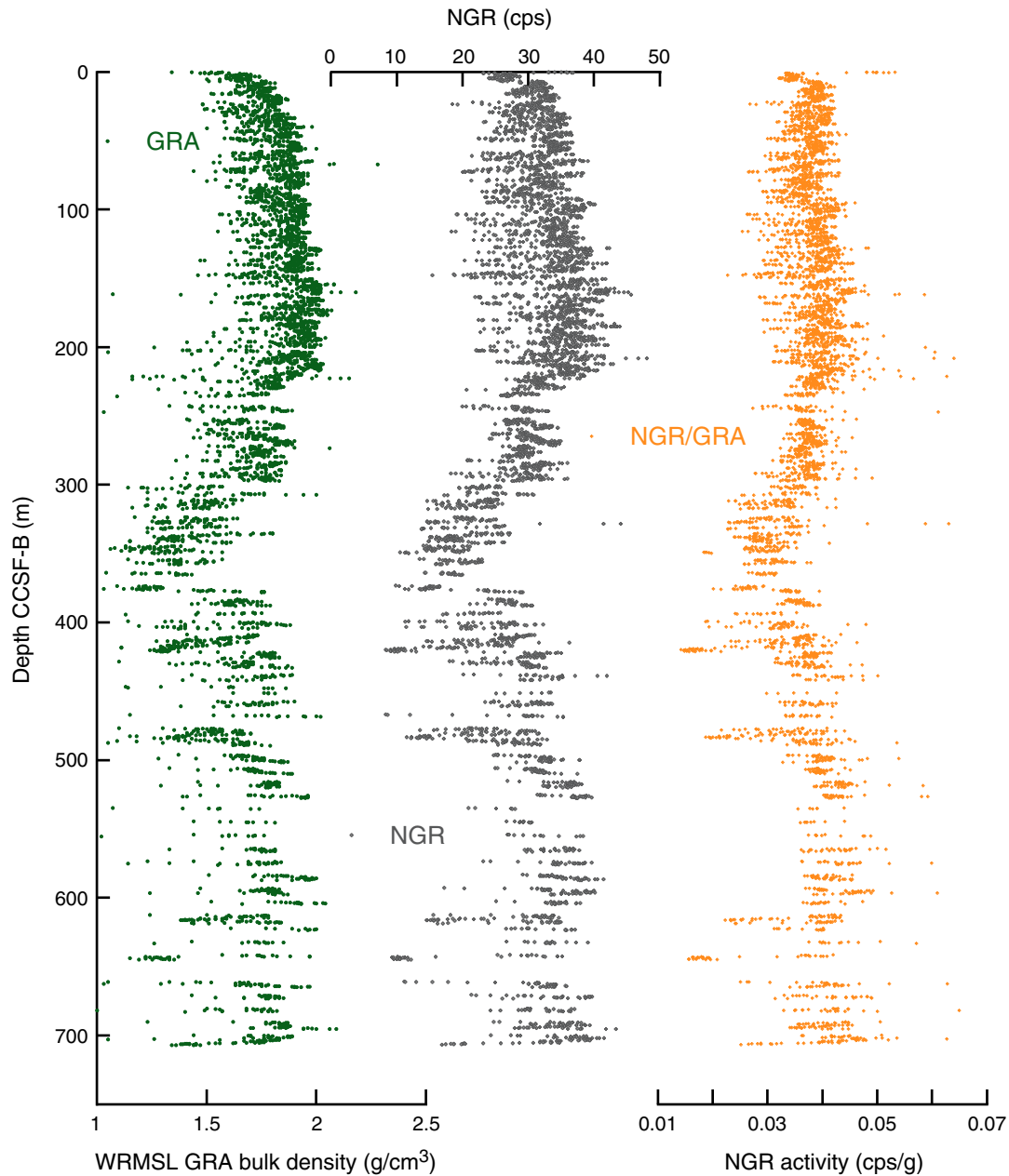


Figure F43. GRA bulk density data measured on the WRMSL (dots) vs. discrete wet bulk density data (circles), Holes U1417A, U1417D, and U1417E.

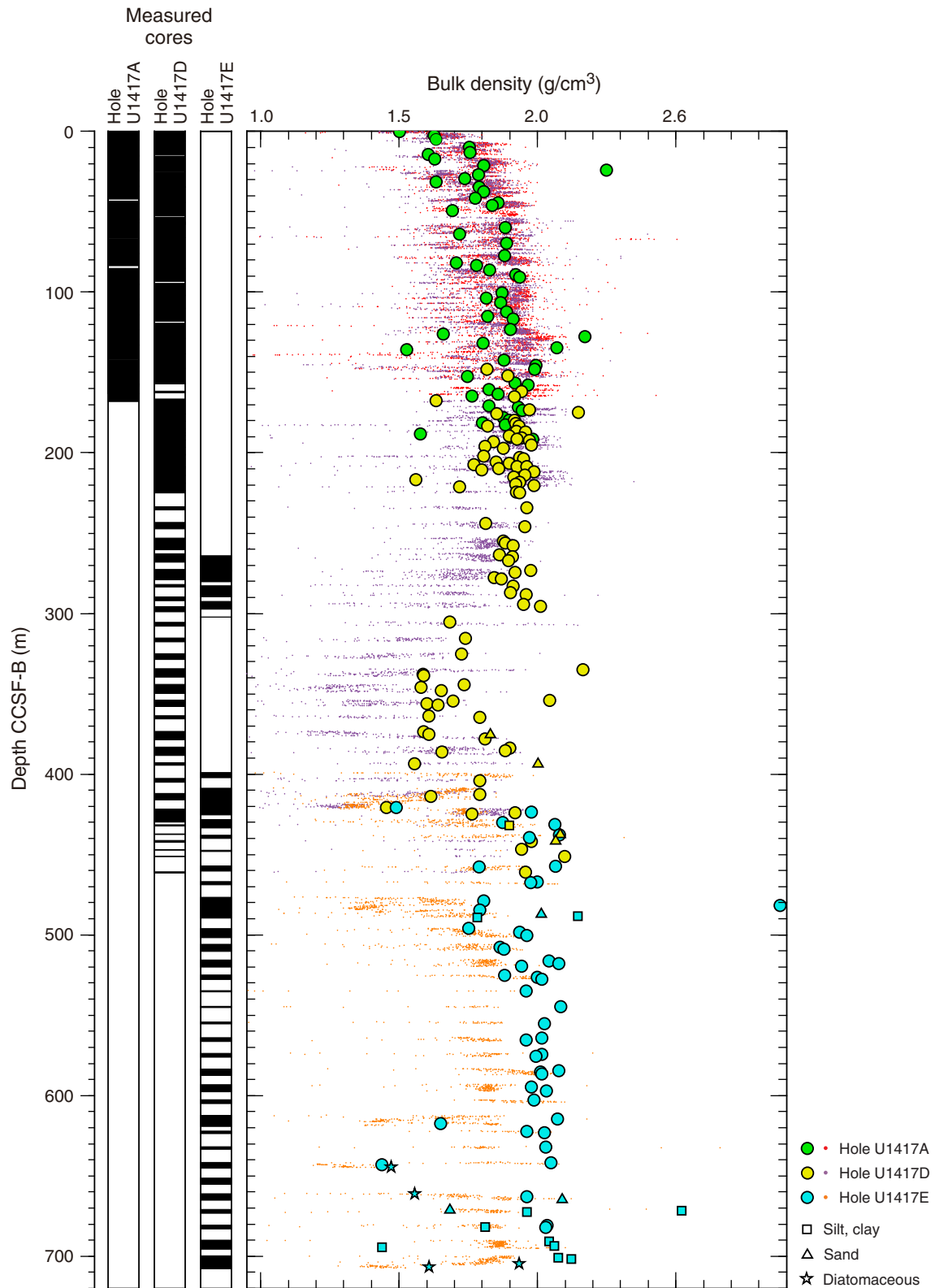




Figure F44. Bulk density, grain density, porosity, and void ratio measured using the moisture and density method, Holes U1417A, U1417D, and U1417E. Circles denote measurements without a denoted lithology, reflecting sampling of the major lithofacies (gray-green mud; see “**Lithostratigraphy**”).

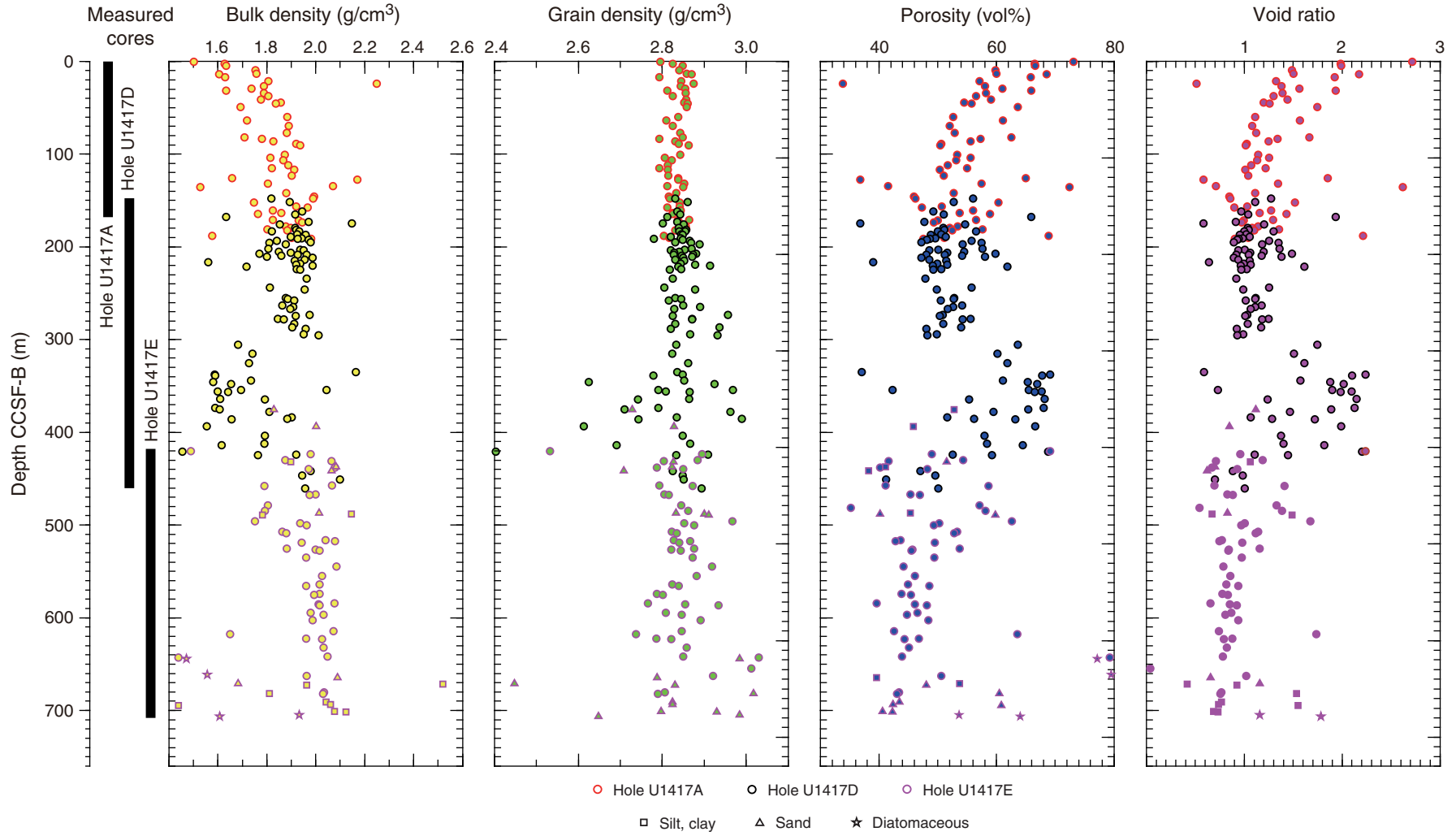


Figure F45. Shear strength values measured by the automatic vane shear system from Holes U1417A and U1417D.

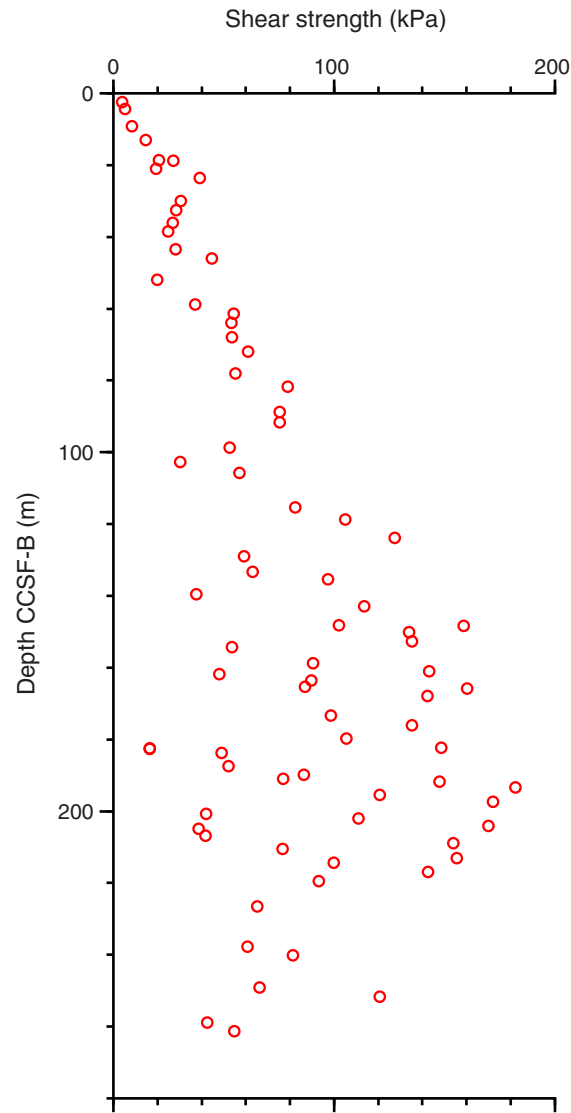




Figure F46. A. Temperature data from the advanced piston corer temperature tool, Cores 341-U1417-4H, 10H, and 13H. An exponential decrease in temperature is expected for the time interval shown and was used to estimate ambient temperature. Data for the time interval t_i to t_f (solid circles) were used to estimate asymptotic temperature. B. Resulting geothermal gradient ($61^\circ\text{C}/\text{km}$).

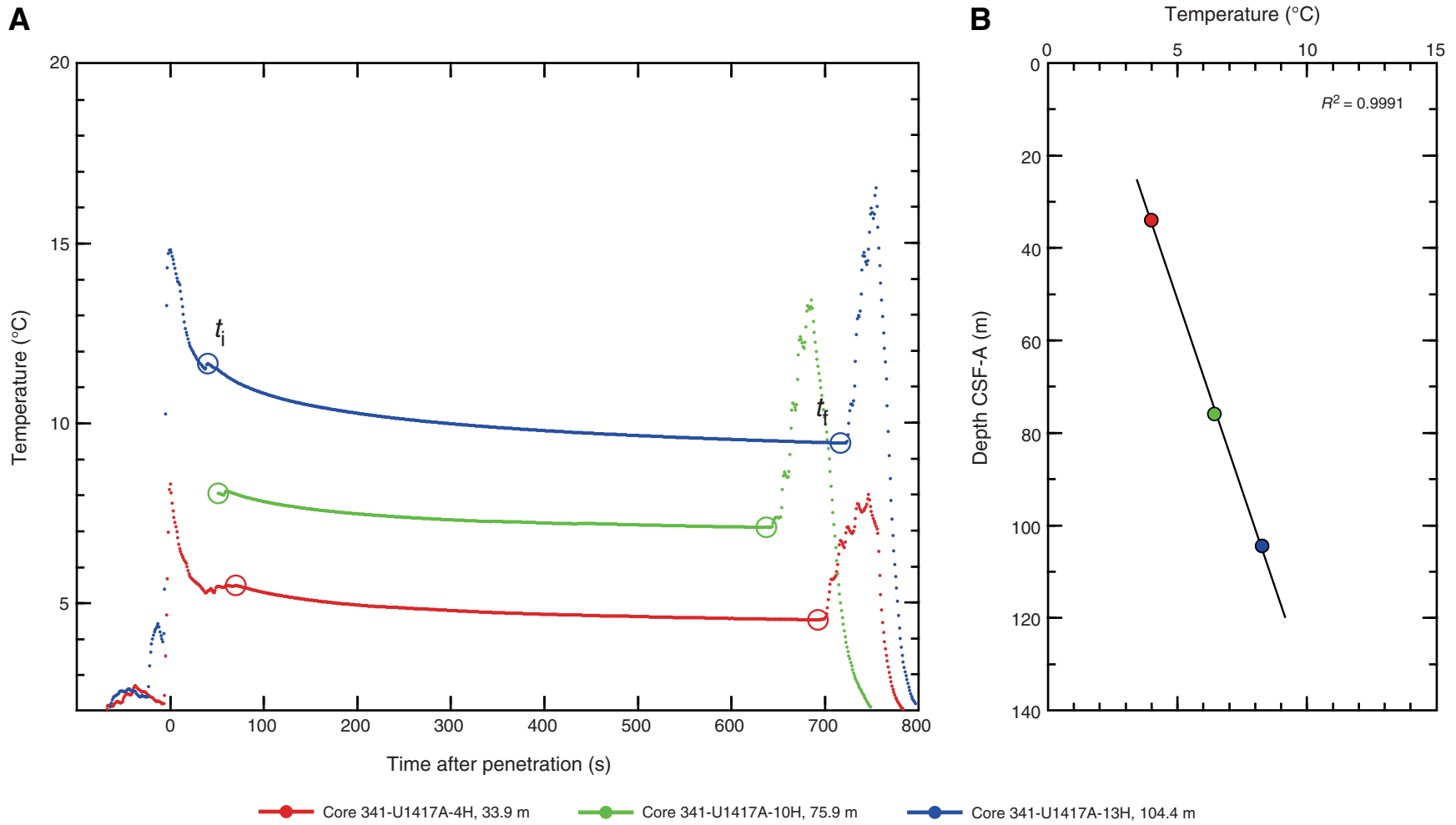




Figure F47. Natural remanent magnetization intensity measured before and after 10 and 20 mT peak alternating field demagnetization in the recovered APC interval, Site U1417. Polarity interpretation and correlation to the geomagnetic polarity timescale (GPTS) on the geological time-scale (Hilgen et al., 2012) is developed in the text (see “Paleomagnetism”) and in Figure F49.

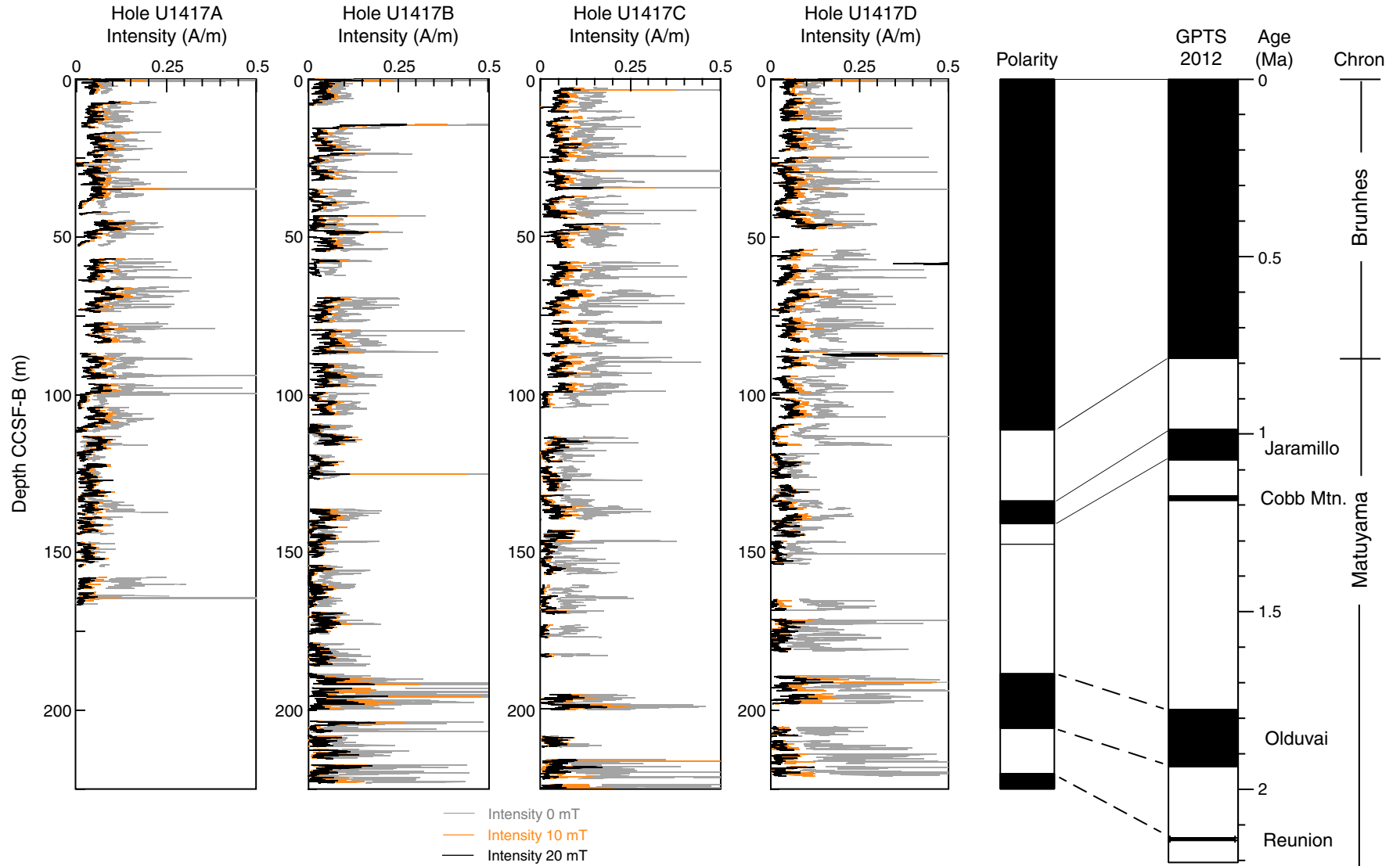




Figure F48. Natural remanent magnetization intensity plotted on a log scale before and after 20 mT peak alternating field demagnetization in recovered APC, XCB, and RCB intervals, Site U1417.

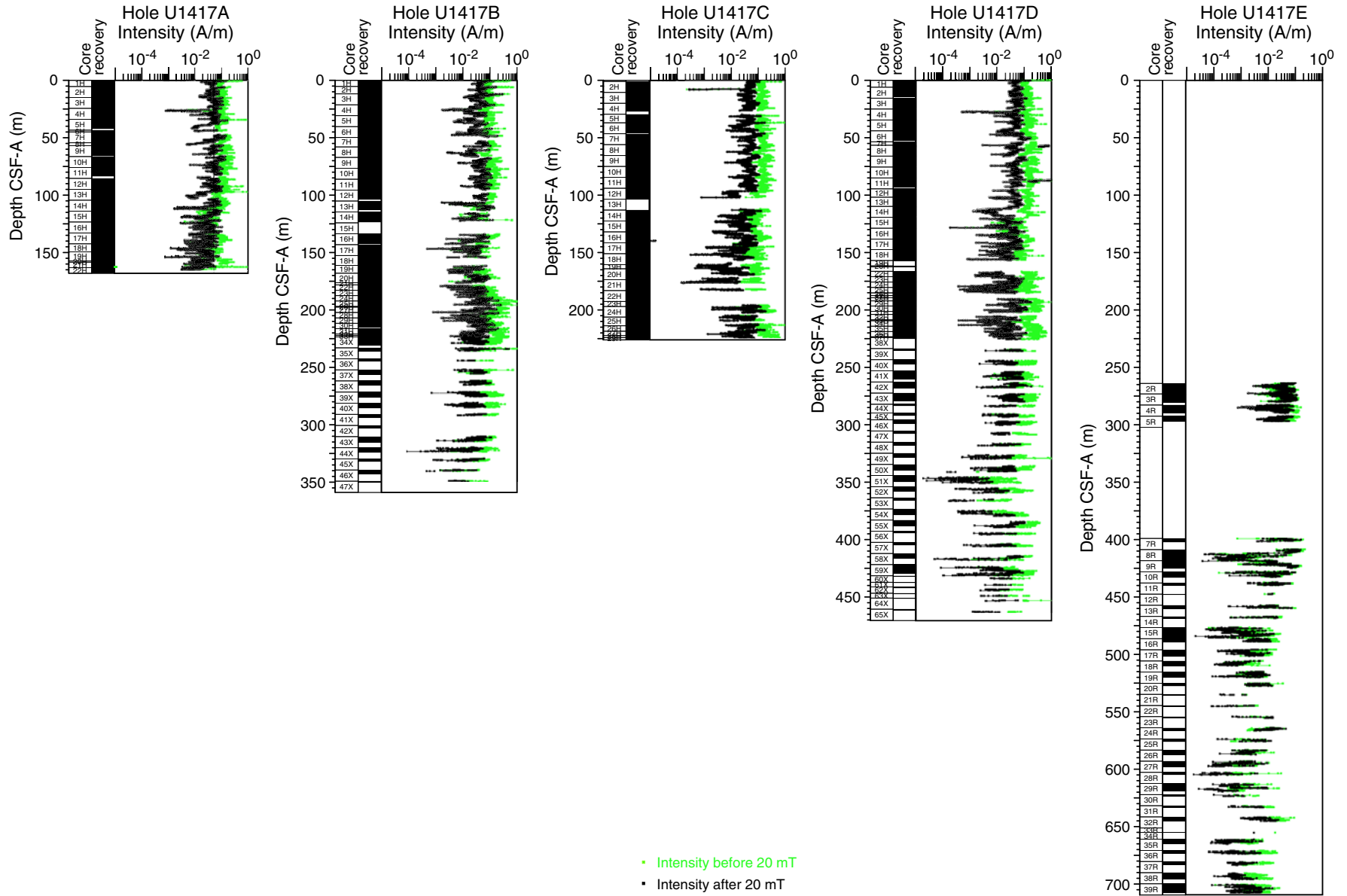




Figure F49. Inclination and polarity interpretations before and after peak alternating field demagnetization at 20 mT in recovered APC intervals, Site U1417. Polarity interpretation and correlation to the geomagnetic polarity timescale (GPTS) on the geological timescale (Hilgen et al., 2012) is shown and developed in the text (see “Paleomagnetism”).

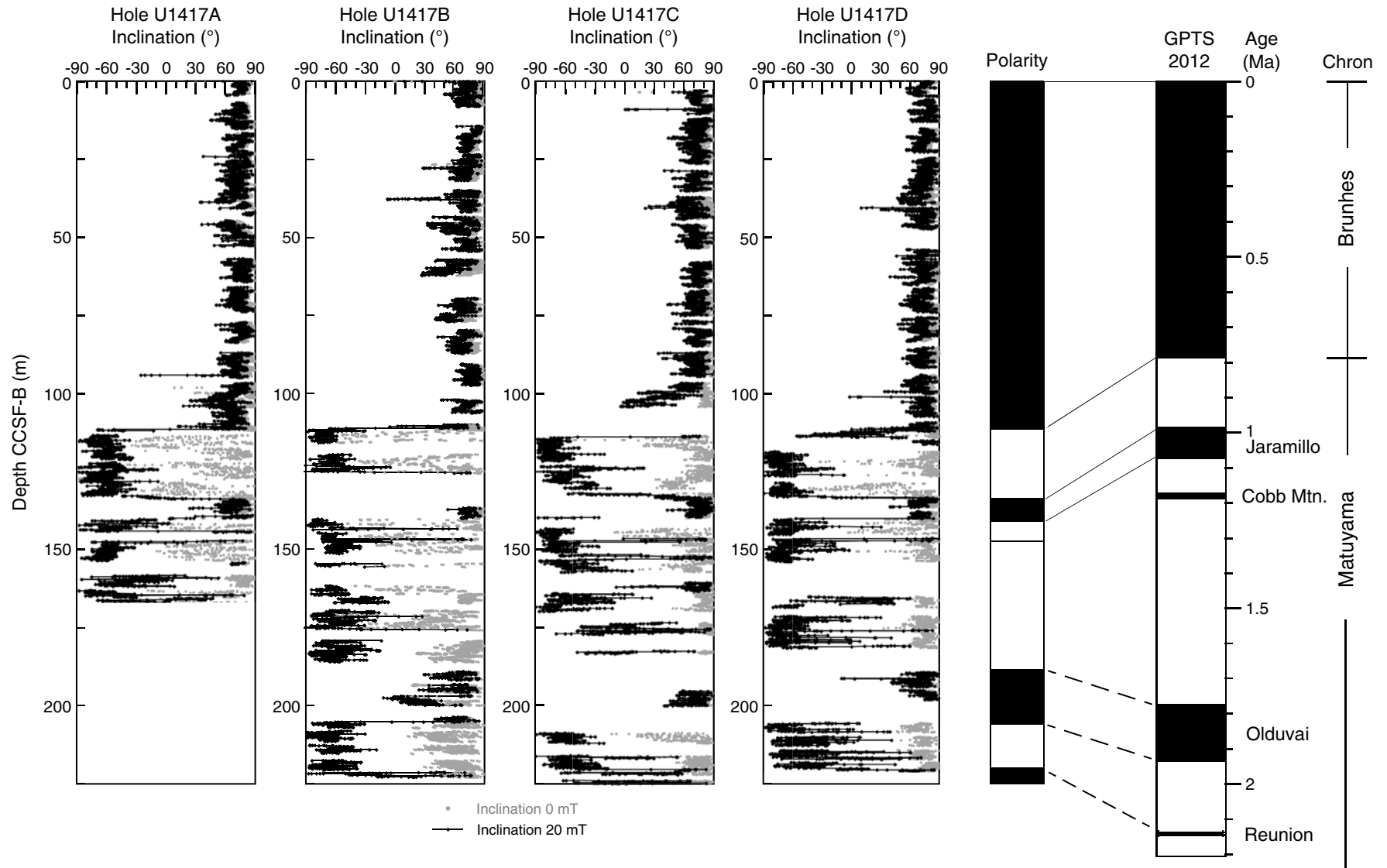


Figure F50. Inclination and polarity interpretations after peak alternating field demagnetization (20, 30, or 40 mT) in recovered XCB intervals of Holes U1417B and U1417D, and the recovered RCB interval of Hole U1417E. The smoothed line (50 cm running mean) is derived from expanded data that attempts to account for poor core recovery. See “Paleomagnetism” for explanation of expansion methodology. The geomagnetic polarity timescale (GPTS) on the geological timescale is shown for reference (Hilgen et al., 2012).

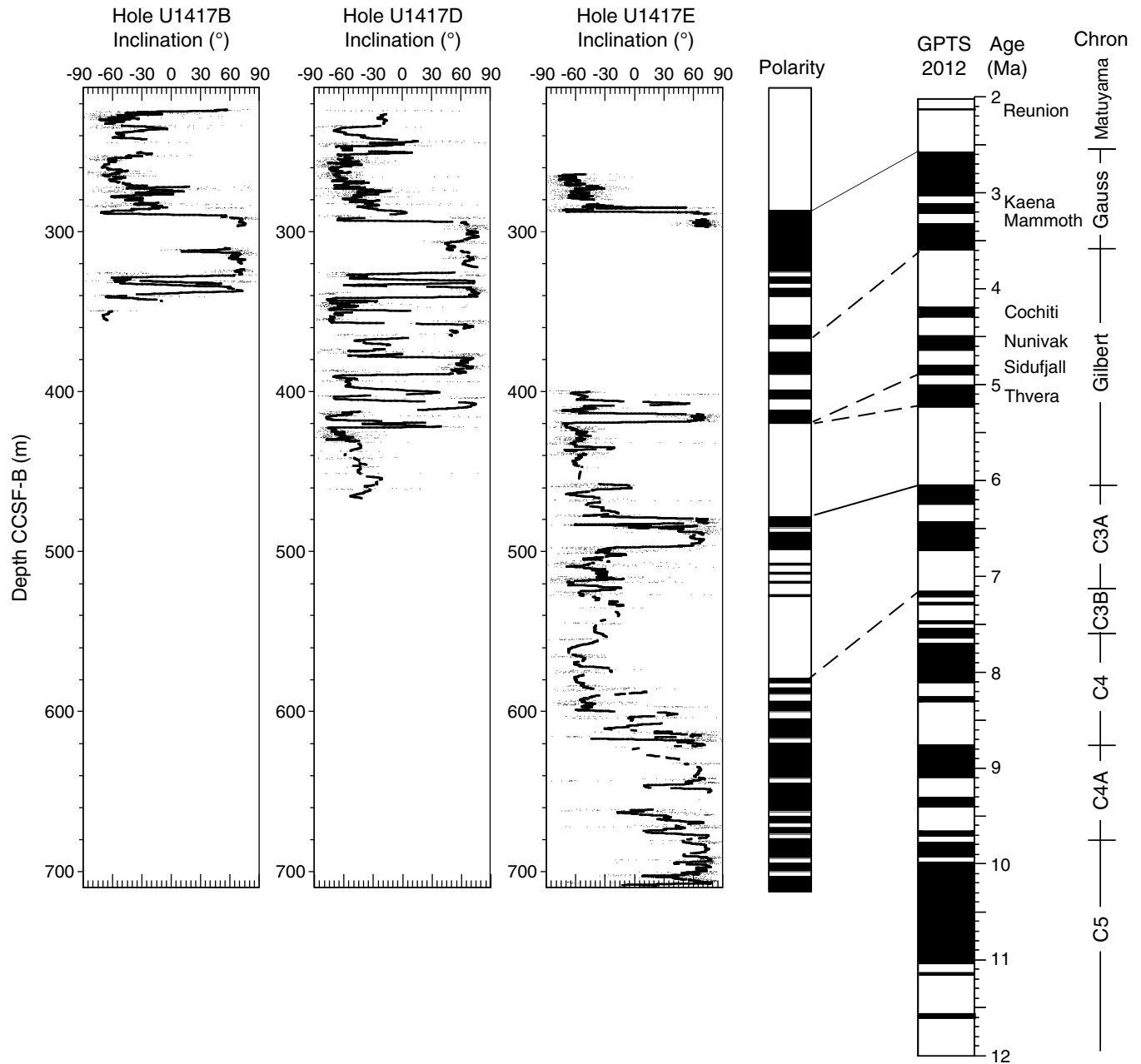


Figure F51. Logging operations summary diagram for Hole U1417E, showing wireline depths reached during different logging passes and borehole depths. See Table T6 in the “Methods” chapter (Jaeger et al., 2014) for definitions of depth scales. FMS = Formation MicroScanner, MSS = Magnetic Susceptibility Sonde. Star = depth of stations that yielded good first arrival times in vertical seismic profile (VSP).

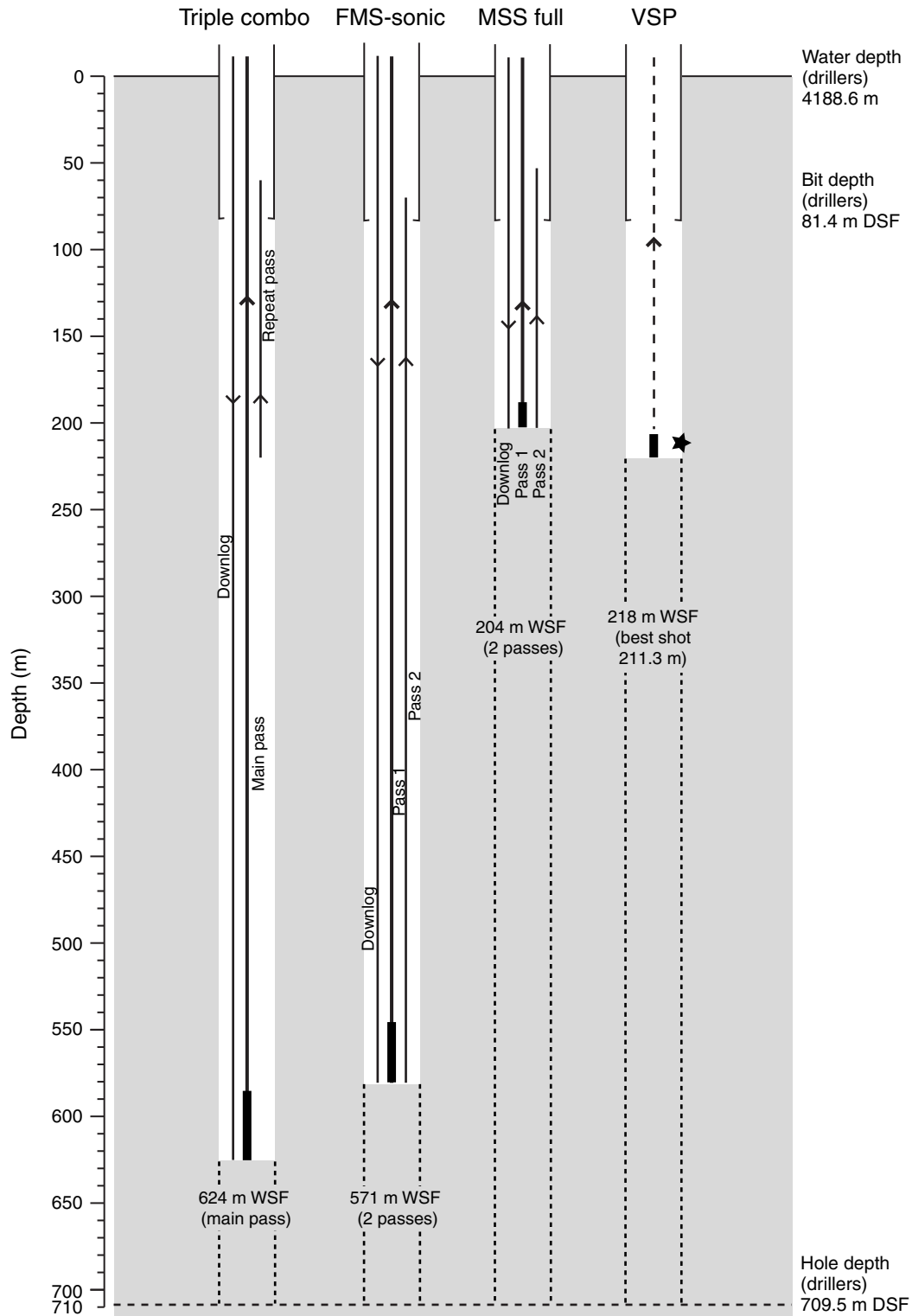


Figure F52. Summary of logs from the triple combo tool string and logging units, Hole U1417E. Core data are plotted in CSF-A: NGR = natural gamma radiation (gray = Hole U1417D, green = Hole U1417E), MAD = moisture and density (open symbols = Hole U1417D, solid symbols = Hole U1417E). Resistivity: R3 = medium resistivity reading of High-Resolution Laterolog Array, R5 = deepest resistivity, RT = true resistivity modeled from all depths.

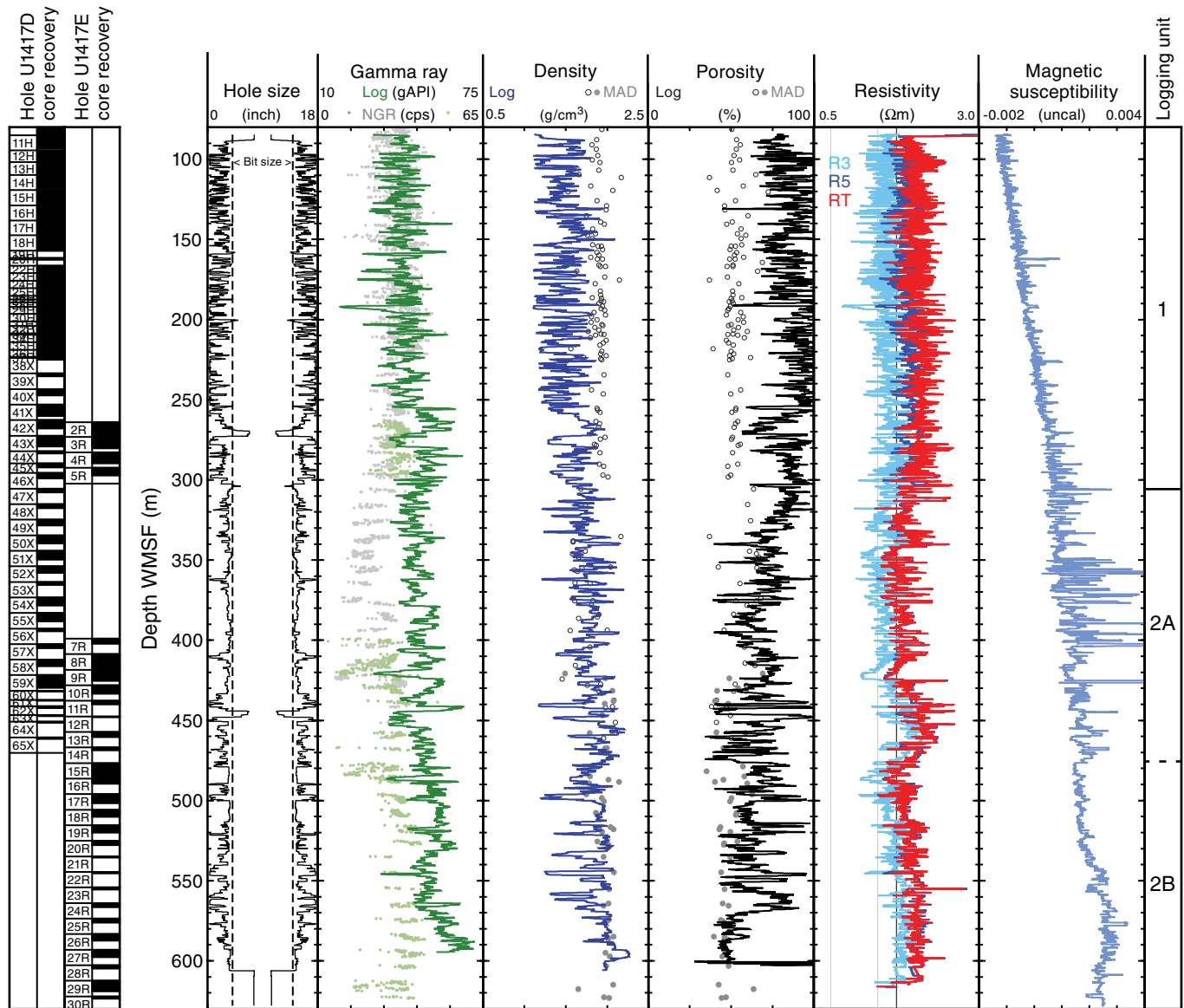


Figure F53. Summary of logs from Pass 2 of the Formation MicroScanner (FMS)-sonic tool string and logging units, Hole U1417E. Hole size is measured by the two orthogonal calipers of the FMS (C1 and C2). Waveform coherence in the velocity tracks is a measure of the reliability of the slowness/time coherence algorithm used to derive compressional (V_p) and shear (V_s) velocities from monopole and lower dipole sonic waveforms, respectively. Particularly below ~305 m WMSF, V_p shows similar trends to resistivity.

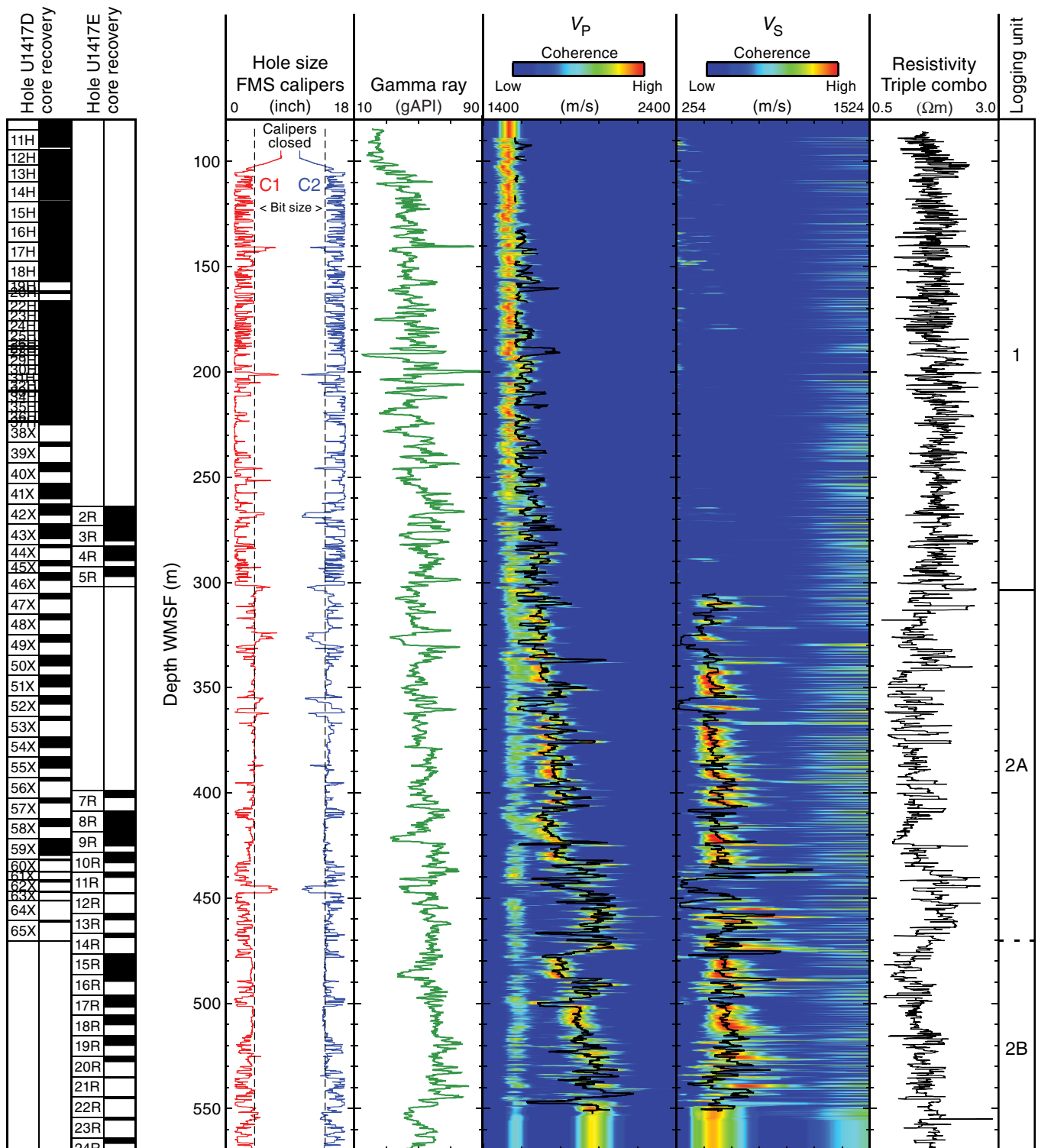


Figure F54. Summary of natural gamma ray logs, Hole U1417E. SGR = standard (total) gamma ray, CGR = computed gamma ray.

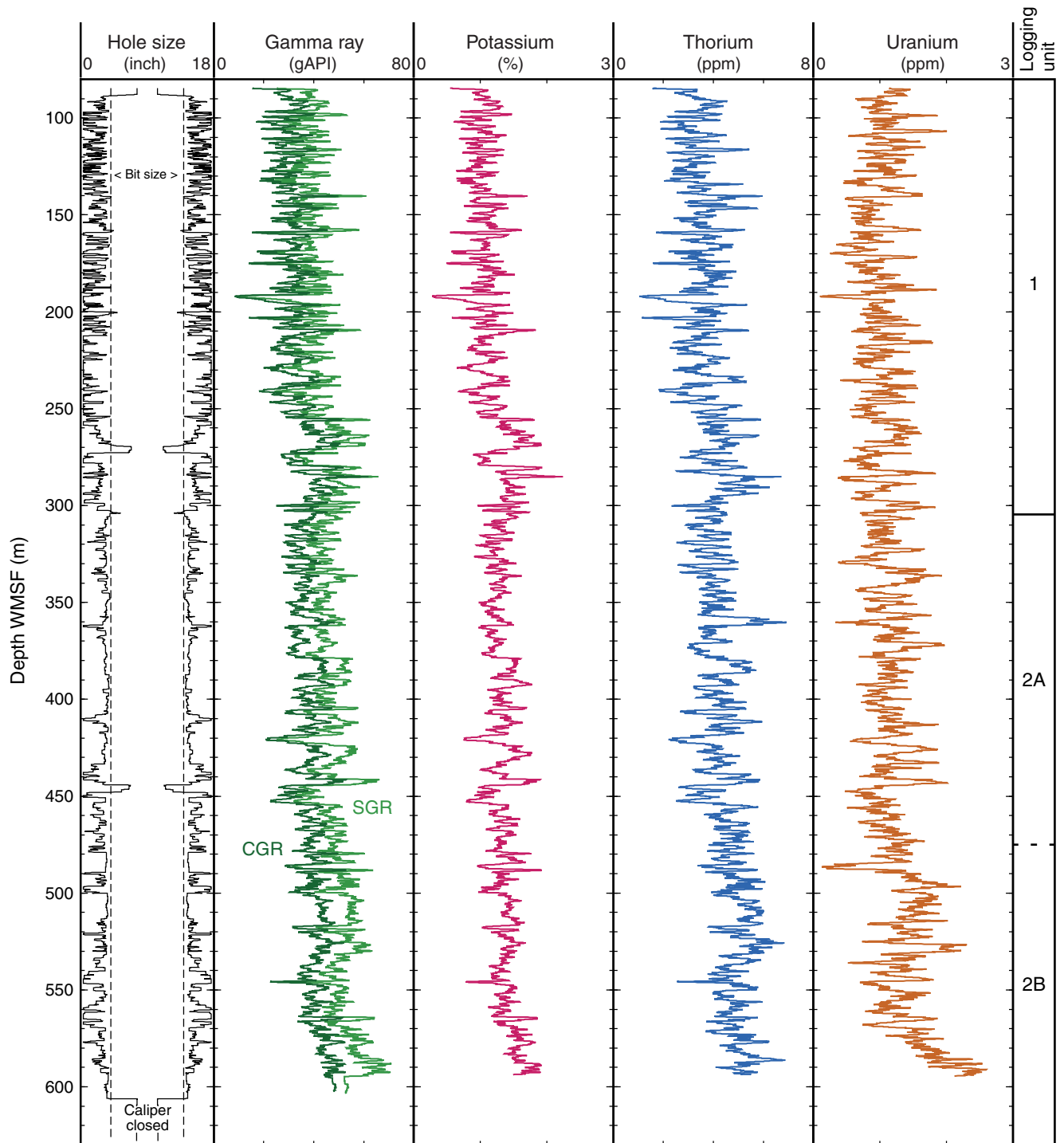


Figure F55. Summary of magnetic susceptibility logs recorded by the triple combo (TC) and Magnetic Susceptibility Sonde (MSS) tool string, Hole U1417E. Temperature-corrected (T-corrected) magnetic susceptibility shown for logging passes where tool temperature is linear. High-resolution magnetic susceptibility shows similar trends to natural gamma radiation (HSGR = total gamma radiation). Downlog = measurement made while tool is run from seafloor to the bottom of the hole. Pass 2 for MSS tool string = second pass of tool string from the bottom of the hole to the seafloor (Fig. F51).

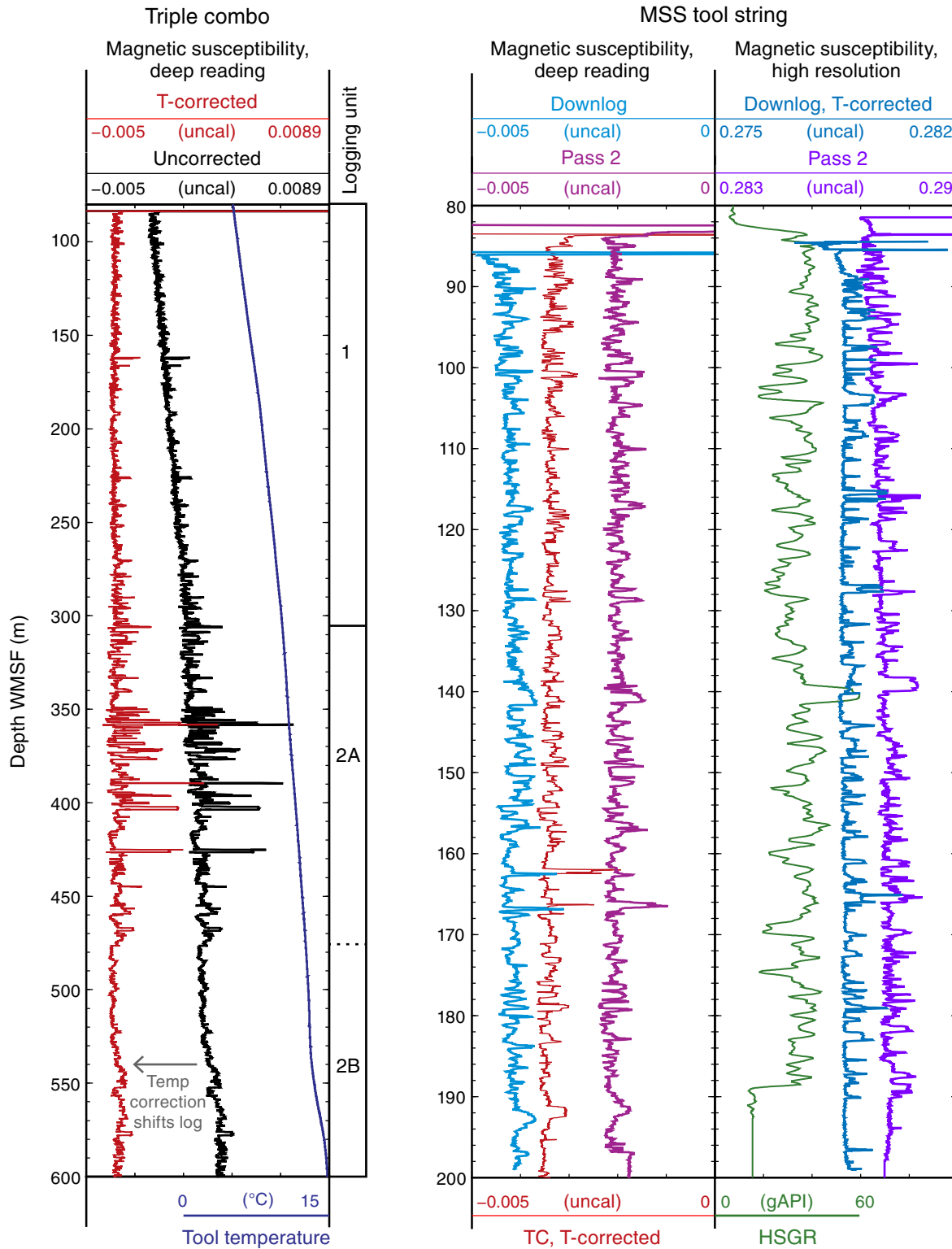


Figure F56. Examples of statically processed Formation MicroScanner (FMS) images from FMS-sonic Pass 1, Hole U1417E. Images show typical resistivity features and textures from (A) ~95 to 102 m WSSF in logging Unit 1, (B) ~305 to 312 m WSSF in logging Subunit 2A, and (C) ~510 to 516 m WSSF in logging Subunit 2B. See “Downhole logging” in the “Methods” chapter (Jaeger et al., 2014) for explanation of WSSF depth scale.

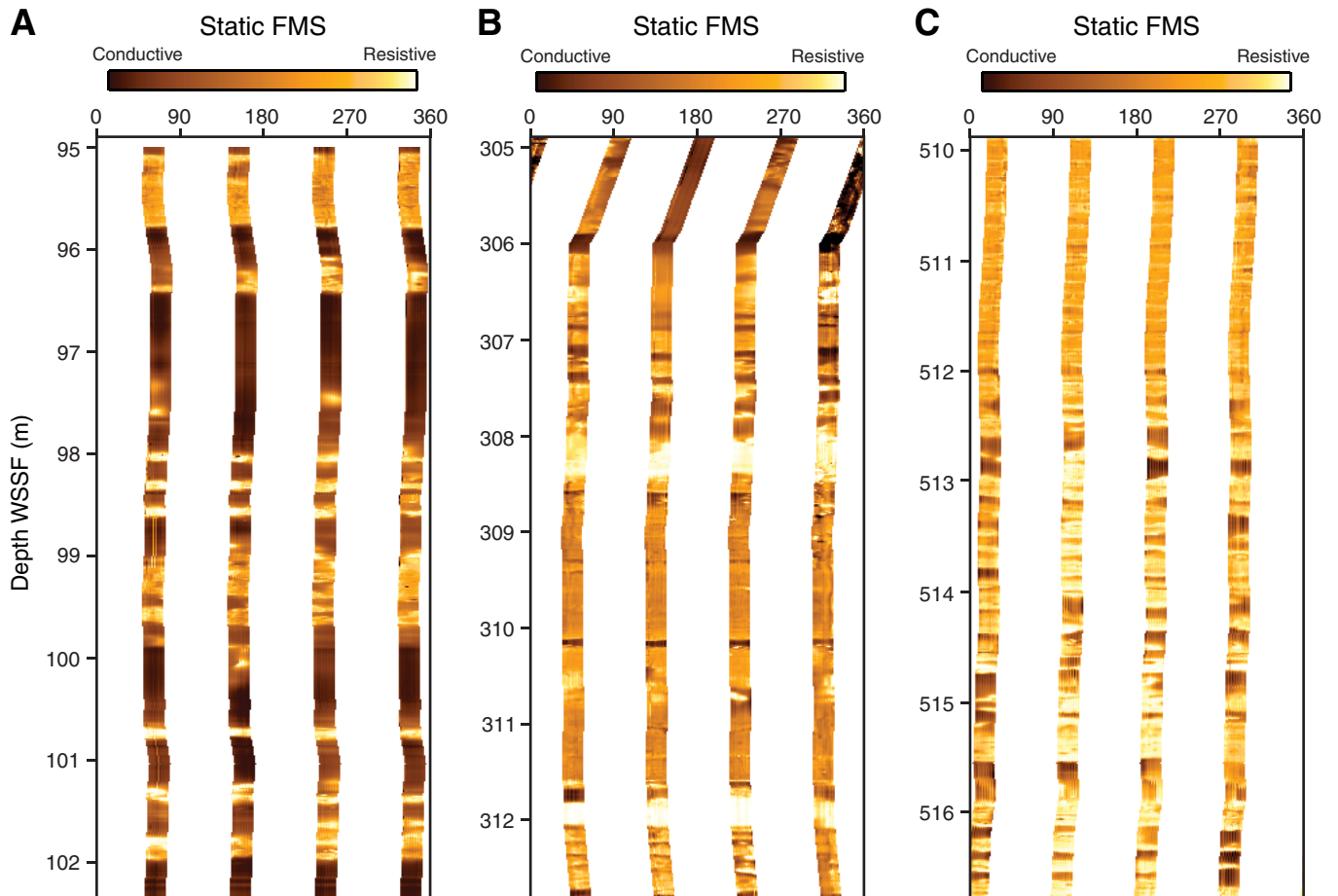


Figure F57. Vertical seismic profile waveforms and one-way arrival time picks (red stars) at two closely spaced stations, Hole U1417E.

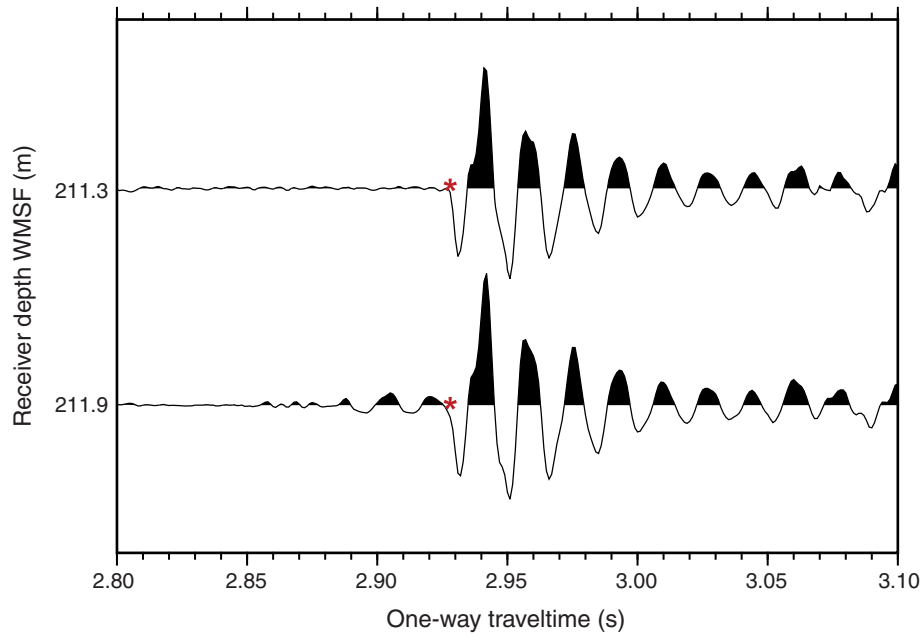




Figure F58. Comparison of core and logging magnetic susceptibility (MS), Site U1417. Diamict and sand are combined observations from Holes U1417A–U1417E, and logging data are from Hole U1417E. Green rectangle = interval of diamict interbedded with mud where MS is highest and most variable in logging data. Horizontal dashed lines = lithostratigraphic unit boundaries. Inset figure highlights correlation between diamict and high MS values in the core data. Red star = position of core image in overall stratigraphy. Overall, inset figure provides evidence for the diamict intervals causing high MS values in logging data. Up to ~10 m difference may exist when comparing the CCSF-B and WMSF depth scales. WRMSL = Whole-Round Multisensor Logger.

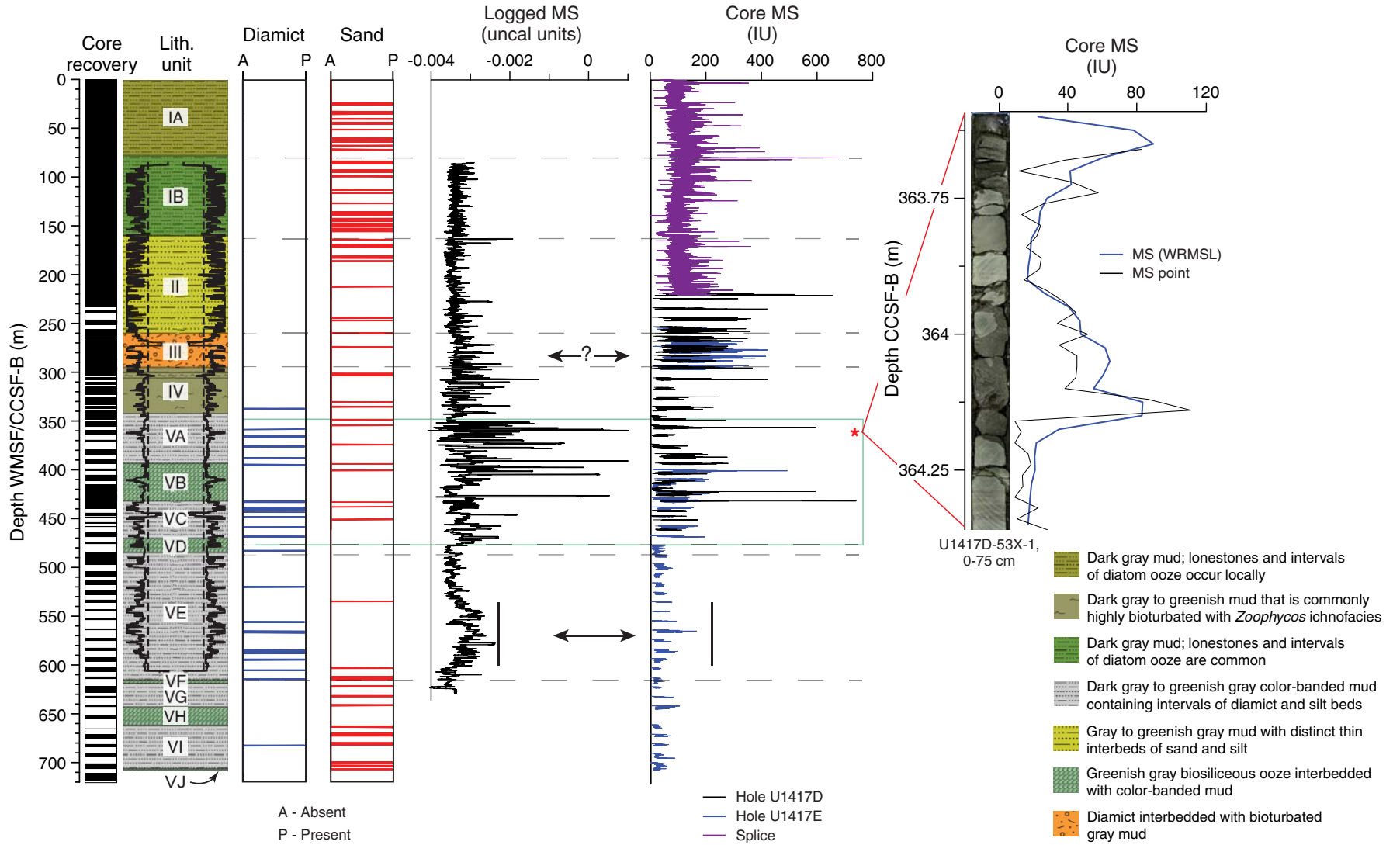




Figure F59. Comparison of core and logging natural gamma radiation, Site U1417. Sand, ash, and volcanoclastic sediment intervals are combined observations from Holes U1417A–U1417E. Green dashed line = correspondence between sand intervals and low gamma ray, gray dashed lines = correspondences between ash and higher K counts. Up to ~10 m difference may exist when comparing the CCSF-B and WMSF depth scales.

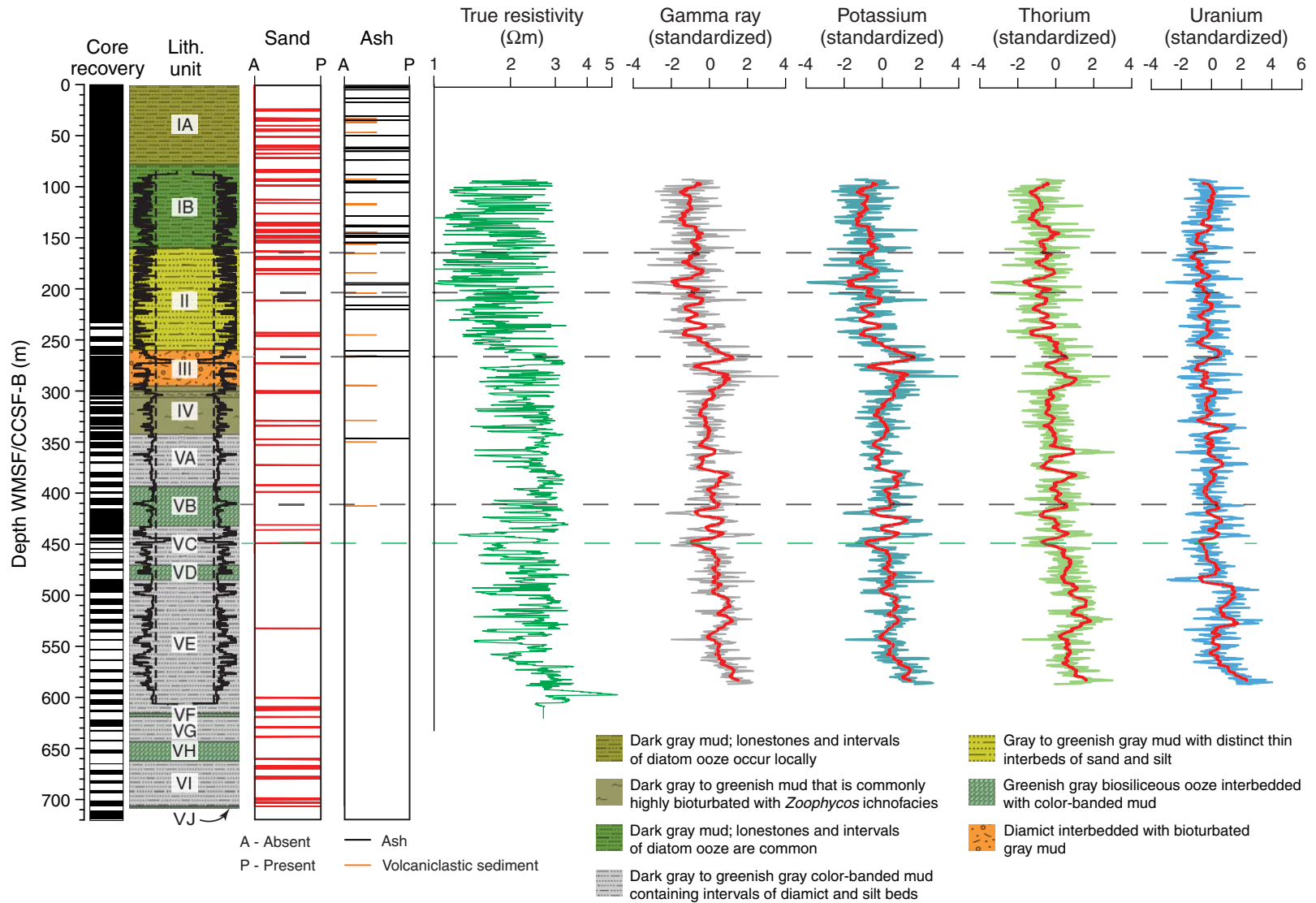


Figure F60. Comparison of core and logging physical properties, Site U1417. Downhole logging data are from Hole U1417E, within logging Unit 2 (see “Downhole logging”). Core natural gamma radiation (NGR) and magnetic susceptibility have been volume corrected (corr; see “Physical properties” 2014); magnetic susceptibility log has been temperature corrected (T-corr; see “Downhole logging”). MAD = moisture and density, GRA = gamma ray attenuation density. *P*-wave data: closed symbols = automatic velocity picks, open symbols = manual velocity picks. Dashed line = logging subunit boundary. Up to a 10 m error exists when comparing the WMSF and CCSF depth scales.

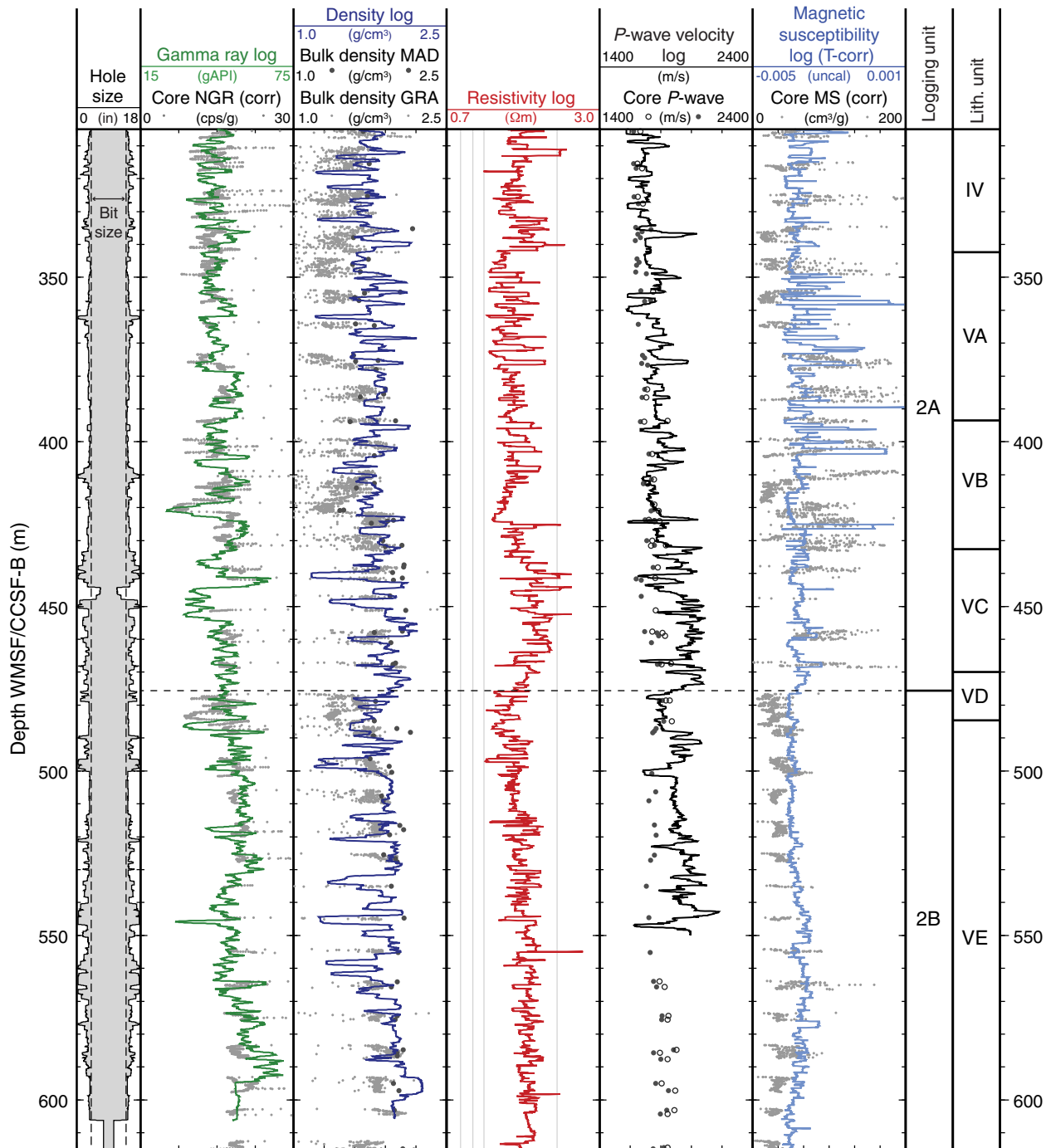




Figure F61. Seismic Line MGL1109MCS01 from 2011 USGS Law of the Sea survey aboard the R/V *Marcus Langseth*. Seismic Sequences I–III are interpreted after Reece et al. (2011) and demarcated by yellow horizons. Subsections of Sequence I (A–C) are demarcated by green horizons. Subsections of Sequence IA (1 and 2) are demarcated by a blue horizon. Subsections are interpreted based on dominant seismic character.

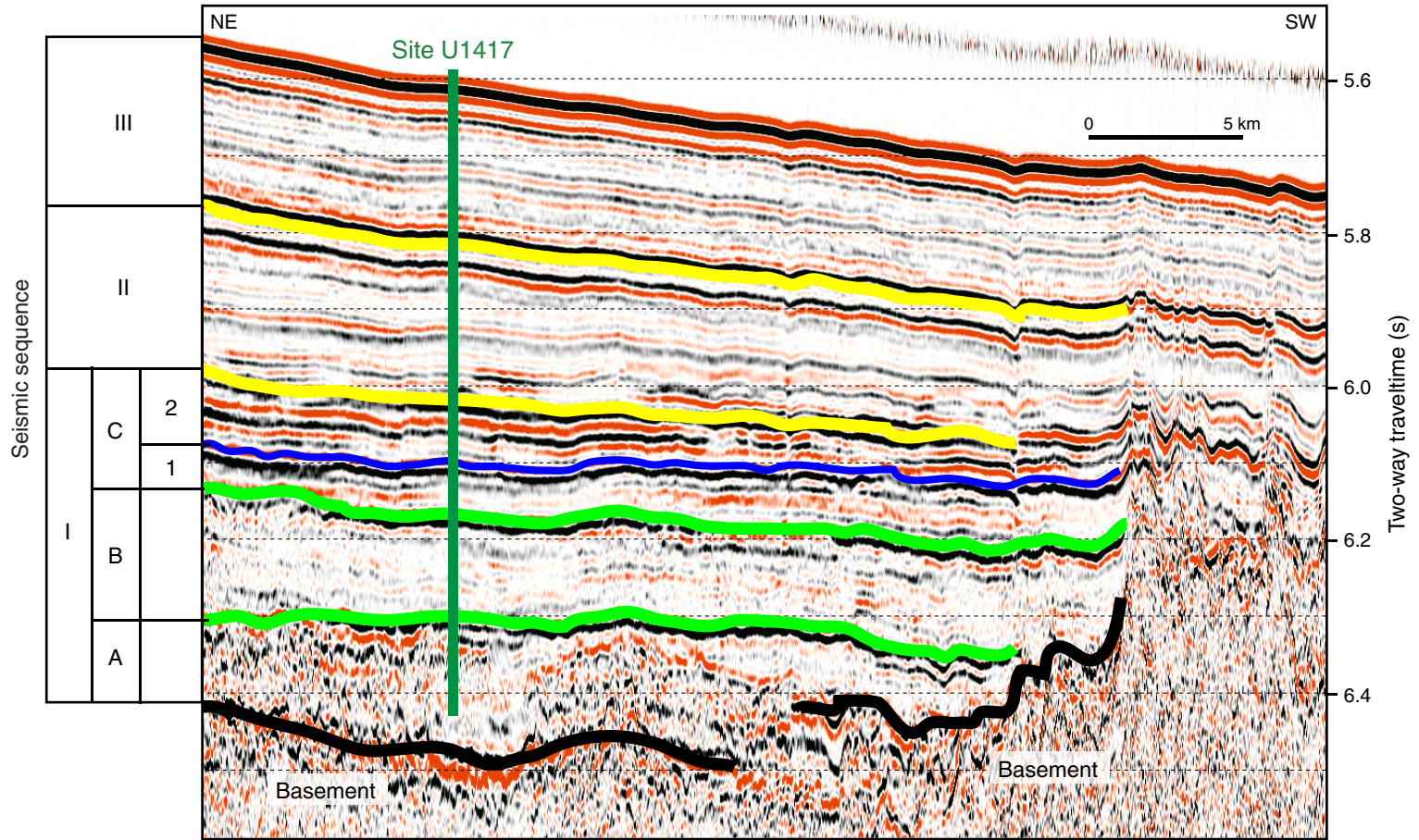


Figure F62. Seismic Line MGL1109MCS14 from 2011 USGS Law of the Sea survey aboard the R/V *Marcus Langseth*. Seismic Sequences I–III are interpreted after Reece et al. (2011) and demarcated by yellow horizons. Subsections of Sequence I (A–C) are demarcated by green horizons. Subsections of Sequence IC (IC1 and IC2) are demarcated by a blue horizon. Subsections are interpreted based on dominant seismic character.

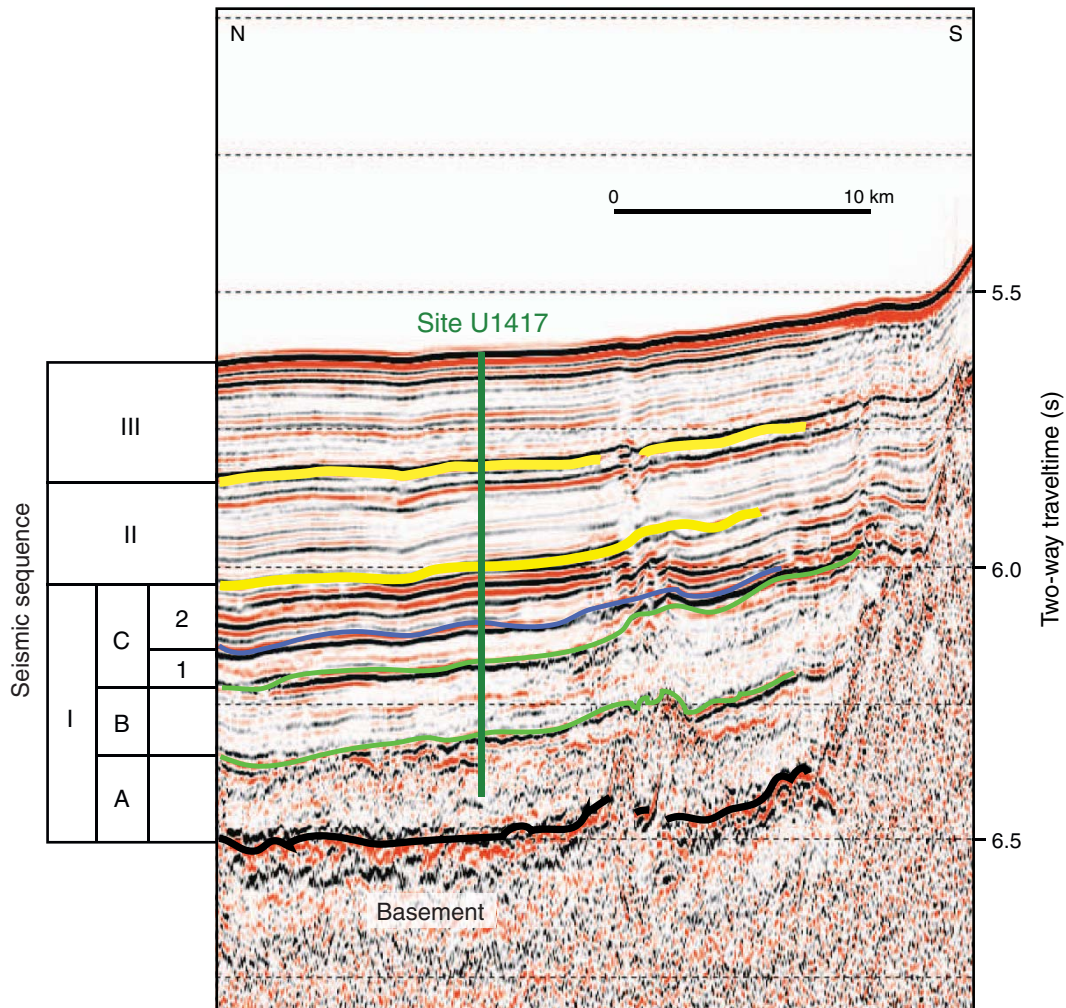


Table T1. Coring summary, Site U1417. (Continued on next four pages.)

Hole U1417A
 Latitude: 56°57.5996'N
 Longitude: 147°6.5985'W
 Time on hole (h): 46.5
 Seafloor (drill pipe measurement below rig floor, m DRF): 4198.6
 Distance between rig floor and sea level (m): 10.9
 Water depth (drill pipe measurement from sea level, mbsl): 4187.7
 Total penetration (drilling depth below seafloor, m DSF): 168.0
 Total length of cored section (m): 168.0
 Total core recovered (m): 167.74
 Core recovery (%): 99.8
 Total number of cores: 22

Hole U1417B
 Latitude: 56°57.5999'N
 Longitude: 147°6.5781'W
 Time on hole (h): 79.3
 Seafloor (drill pipe measurement below rig floor, m DRF): 4200.7
 Distance between rig floor and sea level (m): 10.9
 Water depth (drill pipe measurement from sea level, mbsl): 4189.8
 Total penetration (drilling depth below seafloor, m DSF): 358.8
 Total length of cored section (m): 358.8
 Total core recovered (m): 262.96
 Core recovery (%): 73.3
 Total number of cores: 47

Hole U1417C
 Latitude: 56°57.5888'N
 Longitude: 147°6.5769'W
 Time on hole (h): 38.8
 Seafloor (drill pipe measurement below rig floor, m DRF): 4199
 Distance between rig floor and sea level (m): 10.9
 Water depth (drill pipe measurement from sea level, mbsl): 4188.1
 Total penetration (drilling depth below seafloor, m DSF): 226
 Total length of cored section (m): 225
 Total core recovered (m): 216.83
 Core recovery (%): 96.4
 Total number of cores: 28

Hole U1417D
 Latitude: 56°57.5896'N
 Longitude: 147°6.5973'W
 Time on hole (h): 127.0
 Seafloor (drill pipe measurement below rig floor, m DRF): 4198
 Distance between rig floor and sea level (m): 10.9
 Water depth (drill pipe measurement from sea level, mbsl): 4187
 Total penetration (drilling depth below seafloor, m DSF): 470.3
 Total length of cored section (m): 466.5
 Total core recovered (m): 304.4
 Core recovery (%): 65.3
 Total number of cores: 64

Hole U1417E
 Latitude: 56°57.5896'N
 Longitude: 147°6.5993'W
 Time on hole (h): 155.3
 Seafloor (drill pipe measurement below rig floor, m DRF): 4199.5
 Distance between rig floor and sea level (m): 10.9
 Water depth (drill pipe measurement from sea level, mbsl): 4188.6
 Total penetration (drilling depth below seafloor, m DSF): 709.5
 Total length of cored section (m): 348.7
 Total core recovered (m): 146.9
 Core recovery (%): 42.1
 Total number of cores: 37

Core	Date (2013)	UTC time (h)	Depth DSF (m)			Depth CSF (m)		Length of core recovered (m)	Recovery (%)	Sections (N)	APC system
			Top of cored interval	Bottom of cored interval	Interval advanced (m)	Top of cored interval	Bottom of cored interval				
341-U1417A-											
1H	5 Jun	1140	0	5.4	5.4	0	5.48	5.48	101	5	Full
2H	5 Jun	1310	5.4	14.9	9.5	5.4	15.37	9.97	105	8	Full



Table T1 (continued). (Continued on next page.)

Core	Date (2013)	UTC time (h)	Depth DSF (m)			Depth CSF (m)		Length of core recovered (m)	Recovery (%)	Sections (N)	APC system
			Top of cored interval	Bottom of cored interval	Interval advanced (m)	Top of cored interval	Bottom of cored interval				
3H	5 Jun	1410	14.9	24.4	9.5	14.9	24.67	9.77	103	8	Full
4H	5 Jun	1530	24.4	33.9	9.5	24.4	34.58	10.18	107	8	Full
5H	5 Jun	1625	33.9	43.4	9.5	33.9	42.24	8.34	88	7	Full
6H	5 Jun	1720	43.4	44.9	1.5	43.4	44.9	1.5	100	2	Full
7H	5 Jun	1845	44.9	54.4	9.5	44.9	54.95	10.05	106	8	Full
8H	5 Jun	1945	54.4	56.9	2.5	54.4	56.91	2.51	100	3	Full
9H	5 Jun	2110	56.9	66.4	9.5	56.9	65.92	9.02	95	7	Full
10H	5 Jun	2245	66.4	75.9	9.5	66.4	76.13	9.73	102	8	Full
11H	5 Jun	2345	75.9	85.4	9.5	75.9	83.72	7.82	82	7	Full
12H	6 Jun	0045	85.4	94.9	9.5	85.4	95.18	9.78	103	8	Full
13H	6 Jun	0210	94.9	104.4	9.5	94.9	104.4	9.5	100	8	Full
14H	6 Jun	0305	104.4	113.9	9.5	104.4	113.95	9.55	101	8	Full
15H	6 Jun	0400	113.9	123.4	9.5	113.9	123.49	9.59	101	8	Full
16H	6 Jun	0500	123.4	132.9	9.5	123.4	133.16	9.76	103	8	Full
17H	6 Jun	0600	132.9	142.4	9.5	132.9	142.3	9.4	99	7	Full
18H	6 Jun	0715	142.4	149.4	7	142.4	149.42	7.02	100	7	Full
19H	6 Jun	1120	149.4	157.3	7.9	149.4	157.37	7.97	101	7	Full
20H	6 Jun	1245	157.3	158.4	1.1	157.3	158.45	1.15	105	2	Full
21H	6 Jun	1410	158.4	163.2	4.8	158.4	163.25	4.85	101	4	Half
22H	6 Jun	1530	163.2	168	4.8	163.2	168	4.8	100	4	Half
341-U1417B-											
1H	6 Jun	2050	0	5.3	5.3	0	5.33	5.33	101	5	Full
2H	6 Jun	2210	5.3	11.8	6.5	5.3	14.78	9.48	146	8	Full
3H	6 Jun	2330	11.8	21.3	9.5	11.8	21.47	9.67	102	8	Full
4H	7 Jun	0325	21.3	30.8	9.5	21.3	31.12	9.82	103	8	Full
5H	7 Jun	0525	30.8	40.3	9.5	30.8	40.73	9.93	105	8	Full
6H	7 Jun	0650	40.3	49.8	9.5	40.3	49.04	8.74	92	7	Full
7H	7 Jun	0805	49.8	58	8.2	49.8	58.07	8.27	101	7	Full
8H	7 Jun	1030	58	67.1	9.1	58	67.08	9.08	100	7	Full
9H	7 Jun	1150	67.1	76.6	9.5	67.1	76.3	9.2	97	7	Full
10H	7 Jun	1250	76.6	86.1	9.5	76.6	86.21	9.61	101	8	Full
11H	7 Jun	1350	86.1	95.6	9.5	86.1	94.95	8.85	93	7	Full
12H	7 Jun	1450	95.6	105.1	9.5	95.6	103.8	8.2	86	7	Full
13H	7 Jun	1550	105.1	114.6	9.5	105.1	112.9	7.8	82	7	Full
14H	7 Jun	1650	114.6	124.1	9.5	114.6	123.55	8.95	94	8	Full
15H	7 Jun	1745	124.1	133.6	9.5	124.1	124.1	0	0	0	Full
16H	7 Jun	1855	133.6	143.1	9.5	133.6	142.56	8.96	94	7	Full
17H	7 Jun	1940	143.1	152.6	9.5	143.1	151.87	8.77	92	8	Full
18H	7 Jun	2055	152.6	161.2	8.6	152.6	161.29	8.69	101	7	Full
19H	7 Jun	2235	161.2	168	6.8	161.2	168.01	6.81	100	6	Full
20H	8 Jun	0010	168	176.3	8.3	168	176.36	8.36	101	8	Full
21H	8 Jun	0245	176.3	178.1	1.8	176.3	178.19	1.89	105	2	Half
22H	8 Jun	0350	178.1	182.8	4.7	178.1	183.07	4.97	106	5	Half
23H	8 Jun	0455	182.8	187.5	4.7	182.8	187.73	4.93	105	5	Half
24H	8 Jun	0555	187.5	192.2	4.7	187.5	192.25	4.75	101	5	Half
25H	8 Jun	0650	192.2	196.9	4.7	192.2	196.32	4.12	88	4	Half
26H	8 Jun	0750	196.9	197.5	0.6	196.9	197.57	0.67	112	2	Half
27H	8 Jun	0905	197.5	202.2	4.7	197.5	202.56	5.06	108	5	Half
28H	8 Jun	1015	202.2	206.9	4.7	202.2	207.31	5.11	109	5	Half
29H	8 Jun	1115	206.9	211.6	4.7	206.9	211.8	4.9	104	5	Half
30H	8 Jun	1220	211.6	216.3	4.7	211.6	215.46	3.86	82	4	Half
31H	8 Jun	1310	216.3	221	4.7	216.3	221.03	4.73	101	4	Half
32H	8 Jun	1410	221	222.2	1.2	221	222.21	1.21	101	2	Half
33H	8 Jun	1515	222.2	223.4	1.2	222.2	223.45	1.25	104	2	Half
34X	8 Jun	1725	223.4	233	9.6	223.4	230.8	7.4	77	6	
35X	8 Jun	1850	233	242.6	9.6	233	235.88	2.88	30	3	
36X	8 Jun	2025	242.6	252.2	9.6	242.6	244.74	2.14	22	3	
37X	8 Jun	2245	252.2	261.8	9.6	252.2	256.19	3.99	42	4	
38X	9 Jun	0125	261.8	271.5	9.7	261.8	265.8	4	41	4	
39X	9 Jun	0355	271.5	281.2	9.7	271.5	276.32	4.82	50	4	
40X	9 Jun	0555	281.2	290.9	9.7	281.2	285.56	4.36	45	4	
41X	9 Jun	0755	290.9	300.6	9.7	290.9	293.82	2.92	30	3	
42X	9 Jun	1015	300.6	310.3	9.7	300.6	303.11	2.51	26	3	
43X	9 Jun	1210	310.3	320	9.7	310.3	315.19	4.89	50	4	
44X	9 Jun	1400	320	329.7	9.7	320	324.07	4.07	42	4	
45X	9 Jun	1555	329.7	339.4	9.7	329.7	332.17	2.47	25	3	
46X	9 Jun	1750	339.4	349.1	9.7	339.4	342.83	3.43	35	3	

Table T1 (continued). (Continued on next page.)

Core	Date (2013)	UTC time (h)	Depth DSF (m)		Interval advanced (m)	Depth CSF (m)		Length of core recovered (m)	Recovery (%)	Sections (N)	APC system
			Top of cored interval	Bottom of cored interval		Top of cored interval	Bottom of cored interval				
47X	9 Jun	1935	349.1	358.8	9.7	349.1	350.21	1.11	11	2	
341-U1417C-											
11	10 Jun				*****Drilled interval from 0 to 1 m DSF*****						
2H	10 Jun	0415	1	10.5	9.5	1	10.61	9.61	101	8	Full
3H	10 Jun	0525	10.5	20	9.5	10.5	20.32	9.82	103	8	Full
4H	10 Jun	0625	20	29.5	9.5	20	27.17	7.17	75	6	Full
5H	10 Jun	0735	29.5	37	7.5	29.5	38.44	8.94	119	7	Full
6H	10 Jun	0835	37	46.5	9.5	37	45.73	8.73	92	7	Full
7H	10 Jun	0950	46.5	56	9.5	46.5	56.18	9.68	102	8	Full
8H	10 Jun	1100	56	65.5	9.5	56	65.43	9.43	99	8	Full
9H	10 Jun	1200	65.5	75	9.5	65.5	75.13	9.63	101	7	Full
10H	10 Jun	1300	75	84.5	9.5	75	84.9	9.9	104	8	Full
11H	10 Jun	1420	84.5	94	9.5	84.5	94.07	9.57	101	8	Full
12H	10 Jun	1520	94	103.5	9.5	94	103.27	9.27	98	8	Full
13H	10 Jun	1625	103.5	113	9.5	103.5	103.55	0.05	1	1	Full
14H	10 Jun	1730	113	122.5	9.5	113	122.66	9.66	102	8	Full
15H	10 Jun	1855	122.5	132	9.5	122.5	132.32	9.82	103	8	Full
16H	10 Jun	2025	132	141.5	9.5	132	141.59	9.59	101	7	Full
17H	10 Jun	2130	141.5	151	9.5	141.5	151.26	9.76	103	8	Full
18H	10 Jun	2255	151	160.5	9.5	151	161.01	10.01	105	8	Full
19H	11 Jun	0005	160.5	164.1	3.6	160.5	164.17	3.67	102	4	Full
20H	11 Jun	0120	164.1	173.6	9.5	164.1	173.93	9.83	103	8	Full
21H	11 Jun	0245	173.6	183.1	9.5	173.6	183.29	9.69	102	8	Full
22H	11 Jun	0355	183.1	192.6	9.5	183.1	192.6	9.5	100	8	Full
23H	11 Jun	0500	192.6	197	4.4	192.6	197.06	4.46	101	4	Full
24H	11 Jun	0610	197	206.2	9.2	197	206.23	9.23	100	7	Full
25H	11 Jun	0735	206.2	213.8	7.6	206.2	213.8	7.6	100	7	Full
26H	11 Jun	0930	213.8	218.5	4.7	213.8	218.43	4.63	99	4	Half
27H	11 Jun	1110	218.5	222.2	3.7	218.5	222.23	3.73	101	3	Half
28H	11 Jun	1220	222.2	223.9	1.7	222.2	223.95	1.75	103	3	Half
29H	11 Jun	1330	223.9	226	2.1	223.9	226	2.1	100	3	Half
341-U1417D-											
1H	11 Jun	2020	0	6	6	0	6.05	6.05	101	5	Full
2H	11 Jun	2125	6	15.5	9.5	6	14.51	8.51	90	7	Full
3H	11 Jun	2220	15.5	25	9.5	15.5	24.56	9.06	95	8	Full
4H	11 Jun	2345	25	34.5	9.5	25	34.83	9.83	103	8	Full
5H	12 Jun	0045	34.5	44	9.5	34.5	44.2	9.7	102	8	Full
6H	12 Jun	0140	44	53.5	9.5	44	52.59	8.59	90	7	Full
7H	12 Jun	0300	53.5	56.5	3	53.5	58.1	4.6	153	4	Full
8H	12 Jun	0425	56.5	66	9.5	56.5	66.1	9.6	101	8	Full
9H	12 Jun	0515	66	75.5	9.5	66	75.16	9.16	96	8	Full
10H	12 Jun	0610	75.5	85	9.5	75.5	85.05	9.55	101	8	Full
11H	12 Jun	0730	85	94.5	9.5	85	93.24	8.24	87	7	Full
12H	12 Jun	0900	94.5	101.8	7.3	94.5	101.86	7.36	101	6	Full
13H	12 Jun	1030	101.8	109.8	8	101.8	110.06	8.26	103	7	Full
14H	12 Jun	1205	109.8	119.3	9.5	109.8	118.3	8.5	89	7	Full
15H	12 Jun	1300	119.3	128.8	9.5	119.3	128.88	9.82	103	7	Full
16H	12 Jun	1400	128.8	138.3	9.5	128.8	138.28	9.48	100	8	Full
17H	12 Jun	1500	138.3	147.4	9.1	138.3	147.42	9.12	100	7	Full
18H	12 Jun	1555	147.4	156.9	9.5	147.4	156.96	9.56	101	7	Full
19H	12 Jun	1710	156.9	161.6	4.7	156.9	157.08	0.18	4	1	Half
20H	12 Jun	1805	161.6	162.5	0.9	161.6	162.54	0.94	104	2	Half
21H	12 Jun				*****Drilled interval from 162.5 to 166.3 m DSF*****						
22H	12 Jun	1930	166.3	171	4.7	166.3	170.66	4.36	93	4	Half
23H	12 Jun	2035	171	175.7	4.7	171	176.01	5.01	107	5	Half
24H	12 Jun	2125	175.7	180.4	4.7	175.7	180.45	4.75	101	4	Half
25H	12 Jun	2220	180.4	185.1	4.7	180.4	185.38	4.98	106	5	Half
26H	12 Jun	2315	185.1	187.5	2.4	185.1	187.54	2.44	102	3	Half
27H	13 Jun	0025	187.5	189.3	1.8	187.5	189.32	1.82	101	3	Half
28H	13 Jun	0140	189.3	192.1	2.8	189.3	192.15	2.85	102	3	Half
29H	13 Jun	0255	192.1	196.5	4.4	192.1	196.59	4.49	102	4	Half
30H	13 Jun	0520	196.5	201.2	4.7	196.5	201.29	4.79	102	4	Half
31H	13 Jun	0730	201.2	203.9	2.7	201.2	203.9	2.7	100	3	Half
32H	13 Jun	0850	203.9	208.6	4.7	203.9	208.92	5.02	107	5	Half
33H	13 Jun	0950	208.6	209.4	0.8	208.6	209.42	0.82	102	2	Half
34H	13 Jun	1125	209.4	214.1	4.7	209.4	214.07	4.67	99	4	Half

Table T1 (continued). (Continued on next page.)

Core	Date (2013)	UTC time (h)	Depth DSF (m)			Depth CSF (m)		Length of core recovered (m)	Recovery (%)	Sections (N)	APC system
			Top of cored interval	Bottom of cored interval	Interval advanced (m)	Top of cored interval	Bottom of cored interval				
35H	13 Jun	1255	214.1	218.8	4.7	214.1	218.77	4.67	99	4	Half
36H	13 Jun	1430	218.8	223.3	4.5	218.8	223.37	4.57	102	4	Half
37H	13 Jun	1540	223.3	223.9	0.6	223.3	223.89	0.59	98	2	Half
38X	13 Jun	1825	223.9	233.6	9.7	223.9	225.09	1.19	12	2	
39X	13 Jun	2015	233.6	243.3	9.7	233.6	235.37	1.77	18	2	
40X	13 Jun	2325	243.3	253	9.7	243.3	247.33	4.03	42	4	
41X	14 Jun	0135	253	262.7	9.7	253	260.21	7.21	74	6	
42X	14 Jun	0415	262.7	272.4	9.7	262.7	267.96	5.26	54	5	
43X	14 Jun	0645	272.4	282.1	9.7	272.4	279.19	6.79	70	6	
44X	14 Jun	0940	282.1	289.7	7.6	282.1	283.5	1.4	18	2	
45X	14 Jun	1140	289.7	295.7	6	289.7	292.2	2.5	42	3	
46X	14 Jun	1335	295.7	305.4	9.7	295.7	299.13	3.43	35	4	
47X	14 Jun	1600	305.4	315.1	9.7	305.4	307.86	2.46	25	4	
48X	14 Jun	1815	315.1	324.8	9.7	315.1	317.76	2.66	27	3	
49X	14 Jun	2005	324.8	334.5	9.7	324.8	328.44	3.64	38	4	
50X	14 Jun	2205	334.5	344.2	9.7	334.5	339.62	5.12	53	5	
51X	14 Jun	2350	344.2	353.9	9.7	344.2	349.66	5.46	56	5	
52X	15 Jun	0145	353.9	363.6	9.7	353.9	357.91	4.01	41	4	
53X	15 Jun	0330	363.6	373.3	9.7	363.6	365.6	2	21	3	
54X	15 Jun	0555	373.3	383	9.7	373.3	378.47	5.17	53	5	
55X	15 Jun	0815	383	392.7	9.7	383	388.19	5.19	54	5	
56X	15 Jun	1100	392.7	402.4	9.7	392.7	394.46	1.76	18	2	
57X	15 Jun	1355	402.4	412.1	9.7	402.4	404.9	2.5	26	3	
58X	15 Jun	1700	412.1	421.8	9.7	412.1	416.12	4.02	41	4	
59X	15 Jun	1920	421.8	431.5	9.7	421.8	429.7	7.9	81	7	
60X	15 Jun	2210	431.5	437.2	5.7	431.5	432.11	0.61	11	2	
61X	16 Jun	0045	437.2	441.2	4	437.2	437.7	0.5	12	2	
62X	16 Jun	0415	441.2	446.7	5.5	441.2	442.33	1.13	21	2	
63X	16 Jun	0615	446.7	450.9	4.2	446.7	447.33	0.63	15	2	
64X	16 Jun	0835	450.9	460.6	9.7	450.9	451.48	0.58	6	2	
65X	16 Jun	1100	460.6	470.3	9.7	460.6	461.46	0.86	9	2	
341-U1417E-											
11	17 Jun					*****Drilled interval from 0 to 264 m DSF*****					
2R	17 Jun	2125	264	273.1	9.1	264	273.74	9.74	107	8	
3R	17 Jun	2325	273.1	282.8	9.7	273.1	280.37	7.27	75	6	
4R	18 Jun	0110	282.8	292.5	9.7	282.8	289.62	6.82	70	6	
5R	18 Jun	0255	292.5	302.2	9.7	292.5	297.25	4.75	49	5	
61	18 Jun					*****Drilled interval from 302.2 to 399 m DSF*****					
7R	18 Jun	1100	399	408.7	9.7	399	402.23	3.23	33	4	
8R	18 Jun	1255	408.7	418.4	9.7	408.7	418.32	9.62	99	8	
9R	18 Jun	1440	418.4	428.1	9.7	418.4	425.29	6.89	71	6	
10R	18 Jun	1620	428.1	437.8	9.7	428.1	433.31	5.21	54	5	
11R	18 Jun	1820	437.8	447.5	9.7	437.8	440.09	2.29	24	3	
12R	18 Jun	2000	447.5	457.2	9.7	447.5	447.98	0.48	5	2	
13R	18 Jun	2140	457.2	466.9	9.7	457.2	460.4	3.2	33	3	
14R	18 Jun	2330	466.9	476.6	9.7	466.9	468.72	1.82	19	3	
15R	19 Jun	0110	476.6	486.3	9.7	476.6	486.24	9.64	99	8	
16R	19 Jun	0250	486.3	496	9.7	486.3	489.54	3.24	33	4	
17R	19 Jun	0425	496	505.7	9.7	496	501.75	5.75	59	5	
18R	19 Jun	0620	505.7	515.4	9.7	505.7	510.1	4.4	45	4	
19R	19 Jun	0800	515.4	525.1	9.7	515.4	520.04	4.64	48	4	
20R	19 Jun	0935	525.1	534.8	9.7	525.1	527.72	2.62	27	3	
21R	19 Jun	1115	534.8	544.5	9.7	534.8	535.55	0.75	8	2	
22R	19 Jun	1320	544.5	554.2	9.7	544.5	545.39	0.89	9	2	
23R	19 Jun	1500	554.2	563.9	9.7	554.2	555.44	1.24	13	2	
24R	19 Jun	1700	563.9	573.6	9.7	563.9	566.45	2.55	26	3	
25R	19 Jun	1840	573.6	583.3	9.7	573.6	576.14	2.54	26	3	
26R	19 Jun	2025	583.3	593	9.7	583.3	587.46	4.16	43	4	
27R	19 Jun	2210	593	602.7	9.7	593	597.68	4.68	48	5	
28R	19 Jun	2350	602.7	612.4	9.7	602.7	604.81	2.11	22	3	
29R	20 Jun	0130	612.4	622.1	9.7	612.4	619.09	6.69	69	6	
30R	20 Jun	0310	622.1	631.8	9.7	622.1	623.57	1.47	15	2	
31R	20 Jun	0450	631.8	641.5	9.7	631.8	633.3	1.5	15	2	
32R	20 Jun	0620	641.5	651.2	9.7	641.5	645.14	3.64	38	4	
33R	20 Jun	0950	651.2	655	3.8	651.2	654.84	0	0	0	
34R	20 Jun	1215	655	661	6	655	655.12	0.12	2	1	
35R	20 Jun	1400	661	670.7	9.7	661	665.19	4.19	43	4	

Table T1 (continued).

Core	Date (2013)	UTC time (h)	Depth DSF (m)			Depth CSF (m)		Length of core recovered (m)	Recovery (%)	Sections (N)	APC system
			Top of cored interval	Bottom of cored interval	Interval advanced (m)	Top of cored interval	Bottom of cored interval				
36R	20 Jun	1530	670.7	680.4	9.7	670.7	673.37	2.67	28	3	
37R	20 Jun	1710	680.4	690.1	9.7	680.4	683.01	2.61	27	3	
38R	20 Jun	1900	690.1	699.8	9.7	690.1	695.57	5.47	56	5	
39R	20 Jun	2115	699.8	709.5	9.7	699.8	707.83	8.03	83	8	

DSF = drilling depth below seafloor, CSF = core depth below seafloor. Core: 1 = drilled interval, H = advanced piston corer (APC) core, X = extended core barrel core, R = rotary core barrel core.



Table T2. Summary of observed lithofacies, Site U1417. (Continued on next two pages.)

Main facies	Subfacies	Facies	Description	Marine microfossils	Lithostratigraphic unit	Tentative depositional environment/diagenesis
Mud	Massive mud with lonestones	F1a	Dark gray to (dark) greenish gray; Bioturbated (none to heavy); Occasionally calcareous bearing; Occasionally diatom rich/bearing; Lonestones of granule and pebble sizes occur in varying amounts; Occasional color banding and black mottles; Occasional sand pods; Interbedded with Facies F1b, F2a, F2b, F3a, F3b, F3c, F4a, F4b, F4c, F4d, F5a, F5b, F5c, F6, F7, and F8.	Variable	IA, IB, II, III, IV, VA, VB, VC, VD, VE, VG, VI	Suspension fall-out, ice rafting, or sediment gravity flows
	Massive mud without lonestones	F1b	Dark gray to (dark) greenish gray; Bioturbated (none to heavy); Occasional <i>Zoophycos</i> burrows; Occasionally calcareous bearing; Occasionally diatom rich/bearing; Occasional color banding and black mottles; Occasional silt pods/lenses; Interbedded with Facies F1a, F2a, F2b, F3a, F3c, F4a, F4c, F4d, F5a, F5b, F5c, F6, and F7.	Diatoms may occur	IA, IB, II, IV, VA, VB, VC, VD, VE, VG, VI	Suspension fall-out, ice rafting, or sediment gravity flows
Silt	Silt	F2a	Dark gray to greenish gray; Often interbedded with mud; Sharp to gradational upper and lower contacts; Diatoms may occur; Interbedded with Facies F1a, F1b, F2b, F3a, F4d, F5a, F5b, F5c, F6, and F7.	Diatoms may occur	IA, IB, II, VE, VF, VG, VH, VI	Sediment gravity flows
	Interbedded silt and mud	F2b	Dark gray to greenish gray; Facies thickness 2 to 360 cm; Occasional color banding; None to moderate bioturbation; Occasionally with terrestrial organic components; Interbedded with Facies F1a, F1b, F2a, F3a, F4d, F4e, F4f, F6, and F8.	Not documented	IA, II, VE	Mud: suspension fall-out from surface water plumes and from sediment gravity flows Silt: sediment gravity flows
Sand	Very fine to coarse sand	F3a	Dark gray to gray; Bed thickness from 1 to 5 cm, occasionally thicker; Massive and normal grading; Sharp and frequently erosional lower contacts; Gradational and sharp upper contacts; Composition includes quartz and feldspar; Interbedded with Facies F1a, F1b, F2a, F2b, F4b, F4d, F5a, F5b, F5c, and F6.	Not documented	IA, IB, II, IV, VA, VB, VC, VE, VG, VI	Sediment gravity flows
	Medium to coarse sand	F3b	Dark gray to gray; Bed thickness up to 40 cm; Rip-up clasts common; Plant debris, organic matter, and diatoms may occur; Sharp bases and sharp to gradational upper contacts; Interbedded with Facies F1a and F4b.	Not documented	VA	Sediment gravity flows
	Interbedded sand and mud	F3c	Dark gray to dark greenish gray; Facies thickness 7–710 cm; Partly diatom bearing; None to moderate bioturbation; Partly with volcanic ash; Occasional color banding; Lonestones may occur; Interbedded with Facies F1a, F1b, F5a, F5b, F5b, F6, and F7.	Diatoms may occur	IB, II, VA	Suspension fall-out from surface water plumes (mud), ice rafting (mud, sand, lonestones), and sediment gravity flows (sand, mud)



Table T2 (continued). (Continued on next page.)

Main facies	Subfacies	Facies	Description	Marine microfossils	Lithostratigraphic unit	Tentative depositional environment/diagenesis
Diamict	Muddy diamict	F4a	Dark gray; Muddy matrix; Clast concentration variable; Thin bedded or pods; Lower contacts are gradational; Upper contacts are sharp and defined by concentration of clasts; Granule and small pebble clasts are commonly subangular to subrounded; Interbedded with Facies F1a and F5c	Not documented	IB, III	Suspension settling and ice rafting (mainly by icebergs)
	Muddy and sandy diamict with lithic and mud clasts and/or terrigenous organic components	F4b	Dark gray; Mud to sand matrix; Bed thickness up to 40 cm; Sharp upper and lower contacts; Lithic and mud clasts up to 3 cm; Occasional plant debris and terrestrial organic components (coal?); Interbedded with Facies F1a, F1b, F3a, F3b, F5a, F5b, F7, and F8 (in disturbed sequence).	Diatoms (partly freshwater)	VA, VC, VD, VE, VF, VG, VI	Sediment gravity flows
	Breccia	F4c	Dark gray matrix; Sandy mud matrix; Bed thickness typically 100 cm; Sharp erosive lower contacts; Gradational upper contacts; Most often clasts of indurated diatom ooze; Interbedded with Facies F1a and 5a.	Not documented	VF	Sediment gravity flows (e.g., slump)
	Interbedded mud and diamict	F4d	Dark gray to greenish gray; Occasional color banding and parallel lamination; None to moderate bioturbation; Occasionally calcareous bearing; Interbedded with Facies F1a, F1b, F2a, F2b, F3a, F4e, F5b, F5c, and F7.	Not documented	III, VC, VE	Suspension settling and ice rafting (icebergs and/or sea ice)
Diatom ooze		F5a	Greenish gray; 20 cm to 1.5 m; Bioturbation (including <i>Zoophycos</i> burrows); Sharp to gradational upper and lower contacts; Interbedded with Facies F1a, F1b, F2a, F3a, F3c, F4b, F4c, F5b, and F6.	Diatoms and other biosiliceous material; occasional carbonate (foraminifers and coccolithophores)	IA, IB, II, VA, VB, VD, VE, VH, VI	High-productivity environment and/or low terrigenous input and/or better preservation
Biosiliceous ooze; biosiliceous-rich/bearing mud and sand; mud with diatoms/biosilica		F5b	(Very) dark gray to (dark) greenish gray and brown; Facies thickness 2–445 cm; Mostly mud, rarely sand; Diatom and biosiliceous rich/bearing; Lonestones are absent or present; Occasional color banding; Partly mottled; Occasionally laminated; None to heavy bioturbation; Interbedded with Facies F1a, F1b, F2a, F3a, F3c, F4b, F5a, F5c, F6, F7, and F8.	Diatoms and other biosiliceous material	IA, IB, II, IV, VA, VB, VC, VD, VE, VH, VI	High-productivity environment and/or low terrigenous input and/or better preservation
Calcareous/carbonate-bearing/rich mud, silt, sand, diamict, and/or diatom ooze		F5c	(Very) dark gray to greenish gray; Facies thickness 3–316 cm; Occasionally with volcanic ash; None to heavy bioturbation; Occasional color banding and lamination; Interbedded with Facies F1a, F1b, F2a, F3a, F4a, F4b, F5b, and F8.	Foraminifers; occasionally diatoms	II, III, IV, VB, VE, VI	Temporarily increased productivity and/or reduced suspension settling and/or better preservation
Ash	Volcanic ash	F6	Usually gray to brown; Bed thickness typically 1–5 cm; Sharp lower contacts; Sharp to gradational upper contacts; Primarily vitric shards (glass); Some intervals affected by bioturbation; Often interbedded with Facies F1a, F1b, F2a, F3a, F3c, F5a, and F5b.	Not documented	IA, IB, II, VA	Suspension settling after subaerial eruptions



Table T2 (continued).

Main facies	Subfacies	Facies	Description	Marine microfossils	Lithostratigraphic unit	Tentative depositional environment/diagenesis
Volcaniclastic mud, sand, diamict and/or ooze		F7	Usually grayish, greenish, or brownish; Bed thickness typically 1–5 cm; Sharp and frequently erosive lower contacts; Gradational to sharp upper contacts; Primarily vitric shards (glass); Some intervals affected by bioturbation; Often interbedded with Facies F1a, F1b, F2a, F3c, F4d, F5b, and F7.	Diatoms	IA, IB, II, III, IV	Volcanic detritus either bioturbated or reworked/redeposited by sediment gravity flows
Rock		F8	Siltstone with carbonate cement; Often interbedded with Facies F1a, F2b, F4b, F5b, and F5c.		VC, VE, VH	In situ carbonate sedimentation

**Table T3.** Distribution of lithostratigraphic units and associated facies, Site U1417.

Lithostratigraphic units and associated facies	Hole U1417A	Hole U1417B	Hole U1417C	Hole U1417D	Hole U1417E
Subunit IA F1a, F1b, F2a, F2b, F3a, F5a, F5b, F6, F7	0–77.0 m CSF-A; Interval 1H-1, 0 cm, to 11H-2, 18 cm	0–79.4 m CSF-A; Interval 1H-1, 0 cm, to 10H-2, 131 cm	0–77.0 m CSF-A; Interval 2H-1, 0 cm, to 10H-2, 48 cm	0–78.8 m CSF-A; Interval 1H-1, 0 cm, to 10H-3, 38 cm	Drilled interval
Subunit IB F1a, F1b, F2a, F3a, F3c, F4a, F5a, F5b, F6, F7	77.0–168.0 m CSF-A; Interval 11H-2, 18 cm, to 22H-CC, 38 cm	79.4 – 151.9 m CSF-A; Interval 10H-2, 131 cm, to 17H-CC, 17 cm	77.0–154.1 m CSF-A; Interval 10H-2, 48 cm, to 18H-3, 18 cm	78.8–166.3 m CSF-A; Interval 10H-3, 38 cm, to 22H-1, 0 cm	Drilled interval
Unit II F1a, F1b, F2a, F2b, F3a, F3c, F5a, F5b, F5c, F6, F7		151.9–256.2 m CSF-A; Interval 17H-CC, 17 cm, to 37X-CC, 30.5 cm	154.1–226.0 m CSF-A; Interval 18H-3, 18 cm, to 29H-CC, 7 cm	166.3–263.5 m CSF-A; Interval 22H-1, 0 cm, to 42X-1, 85 cm	Drilled interval
Unit III F1a, F1b, F4a, F4d, F5c, F7		256.2–291.3 m CSF-A; Interval 38X-1, 0 cm, to 41X-1, 40 cm		263.5–296.6 m CSF-A; Interval 42X-1, 85 cm, to 46X-1, 92 cm	264.1–297.3 m CSF-A; Interval 2R-1, 7.5 cm, to 5R-CC, 10 cm
Unit IV F1a, F1b, F3a, F5b, F5c, F7		291.3–350.0 m CSF-A; Interval 41X-1, 40 cm, to 47X-CC, 26 cm		296.6–335.1 m CSF-A; Interval 46X-1, 92 cm, to 50X-1, 63 cm	Drilled interval
Subunit VA F1b, F3a, F3b, F3c, F4a, F4b, F5a, F5b, F5c, F6				335.1–394.3 m CSF-A; Interval 50X-1, 63 cm, to 56X-CC, 19 cm	Drilled interval
Subunit VB F1b, F5a, F5b, F7				394.3–432.0 m CSF-A; Interval 56X-CC, 19 cm, to 60X-CC, 10 cm	399.0–431.0 m CSF-A; Interval 7R-1, 0 cm, to 10R-3, 0 cm
Subunit VC F1a, F1b, F2a, F4a, F4b, F4d, F5b, F8				432.0–461.5 m CSF-A; Interval 60X-CC, 10 cm, to 65X-CC, 21 cm	431.0–477.7 m CSF-A; Interval 10R-3, 0 cm, to 15R-1, 66 cm
Subunit VD F1b, F4a, F5a					477.7–484.6 m CSF-A; Interval 15R-1, 66 cm, to 15R-6, 55 cm
Subunit VE F1a, F1b, F2a, F2b, F3a, F3b, F3c, F4b, F4d, F5b, F5c, F7, F8					484.6–615.4 m CSF-A; Interval 15R-6, 55 cm, to 29R-3, 11 cm
Subunit VF F2a, F4c, F5a					615.4–619.0 m CSF-A; Interval 29R-3, 11 cm, to 29R-CC, 17 cm
Subunit VG F1b, F3a, F4b, F8					619.0–642.8 m CSF-A; Interval 29R-CC, 17 cm, to 32R-2, 0 cm
Subunit VH F5b, F8					642.8–661.5 m CSF-A; Interval 32R-2, 0 cm, to 35R-1, 53 cm
Subunit VI F1b, F2a, F3a, F4b, F5b, F5c					661.5–705.9 m CSF-A; Interval 35R-1, 53 cm, to 39R-6, 13 cm
Subunit VJ F1b, F5a					705.9–708.0 m CSF-A; Interval 39R-6, 13 cm, to 39R-CC, 23 cm

Table T4. X-ray diffraction mineral composition, Holes U1417A, U1417C, U1417D, and U1417E. (Continued on next page.)

Hole, core, section, interval (cm)	Top depth (m)		Mica (counts)	Hornblende (counts)	Chlorite + kaolinite (counts)	Total clays (counts)	Quartz (counts)	Plagioclase (counts)	Calcite (counts)	Pyrite (counts)
	CSF-A	CCSF-B								
341-										
U1417D-1H-1, 4–5	0.04	0.03	3,896	3,580	5,019	2,903	4,212	5,054	NA	2,187
U1417A-1H-1, 24–25	0.24	0.23	7,652	5,897	12,074	2,794	4,844	6,318	2,383	2,464
U1417D-1H-1, 31–32	0.31	0.27	3,545	3,184	3,756	2,738	3,313	6,599	3,068	2,457
U1417D-1H-1, 65–66	0.65	0.56	3,373	2,980	3,282	2,780	3,931	5,546	3,545	2,327
U1417A-1H-1, 71–72	0.71	0.63	5,054	4,072	5,756	3,043	5,230	6,915	2,840	2,397
U1417D-1H-1, 100–101	1.01	0.87	5,546	4,317	6,950	3,268	5,265	6,423	2,864	2,559
U1417A-1H-2, 72–73	2.22	1.94	5,230	4,072	7,266	3,022	5,897	6,458	3,363	2,478
U1417D-1H-3, 14–15	3.14	2.72	3,468	2,710	4,317	2,955	4,352	5,827	2,562	2,211
U1417A-2H-1, 80–81	6.20	7.59	5,265	3,475	7,511	3,313	6,529	6,388	2,847	2,415
U1417A-2H-3, 50–51	8.90	9.93	8,178	3,686	13,514	3,184	6,037	6,458	NA	2,239
U1417A-3H-2, 65–66	17.05	18.29	4,633	3,756	6,423	3,250	6,143	6,809	2,783	2,422
U1417A-3H-6, 121–122	23.61	23.96	4,633	3,433	6,107	2,987	5,054	5,616	2,250	2,194
U1417A-4H-3, 48–49	27.88	28.01	8,143	5,090	12,074	3,127	6,529	7,090	2,348	2,590
U1417A-5H-3, 48–49	37.32	36.70	5,792	3,686	8,810	3,163	6,423	6,774	2,833	2,306
U1417A-6H-1, 46–47	43.86	42.18	9,126	5,721	13,619	2,917	5,511	7,160	NA	2,464
U1417A-7H-2, 61–62	47.01	43.88	12,671	5,265	20,885	3,047	6,423	7,757	2,324	2,482
U1417C-7H-3, 27–28	49.77	48.68	6,774	5,897	8,564	3,489	5,441	6,529	NA	2,984
U1417A-8H-2, 59–60	56.49	52.70	11,021	7,125	18,006	2,941	6,143	8,424	NA	2,492
U1417D-7H-2, 141–142	56.41	56.00	4,352	2,482	6,423	3,721	7,792	7,055	2,668	2,152
U1417A-9H-1, 129–130	58.19	57.65	5,546	3,756	8,003	3,268	6,143	6,318	2,931	2,436
U1417A-9H-4, 74–75	62.14	61.07	3,931	3,205	4,844	2,945	4,809	4,949	3,345	2,050
U1417A-9H-6, 58–59	64.98	63.52	4,984	4,598	7,055	3,187	5,160	6,248	2,819	2,696
U1417A-10H-3, 74–75	70.14	68.80	5,195	3,756	7,511	3,043	6,669	6,423	2,833	2,334
U1417A-11H-3, 31–32	79.21	79.80	6,248	6,985	11,408	3,057	5,862	6,950	2,601	2,910
U1417A-12H-3, 40–41	88.80	89.63	4,177	3,686	5,230	3,085	5,160	5,827	2,720	2,390
U1417A-13H-3, 60–61	98.50	99.47	10,319	4,809	16,883	3,345	7,441	7,827	2,966	2,840
U1417A-14H-3, 41–42	107.81	106.58	5,511	3,650	8,951	3,047	5,721	6,423	NA	2,552
U1417A-15H-2, 47–48	115.87	114.69	5,792	4,142	8,740	3,327	6,037	6,458	2,453	2,615
U1417A-16H-3, 43–44	126.83	124.72	9,126	4,774	15,233	3,036	5,897	7,898	2,345	2,418
U1417A-17H-3, 41–42	136.31	132.90	5,370	4,037	8,564	3,033	6,107	6,669	NA	2,475
U1417C-16H-4, 102–103	137.52	136.68	3,082	2,748	3,152	2,692	3,433	7,722	2,650	2,257
U1417A-18H-4, 88–89	146.83	142.36	4,528	3,391	5,932	3,064	5,546	5,827	2,594	2,260
U1417D-18H-1, 28–29	147.68	146.49	4,107	3,506	5,195	3,050	4,879	5,195	2,338	2,524
U1417C-17H-4, 17–18	146.17	146.73	4,177	3,405	3,791	3,317	4,177	4,984	2,703	2,517
U1417C-17H-4, 34–35	146.34	146.88	2,387	NA	1,955	2,696	2,790	4,423	2,629	NA
U1417C-17H-4, 67–68	146.67	147.17	5,265	4,212	6,880	2,910	5,090	5,511	2,562	2,327
U1417A-19H-2, 139–140	152.29	149.21	5,651	4,668	8,670	3,292	5,932	6,458	2,938	2,576
U1417D-18H-4, 52–53	152.42	150.59	5,125	3,896	7,968	3,261	6,423	6,634	2,903	2,496
U1417D-18H-6, 39–40	155.29	153.07	3,931	3,380	4,703	1,973	11,688	11,408	2,088	1,481
U1417D-18H-6, 109–110	155.99	153.67	4,914	3,931	4,352	3,721	6,388	6,072	3,001	3,292
U1417C-18H-2, 108–112	153.58	153.69	2,594	2,292	2,573	2,731	3,686	3,791	2,285	1,902
U1417C-18H-2, 132–137	153.82	153.90	6,423	2,148	10,881	2,731	9,547	22,218	2,001	1,527
U1417A-20H-1, 86–87	158.16	154.46	9,021	5,546	11,513	2,903	5,827	7,336	NA	2,604
U1417C-18H-4, 21–22	155.71	155.53	2,401	2,611	2,117	1,057	3,545	4,809	1,271	1,464
U1417A-21H-2, 83–84	160.73	159.80	5,721	4,879	6,283	3,275	5,125	6,353	2,812	2,752
U1417A-22H-2, 121–122	165.91	164.97	7,020	3,756	11,162	3,117	6,529	6,950	NA	2,296
U1417D-22H-2, 106–107	168.86	167.07	4,388	4,423	5,335	2,215	7,968	8,740	2,425	2,492
U1417D-22H-3, 80–81	170.10	168.14	5,405	4,037	5,125	3,510	5,511	6,388	2,868	2,731
U1417D-23H-1, 29–31	171.29	171.32	5,546	4,949	6,107	3,580	6,353	7,266	3,008	2,654
U1417D-23H-3, 88–89	174.88	174.42	5,967	4,528	7,020	3,120	6,002	6,774	2,815	2,450
U1417D-24H-1, 141–143	177.11	175.61	5,160	3,721	5,827	3,247	5,686	6,494	2,804	2,443
U1417D-25H-1, 30–32	180.70	178.40	5,019	4,177	5,370	3,412	5,405	6,143	2,941	2,794
U1417D-25H-2, 133–135	183.23	180.59	4,317	10,319	3,419	2,390	8,319	12,390	2,366	2,369
U1417D-32H-2, 38–39	205.78	206.40	6,950	4,493	9,968	3,264	5,335	6,178	NA	2,552
U1417D-34H-1, 94–95	210.34	210.23	4,668	3,461	5,756	3,436	5,616	6,002	2,815	2,527
U1417D-35H-2, 45–46	216.05	215.29	4,879	3,861	5,897	3,366	5,441	5,967	NA	2,443
U1417C-27H-2, 12–13	220.02	219.20	2,724	2,369	2,390	2,545	2,903	2,689	2,310	1,923
U1417D-36H-2, 50–51	220.80	219.32	5,160	3,422	6,353	3,447	6,423	6,704	2,931	2,327
U1417D-38X-1, 23–24	224.13	224.13	4,879	3,861	6,774	3,096	5,265	5,862	4,703	2,411
U1417D-39X-1, 133–135	234.93	234.93	4,844	5,300	5,054	2,088	8,003	8,459	3,650	2,503
U1417D-40X-3, 93–95	246.77	246.77	5,827	4,388	7,968	3,163	5,581	6,494	2,861	2,506
U1417D-41X-2, 35–37	254.85	254.85	6,458	5,195	8,775	3,043	5,897	7,125	3,163	2,464
U1417D-41X-5, 48–50	259.48	259.48	5,967	NA	7,827	3,457	6,529	6,634	3,159	2,246
U1417D-42X-1, 31–32	263.01	263.01	5,300	4,142	7,125	3,268	5,019	6,037	3,791	2,734
U1417D-42X-2, 127–128	265.47	265.47	2,955	2,450	2,699	2,601	3,650	3,721	NA	2,081
U1417D-42X-CC, 27–29	267.75	267.75	5,511	4,352	7,898	2,896	5,405	6,388	4,598	2,499

Table T4 (continued).

Hole, core, section, interval (cm)	Top depth (m)		Mica (counts)	Hornblende (counts)	Chlorite + kaolinite (counts)	Total clays (counts)	Quartz (counts)	Plagioclase (counts)	Calcite (counts)	Pyrite (counts)
	CSF-A	CCSF-B								
U1417D-44X-1, 81–83	282.91	282.91	5,265	4,282	7,371	2,959	5,792	6,704	3,071	2,738
U1417D-45X-1, 81–83	290.51	287.50	4,879	3,791	5,827	3,545	5,335	5,897	NA	2,847
U1417D-48X-1, 42–43	315.52	315.52	6,423	4,458	8,424	3,464	5,230	6,318	NA	2,685
U1417D-49X-3, 30–32	327.67	327.67	4,528	3,387	5,054	3,615	5,160	5,616	NA	2,394
U1417D-50X-1, 102–103	335.52	335.52	5,581	9,266	8,108	2,036	11,197	16,006	2,296	2,124
U1417D-50X-2, 102–103	336.89	336.89	4,528	3,436	4,844	2,882	3,580	4,001	2,538	3,145
U1417D-50X-2, 125–126	337.12	337.12	4,247	3,233	4,388	3,166	4,037	5,862	NA	2,296
U1417D-51X-1, 83–84	345.03	345.03	3,861	3,078	3,686	3,826	4,879	4,879	2,699	2,303
U1417D-51X-2, 57–58	346.27	346.27	5,090	3,686	5,090	3,650	5,335	5,370	NA	2,345
U1417D-51X-3, 16–17	346.77	346.77	6,143	5,405	5,651	3,352	5,441	6,318	2,819	2,601
U1417D-52X-1, 106–107	354.96	354.96	4,493	3,268	4,282	3,615	4,984	5,265	2,587	2,166
U1417D-52X-3, 98–99	357.58	357.58	4,984	3,615	5,265	3,580	5,125	5,019	NA	3,443
U1417D-53X-2, 36–37	364.97	364.97	5,230	3,966	6,739	3,580	4,949	5,019	2,780	3,356
U1417D-54X-3, 22–23	375.98	375.98	2,689	2,429	2,376	2,780	3,454	4,212	2,197	1,755
U1417D-54X-4, 66–67	377.90	377.90	5,160	3,756	6,880	3,454	5,019	5,967	NA	2,685
U1417D-55X-1, 58–59	383.58	383.58	5,581	3,966	7,792	3,468	5,125	6,213	2,984	2,710
U1417D-55X-3, 74–76	386.68	386.68	7,266	7,266	9,231	2,654	6,564	15,198	3,545	2,187
U1417D-55X-3, 119–120	387.13	387.13	6,739	5,370	8,880	3,236	5,827	7,336	NA	2,594
U1417D-56X-1, 69–70	393.39	393.39	5,265	3,931	5,967	2,797	6,985	6,669	2,566	2,341
U1417D-57X-1, 36–37	402.76	402.76	6,880	4,493	8,845	2,959	6,178	6,599	2,945	2,903
U1417D-58X-2, 80–81	414.39	412.74	3,826	2,439	4,001	3,292	4,247	4,072	2,274	1,923
U1417E-9R-1, 10–11	418.50	418.50	5,546	3,756	4,423	3,650	4,879	5,370	NA	2,647
U1417D-59X-1, 122–123	423.02	419.68	3,686	2,520	3,012	3,650	4,633	4,072	NA	1,902
U1417D-59X-3, 100–101	425.72	422.38	6,739	4,177	8,740	3,320	5,265	6,353	2,587	2,580
U1417E-9R-4, 136–137	424.26	424.26	5,686	4,037	7,862	3,040	6,072	6,880	2,576	2,573
U1417E-10R-1, 19–20	428.29	428.29	4,844	3,510	4,949	3,482	5,546	6,283	2,843	2,604
U1417E-10R-3, 19–21	431.29	431.29	8,389	3,166	7,792	2,727	7,617	7,090	2,636	2,190
U1417E-11R-1, 22–23	438.02	438.02	5,125	NA	6,283	3,177	11,864	9,372	2,594	NA
U1417E-11R-1, 116–117	438.96	438.96	4,037	2,685	4,949	2,910	8,740	9,126	2,418	1,881
U1417D-62X-CC, 26–27	442.21	442.21	4,423	2,510	6,037	2,822	9,512	8,810	2,622	1,769
U1417D-63X-CC, 18–20	447.23	447.23	6,178	3,791	8,740	3,415	5,335	6,353	3,064	2,566
U1417E-14R-1, 26–27	467.16	467.16	10,811	4,001	6,774	2,924	7,898	8,249	2,692	2,081
U1417E-14R-CC, 2–3	468.62	468.62	3,861	3,756	4,177	4,037	4,668	4,739	2,980	4,001
U1417E-15R-2, 69–70	478.79	478.79	6,388	3,791	7,476	3,650	5,511	6,107	3,064	NA
U1417E-16R-2, 66–67	488.09	488.09	12,355	3,324	6,037	2,250	9,442	13,303	NA	1,759
U1417E-17R-3, 97–98	499.83	499.83	5,686	3,173	5,405	2,475	8,073	6,774	2,503	2,134
U1417E-18R-3, 69–70	509.18	509.18	5,441	3,177	5,581	3,401	6,634	6,318	2,843	2,246
U1417E-19R-1, 65–66	516.05	516.05	5,721	2,826	5,090	2,594	7,968	6,880	1,945	2,106
U1417E-20R-2, 61–62	527.21	527.21	5,370	2,920	6,458	3,650	6,564	5,967	2,955	2,253
U1417E-21R-1, 37–38	535.17	534.80	5,300	3,001	5,019	2,559	9,758	7,547	2,443	2,573
U1417E-22R-1, 55–56	545.05	544.50	5,581	3,141	7,511	3,510	5,967	6,248	NA	2,453
U1417E-24R-1, 14–15	564.04	564.04	6,809	3,447	8,775	3,433	5,967	6,072	3,099	2,703
U1417E-24R-2, 11–12	565.00	565.00	9,266	3,292	7,055	2,769	8,600	10,004	2,555	2,415
U1417E-25R-1, 25–26	573.85	573.85	6,248	3,085	7,792	3,650	5,616	5,616	2,552	2,310
U1417E-25R-2, 29–30	575.31	575.31	5,405	3,187	7,266	3,650	5,827	5,827	3,064	2,548
U1417E-26R-1, 20–21	583.50	583.50	10,004	3,615	12,566	3,391	5,967	6,809	NA	2,489
U1417E-27R-4, 57–59	597.13	597.13	6,388	3,089	7,476	3,342	7,862	6,950	2,366	2,106
U1417E-28R-1, 52–54	603.22	603.22	5,932	3,208	6,002	3,931	5,511	5,616	2,776	2,436
U1417E-29R-2, 42–43	614.23	614.23	6,985	3,313	9,337	3,580	5,756	5,792	NA	2,745
U1417E-29R-3, 78–80	616.09	616.09	2,836	2,145	2,208	3,050	3,475	3,415	2,387	1,860
U1417E-29R-4, 90–91	617.64	617.64	11,618	4,493	6,318	2,668	8,354	13,022	2,461	2,095
U1417E-31R-1, 43–44	632.23	632.23	5,476	2,941	6,037	3,615	6,178	5,862	2,489	2,306
U1417E-31R-1, 53–54	632.33	632.33	6,529	2,955	7,441	3,208	6,704	6,704	2,299	2,141
U1417E-32R-1, 47–48	641.97	641.97	24,114	4,914	9,337	2,218	9,828	16,708	NA	1,860
U1417E-32R-2, 72–72	643.52	643.52	4,212	2,861	2,710	4,247	3,966	5,054	2,587	NA
U1417E-35R-1, 14–15	661.14	661.14	4,072	2,878	2,643	4,528	4,142	4,668	2,625	2,183
U1417E-35R-2, 51–53	662.97	662.97	17,164	4,247	11,829	2,706	9,021	14,777	2,706	2,253
U1417E-35R-3, 100–102	664.73	664.73	6,564	3,275	6,809	3,545	4,563	5,897	3,071	2,418
U1417E-37R-2, 39–40	682.31	682.31	13,759	3,187	6,318	2,566	8,459	9,231	2,552	2,415
U1417E-38R-1, 61–62	690.71	690.71	6,809	2,776	6,704	3,306	6,458	6,353	2,857	2,204
U1417E-38R-3, 6–8	693.16	693.16	11,794	2,931	6,458	2,822	7,090	7,687	2,861	2,274
U1417E-39R-1, 7–9	699.87	699.87	6,669	3,001	7,371	3,966	5,932	5,721	NA	2,394
U1417E-39R-1, 51–52	700.31	700.31	5,686	2,896	5,511	2,559	8,600	11,443	2,387	2,060
U1417E-39R-6, 96–98	706.62	706.62	4,107	2,668	2,899	3,931	4,528	4,247	2,583	1,990

NA = not applicable.



Table T5. Datum events for radiolarians, diatoms, and foraminifers, Site U1417.

Datum event	Datum type	Age (Ma)	Hole, core, section, interval (cm)		Depth CSF-A (m)			Depth CCSF-A (m)			Depth CCSF-B (m)		
			Top	Bottom	Top (middle)	Bottom (middle)	Median	Top (middle)	Bottom (middle)	Median	Top (middle)	Bottom (middle)	Median
			341-										
LO <i>Lynchocanoma nipponica sakaii</i>	R	0.03 ± 0.03	U1417D-1H-CC	U1417B-2H-CC	6.03	14.76	10.39	6.03	9.59	7.81	5.21	8.29	6.75
LO <i>Proboscia curvirostris</i> (D120)	D	0.3 ± 0.1	U1417B-6H-CC	U1417A-8H-CC	49.02	56.89	52.95	57.17	61.32	59.24	49.45	53.04	51.24
LO <i>Styloantharium acuilonium</i>	R	0.4 ± 0.1	U1417B-6H-CC	U1417B-7H-CC	49.02	58.05	53.53	57.17	63.31	60.24	49.45	54.76	52.10
LO <i>Stylatractus univervus</i>	R	0.5 ± 0.1	U1417B-7H-CC	U1417B-8H-CC	58.05	67.06	62.55	63.31	73.55	68.43	54.76	63.62	59.19
LO <i>Neogloboquadrina inglei</i>	F	0.7 ± 0.1	U1417B-6H-CC	U1417B-10H-CC	49.02	86.16	67.59	57.17	101.49	79.33	49.45	87.79	68.62
LO <i>Actinocyclus oculatus</i> (D110)	D	1.1 ± 0.1	U1417C-8H-CC	U1417D-9H-3, 80	65.41	69.80	67.60	76.46	80.30	78.38	66.13	69.46	67.80
LO <i>Eucyrtidium matuyamai</i>	R	1.3 ± 0.1	U1417D-16H-CC	U1417C-17H-CC	138.26	151.24	144.75	157.94	174.70	166.32	136.61	151.11	143.86
FO <i>Proboscia curvirostris</i> (D105)	D	1.8 ± 0.1	U1417B-22H-3, 46	U1417D-25H-CC	181.58	185.36	183.47	210.25	210.90	210.57	181.72	182.20	181.96
FO <i>Eucyrtidium matuyamai</i>	R	1.9 ± 0.1	U1417B-27H-CC	U1417B-28H-CC	202.54	207.29	204.91	235.31	244.99	240.15	200.24	207.40	203.82
LO <i>Neodenticula koizumii</i> (D100)	D	2 ± 0.4	U1417C-14H-CC	U1417D-15H-3, 130	122.64	123.60	123.12	140.93	141.18	141.05	121.90	122.12	122.01
FO <i>Neodenticula seminae</i> (D95)	D	2.2 ± undet.	U1417B-29H-CC	U1417C-25H-CC	211.78	213.78	212.78	250.84	254.14	252.49	211.72	214.16	212.94
LO <i>Neodenticula kamtschatica</i> (D90)	D	2.6 ± 0.2	U1417D-48X-CC	U1417B-44X-CC	317.74	324.05	320.89	361.00	370.73	365.86	317.74	327.47	322.60
FO <i>Cycladophora davisiana</i>	R	2.8 ± 0.1	U1417B-42X-CC	U1417B-43X-CC	303.09	315.17	309.13	346.35	358.43	352.39	303.09	315.17	309.13
LO <i>Stylocorys peregrina</i>	R	3.3 ± 0.1	U1417D-47X-CC	U1417D-49X-CC	307.84	328.42	318.13	351.10	371.68	361.39	307.84	328.42	318.13
FO <i>Neodenticula koizumii</i> (D80)	D	3.75 ± 0.35	U1417D-52X-CC	U1417D-53X-1, 69	357.89	364.29	361.09	401.15	407.55	404.35	357.89	364.29	361.09
LO <i>Phormocyrtis fistula</i>	R	4.4 ± 0.1	U1417D-56X-CC	U1417D-58X-CC	394.44	416.10	405.27	437.70	457.72	447.71	394.44	414.46	404.45
LO <i>Thalassionema schraderi</i>	D	7.9 ± 0.4	U1417E-29R-4, 50	U1417E-29R-5, 43	617.24	618.66	617.95	660.50	661.92	661.21	617.24	618.66	617.95
LO <i>Cyrtocapsella japonica</i>	R	10 ± 0.1	U1417E-29R-CC	U1417E-32R-CC	619.07	645.12	632.09	662.33	688.38	675.35	619.07	645.12	632.09

LO = last occurrence, FO = first occurrence. R = radiolarian, D = diatom, F = foraminifer. undet. = undetermined.

Table T6. Diatoms, Site U1417. This table is available in an [oversized format](#).

Table T8. Planktonic foraminifers, Site U1417. (Continued on next page.)

Core, section	Preservation	Group abundance	<i>Globigerina bulloides</i>	<i>Globigerina umbilicata</i>	<i>Globigerinita glutinata</i>	<i>Globigerinita uvula</i>	<i>Globorotalia scitula</i>	<i>Neogloboquadrina inglei</i>	<i>Neogloboquadrina kagaensis</i>	<i>Neogloboquadrina incompta</i> (sinistral)	<i>Neogloboquadrina pachyderma</i> (dextral)	<i>Neogloboquadrina pachyderma</i> (sinistral)	<i>Neogloboquadrina pachyderma</i> A (dextral, inflated form)	<i>Neogloboquadrina pachyderma</i> B (sinistral, inflated form)	<i>Orbulina universa</i>	Comments
341-U1417A-																
1H-CC	G	D	D	R	F					P	D			P		
2H-CC	M	A	D	F						P	D					Contains ice-rafted debris (>710 µm)
3H-CC	P	A	A								D					Pebbles, sandy
4H-CC	M	R	A							R	D					Sandy
5H-CC	M	F	D	P						R	D					Pebbles, sandy
6H-CC	P	B									D					Pebbles, sandy
7H-CC	M	R														Sandy, wood fragment
8H-CC	M	R	A							R	D					Pebbles, sandy
9H-CC, 11H-CC, 12H-CC, 13H-CC	B															Pebbles, sandy
14H-CC	G	P	D								D					Pebbles, sandy, pyrite, brownish foraminifer shells
15H-CC	M	R								R	D					Sandy
16H-CC	G	F	R	P						P	D					Pebbles, sandy, brownish foraminifer shells
17H-7 (bottom), 18H-CC, 19H-CC, 20H-CC	B															Diatom rich
341-U1417B-																
2H-CC	G	R	D	R						R	D					Sandy
4H-CC	G	C	A	P						R	D					Sandy
6H-CC	P	P	D								D					Diatom ooze, pyritized planktonic foraminifers
9H-CC	B															Pebbles, sandy, pyrite
10H-CC	G	A	D	P			P			R	D					Pebbles, sandy, pyrite
12H-CC	P	P	D								D					Sandy, pumice
21H-2 (bottom), 23H-CC, 25H-CC, 28H-CC, 29H-CC, 31H-CC	B															Poorly disaggregated, pebbles
32H-CC	P	P	D													Pebbles, sandy
34X-CC	M	P						D								Sandy
39X-CC	M	P	D							D						Sandy
41X-CC	M	P	D							A	D					Poorly disaggregated, pebbles, brownish foraminifer shells
45X-CC	B															Poorly disaggregated
341-U1417C-																
2H-CC	P	P	D	A							D					Pebbles, sandy
3H-CC	P	P	A								D					Sandy
4H-CC	B															Diatom and radiolarian rich
6H-CC	M	R	A	R						R	D	R				Sandy
8H-CC	G	A	D		P					R	D	R				Pebbles, sandy
10H-CC	G	F	A	R						R	D	P				Sandy
12H-CC	P	P									D					Pebbles, sandy
13H-CC	P	P									D					
14H-CC	P	C	A				R			R	D	R				Brownish foraminifer shells dominant
15H-CC	P	F	D				R			R	D	R				Brownish foraminifer shells dominant
16H-7	P	P	D													Brownish foraminifer shells dominant
18H-CC, 20H-CC, 22H-CC, 24H-CC, 26H-CC	B															Sandy
28H-CC	P	P	D		A					A	A					Brownish foraminifer shells
341-U1417D-																
1H-CC	M	D	A	P	P	P				R	D		R			Planktonic foraminifers dominant
2H-CC	G	A	P	A	P	P			F	P	D		F			
3H-CC	M	R	F			R					D		R			
4H-CC	M	F	F							P	D					Sandy
5H-CC	M	P	R	A							D		A			Sandy
6H-CC	G	R	D						R	R	D					Diatom rich
8H-CC	P	P				A					D					Sandy



Table T8 (continued).

Core, section	Preservation	Group abundance	<i>Globigerina bulloides</i>	<i>Globigerina umbilicata</i>	<i>Globigerinita glutinata</i>	<i>Globigerinita uvula</i>	<i>Globorotalia scitula</i>	<i>Neogloboquadrina inglei</i>	<i>Neogloboquadrina kagaensis</i>	<i>Neogloboquadrina incompacta</i> (sinistral)	<i>Neogloboquadrina pachyderma</i> (dextral)	<i>Neogloboquadrina pachyderma</i> (sinistral)	<i>Neogloboquadrina pachyderma</i> A (dextral, inflated form)	<i>Neogloboquadrina pachyderma</i> B (sinistral, inflated form)	<i>Orbulina universa</i>	Comments
10H-CC		B														Sandy
12H-CC	P	P											D			Sandy
16H-7	P	P											D			Poorly disaggregated
20H-CC, 24H-CC, 26H-CC		B														Poorly disaggregated
28H-CC	M	F	A			F	A	A		D	F					Sandy, brownish foraminifer shells dominant
30H-CC, 32H-CC, 34H-CC		B														Sandy
36H-CC	M	P								D						Volcanic shards
37H-CC	P	P								D				D		Sandy, pyritized radiolarians
38X-CC	P	P				F	A	A		D	F					Brownish foraminifer shells
40X-CC	G	P				F	A	A		D	A					Mixture of light and white foraminifer shells
42X-CC	M	P				A	D			F	F					Mixture of light and white foraminifer shells
43X-CC	P	P	D							A	A					Poorly disaggregated
44X-CC, 46X-CC, 48X-CC, 50X-CC, 51X-CC, 54X-CC, 58X-CC, 60X-CC, 62X-CC, 64X-CC		B														Poorly disaggregated
46X-CC		B														Poorly disaggregated
48X-CC		B														Poorly disaggregated
49X-CC		B														Poorly disaggregated
50X-CC		B														Poorly disaggregated
51X-CC		B														Sandy, mica present
54X-CC		B														Sandy, poorly disaggregated
58X-CC		B														Black coal-like fragments, sandy
60X-CC		B														Black coal-like fragments, sandy
62X-CC		B														Black coal-like fragments, sandy
64X-CC		B														Sandy

Preservation: G = good, M = moderate, P = poor. Abundance: D = dominant, A = abundant, F = few, R = rare, P = present, B = barren. This table is available in [.CSV](#).

Table T9. Benthic foraminifers, Site U1417. This table is available in an [oversized format](#).



Table T10. Affine table, Site U1417.

Core	Offset (m)	Core	Offset (m)	Core	Offset (m)	Core	Offset (m)
341-U1417A-		30H	40.61	6H	2.69	60X	43.26
1H	0.02	31H	42.37	7H	8.33	61X	43.26
2H	2.58	32H	42.84	8H	9.93	62X	43.26
3H	4.09	33H	42.84	9H	10.50	63X	43.26
4H	4.50	34X	43.26	10H	11.61	64X	43.26
5H	5.11	35X	43.26	11H	13.52	65X	43.26
6H	4.90	36X	43.26	12H	14.14		
7H	3.72	37X	43.26	13H	14.84	341-U1417E-	
8H	4.43	38X	43.26	14H	16.52	2R	43.26
9H	8.46	39X	43.26	15H	17.58	3R	43.26
10H	9.40	40X	46.48	16H	19.68	4R	43.26
11H	13.04	41X	43.26	17H	20.84	5R	43.26
12H	14.82	42X	43.26	18H	21.67	61	No core recovery
13H	16.49	43X	43.26	19H	Only 4% recovery	7R	43.26
14H	15.40	44X	46.68	20H	25.34	8R	43.26
15H	16.72	45X	43.26	21H	No core recovery	9R	43.26
16H	17.35	46X	43.26	22H	24.29	10R	43.26
17H	17.33	47X	43.26	23H	26.77	11R	43.26
18H	17.74			24H	25.90	12R	43.26
19H	20.21	341-U1417C-		25H	25.54	13R	43.26
20H	20.41	2H	2.30	26H	26.14	14R	43.26
21H	24.01	3H	3.32	27H	28.88	15R	43.26
22H	24.81	4H	3.59	28H	30.99	16R	43.26
		5H	2.56	29H	30.65	17R	43.26
341-U1417B-		6H	5.78	30H	31.45	18R	43.26
1H	0.01	7H	6.51	31H	36.25	19R	43.26
2H	-5.17	8H	11.05	32H	37.85	20R	43.26
3H	4.79	9H	11.91	33H	37.70	21R	43.26
4H	5.90	10H	13.64	34H	38.48	22R	43.26
5H	7.93	11H	15.76	35H	39.60	23R	43.26
6H	8.15	12H	17.46	36H	40.31	24R	43.26
7H	5.26	13H	Only 1% recovery	37H	40.22	25R	43.26
8H	6.49	14H	18.29	38X	43.26	26R	43.26
9H	12.98	15H	19.35	39X	43.26	27R	43.26
10H	15.33	16H	20.49	40X	46.48	28R	43.26
11H	18.13	17H	23.46	41X	43.26	29R	43.26
12H	19.34	18H	24.10	42X	43.26	30R	43.26
13H	21.36	19H	25.03	43X	43.26	31R	43.26
14H	22.98	20H	25.16	44X	43.26	32R	43.26
15H	No core recovery	21H	26.90	45X	43.26	33R	No core recovery
16H	23.96	22H	28.03	46X	40.92	34R	Only 2% recovery
17H	23.61	23H	31.59	47X	43.26	35R	43.26
18H	25.63	24H	31.55	48X	43.26	36R	43.26
19H	25.44	25H	40.36	49X	43.26	37R	43.26
20H	27.08	26H	42.66	50X	43.26	38R	43.26
21H	26.90	27H	40.93	51X	43.26	39R	43.26
22H	28.67	28H	41.29	52X	43.26		
23H	28.63	29H	43.26	53X	43.26		
24H	32.09			54X	43.26		
25H	33.39	341-U1417D-		55X	43.26		
26H	32.68	1H	0.00	56X	43.26		
27H	32.77	2H	0.80	57X	43.26		
28H	37.70	3H	2.13	58X	41.62		
29H	39.06	4H	3.26	59X	39.91		
		5H	1.84				

Core: H = advanced piston corer, X = extended core barrel, R = rotary core barrel. Cores with very low recovery were not used for correlation purposes.



Table T11. Splice tie points, Site U1417.

Hole, core, section	Tie point (cm)	Depth CSF-A (m)	Depth CCSF-A (m)	Tie/Append	Hole, core, section	Tie point (cm)	Depth CSF-A (m)	Depth CCSF-A (m)
341-					341-			
U1417D-1H-4	55.01	5.05	5.05	Tie to	U1417C-2H-2	25.13	2.75	5.05
U1417C-2H-5	78.14	7.78	10.08	Tie to	U1417D-2H-3	27.80	9.28	10.08
U1417D-2H-6	93.77	14.16	14.96	Tie to	U1417C-3H-1	114.24	11.64	14.96
U1417C-3H-4	133.20	16.33	19.65	Tie to	U1417D-3H-2	52.39	17.52	19.65
U1417D-3H-6	56.21	23.02	25.15	Tie to	U1417C-4H-2	6.09	21.56	25.15
U1417C-4H-5	34.90	26.35	29.94	Tie to	U1417D-4H-2	17.25	26.67	29.94
U1417D-4H-4	83.81	30.34	33.60	Tie to	U1417C-5H-2	4.18	31.04	33.60
U1417C-5H-6	73.25	37.73	40.29	Tie to	U1417D-5H-3	95.09	38.45	40.29
U1417D-5H-6	123.90	43.24	45.08	Tie to	U1417C-6H-2	80.31	39.30	45.08
U1417C-6H-5	44.97	43.45	49.23	Tie to	U1417D-6H-2	103.66	46.54	49.23
U1417D-6H-6	56.81	52.07	54.76	Tie to	U1417C-7H-2	24.60	48.25	54.76
U1417C-7H-7	16.86	55.67	62.18	Tie to	U1417D-7H-1	34.84	53.85	62.18
U1417D-7H-3	126.59	57.77	66.10	Tie to	U1417A-9H-1	73.71	57.64	66.10
U1417A-9H-3	26.98	60.17	68.63	Tie to	U1417C-8H-2	7.96	57.58	68.63
U1417C-8H-7	57.10	65.07	76.12	Tie to	U1417A-10H-1	32.74	66.73	76.12
U1417A-10H-2	103.70	68.94	78.33	Tie to	U1417D-9H-2	33.13	67.83	78.33
U1417D-9H-5	59.64	72.60	83.10	Tie to	U1417B-9H-3	1.79	70.12	83.10
U1417B-9H-6	108.50	75.68	88.66	Tie to	U1417D-10H-2	5.11	77.05	88.66
U1417D-10H-6	110.52	84.12	95.73	Tie to	U1417B-10H-3	79.94	80.40	95.73
U1417B-10H-6	87.13	84.98	100.31	Tie to	U1417D-11H-2	29.14	86.79	100.31
U1417D-11H-6	22.10	92.22	105.74	Tie to	U1417B-11H-2	1.20	87.61	105.74
U1417B-11H-6	32.36	93.92	112.05	Tie to	U1417C-12H-1	59.33	94.59	112.05
U1417C-12H-5	109.96	101.10	118.56	Tie to	U1417D-13H-2	41.74	103.72	118.56
U1417D-13H-6	30.52	109.61	124.45	Tie to	U1417A-14H-4	14.19	109.04	124.45
U1417A-14H-6	94.49	112.84	128.25	Tie to	U1417D-14H-2	42.72	111.73	128.25
U1417D-14H-5	128.80	117.09	133.61	Tie to	U1417C-14H-2	81.77	115.32	133.61
U1417C-14H-6	131.03	121.81	140.10	Tie to	U1417D-15H-3	22.60	122.53	140.10
U1417D-15H-6	113.27	127.93	145.51	Tie to	U1417C-15H-3	65.55	126.16	145.51
U1417C-15H-6	140.17	131.40	150.75	Tie to	U1417D-16H-2	77.63	131.08	150.75
U1417D-16H-6	100.77	137.31	156.99	Tie to	U1417C-16H-3	149.81	136.50	156.99
U1417C-16H-6	73.23	140.23	160.72	Tie to	U1417D-17H-2	8.07	139.88	160.72
U1417D-17H-5	139.97	145.70	166.54	Tie to	U1417C-17H-2	7.58	143.08	166.54
U1417C-17H-5	127.57	148.78	172.24	Tie to	U1417D-18H-3	17.29	150.57	172.24
U1417D-18H-6	123.99	156.14	177.81	Tie to	U1417C-18H-2	120.88	153.71	177.81
U1417C-18H-3	103.75	155.04	179.14	Tie to	U1417B-18H-1	90.79	153.51	179.14
U1417B-18H-5	77.27	159.37	185.00	Tie to	U1417A-21H-2	109.36	160.99	185.00
U1417A-21H-3	135.07	162.75	186.76	Tie to	U1417B-19H-1	12.14	161.32	186.76
U1417B-19H-4	111.97	166.82	192.26	Tie to	U1417C-20H-2	149.74	167.10	192.26
U1417C-20H-5	100.65	171.11	196.26	Tie to	U1417B-20H-2	80.73	169.19	196.26
U1417B-20H-7	38.01	176.06	203.14	Tie to	U1417D-24H-2	3.57	177.24	203.14
U1417D-24H-3	47.73	179.18	205.08	Tie to	U1417C-21H-4	7.77	178.18	205.08
U1417C-21H-4	145.23	179.55	206.45	Tie to	U1417D-25H-1	51.17	180.91	206.45
U1417D-25H-3	106.26	184.46	210.00	Tie to	U1417B-22H-3	21.32	181.33	210.00
U1417B-22H-4	47.19	182.62	211.29	Tie to	U1417C-22H-1	16.37	183.26	211.29
U1417C-22H-7	54.03	192.34	220.37	Tie to	U1417B-24H-1	77.58	188.28	220.37
U1417B-24H-1	77.58	188.28	220.37	Append	U1417B-24H-4	54.00	192.09	224.18

Tie points in bold reflect tentative correlations. See text for details.



Table T12. Polarity chronozone interpretations, Site U1417.

Polarity zone interpretation	Age	± (Ma)	Depth	
	(Ma)		CCSF-B (m)	± (m)
C1n (B) Matuyama/Brunhes	0.781	0.02	111	1
C1r.1n (T) Jaramillo	0.988	0.02	133	1.5
C1r.1n (B) Jaramillo	1.072	0.02	140	1
C1r.2n (M) Cobb Mountain	1.179	0.02	150.5	1.5
C2n (T) Olduvai	1.778	0.02	186	2
C2n (B) Olduvai	1.945	0.02	205.5	1
C2r.1n (T) Reunion	2.128	0.02	220.5	2
C2r.1n (B) Reunion	2.148	0.02	224.5	4
C2r.2r (B) Gauss/Matuyama	2.581	0.02	287.5	1
C2An.3n (B) Gilbert/Gauss	3.596	0.02	365	5
C3n.1n (T) Cochiti	4.187	0.02	375	5
Middle of C3n.3n (B) Sidufjal to C3n.4n (B) Thvera	5.017	0.218	419	5
C3An.1n (T)	6.033	0.1	475	10
C3Bn (T)	7.14	0.1	585	20

B = bottom, T = top, M = middle.

Table T13. Shipboard age-depth models and sedimentation rates, Site U1417.

Age (Ma)	Average depth CCSF-A (m)	Minimum depth CCSF-A (m)	Maximum depth CCSF-A (m)	Average depth CCSF-B (m)	Minimum depth CCSF-B (m)	Maximum depth CCSF-B (m)	Average sed. rate (m/m.y.)	Minimum sed. rate (m/m.y.)	Maximum sed. rate (m/m.y.)
0.0	0.00	0.00	0.00	0.0	0.0	0.0	135.0	118.4	153.0
0.5	78.03	57.80	98.27	67.5	50.0	85.0	135.0	118.4	153.0
0.5	78.03	57.80	98.27	67.5	50.0	85.0	130.0	110.3	148.2
1.0	153.18	144.51	161.85	132.5	125.0	140.0	130.0	110.3	148.2
1.0	153.18	144.51	161.85	132.5	125.0	140.0	75.0	61.2	88.5
1.5	196.53	184.97	208.09	170.0	160.0	180.0	75.0	61.2	88.5
1.5	196.53	184.97	208.09	170.0	160.0	180.0	75.0	63.2	86.4
2.0	245.12	234.97	255.27	207.5	200.0	215.0	75.0	63.2	86.4
2.0	245.12	234.97	255.27	207.5	200.0	215.0	145.0	134.2	156.9
2.5	323.26	313.26	333.26	280.0	270.0	290.0	145.0	134.2	156.9
2.5	323.26	313.26	333.26	280.0	270.0	290.0	85.0	67.1	106.0
3.0	365.76	348.26	383.26	322.5	305.0	340.0	85.0	67.1	106.0
3.0	365.76	348.26	383.26	322.5	305.0	340.0	65.0	42.3	88.0
3.5	398.26	383.26	413.26	355.0	340.0	370.0	65.0	42.3	88.0
3.5	398.26	383.26	413.26	355.0	340.0	370.0	40.0	18.3	58.9
4.0	418.26	403.26	433.26	375.0	360.0	390.0	40.0	18.3	58.9
4.0	418.26	403.26	433.26	375.0	360.0	390.0	40.0	20.1	60.6
4.5	438.26	423.26	453.26	395.0	380.0	410.0	40.0	20.1	60.6
4.5	438.26	423.26	453.26	395.0	380.0	410.0	45.0	23.5	66.9
5.0	460.76	448.26	473.26	417.5	405.0	430.0	45.0	23.5	66.9
5.0	460.76	448.26	473.26	417.5	405.0	430.0	55.0	34.5	72.5
5.5	488.26	473.26	503.26	445.0	430.0	460.0	55.0	34.5	72.5
5.5	488.26	473.26	503.26	445.0	430.0	460.0	55.0	35.6	74.3
6.0	515.76	503.26	528.26	472.5	460.0	485.0	55.0	35.6	74.3
6.0	515.76	503.26	528.26	472.5	460.0	485.0	110.0	68.9	149.2
6.5	570.76	533.26	608.26	527.5	490.0	565.0	110.0	68.9	149.2
6.5	570.76	533.26	608.26	527.5	490.0	565.0	95.0	44.4	140.2
7.0	618.26	593.26	643.26	575.0	550.0	600.0	95.0	44.4	140.2
7.0	618.26	593.26	643.26	575.0	550.0	600.0	60.0	32.9	92.1
7.5	648.26	633.26	663.26	605.0	590.0	620.0	60.0	32.9	92.1
7.5	648.26	633.26	663.26	605.0	590.0	620.0	20.0	1.0	40.1
8.0	658.26	648.26	668.26	615.0	605.0	625.0	20.0	1.0	40.1
8.0	658.26	648.26	668.26	615.0	605.0	625.0	10.0	0.0	25.1
8.5	663.26	653.26	673.26	620.0	610.0	630.0	10.0	0.0	25.1
8.5	663.26	653.26	673.26	620.0	610.0	630.0	10.0	0.0	24.7
9.0	668.26	658.26	678.26	625.0	615.0	635.0	10.0	0.0	24.7
9.0	668.26	658.26	678.26	625.0	615.0	635.0	10.0	0.0	23.2
9.5	673.26	663.26	683.26	630.0	620.0	640.0	10.0	0.0	23.2
9.5	673.26	663.26	683.26	630.0	620.0	640.0	10.0	0.0	23.6
10.0	678.26	668.26	688.26	635.0	625.0	645.0	10.0	0.0	23.6
10.0	678.26	668.26	688.26	635.0	625.0	645.0	5.5	5.3	5.7
39.0	838.26	830.26	846.26	795.0	787.0	803.0	5.5	5.3	5.7



Table T14. Alternating field (AF) demagnetization steps used, Site U1417.

Hole	Cores undertaken	AF demagnetization steps (mT)
U1417A	1H, 2H, 3H, 4H	0, 5, 10, 15, 20
U1417A	All other cores in Hole U1417A	0, 10, 20
U1417B	All cores	0, 10, 20
U1417C	All cores	0, 10, 20
U1417D	Sections 13H-1, 13H-2, 14H-1, 14H-2, 14H-3, 14H-4, 15H-3	0, 5, 10, 15, 20
U1417D	Sections 53X-2, 54X-1, 54X-2, 54X-3, 54X-4, 55X-3	0, 10, 20, 25, 30
U1417D	Sections 51X-1, 51X-2, 51X-3, 52X-3, 54X-1	0, 10, 20, 25, 30, 35, 40
U1417D	Sections 51X-4, 51X-5, 52X-1, 52X-2, 53X-1, 53X-2, 54X-2, 54X-3, 54X-4, 55X-1, 55X-3, 56X-1, 57X-1, 57X-2, 58X-1, 58X-2, 58X-3, 59X-1, 59X-2, 59X-5, 59X-6, 64X-1	0, 10, 20, 25, 30
U1417D	Section 65X-1	0, 10, 20, 25
U1417D	All other cores	0, 10, 20
U1417E	Sections 8R-4, 21R-1, 27R-3, 28R-1, 28R-2, 35R-1, 39R-3, 39R-6	0, 10, 20, 25, 30
U1417E	Section 27R-1	0, 10, 20, 25
U1417E	All other cores	0, 10, 20



Table T15. Position of the top (T) and bottom (B) of polarity chronozones and subchronozones, Site U1417.

Polarity boundary interpretation	Age (Ma)		Hole U1417A				Hole U1417B			
			Core, section, interval (cm)	Depth CSF-A (m)	Depth CCSF-A (m)	Depth CCSF-B (m)	Core, section, interval (cm)	Depth CSF-A (m)	Depth CCSF-A (m)	Depth CCSF-B (m)
C1n (B) Matuyama/Brunhes	0.781	Top	14H-5, 120	111.60	127.00	109.86	13H-1, 90	106	127.36	110.17
		Base	14H-7, 10	113.50	128.90	111.49	13H-2, 90	107.5	128.86	111.46
C1r.1n (T) Jaramillo	0.988	Top	17H-2, 140	135.80	153.13	132.46				
		Base	17H-4, 10	137.50	154.83	133.93				
C1r.1n (B) Jaramillo	1.072	Top	18H-1, 130	143.70	161.44	139.65				
		Base	18H-3, 22.5	144.85	162.59	140.64				
C2n (T) Olduvai	1.778	Top					23H-4, 37.5	187.15	215.78	185.81
		Base					24H-2, 25	189.25	221.34	189.92
C2n (B) Olduvai	1.945	Top					28H-2, 22.5	203.93	241.63	204.92
		Base					28H-2, 127.5	204.98	242.68	205.70
C2r.1n (T) Reunion	2.128	Top								
		Base								
C2r.1n (B) Reunion	2.148	Top					34H-1, 85	224.25	267.51	224.25
		Base					34H-1, 125	224.65	267.91	224.65
C2An.1n (T) Gauss/Matuyama	2.581	Top					40X-3, 05	284.2	330.68	287.42
		Base					40X-3, 60	284.8	331.28	288.02

Polarity chron interpretation	Age (Ma)		Hole U1417C				Hole U1417D				Hole U1417E			
			Core, section, interval (cm)	Depth CSF-A (m)	Depth CCSF-A (m)	Depth CCSF-B (m)	Core, section, interval (cm)	Depth CSF-A (m)	Depth CCSF-A (m)	Depth CCSF-B (m)	Core, section, interval (cm)	Depth CSF-A (m)	Depth CCSF-A (m)	Depth CCSF-B (m)
C1n (B) Matuyama/Brunhes	0.781	Top												
		Base												
C1r.1n (T) Jaramillo	0.988	Top	15H-6, 110	131.1	150.45	130.13925	16H-4, 22	133.52	153.2	132.52				
		Base	16H-2, 105	134.55	155.04	134.1096	16H-5, 20	135	154.68	133.8				
C1r.1n (B) Jaramillo	1.072	Top					17H-2, 120	141	161.84	139.99				
		Base					17H-3, 10	141.4	162.24	140.34				
C2n (T) Olduvai	1.778	Top												
		Base												
C2n (B) Olduvai	1.945	Top												
		Base												
C2r.1n (T) Reunion	2.128	Top					36H-2, 102	221.32	261.63	219.70				
		Base					36H-3, 87	222.68	262.99	220.71				
C2r.1n (B) Reunion	2.148	Top												
		Base												
C2An.1n (T) Gauss/Matuyama	2.581	Top					45X-1, 55	290.25	330.5	287.24	4R-4, 25	287.55	330.81	287.55
		Base					45X-2, 30	291.4	331.65	288.39	4R-4, 57.5	287.88	331.14	287.88
C2An.3n (B) Gilbert/Gauss	3.596	Transition				53X			365 ±5					
C3n.1n (T) Cochiti	4.187	Transition				54X			375 ±5					
Middle of C3n.3n (B) Sidufjal to C3n.4n (B) Thvera	5.017	Transition				59X			422 ±5	8R to 9R			418 ±5	
C3An.1n (T)	6.033	Transition								14R to 15R			475 ±10	
C3Bn (T)	7.14	Transition								25R to 27R			585 ±20	

Table T16. Vertical seismic profile direct arrival times, Hole U1417E.

Receiver depth WRF (m)	Receiver depth WRF (m)	Measured one-way traveltime (s)	Corrected one-way traveltime (s)	Corrected two-way traveltime (s)
4411.3	211.3	2.9299	2.9357	5.8714
4411.9	211.9	2.9309	2.9367	5.8734

Measured traveltimes are times between the arrival of the pulse at a hydrophone located 2 m below the air guns and at the receiver in the borehole. Corrected traveltimes are times between sea level and the borehole receiver.